IPP-Report

MAX-PLANCK-INSTITUT
FÜR PLASMAPHYSIK

Maximilian Fuhr

Deformation mechanisms of drawn tungsten wires

IPP 2024-11
April 2024

Technische Universität München
TUM School of Engineering and Design

Deformation mechanisms of drawn tungsten wires

Maximilian Fuhr

Vollständiger Abdruck der von der TUM School of Engineering and Design der Technischen Universität München zur Erlangung eines

Doktors der Ingenieurwissenschaften (Dr.-Ing.)

genehmigten Dissertation.

Vorsitz: Prof. Dr. techn. Dipl.-Ing. Peter Mayr

Prüfer*innen der Dissertation:

1. Prof. Dr. rer. nat. Rudolf Neu
2. Prof. Dr.-Ing. Wolfgang Pantleon

Die Dissertation wurde am 01.08.2023 bei der Technischen Universität München eingereicht und durch die TUM School of Engineering and Design am 15.01.2024 angenommen.

There's unknown all around at every moment.
That's where you seek knowledge.
—Frank Herbert, Children of Dune (1976)

Abstract

In this study, a series of drawn, potassium doped tungsten wires (potassium content: 75 ppm) with different diameters was investigated in order to determine the cause for the shift of their ductile-to-brittle transition to lower temperatures due to an increase in working strain, i.e. a decrease in wire diameter. The wires contained in the series investigated were drawn from the same forged rod. Thus, the differences in the wires' mechanical properties observed in room-temperature uniaxial tensile tests can be related to the deformation-induced microstructural changes. Using transient mechanical tests, namely repeated stress relaxation experiments and strain-rate jump tests, the motion of screw dislocation via the kink-pair mechanism was determined to be controlling the rate of plastic deformation in wires that showed plasticity at room temperature. The fact that the kink-pair mechanism is also rate-controlling during plastic deformation of tungsten materials with different grain morphology and/or crystallographic texture is a strong indication that the shift of the ductile-to-brittle transition temperatures in drawn tungsten wires is caused by the change in microstructure and crystallographic texture. These changes were quantified using structure-property relationships, which were established by combining the results of the mechanical tests with an extensive microstructural study using Electron Backscattering Diffraction (EBSD), Scanning Transmission Electron Microscopy (STEM) and X-ray Diffraction (XRD). The curling of grains around a $\langle 110 \rangle$ axis in tungsten wires was quantified for the first time. Furthermore, it could be concisely shown that wire drawing leads to a $\langle 110 \rangle$ fibre texture, which sharpens with increasing strain accumulated in wire drawing. In addition to identifying structure-property relationships, the strain hardening behaviour observed in room-temperature tensile tests was successfully modelled using the Kocks-Mecking model. The model is microstructure-informed and uses the dislocation density as governing variable. By combining the results of the modelling with the structure-property relationships, an empirical model explaining the shift of the ductile-to-brittle transition temperature upon cold-working was devised. The model is based on the hypothesis that ductile behaviour is observed if the incremental work spent for plastic deformation is lower than the spent for crack extension. It can be shown that especially the decrease in grain width yields a dilution of foreign atoms per unit grain boundary area, which increases grain boundary cohesion and hampers intragranular crack growth. The emergence of a microstructure consisting of elongated grains with a high grain aspect ratio and an increase in this ratio with increasing accumulated drawing strain furthermore yields an effective crack deflection during intragranular crack growth. These mechanisms considerably increase the incremental work expended during crack growth. Although the incremental work spent during plastic deformation is also increased due to grain boundary strengthening and work hardening, the incremental work during crack extension remains higher, giving tungsten wires with a sufficiently high accumulated drawing strain the ability to deform plastically at room temperature. The devised model is also successfully applied to explain the deformation behaviour of annealed and ion-irradiated tungsten wires and hot- or cold-rolled tungsten plates.

Kurzfassung

In dieser Arbeit wurde eine Serie bestehend aus gezogenen, kaliumdotierten Wolframdrähten (Kaliumgehalt: 75 ppm) mit verschiedenen Durchmessern untersucht, um die Ursache für die Verschiebung ihres Duktil-Spröd-Überganges hin zu niedrigeren Temperaturen infolge einer Erhöhung des Umformgrads, d. h. einer Verringerung des Drahtdurchmessers, zu ermitteln. Die Drähte der untersuchten Serie wurden aus demselben Schmiedestab gezogen. Etwaige Unterschiede in den mechanischen Eigenschaften können damit auf Änderungen in der Mikrostruktur und der kristallographischen Textur zurückgeführt werden. Mit Hilfe transienter mechanischer Tests (wiederholte Spannungsrelaxationsversuche & Dehnratensprungversuche) wurde festgestellt, dass die Bewegung von Schraubenversetzungen mittels des Kinkenpaarmechanismus die Rate der plastischen Verformung bestimmt. Da dies auch bei Wolframwerkstoffen mit anderer Kornmorphologie oder kristallografischer Textur der Fall ist, muss die Ursache für die Verschiebung der Duktil-Spröd-Übergangstemperaturen in Drähten deren verformungsbedingte Veränderung der Mikrostruktur sein. Um diese Änderungen zu quantifizieren, wurden Struktur-Eigenschafts-Beziehungen formuliert, indem die Ergebnisse der bei Raumtemperatur durchgeführten transienten und monotonen mechanischen Tests mit einer umfassenden mikrostrukturellen Analyse mittels Elektronenrückstreubeugung (EBSD), Rastertransmissionselektronenmikroskopie (STEM) und Röntgenbeugung (XRD) kombiniert wurden. Dabei konnte die Krümmung der Körner um eine ⟨110⟩-Achse in Wolframdrähten erstmals quantifiziert werden. Darüber hinaus konnte gezeigt werden, dass das Drahtziehen zur Entwicklung einer ⟨110⟩-Fasertextur führt, die systematisch mit zunehmendem Umformgrad schärfer wird. Neben der Formulierung von Struktur-Eigenschafts-Beziehungen konnte das in den uniaxialen Zugversuchen beobachtete Kaltverfestigungsverhalten erfolgreich mit dem Kocks-Mecking-Modell beschrieben werden. Das Modell bezieht die Mikrostrukturentwicklung mit ein und verwendet die Versetzungsdichte als bestimmende Größe. Durch Kombination der Ergebnisse der Modellierung mit den Struktur-Eigenschafts-Beziehungen wurde ein empirisches Modell entwickelt, das die Verschiebung der Duktil-Spröd-Übergangstemperatur bei Kaltverformung während des Drahtziehens beschreibt. Das Modell basiert auf der Hypothese, dass duktiles Verhalten beobachtet wird, wenn die für die plastische Verformung benötigte inkrementelle Arbeit geringer ist als die für die Rissausdehnung. Es kann gezeigt werden, dass insbesondere die Abnahme der Kornbreite zu einer verringerten Konzentration von Fremdatomen an Korngrenzen führt, was die Korngrenzenkohäsion erhöht und das intragranulare Risswachstum erschwert. Die Entstehung einer Mikrostruktur, die aus länglichen Körnern mit einem hohen Aspektverhältnis besteht, und eine Zunahme dieses Verhältnisses mit zunehmendem Umformgrad, führen zu einer effektiven Rissablenkung bei intragranularem Risswachstum. Obwohl die inkrementelle Arbeit, die für plastische Verformung benötigt wird, durch Kornfeinung und Kaltverfestigung erhöht wird, bleibt die inkrementelle Arbeit bei Risswachstum infolge der genannten Mechanismen höher, was Wolframdrähten mit einem ausreichend hohen Umformgrad die Fähigkeit gibt, sich bei einer bestimmten Temperatur plastisch zu verformen. Das entwickelte Modell kann darüberhinaus auch erfolgreich zur Erklärung des Duktil-Spröd-Übergangs anderer Wolframwerkstoffe eingesetzt werden.

Nomenclature

AKS	Aluminium-Potassium-Silicon (doping)
APT	Ammonium paratungstate
BF	Bright field
BSE	Backscattered electrons
CCD	Charge-coupled device
CG	Coarse-grained
CMOS	Complementary metal-oxide semiconductor
CP	Crystal plasticity
CTEM	Conventional transmission electron microscopy/microscope
CVD	Chemical vapour deposition
DBT	Ductile-to-brittle transition
DBTT	Ductile-to-brittle transition temperature
DEMO	Demonstration power plant
DF	Dark field
EBSD	Electron backscatter diffraction
EBSP	Electron backscatter pattern
ETD	Everhart-Thornley detector
FEM	Finite element model(ing)
FFT	Fast Fourier transformation
FIB	Focused ion beam
FWHM	Full width at half maximum
GBS	Grain boundary sliding
GD-MS	Glow discharge mass spectroscopy
HAADF	High angular annular dark field

HAGB	High-angle grain boundary
HFW	Horizontal field width
KMM	Kocks-Mecking model
LAGB	Low-angle grain boundary
LCFS	Last closed flux surface
LIM	Line intersection method
LOM	Light optical microscopy/microscope
LS	Longitudinal section
NIST	National Institute of Standards and Technology
OM	Orientation map
PCA	Principal component analysis
PE	Primary electrons
PFC	Plasma-facing component
PFMC	Plasma-facing material
REX	Recrystallisation
ROI	Region of interest
RSRE	Repeated stress relaxation experiment(s)
SE	Secondary electrons
SEM	Scanning electron microscopy/microscope
SOL	Scrape-off layer
SPD	Severe plastic deformation
SRE	Stress relaxation experiment(s)
SRJT	Strain-rate jump test(s)
STEM	Scanning transmission electron microscopy/microscope
SX	Single crystal
TCS	Transversal cross-section
TDS	Thermally diffuse scattering
TEM	Transmission electron microscopy/microscope
TKD	Transmission Kikuchi diffraction
UFG	Ultrafine-grained
XRD	X-ray diffraction/diffractogram

Contents

Chapter 1

Introduction

Tungsten (W) features the highest melting point among all pure metals ($T_\mathrm{m} = (3422 \pm 15)\,^\circ\mathrm{C}$ [1]). Historically, the first widespread applications of tungsten were as alloying element in steel, as filament in incandescent lamps as well as in the form of tungsten carbides in hard metals [1]. Tungsten features an exceptional set of properties apart from its high melting point. Among these are a good thermal and electrical conductivity, a high hardness and strength and a high resistance to creep [1–5]. These characteristics in combination with a sufficient endurance against bombardment with high energetic particles make tungsten the most promising material for highly loaded components of a fusion reactor, see section 3.4. Pure bulk tungsten is very rarely used as structural material [4]. This is due to a characteristic called *ductile-to-brittle transition* (DBT) which tungsten shares with other group V (Ta, V, Nb) and VI metals (Cr, Mo) [6] as well as semiconductors [7–9] and some metals with a hexagonally closest packed (h.c.p.) crystal structure. The ductile-to-brittle transition describes the strong temperature dependence of a material's fracture behaviour: If the material is deformed below a certain transition temperature (ductile-to-brittle transition temperature T_DBT), it fails brittle. Above T_DBT, the material behaves ductile, i.e. it can be deformed plastically before failure. The DBT is often described using the fracture toughness, the elongation to fracture, the uniform elongation or any other measure of ductility [3]. A sketch of the temperature dependence of a given measure of ductility for a material showing a ductile-to-brittle transition is shown in figure 1.1.

Due to its high melting point, casting of tungsten is not possible[1]. Thus, bulk materials are commonly produced by powder metallurgy followed by a hot-working[2] procedure. The ductile-to-brittle transition of hot-worked tungsten materials is in the range of 200 °C to 300 °C [11, 12]. Thus, these hot-worked tungsten materials cannot be used as structural materials at room temperature due to their inherent brittleness.

For the application as plasma-facing material and other structural applications, a more damage-tolerant, i.e. ductile material would be desirable. It has been shown that the ductility and fracture toughness of tungsten can be increased by alloying with Re [13–15]. Furthermore, reinforcing a brittle tungsten matrix using high-strength fibres can bestow a pseudo-ductility on the composite [16–18]. Apart from alloying tungsten with rare and expensive elements or using

[1] Theoretically, tungsten could be cast using crucibles produced from graphite or ceramic compounds. Since these are however composed of carbides, oxides or nitrides and the contamination of tungsten with light elements such as C, N or O is detrimental to its ductility, casting tungsten using these crucible materials is not expedient. Moreover, tungsten shows catastrophic oxidation behaviour at $T > 600\,^\circ\mathrm{C}$ [3], i.e. casting of tungsten would need to be performed under reducing atmosphere.

[2] Hot-working means the deformation of a material above its recrystallisation temperature, i.e. the temperature at which the microstructure is recrystallised after an annealing duration of 1 h [10].

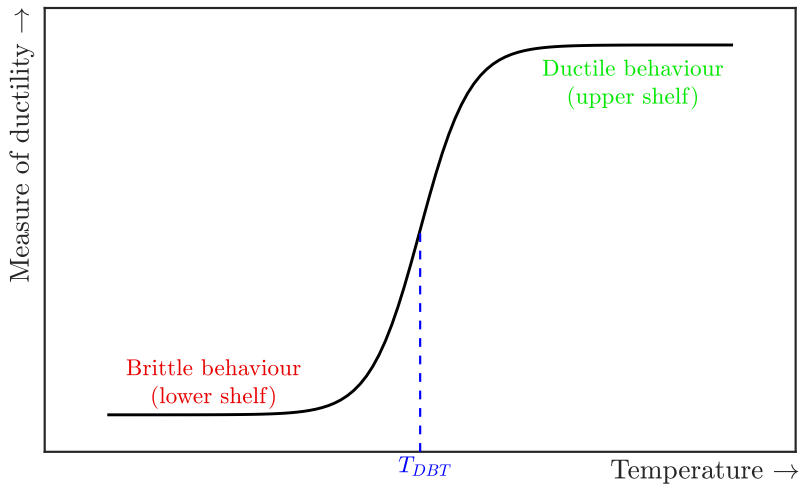

Figure 1.1: Sketch of the temperature dependence of a measure of ductility of a material exhibiting a ductile-to-brittle transition. Below the transition temperature T_{DBT}, in the so-called *lower shelf*, the material fails in a brittle manner without allowing for plastic deformation. Above T_{DBT}, in the *upper shelf* the material is ductile and can be deformed plastically before failure.

fibre-reinforcements, applying cold-working[3] procedures like wire drawing or rolling[4] have proven to shift the ductile-to-brittle transition to lower temperatures, making sufficiently worked materials ductile at ambient temperatures and below. This knowledge is exploited since more than a century in order to produce ductile and thus coilable filaments for incandescent lighting [23]. The reasons for the shift of T_{DBT} are however not yet understood completely. Excessive studies on rolled tungsten plates [24–31] point to the role of the microstructure in the shift of the transition, see section 4.2.1.2.1. The causes of the shift of T_{DBT} in drawn tungsten wires were however so far not studied systematically. This means that studies available so far either compare material from different manufacturers, restrict themselves to one diameter and thus only cover parts of the drawing process, or concentrate only on a certain aspect of the properties of the wire. An improvement of the understanding of the mechanisms behind the change of the ductile-to-brittle transition in tungsten by wire drawing is relevant both for the development of bulk ductile tungsten materials and their application as reinforcement fibres in advanced composites such as those envisioned for the use in future fusion reactors.

[3] Analogous to hot-working, cold-working means a working procedure that has to be performed at temperatures below the recrystallisation temperature.

[4] In addition, tungsten processed by severe plastic deformation processes shows the characteristic shift of T_{DBT} to lower temperatures upon cold-working [19–22].

Chapter 2

Objectives and approach

The main objective of the present study is to identify the reasons for the change in mechanical properties of cold-worked tungsten materials which give rise to the shift of the ductile-to-brittle transition temperature. Drawn wire was selected since wire drawing allows for reaching a very high level of accumulated cold-working strain and since wire drawing is an industrially mature process due to the use of drawn tungsten wires as filaments for incandescent lighting. The present study was performed on a wire series consisting of AKS-doped tungsten wires manufactured by OSRAM GmbH[1], Schwabmünchen. This series of wires covers the whole drawing process (see section 5.1.2) from the forged rod to heavily cold-drawn wires. Tungsten shows starkly different deformation and fracture behaviour before and after cold-working: While forged rods are brittle at ambient temperature [32], several authors [33, 34] report that wires with a diameter of less than approximately[2] 1 mm deform plastically and exhibit a ductile fracture mode at room temperature. Thus, there is a shift of T_{DBT} with increasing strain accumulated during wire drawing. In theory, the mentioned differences in mechanical properties between the different wires before and after cold-working could be caused by variations in their impurity level [35]. Since all wires contained in the series investigated in this study were subsequently drawn from the same forged rod and their chemical composition is not altered significantly[3] during wire drawing [32], they exhibit similar impurity levels. Thus, differences in the deformation behaviour of the investigated wires can only be expected from the following reasons:

1. Differences in the rate-controlling deformation mechanism
2. Differences in the microstructure and crystallographic texture through structure-property relations

The mechanisms controlling the rate of plastic deformation of drawn tungsten wires at room-temperature were investigated using transient mechanical tests, namely strain-rate jump tests and repeated stress relaxation experiments. Structure-property relations were established by quantifying the complex microstructure of drawn tungsten wires (see section 5.1.4) in as many ways possible and reasonable using Electron Backscattering Diffraction (EBSD), Scanning Transmission Electron Microscopy (STEM) and X-ray Diffraction (XRD) and linking the results to the stress-strain characteristic observed in room-temperature tensile tests. An improved understanding of the governing deformation mechanisms in tungsten wires and their change with the accumulated drawing strain was achieved by performing microstructure-informed modelling of the strain hardening behaviour using the Kocks-Mecking model (see section 4.2.2.1.2).

[1] now ams OSRAM GmbH

[2] Slight variations in this value caused by different working procedures and different chemical compositions have to be taken into account.

[3] The wire is closed off from impurities due to a thin oxide film acting as diffusion barrier [32] during the drawing process.

Chapter 3

Motivation: Materials for controlled nuclear fusion technology

3.1 Basics of controlled nuclear fusion

Nuclear fusion is the process that powers the stars, among them also our sun. It describes the fusion of light atomic nuclei to form heavier ones. For a successful fusion of two nuclei to take place, they have to possess enough kinetic energy to overcome the Coulomb repulsion [36]. The conditions needed for nuclear fusion can be met in a plasma, i.e. a superheated gas in which the atoms are largely ionized. The temperatures required for fusion are lower than expected from classical calculations, since nuclei can tunnel through the Coulomb barrier. The rate of fusion can be described as a convolution of the Maxwell distribution that describes the velocity of the particles in the plasma and the cross-section of the fusion reaction, which is strongly energy-dependent. The highest rate of fusion at the lowest temperature is found for the fusion of heavy ($^{2}_{1}$H, deuterium) and super heavy ($^{3}_{1}$H, tritium) hydrogen [36]

$$^{2}_{1}\mathrm{H} + {}^{3}_{1}\mathrm{H} \rightarrow {}^{4}_{2}\mathrm{He} + {}^{1}_{0}\mathrm{n} \tag{3.1}$$

The negative mass difference between the educts (m_{ed}) and products (m_{prod}) in the above-mentioned reaction

$$\Delta m = m_{\mathrm{prod}} - m_{\mathrm{ed}} < 0$$

yields a release of energy following Einstein's equation [37]

$$E = m\,c^2 \tag{3.2}$$

where E : Energy
m : Mass
c : Velocity of light in vacuum.

The fusion of deuterium and tritium releases an energy of 17.58 MeV. Due to the difference in

rest mass, the alpha particle takes 3.52 MeV while the neutron takes 14.06 MeV [38]. The sources for the D-T reaction (see equation (3.1)) are abundant: About 0.0035 % of the earth's oceans' water is deuterium[1] in the form of DHO [38], while tritium can be bred from a Li isotope [36].

3.2 Nuclear fusion reactor concepts

Since the ignition of the first hydrogen bomb on 31.10.1952 [38], which utilises the nuclear fusion reaction in a military context, there are ongoing attempts to use nuclear fusion as a controlled energy source. Currently, two major approaches are pursued by the international research community: Magnetic confinement fusion and inertial confinement fusion.

In inertial confinement fusion, a pellet containing the fusion fuel is uniformly illuminated from all sides by powerful lasers [38]. Depositing the photon energy in the outer layers of the pellet generates a shock wave which compresses the pellet core and eventually creates the plasma conditions (pressure, temperature, density) to initiate fusion processes [39]. The term *inertial confinement* refers to the exploitation of the finite inertia of the atoms in the pellet, which keeps them inside the critical radius in which the plasma conditions are sufficient for fusion reactions to occur.

In magnetic confinement fusion, the shape of the plasma is controlled by a number of external magnets. The general purpose of the magnetic field is two-fold: On the one hand, the plasma has to be kept apart from the walls of the reactor since sputtering of the wall materials due to bombardment of the wall by plasma particles introduces heavier elements into the plasma, which emit energy away from the plasma core by ionisation[2] and radiation losses[3] and thereby cool it. On the other hand, the shape of the plasma has a direct influence on its stability and the magnetic field can thus influence the efficiency of the fusion reaction. The first (unsuccessful) concepts of magnetic confinement fusion, the so-called *mirror machines*, used linear configurations and inhomogeneous magnetic fields to confine the plasma. Modern approaches use toroidal configurations in which field lines are contained in closed magnetic flux surfaces [36]. The two most advanced magnetic confinement fusion reactor concepts are the Tokamak (see figure 3.1a) and the Stellarator (see figure 3.1b).

In a Tokamak, the magnetic field confining the plasma has the shape of a torus and is composed of two major components, namely the poloidal and the toroidal field component. The toroidal field component yields the donut-shape of the plasma. In addition, the plasma itself acts as a secondary transducer coil, with the central solenoid representing the primary transducer coil. By continuously changing the current in the primary coil, a current is induced in the secondary coil, i.e. the plasma. This generates the poloidal magnetic field component. The combined field comprising all field components can be described as nested helices that wind around the torus. This configuration facilitates an effective and stable confinement of the plasma. In order to further shape the plasma, additional coils like the vertical field coils shown in figure 3.1a can be installed. The plasma current is achieved by continuously changing the current in the primary coil. The primary coil however needs to be turned off[4] prior to reaching its current limits. Afterwards, the current can be ramped up again. Thus, Tokamaks can only be operated in a pulsed manner if there are no other means for current drive [41]. The induced current additionally heats the plasma due

[1] Apart from DHO, also D_2O can be found, but this configuration is significantly rarer.

[2] In order to strip electrons from an atom/ion, the ionisation energy has to be overcome.

[3] The electrons attached to ions that are not fully ionised can be excited and radiate energy in the form of photons by de-excitation. This is especially critical for high-Z elements like tungsten, which require very high energies to be fully ionised [40]. The influence of radiation cooling is immense: The ignition of a D-T plasma with as little as 0.1 %W would not be possible [38, p. 99].

[4] Changing the current direction is not practical since this would change many plasma characteristics and could cause plasma instabilities.

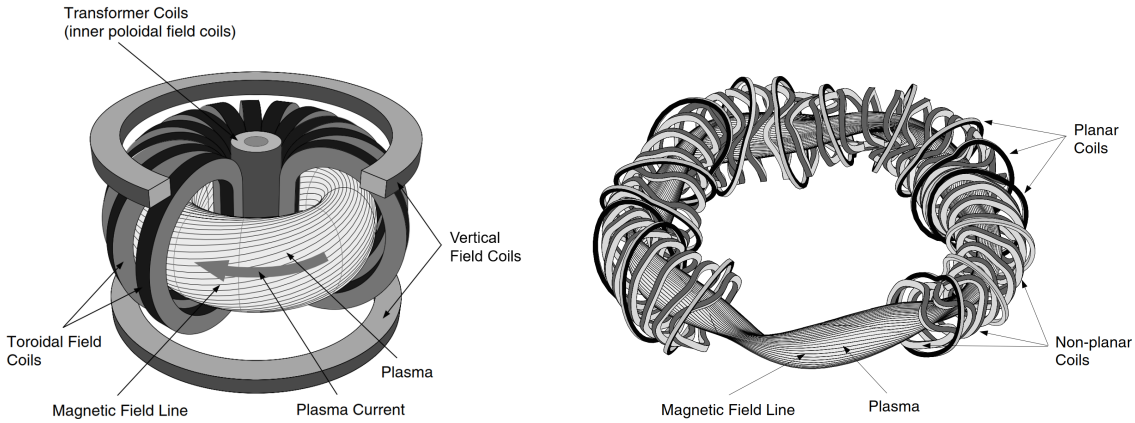

(a) Tokamak reactor concept (b) Stellarator reactor concept

Figure 3.1: Magnetic confinement fusion reactor concepts (adapted from [41]).

to Ohm's law. Since the electrical resistance of the plasma however is proportional to $T^{-3/2}$ and thus decreases with increasing plasma temperature [36], additional plasma heating techniques need to be employed in order to be able to reach higher plasma temperatures. One of these methods is neutral beam heating, in which high energetic neutral particles are injected into the plasma and transfer a part of their kinetic energy to the plasma particles. Another technique is electron and ion cyclotron resonance heating, i.e. the transfer of energy by microwave/radio frequency wave radiation tuned to the cyclotron resonance frequency of electrons or ions, respectively [36].

Renowned Tokamaks include JET (Joint European Torus) in Culham (United Kingdom), ASDEX Upgrade (Axisymmetrical Divertor Experiment) in Garching (Germany) and ITER (International Thermonuclear Experimental Reactor), which is currently under construction in Cadarache (France).

The toroidal field component of a classic Stellarator is also generated by external coils, similar to a Tokamak. The poloidal component is generated by coils that wind around the torus. Advanced, modular Stellarators like Wendelstein 7-X situated in Greifswald (Germany) employ complexly shaped individual coils in order to generate the composite magnetic field (see figure 3.1b). Since no current is needed in a Stellarator plasma, it can be operated in steady-state [41]. The development of modular Stellarators is slightly lagging behind the one of Tokamaks, since the exact shape of the magnets could not be computed up until the 1980s [42].

The principal structure of a nuclear fusion power plant does not depend on whether the reactor is built as Tokamak or Stellarator. A schematic overview of a power plant containing all relevant components is shown in figure 3.2.

The burning plasma is surrounded by the first wall, which directly borders the breeding blanket. Both components are required to shield the magnets and the outer vessel systems from the fusion neutrons, which might deteriorate their functionality [44]. In the breeding blanket, Li reacts with neutrons in order to produce tritium. Furthermore, the neutrons deposit their energy in the blanket, which heats a coolant and thus produces steam that powers a generator and eventually produces net energy. Through the divertor (see section 3.3), plasma constituents (mainly hydrogen isotopes) and the fusion ash consisting of He and plasma impurities is pumped out of the vessel. The pumped gas is then separated and processed further [43]. The unreacted educts of the fusion reaction are pumped back into the reactor. All fusion reactor concepts have in common that a nuclear meltdown like in fission reactors is not possible. If the hot plasma touches the reactor walls, the particles lose energy and the fusion process stops immediately [36]. A power plant

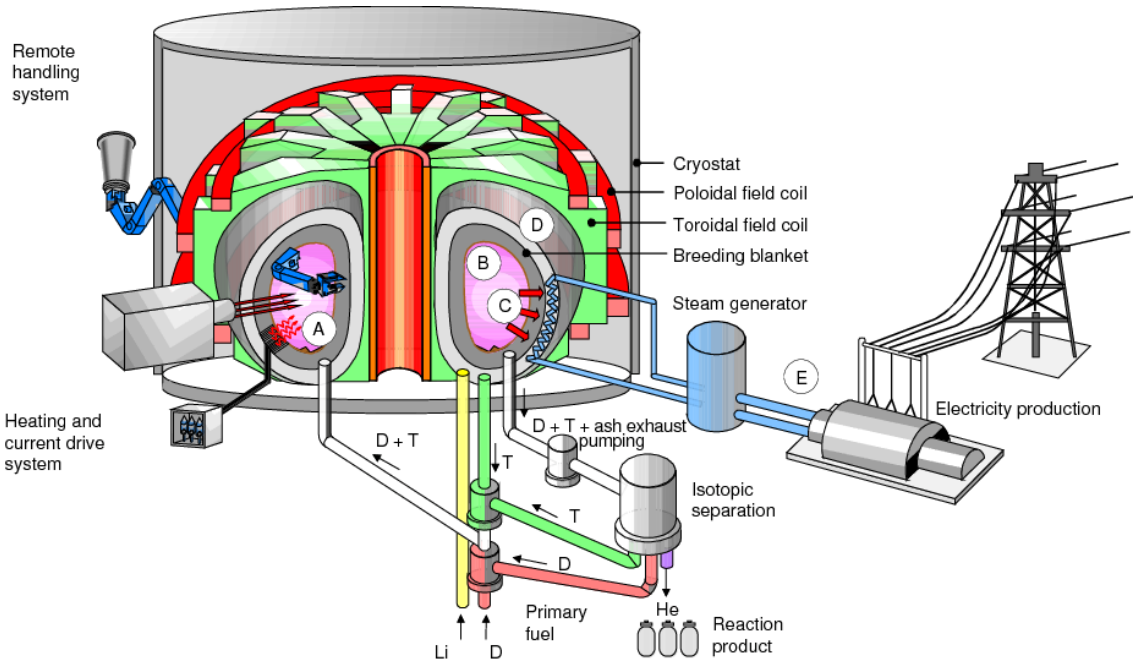

Figure 3.2: Sketch of a fusion power plant according to [43].

requires stringent safety regulations due to two main risks: On the one hand, tritium has to be handled safely since it is a β emitter with a half-life of 12.32 a [45] and can cause severe health problems when inhaled or otherwise ingested. On the other hand, the neutron irradiation will activate the wall components[5] and necessitate secure handling and disposal.

3.3 Plasma-facing components and plasma material interaction

3.3.1 Limiter and divertor concept

In modern fusion reactors, the magnetic flux surfaces are nested into each other. The last closed flux surface is called *separatrix* since it separates the confined plasma region from the so-called *scrape-off layer*, i.e. the flux surfaces along which the plasma is directed to the walls of the reactor [36]. The plasma particles contained in the SOL interact with the plasma-facing (wall) components (PFC). By using dedicated concepts, the area in which this interaction takes place can be restricted to certain components and the interaction can thereby be controlled. The two main concepts are the following: The location of so-called *limiters*, i.e. specially designed and geometrically optimized components, defines the position of the separatrix [36]. The drawback of limiters is that eroded particles can reach the plasma core by cross-field diffusion [41]. If especially high-Z nuclei enter the plasma core, they might not be fully ionised even at the high temperatures in the plasma core. By excitation and de-excitation of the remaining electrons, the ions effectively remove energy from the plasma and cool it [40]. Alternatively, the *divertor* concept can be utilised. In this configuration, the shape of the magnetic field is altered by supplemental magnetic coils in a way that previously closed flux lines are opened so that particles moving along these lines can be directed to specially designed target plates. These plates are deliberately placed at some

[5] In contrast to fission reactors, the half life of the activated reactor components will not be in the range of thousands or millions of years but only of several hundred [44].

distance to the confined plasma regions in order to avoid cross-contamination by eroded wall ions. The divertor can thus be used for controlling the power output while also efficiently removing the fusion ash, i.e. He and impurities, from the plasma [38].

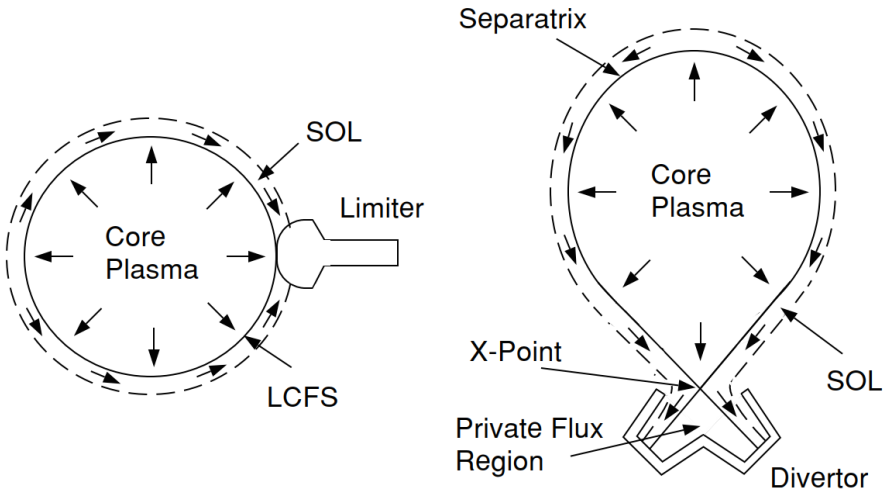

Figure 3.3: Concepts for plasma exhaust: Position of a limiter (left) with respect to the last closed flux surface (LCFS) and the scrape-off layer (SOL) and divertor geometry (right) showing the separatrix and the X-point (from [41]). The scrape-off layer is the region where particles follow open field lines towards the limiter or divertor.

3.3.2 Plasma material interaction processes

Before discussing the individual loads on plasma-facing materials (PFM) separately in the following, it should be noted that these loads need to be understood in a synergistic manner – this means that one load might change the response of the material to another load.

3.3.2.1 Heat load

Upon bombardment of the first wall components with energetic particles, the component has to withstand considerable heat fluxes. For the European design of the demonstration reactor DEMO[6] [46], peak heat fluxes in normal operation of $10\,\mathrm{MW\,m^{-2}}$ at the divertor [46] and maximum $1\,\mathrm{MW\,m^{-2}}$ at the first wall [47] are envisioned. In the case of transients and disruptions, peak heat fluxes of up to $70\,\mathrm{MW\,m^{-2}}$ for 1 s (short transients) or $100\,\mathrm{GW\,m^{-2}}$ for 1 ms to 4 ms (major disruptions) are expected in the divertor. Thus, the geometry and material combination of the plasma-facing components need to be designed[7] in a way that the thermal power can be dissipated fast enough in order to prevent overheating and the loss of structural integrity. In addition, the pulsed operation of Tokamaks means that the component has to withstand thermal fatigue [41].

3.3.2.2 Sputtering and erosion

The impingement of highly energetic particles leads to sputtering of the component surface. This can occur in the form of physical sputtering, where the plasma particle transfers a fraction of its energy to atoms of the plasma-facing material, which are then ejected and can enter the plasma

[6]The DEMO reactor is envisioned to demonstrate that a fusion reactor can be built in an economical way.
[7]The design for example involves the thickness of the components, their thermal conductivity and the inlet temperature and flow velocity of the coolant.

[41]. Especially for certain elements like carbon[8], also chemical erosion, i.e. the reaction of plasma particles (mainly hydrogen isotopes and oxygen) with the plasma-facing material to form volatile molecules, plays an important role. Both processes yield a loss of plasma-facing material (PFM) and introduce impurities into the plasma, which leads on the one hand to a dilution of the plasma fuel and on the other hand radiative losses and thus a cooling of the plasma by ionization of medium- or high-Z ions [50]. The uptake of particles that are able to form gas molecules into the PFM (mainly hydrogen isotopes and helium) can lead to the formation of blisters, which in turn facilitates the formation of flakes and thus the exfoliation of parts of the component surface. A further mechanism of material erosion is arcing: If irregularities in the surface of the plasma-facing material are present and if there is a sufficient electrical potential difference between material and plasma, a discharge can be ignited leading to evaporation and melting of the PFM [50].

3.3.2.3 Neutron irradiation

Fusion neutrons (and in addition also charge exchange hydrogen neutrals) can strongly deteriorate the properties of PFM in a fusion reactor. Since neutrons are uncharged, they are not confined by the magnetic field and impinge on the whole vessel wall. Several processes play a role in the interaction of neutrons with the plasma-facing components: For one, neutrons produce displacement damage by knocking lattice atoms from their initial sites and thereby creating different defects like Frenkel pairs [51], i.e. the combination of a self-interstitial atom and a vacancy, or dislocation loops. In addition, neutrons can react with the nuclei of the atoms of the plasma-facing material. As a result, one chemical element can transform into another one, which is called transmutation [52]. In the course of transmutation, also radioactive isotopes can be generated, which leads to the activation of the whole component. Transmutation products and other irradiation defects considerably change the material's mechanical (embrittlement, irradiation hardening, irradiation creep, loss of ductility) and thermal behaviour (degradation of thermal conductivity, loss of superconductivity) as well as their shape (volumetric swelling) [53]. The current European DEMO design estimates irradiation damages[9] of 2 dpa/fpy for the plasma-facing material tungsten in the divertor (see section 3.4) [46].

3.3.2.4 Uptake and retention of helium and hydrogen isotopes

Hydrogen isotopes from the plasma can enter plasma-facing materials and get trapped there. The number and efficiency of trapping sites is increased by neutron damage [54]. As mentioned above, the agglomeration of hydrogen isotopes can lead to the formation of gas molecules[10], which leads to the formation of bubbles, blisters and eventually to exfoliation. Thus, the trapping of helium and hydrogen isotopes can deteriorate the properties of the PFM [50]. If tritium is trapped in the PFM, it is removed from the fuel cycle, which endangers the fuel self-sufficiency and could pose a radiation hazard [41].

[8] Another example for chemical erosion is Sn, which is developed for the use in liquid metal divertor concepts, see [48]. Sn can form stannane (SnH_4), a volatile molecule similar to methane or silane [49].

[9] The displacement damage is normally given as dpa, i.e. displacements per atom. Thus, 1 dpa means that each atom in the material in average has changed its site once. The displacement damage in a reactor is given as dpa/fpy, where fpy represents one full power year.

[10] Another source for gas molecules is transmutation, see section 3.3.2.3.

3.4 Advanced tungsten materials for highly loaded components of fusion reactors

After encountering severe issues with high chemical erosion rates and co-deposition of tritium-containing layers when using graphite or Be as plasma-facing materials [55], the international fusion community is currently in the transition phase to using tungsten for the most highly loaded components in future fusion reactors [41]. Tungsten features the highest melting point ($T_\mathrm{m} = (3422 \pm 15)\,^\circ\mathrm{C}$) among all metals [1]. Due to its high activation energy for self-diffusion, tungsten has a very low creep rate [56]. The high threshold energy of at least 120.5 eV for the different hydrogen and He isotopes [57] below which no (physical) sputtering occurs, keeps the erosion rate of tungsten in a reactor at reasonably low levels. Furthermore, the low vapour pressure of tungsten [58] prevents disproportionately high thermal evaporation during operation. The low solubility for hydrogen isotopes in tungsten is another argument for the use of tungsten as plasma-facing material [54]. The utilisation of tungsten-based materials in a fusion environment however also comes with drawbacks. For one, in the presence of oxygen, tungsten forms an oxide which is volatile at temperatures above 900 °C [4]. This on the one hand leads to a fast loss of material and poses a safety risk in the case of a loss-of-coolant accident since highly activated (WO_3)x clusters [59] and tritium-containing layers could escape the containment [41]. In order to prevent oxidation, self-passivating tungsten materials containing Cr and Y are under development [59–62]. The standard tungsten material used in current fusion reactors is a hot rolled material [46] with a ductile-to-brittle transition temperature (T_DBT, see section 4.2.1.2.1) around 300 °C [11]. During operation, the inherent brittleness of tungsten will deteriorate further, i.e. T_DBT will increase due to neutron irradiation and the retention of hydrogen/helium isotopes. As discussed in section 3.3.2.3, neutron irradiation leads to hardening and thus a further increase of T_DBT [63]. Furthermore, the high temperature inevitably triggers recrystallisation processes, which in turn lead to a loss of the material's deformed microstructure and thus means a deterioration of materials properties [10]. Pantleon [64] reports that half of the material's microstructure will be recrystallised after 5 fpy at 800 °C and after 2 fpy at 1050 °C. Low-cycle fatigue loading with thermal stresses in a tungsten plasma-facing component in combination with partial recrystallisation can lead to cracking once the component temperature falls below the ductile-to-brittle transition temperature [65].

Several strategies with the aim of developing a tungsten material suited for the harsh fusion environment are currently pursued. Using cold working, tungsten materials with a fine-grained microstructure and a low T_DBT can be achieved [27, 66]. Due to the high operating temperatures in a fusion reactor, the deformation structure is quickly lost due to recovery and recrystallisation processes. Grain growth, recrystallisation (and creep deformation) can be reduced by means of particle reinforcement [67], which however comes at the expense of a considerable increase of the ductile-to-brittle transition temperature [68]. Alloying tungsten with Re slightly improves its ductility due to the beneficial effect of the solute atoms on the mobility of screw dislocations. Unfortunately, W−Re suffers from an increased radiation embrittlement [69] and is too costly for large-scale production [70, 71]. A promising concept for advanced tungsten materials for the use as plasma-facing material is reinforcing them with fibres, similar to fibre-reinforced ceramics. Tungsten fibre-reinforced tungsten composites [16] consist of a pure tungsten matrix, which is produced either by chemical vapour deposition (CVD) or a powder metallurgical route and thin drawn, K-doped tungsten wires as reinforcement fibres (see figure 3.4). Fibres and matrix are separated by an interface, which is of great importance for the mechanical behaviour of the whole composite, see [72]. It was experimentally proven that processes like pull-out and ductile deformation of the fibre, crack bridging, crack wake and crack front debonding dissipate energy, thereby bestowing a pseudo-ductility on the brittle tungsten matrix [73]. The properties of the composite

are hereby mainly determined by the properties of the reinforcing fibres [17, 74]. Some extrinsic toughening mechanisms are also working even if the fibres show brittle fracture behaviour as verified using bending tests [75]. Recent experiments demonstrated that the tungsten wires show ductile fracture behaviour even after neutron[11] or ion irradiation [76, 77]

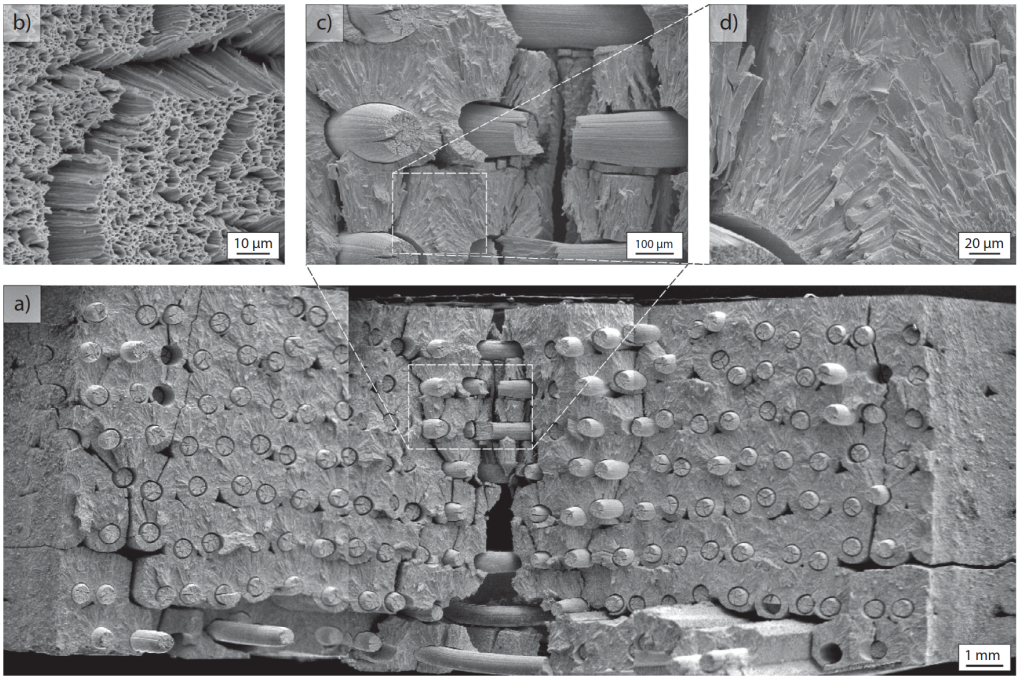

Figure 3.4: Fracture surface of a tungsten fibre-reinforced tungsten composite after Charpy impact testing [78]: Subfigures b) and d) show the ductile fracture surface of the tungsten wire and the brittle fracture surface of the CVD tungsten matrix, respectively.

[11] Neutron irradiation was performed in a fission reactor, which produces a neutron energy spectrum that is different from the one expected in a fusion reactor.

Chapter 4

Theoretical background

4.1 Thermally activated dislocation motion

Many important processes involved in the deformation of metals are thermally activated [79]. Examples for such processes are the overcoming of the lattice friction (Peierls-Nabarro force, see section 4.2.1.1), dislocation climb, the motion of gliding dislocation through an array of forest dislocations, cross-slip, the interaction of dislocations with small particles and the non-conservative motion of jogs. A very detailed review of all topics related to thermally activated dislocation motion can be found in [80]. Thermally activated dislocation motion means that dislocations can overcome barriers easier at higher temperature. The (shear) strain rate of a material which deforms by the motion of dislocations is given by the Orowan relation [81]:

$$\dot{\gamma} = b\,\rho_{\mathrm{m}}\,\bar{v} \tag{4.1}$$

where
$\dot{\gamma}$: Shear strain rate
b : Norm of the Burgers vector
ρ_{m} : Mobile dislocation density
$\bar{v}$: Mean dislocation velocity

In the context of thermally activated dislocation motion, the deformation rate can be written as follows [80]:

$$\dot{\gamma} = \dot{\gamma}_0 \exp\left(-\frac{\Delta G\,(\sigma^*)}{k_{\mathrm{B}}\,T}\right) \tag{4.2}$$

where
$\dot{\gamma}$: Shear strain rate
$\dot{\gamma}_0$: Pre-factor
ΔG : Potential barrier height
σ^* : Effective stress
k_{B} : Boltzmann factor
T : Absolute temperature

The effective stress σ^* in equation (4.2) is the excess of the applied stress σ over the athermal stress component σ_μ [82]:

$$\sigma^* = \sigma - \sigma_\mu \tag{4.3}$$

where σ^* : Effective stress component
σ : Applied stress
σ_μ : Athermal stress component

The athermal stress component is caused by the microstructure (grain boundaries, forest dislocations, secondary particles) and shares its temperature dependence with that of the shear modulus μ [80]. The effective stress is both temperature and strain rate dependent. The height ΔG of the barrier a dislocation needs to overcome in order to glide is a function of the effective stress: The higher the effective stress, the lower the barrier height [83]. Thus, the thermally activated motion of dislocations is facilitated by high temperatures (Arrhenius term in equation (4.2)) and an applied stress.

The stress dependence of the barrier height is referred to as activation volume:

$$V = \frac{\partial \Delta G}{\partial \sigma} \tag{4.4}$$

where V : Activation volume
ΔG : Potential barrier height
σ : Applied stress

The activation volume is linked to the activation area, i.e. the area that is swept during a successful activation event, through the Burgers vector [80]:

$$A = \frac{V}{b}, \tag{4.5}$$

where A : Activation area
V : Activation volume
b : Norm of the Burgers vector

Together with the activation volume, the strain-rate sensitivity, i.e. the sensitivity of a material's stress to a change in strain rate,

$$m = \frac{\partial \ln \sigma}{\partial \ln \dot{\varepsilon}}, \tag{4.6}$$

where m : Strain-rate sensitivity
σ : True stress
$\dot{\varepsilon}$: Strain rate

characterises a thermally activated process. Using equations (4.3) and (4.6) and the by definition non-existent strain-rate sensitivity of the athermal stress component [82], a relationship between the strain-rate sensitivity and the athermal stress component can be formulated [84]:

$$m = m^* \left(1 - \frac{\sigma_\mu}{\sigma}\right) \tag{4.7}$$

where m : Strain-rate sensitivity of the applied stress

m^* : Strain-rate sensitivity of the effective stress
σ : Applied stress
σ_μ : Athermal stress component

Strain-rate sensitivity and activation volume are linked through [80]

$$V = \frac{k_\mathrm{B}\, T}{m\, \sigma}. \tag{4.8}$$

where V : Activation volume
T : Absolute temperature
σ : Applied stress
m : Strain-rate sensitivity

4.2 Deformation mechanisms of refractory metals

4.2.1 The kink pair mechanism and its link to the ductile-to-brittle transition

4.2.1.1 Kink pair mechanism

The deformation of metals with a bcc crystal structure+ can be understood by taking into account the mobility of dislocations. The mobility of dislocations in bcc metals is strongly dependent on their character (edge/screw/mixed) [82]. Due to its non-planar nature[1] the core of a screw dislocation has to constrict before the dislocation can glide [86]. This configuration yields a lattice friction (Peierls stress) that is more than one order of magnitude higher compared to edge dislocations [87, 88]. Thus, in order to overcome the Peierls stress, which varies periodically with the spacing a of atoms along the glide path[2] [89], the dislocation forms a so-called kink pair (see figure 4.1), which connects neighbouring Peierls valleys. Under an externally applied stress, the two kinks forming the protrusion increase their separation and the dislocation line can move to the neighbouring Peierls valley. An illustration of this process is shown schematically in figure 4.1.

The kink pair mechanism can be described as a thermally activated process [90]. Depending on the effective stress and the resulting configuration of the kink pair, two regimes can be discerned: For low effective stresses, when the force counteracting the effective stress is the mutual elastic interaction of the kinks, the activation volume is given as [83]:

$$V_\mathrm{KP,EI} = \sqrt{\frac{\lambda^3\, b\, \gamma_0}{2\sigma^*}} \tag{4.9}$$

where $V_\mathrm{KP,EI}$: Activation volume of the kink pair mechanism in the elastic interaction approximation
λ : Kink height
b : Norm of the Burgers vector
γ_0 : Pre-logarithmic factor of a dislocation's line tension (see equation (4.10))
σ^* : Effective stress component.

The line tension of a dislocation can be determined via [91]

[1] The core is spread across multiple {110} [85].
[2] The resulting Peierls potential is denoted $U(u)$.

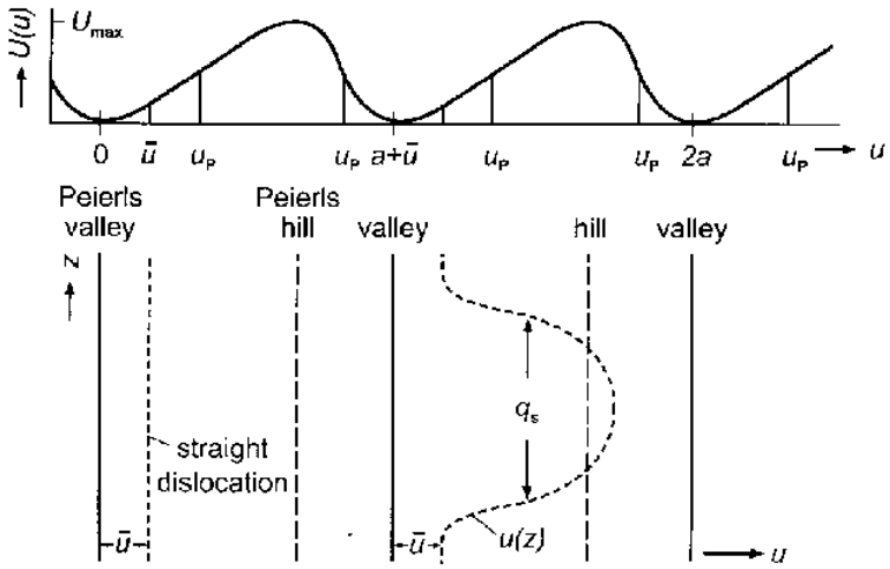

Figure 4.1: Asymmetric Peierls valley in lateral (top) and top view (bottom) [89]. The Peierls valleys have a spacing a along the slip direction. Under an applied stress, the dislocation is displaced by $\bar{u}$ from the Peierls valley. The dislocation line to the right of the top view image (bottom) contains two kinks with a separation of q_s.

$$\gamma_d = \gamma_0 \ln \frac{r_\infty}{r_0} \tag{4.10}$$

where γ_d : Line tension
γ_0 : Constant
r_∞ : Outer cut-off radius
r_0 : Inner cut-off radius

In the case of dislocations, gliding via the kink pair mechanism, r_∞ is of the order of the kink width [83].

At higher effective stresses, the separation between the kinks in a kink pair is so small, that the single kink cannot be discerned any more. This configuration can then not be treated by elasticity theory. Thus, the line tension counteracting the effective stress is used to describe the stress dependence of the activation volume:

$$V_{KP,LT} = \lambda\, b \sqrt{\frac{\gamma_d}{U''(u=\lambda)} \ln \frac{\tilde{\sigma}}{\sigma^*}} \tag{4.11}$$

where $V_{KP,LT}$: Activation volume of the kink pair mechanism in the line tension approximation
λ : Kink height
b : Norm of the Burgers vector
γ_d : Line tension of a dislocation
$U''(u=\lambda)$: Curvature of the Peierls potential at its (local) maximum $u = \lambda$
$\tilde{\sigma}$: Shape factor of the Peierls potential

σ^* : Effective stress component.

The change-over from the elastic interaction to the line tension approximation occurs at a stress $\tilde{\sigma}^*$, a definition of which can be found in [83]. The kink pair mechanism is characterised by activation volumes in the range of $10\,b^3$ to $100\,b^3$. The strain-rate sensitivity m of the process follows from equation (4.8). Very detailed analyses of the kink pair mechanism performed on a variety of single-crystalline refractory metals, among them Nb [83, 92], Mo [93, 94], Fe [95–97], Ta [98, 99] and W [100, 101], are available in the literature. Studies with a comparable level of detail on polycrystalline materials are rare and are mostly content with determining the order of magnitude and sometimes the stress dependence of the activation volume [25, 102–104].

4.2.1.2 Ductile-to-brittle transition in tungsten

The tendency of certain materials such as steels to fracture in a brittle manner below a certain transition temperature was known since the early days of metalworking and contributed to major catastrophes such as the sinking of the MS Titanic in 1912 or the mass failure of the US Liberty ships during World War II [105, 106]. The transition from a low fracture toughness[3] at low temperatures (lower shelf) to a high fracture toughness at high temperatures (upper shelf) is observed for most b.c.c. metals (see figure 4.2) [6] as well as some h.c.p. metals, non-metallic crystals and polymers but not for f.c.c. metals [107].

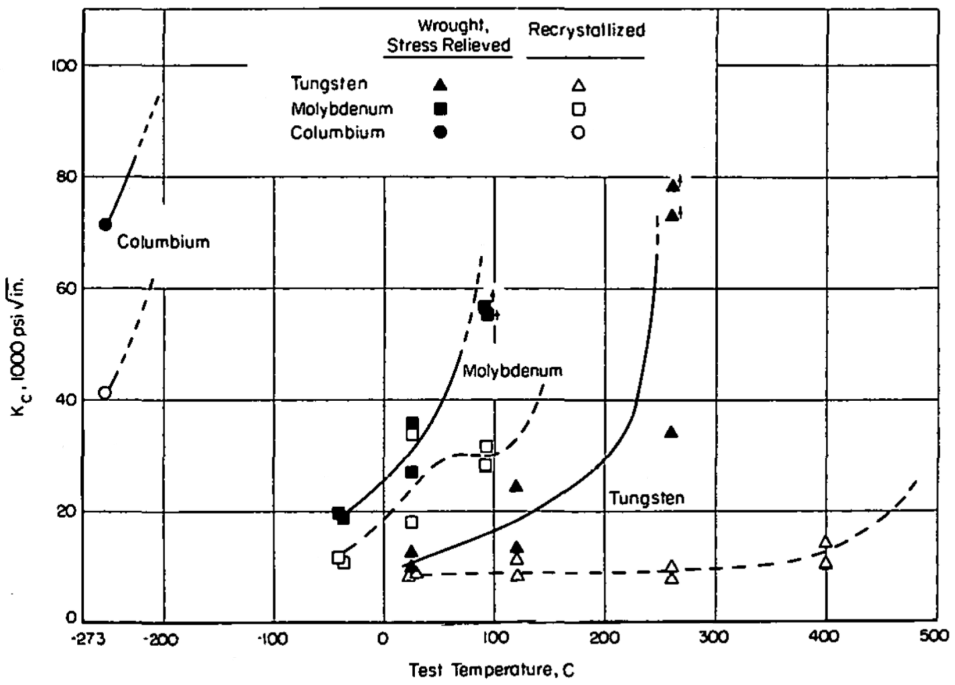

Figure 4.2: Fracture toughness vs. test temperature for worked (empty symbols) and recrystallised (filled symbols) tungsten, niobium and molybdenum [108]. Note that columbium is a dated term for niobium.

The transition from the upper to the lower shelf is usually modelled using an S-shaped function, e.g. tanh, in order to determine the transition temperature T_{DBT} [109]. Apart from the temperature, the ductile-to-brittle transition is also influenced by the strain rate. As pioneered

[3]Similar transitions are reported for example for the yield strength.

by St. John [7], the strain-rate dependence of the ductile-to-brittle transition can be described by an Arrhenius-type relation [110]:

$$\dot{\varepsilon} = \dot{\varepsilon}_0 \exp\left(-\frac{E_\mathrm{A}}{k_\mathrm{B}\, T_\mathrm{DBT}}\right) \tag{4.12}$$

where
$\dot{\varepsilon}$: Strain rate
$\dot{\varepsilon}_0$: Initial strain rate
E_A : Activation energy of the ductile-to-brittle transition
k_B : Boltzmann's constant
T_DBT : Ductile-to-brittle-transition temperature

In the case of tungsten, an activation energy of the ductile-to-brittle transition of (1.13±0.49) eV could be determined from fracture tests of various single- and polycrystalline materials [29]. Since this value corresponds well with the kink pair formation enthalpy, which Brunner [100] determined to be 0.75 eV to 1.0 eV in the case of tungsten, it is generally concluded that the ductile-to-brittle transition is controlled by the formation and propagation of kink pairs on screw dislocations. This conclusion does fall short to explain why the ductile-to-brittle transition temperature shifts to lower temperatures upon cold-working. Some theories from the literature that try to explain this effect are discussed in the following section.

4.2.1.2.1 Theories on the shift of T_DBT in worked tungsten materials

The ductile-to-brittle transition temperature of hot-worked tungsten is in the range of 200 °C to 600 °C [1, 11, 12]. If tungsten is however cold-worked by processes like wire drawing or rolling, its transition temperature can be lowered below room temperature, i.e. it can be ductile at room temperature and even at cryogenic temperatures [27, 34, 111]. Systematic studies performed on rolled tungsten plates [24, 26–30, 112] tried to identify the reasons for the shift of T_DBT. Similar to hot-worked or single crystalline tungsten, the kink pair mechanism was identified as rate-controlling during plastic deformation of tungsten plates. Thus, the origin of the shift is supposed to lie in the deformation-induced microstructural changes. It could be shown that the grain size increases with increasing strain during deformation [27]. Concurrently, the (redundant) dislocation density and the grain aspect ratio increased. Based on the currently available studies, the influence of impurities and the crystallographic texture on the ductility of tungsten seem to be minor. Based on these results, two different theories were developed trying to explain the anomalous ductility of rolled tungsten plates:
Bonk [25] uses the fact that the grain aspect ratio increases with increasing strain accumulated during rolling combined with the relaxed constraints model. In the classical Taylor theory, five independent slip systems are required to account for an arbitrary shape change of a grain [113]. If the grain has a special shape, for example if at least one dimension is much larger than the other two as in the case of the rolled tungsten plates, the requirements of the Taylor model can be relaxed so that less than five independent slip systems would suffice to account for the deformation of the grain. Bonk concludes that the reduction of the number of independent slip systems would give rise to the occurrence of dislocations with the same Burgers vector. This would increase the possibility of annihilation and thus improve recovery during work hardening (see section 4.2.2.1). On that note, Bonk furthermore assumes that dislocations could channel through the grains. This would in turn decrease the possibility of cutting processes and might be beneficial for ductility. Apart from the increase of the grain aspect ratio, the decrease of the work hardening rate with increasing strain accumulated during rolling support Bonk's theory.
A second explanation attempt is made by Bonnekoh [28] based on the increase of the density of

dislocations sources in the form of grain boundary ledges, dislocation boundaries or debris loops with increasing accumulated rolling strain. According to Bonnekoh, the shift of T_{DBT} should scale with the spacing of these sources along the crack front. The increase of mobile dislocation density would improve crack blunting and thus inhibit catastrophic failure in the presence of a crack. The empirical link between grain boundary dislocation source spacing and the transition temperature was modelled numerically by Reiser & Hartmaier [112]. Their study showed that the transition temperature decreases if both the spacing between dislocation sources along the crack front and the mean free path for dislocation glide decreases.
Although drawn tungsten wires are used in incandescent lightning since more than one century, the shift of their ductile-to-brittle transition temperature with the accumulated drawing strain has not been explained satisfactorily yet [114, 115]. The same is true for the materials produced by severe plastic deformation (SPD) [20, 22].

4.2.2 Strengthening mechanisms in metals

4.2.2.1 Work hardening

Work hardening[4] comprises all processes which take place if a ductile material is stressed above its yield point and deforms without macroscopic strain localisation. From the parabolic course of the stress-strain curve it is evident, that during work hardening, more and more force is required to deform the material further. This increase in strength is described by the so-called Taylor relation [116]

$$\sigma = \sigma_0 + M_{\mathrm{T}}\,\alpha\,\mu\,b\,\sqrt{\rho} \tag{4.13}$$

where
σ : Strength[5]
σ_0 : Initial strength
M_{T} : Taylor factor
α : Interaction constant
μ : Shear modulus
b : Norm of the Burgers vector
ρ : Dislocation density

The constant α characterising the interaction of dislocations on their glide planes is of the order $0.5 \ldots 1$ for a large number of different materials [117]. The Taylor factor is used in equation 4.13 to convert shear stresses and strains to normal stresses and strains. Note that in order to describe the deformation of a polycrystal, a volume weighted-average of the Taylor factor taking the different orientations and volume fractions of the grains in the polycrystal into account, has to be used in equation 4.13.

4.2.2.1.1 Work hardening stages

The extent of work hardening is best quantified by the so-called work hardening rate

$$\theta = \frac{\partial \sigma}{\partial \varepsilon} = M_{\mathrm{T}}^2 \frac{\partial \tau}{\partial \gamma} \tag{4.14}$$

[4]Note that the terms *work hardening* and *strain hardening* will be used synonymously in this work.
[5]Note that the strength can be used synonymously to the stress: If a certain stress is needed to deform (or break) a material, this stress is usually defined as the material's yield (or fracture) strength.

where θ : Work hardening rate
σ : Normal stress
ε : Strain
τ : Shear stress
γ : Shear strain
M_{T} : Taylor factor

Plotting the work hardening rate as a function of the stress (Kocks-Mecking plot) for single- and polycrystalline materials reveals distinct work hardening stages, see figure 4.3.

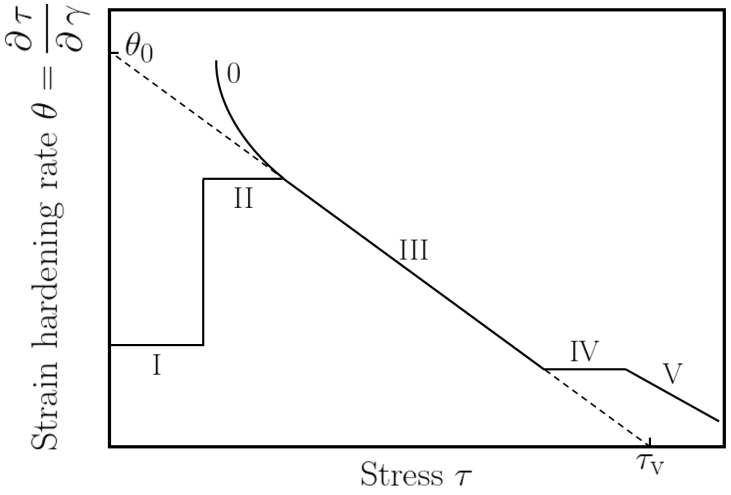

Figure 4.3: Schematic Kocks-Mecking plot illustrating the different stages during work hardening of metallic single- and polycrystals. The saturation stress τ_{V} is indicated at the abscissa.

4.2.2.1.1.1 Hardening stages in single crystals

Stage I: Stage I can only be observed in single crystals oriented for single slip. It is characterised by a very low constant hardening rate. In this stage, dislocations accumulate on primary slip planes or in the form of dipoles [118]. The end of stage I is marked by a strong increase in work hardening rate, which is due to dislocation activity on a secondary slip system [119].

Stage II: Stage II is described as athermal hardening stage [118]: The accumulation of dislocations on the primary slip systems leads to the development of a resolved shear stress on a secondary slip system, leading to a tangling of both systems. The strain hardening rate is only mildly influenced by temperature or strain rate, and thus only depending on the crystal orientation. Furthermore, sessile locks form that contribute to the storage of dislocations. Stage II does not occur at high temperatures or in materials with a high stacking fault energy.

Stage III: Stage III is marked by a monotonic decrease of the work hardening rate. The cross-slip of dislocation (segments) leads to dynamic recovery [118]. Since cross-slip is a thermally activated process [80], stage III is characterised by a distinct temperature dependence[6]. Stage III is described by [120, 121]:

[6]Note that it falls short only trying to explain stage III by cross slip processes only. Other effects are also needed for a full description [118].

$$\theta = \theta_0 \left(1 - \frac{\tau}{\tau_\mathrm{v}}\right), \tag{4.15}$$

where θ : Work hardening rate
θ_0 : Initial work hardening rate
τ : Shear stress
τ_v : Saturation stress

4.2.2.1.1.2 Polycrystal effects on hardening

There are some decisive differences between the strain hardening of single and polycrystals. As stated before, stage I is absent in polycrystals since there is no single slip. It is rather replaced by a stage called stage 0, which arises due to the fact that grain boundaries limit the mean free dislocation path at the onset of plastic deformation [119]. Since a steady state is usually not reached during stage III work hardening of polycrystals, several other hardening stages at a high strain level follow the ones discussed in the previous section. Stage IV again shows a constant hardening rate and shares its temperature and strain rate dependence with stage III [119]. It is only relevant for $T \leq 0.5\,T_\mathrm{m}$, i.e. at low homologous temperatures. Stage IV occurs without marked changes in the character of obstacles obstructing dislocation motion [118]. Large-strain effects like the grain curling in bcc materials contribute significantly to this work hardening stage and further high-strain stages [119]. Many theories exist for the mechanisms behind stage V in f.c.c. materials, among them the formation of voids alongside the initiation and propagation of cracks [122] or the generation and absorption of point defects [123, 124].

4.2.2.1.2 The Kocks-Mecking model: A phenomenological model to describe the work hardening of metallic materials

One of the most commonly used model for describing the work hardening behaviour of metals is the Kocks-Mecking (KM) model [119, 121, 125–127]. It is based on the assumption that the flow stress σ of a material is a function of a single structure parameter S, the strain rate $\dot{\varepsilon}$ and the temperature T [125]. In order to fully describe the plastic behaviour, also an expression for $\partial S/\partial \gamma$, i.e. the evolution of S with strain, is needed. As a consequence, the flow stress evolves from an initial value towards a certain saturation value. The governing structure parameter in the KM model is the dislocation density ρ. The dislocation density is defined as a line density, i.e. as length of dislocation lines per volume. Several terms can be included to account for the storage and recovery of the dislocation density during strain hardening. If dislocations are assumed to accumulate both at other (forest) dislocations and at fixed obstacles like grain boundaries or the sample surface (so-called hybrid model, see [119, 125, 128]), as it is the case in a realistic engineering material, the evolution equation can be written as follows:

$$\frac{\partial \rho}{\partial \gamma} = \frac{1}{b\,\lambda_\mathrm{f}} + \frac{\sqrt{\rho}}{b\,\beta} - k_2\rho = k_0 + k_1\sqrt{\rho} - k_2\rho \tag{4.16}$$

where ρ : Dislocation density
γ : Shear strain
b : Norm of the Burgers vector
β : Factor characterizing the ratio between the mean free path of dislocation and their mean spacing $\sqrt{\rho}^{-1}$

λ_f : Mean spacing between fixed obstacles
k_0 : Coefficient characterising the accumulation of dislocations at fixed obstacles
k_1 : Coefficient characterising the accumulation of dislocations at other dislocations
k_2 : Recovery coefficient

The work hardening stages II and III are combined in equation (4.16). k_0 and k_1 cover the athermal storage of stage II, while k_2 contains the dynamic recovery of stage III. β can be interpreted as the number of forest dislocations a gliding dislocation can cross before it is stored. The only variable in the KM model that should show a distinctive strain rate dependence is the recovery coefficient k_2 [121]:

$$k_2 = k_{2,0} \left(\frac{\dot{\varepsilon}_\mathrm{pl}}{\dot{\varepsilon}_0} \right)^{-n'} \tag{4.17}$$

where k_2 : Recovery coefficient
$k_{2,0}$: Constant
$\dot{\varepsilon}_\mathrm{pl}$: Plastic strain rate
$\dot{\varepsilon}_0$: Reference strain rate
n' : True strain-rate sensitivity of the recovery coefficient

At low temperatures, the true strain-rate sensitivity is relatively small ($n' \ll 1$). The temperature dependence of the recovery coefficient is either contained in n' or $\dot{\varepsilon}_0$. The recovery coefficient can be converted into an annihilation length y using [129]

$$y = \frac{k_2\, b}{2} \tag{4.18}$$

where y : Annihilation length
k_2 : Recovery coefficient
b : Norm of the Burgers vector.

Essmann & Mughrabi [129] interpret

$$P_\mathrm{s} = \pi\, y^2$$

as a capturing cross-section, i.e. the probability that a gliding cross-section is captured by another dislocation for mutual annihilation. Another interpretation of

$$k_2 = L_\mathrm{a}\, b^{-1}$$

as an annihilated dislocation length L_a is given by Kocks [121], where b is the Burgers vector (see equation (4.16)).

In order to describe an experimentally determined Kocks-Mecking plot (θ vs. σ), the relation between the true shear and normal strain [113]

$$\gamma = M_\mathrm{T}\, \varepsilon_\mathrm{z} \tag{4.19}$$

where γ : Shear strain
M_T : Taylor factor
ε_z : True normal strain for a uniaxial deformation in z direction

and equation (4.13) can be used to arrive at the following evolution equation for the work hardening rate [119]:

$$\theta = \theta_0 \left(\frac{\sigma_\mathrm{D}}{\sigma_\mathrm{tr}} + 1 - \frac{\sigma_\mathrm{tr}}{\sigma_\infty} \right) \tag{4.20}$$

where
θ : Work hardening rate
$\theta_0 = \frac{M_\mathrm{T}^2 \, \alpha \, \mu}{2 \, \beta}$: Initial work hardening rate
$\sigma_\mathrm{D} = \frac{M_\mathrm{T} \, \alpha \, \mu \, b \, \beta}{\lambda_\mathrm{f}}$: Stress contribution of fixed obstacles
σ_tr : True stress
$\sigma_\infty = \frac{M_\mathrm{T} \, \alpha \, \mu \, b}{\beta \, k_2}$: Saturation stress
k_2 : Recovery coefficient
b : Norm of the Burgers vector
β : Factor characterizing the ratio between the mean free path of dislocation and their mean spacing $\sqrt{\rho}^{-1}$
λ_f : Mean spacing between fixed obstacles
α : Interaction coefficient
M_T : Taylor factor

Equation (4.20) reveals in which stress regimes the contribution of the different storage terms is strongest: While storage at grain boundaries is strongest at low applied stresses, the accumulation at forest dislocations prevails at high applied stresses. This is in line with the increase of the total dislocation density ρ and in turn the decreasing spacing of dislocation, which is proportional to $\sqrt{\rho}^{-1}$, with progressing work hardening. In order to directly model the experimental stress-strain behaviour, equation (4.20) can be integrated. This yields a relation between the plastic strain and the (applied) true stress [130]:

$$\varepsilon_\mathrm{pl} = \frac{\sigma_\infty}{\theta_0} \frac{1}{\sigma^+ - \sigma^-} \left[\sigma^- \ln \left(\frac{\sigma_\mathrm{tr} - \sigma^-}{\sigma_\mathrm{y} - \sigma^-} \right) - \sigma^+ \ln \left(\frac{\sigma_\mathrm{tr} - \sigma^+}{\sigma_\mathrm{y} - \sigma^+} \right) \right] . \tag{4.21}$$

where
ε_pl : True plastic strain
σ_∞ : Saturation stress
θ_0 : Initial work-hardening rate
$\sigma^\pm = \frac{\sigma_\infty}{2} \pm \sqrt{\frac{\sigma_\infty^2}{4} - \sigma_\infty \sigma_\mathrm{D}}$: Auxiliary stress
σ_D : Stress contribution of the fixed obstacles
σ_y : True yield stress
σ_tr : True stress

The KM model was initially developed for describing the strain hardening of f.c.c. metals. Thus, many metals with this crystal structure have been studied using the KM model; see [119] for a review. Extensions to h.c.p. metals [121, 131] or b.c.c. metals [132, 133] are still very scarce.

4.2.2.2 Grain boundary strengthening

Hall [134] and Petch [135] were the first to cast the link between a material's strength and its grain size into an empirical relationship in the early 1950s. In its initial form linking the yield strength of a material to its grain size d, the Hall-Petch relation [134, 135] reads as

$$\sigma_{\mathrm{y}} = \sigma_{\mathrm{y},0} + \frac{k_{\mathrm{HP}}}{\sqrt{d}} \tag{4.22}$$

where σ_{y} : Yield strength
$\sigma_{\mathrm{y},0}$: Initial strength
k_{HP} : Hall-Petch constant
d : Mean grain size

The relation can also be drawn up for other material's properties such as the ultimate tensile strength R_{m}, the fracture toughness or the fatigue endurance stress [136–138]. In all cases, the initial strength σ_0, i.e. the limiting case for $d \to \infty$, describes the properties of a material with a very large grain size, for example a single crystal. The Hall-Petch constant k_{HP} is a material coefficient and exhibits a pronounced temperature dependence. Several theories have been formulated in order to mechanistically explain the link between grain size and strength. The most commonly used theory is the pile-up theory [139, 140]. In it, a dislocation source inside a grain emits dislocations on the same glide plane due to an externally applied stress. The dislocations can glide until they reach the next grain boundary. There, a pile-up is formed. Once the stress at the grain boundary is high enough, a dislocation source is activated in the neighbouring grain. A similar approach was used by Li [141]: The pile-up in his model is not generated by a spiral or Frank-Read source but by a grain boundary ledge source. The importance of ledge sources for the deformation of engineering materials was shown by Murr et al. [142, 143]. Further models based on plastic anisotropy can be found in [144–147]. Apart from the inverse square-root dependence shown in equation (4.22), relationships with a different exponent have been found for certain materials. Langford & Cohen [132] found an exponent of $\sigma \propto d^{-1}$ for drawn steel wire in comparison to the Hall-Petch formulation using $\sigma \propto d^{-0.5}$. Their theory is based on the special microstructure comprising cell walls and the interaction of dislocation with this kind of obstacle [132, 148].

Chapter 5

Materials and Methods

5.1 Drawn tungsten wires

5.1.1 Historical aspects and application

The filaments of the first incandescent lamps were made out of carbon, osmium, or tantalum [23]. Due to various issues with the filaments like brittleness or high evaporation rates, the lifetime of the lamps was limited. The first powder-metallurgical tungsten filaments that did not rely on a complicated binder route were patented by William D. Coolidge in 1912. Coolidge was able to work a sintered tungsten ingot into a thin wire using alternating drawing and annealing steps [149]. Intermediate annealing proved to be vital in order to increase the workability of the material by recovery of the work-hardened microstructure. Coolidge was also the first to notice the increase of filament lifetime if the tungsten powder came in touch with certain oxides prior to sintering [23]. This treatment, namely the doping of the tungsten powder by Al-, Si- and K-containing salts (AKS doping), was later patented by Pacz in 1917 [150]. Extensive research revealed that during sintering of the doped tungsten powder, potassium remains in the material. Since the solubility of K in tungsten is minuscule, the potassium forms reservoirs [149]. During drawing, these reservoirs get elongated and collapse during annealing according to the Plateau-Rayleigh instability [151] leading to the formation of small rows of bubbles parallel to the wire axis that are filled with liquid or gaseous K [152]. During high-temperature operation of the filaments, the potassium bubbles effectively pin grain boundaries and dislocations, thereby creating a creep-resistant microstructure (see also section 5.1.4).

Since Coolidge's development of ductile tungsten wire in the 1910s, tungsten wire has been used as filament material in incandescent lighting. Due to the inefficiency of conventional light bulbs and the need to save energy in face of the global climate crisis (see section 1), several countries have started to phase out this kind of lightning technology in the 2010s, among them the European Union starting in 2012 [153]. Despite this decision, tungsten wires are still vital components of halogen lamps and other light sources [154]. Due to their unique blend of properties, among them a high creep resistance, high strength and ductility, the use of tungsten wires as reinforcement fibres in composites was investigated since the 1960s. The reinforcement of different matrix materials like Ag [155], Cu [156], Al [157], W [18], Ni-base superalloys [158, 159] and ceramics [160] to name a few, have been investigated so far. Recent research is mainly driven by the need for advanced materials for the walls of future fusion reactors [161], see section 3.4. In this context, tungsten wires are either used to further increase the high-temperature strength of Cu alloys [162] or to bestow pseudo-ductility and increase the fracture toughness of an otherwise brittle tungsten matrix [78].

5.1.2 Wire drawing process

Wire manufacturing starts with the purification of the tungsten oxide containing ore[1] [32]. After having extracted the oxide WO_3 from the ore, it is converted into ammonia paratungstate (APT). APT is then converted into tungsten blue oxide, a mixture of $W_{18}O_{43}$ and $W_{20}O_{58}$. The AKS-doping is performed in the blue oxide state by mixing the oxide with an aqueous solution containing $K_2Si_2O_5$ and $Al(NO_3)_3$. Reducing the blue oxide mixture using H_2 yields a tungsten powder with a K content of approximately 60 to 130 wt. ppm and negligible amounts of Si and Al [154]. Prior to sintering, the tungsten powder is compacted into a green body via processes such as cold isostatic pressing. Upon direct current sintering, the Si and Al containing doping compounds decompose and diffuse out of the sintered body. Although the wire is heated up to temperatures of 3000 °C during sintering, K can however not diffuse out due to its large atomic radius leading to a slow diffusion velocity and remains in the sintered workpiece. Once the green body is sintered, thermo-mechanical treatment in the form of rolling/milling and swaging commences. The purpose of thermo-mechanical treatment is two-fold: On the one hand, residual sintering pores are eradicated by thermo-mechanical working. On the other hand, the globular grain structure present after sintering is transformed into a worked microstructure which makes the workpiece more ductile and reduces its ductile-to-brittle transition temperature, respectively. From an economical point of view, the latter effect also reduces pre-heating temperatures and thereby costs for drawing [32].

Due to the high ductile-to-brittle transition temperature, the sintered ingot has to be worked at temperatures around 1500 °C. Kocks milling (see figure 5.1b) is usually employed after sintering in modern-day tungsten wire manufacturing. A Kocks mill consists of two to four rolling stands, with three rolls rotated by an angle of 120° each. Each stand is rotated by 180° with respect to the other. The reduction of area in each stand is approximately 20 % [32]. After certain thermo-mechanical working step, intermediate annealing is required to recover the deformation microstructure created during working. Annealing temperatures that initiate recrystallisation processes are chosen for this purpose. This results in a coarse grained structure which exhibits a low work-hardening rate. During swaging, which is performed after Kocks milling, two or four anvils with a circular opening are brought down onto the ingot in order to forge it using compressive forces directed towards the centre of the ingot (see figure 5.1a). For details on special techniques like rotary swaging, the reader is referred to [32]. The purpose of swaging is similar to the one elucidated for Kocks milling: Reduction of porosity, transformation of a sintered microstructure into a hot-worked microstructure and decrease of the rod diameter in order to prepare the workpiece for wire drawing.

Wire drawing starts at a diameter between 4 mm and 2 mm and describes the process of pulling a rod or wire through a die with a smaller diameter than the initial diameter of the rod or wire, see figure 5.1c. The shape change that is imposed on the wire due to the thinner die diameter leads to the deformation of the wire. In order to fit the thicker wire into the thin die in the first place, it is pointed using an alkaline solution. The dies used for tungsten wire drawing are commonly manufactured from tungsten carbide. The die semi-angle (cf. figure 5.1c) depends on the wire diameter: Thick wires are drawn through dies with a semi-angle of 8° to 10°, while the angle is reduced to 4° at the thin wire stage. For thick wires, the drawing temperature is around 1000 °C but can be lowered as the diameter decreases. Fine wires are drawn at temperatures around 600 °C and below [165]. An overview of exemplary working temperatures for swaged/milled rods and drawn wires is shown in figure 5.2.

During pre-heating of the wire, an oxide layer forms. This oxide layer prevents the uptake of carbon into the material from the graphite lubricant, which is applied right before entering the die in order to reduce friction between wire and die. After passing through the die, the still warm

[1] see [1, 2] for more information on tungsten ores

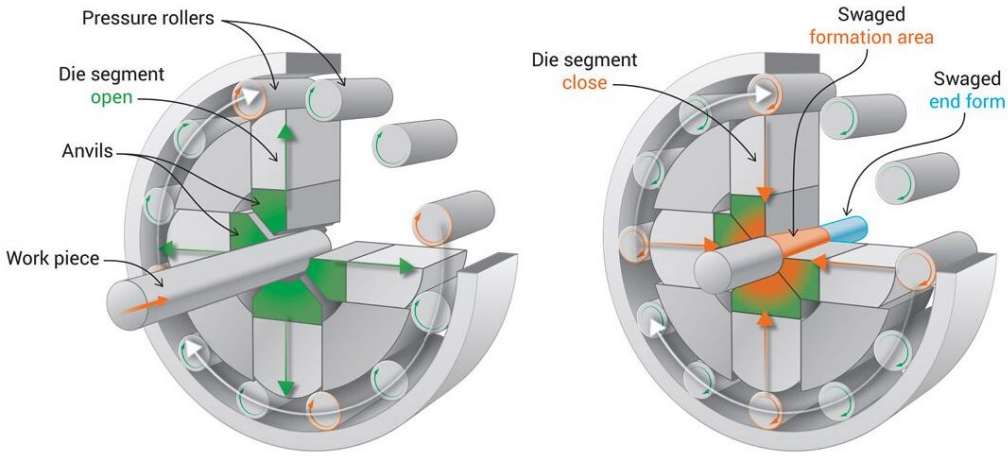

(a) Rotary swaging

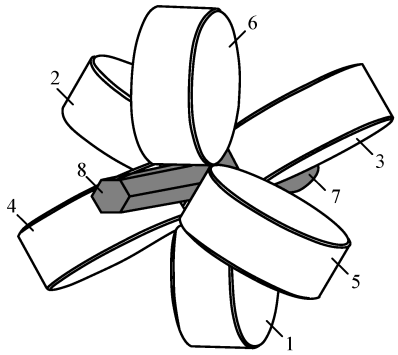

(b) Kocks milling

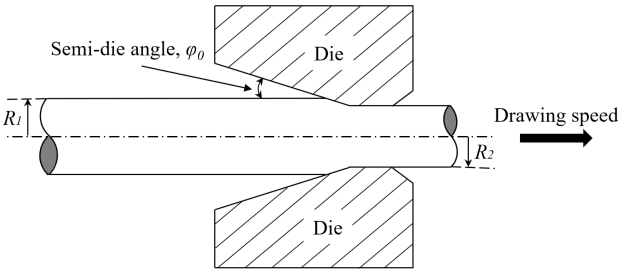

(c) Wire drawing

Figure 5.1: Thermo-mechanical techniques involved in tungsten wire manufacturing: (a) Rotary swaging ©EngineeringClicks, (b) Kocks milling: The mill is segmented into two roll stands (1-3 and 4-6, angle: 180°) with three rolls each (angle: 120°) that deform the workpiece (7/8). Image adapted from [163], (c) Wire drawing: Wire radius R_1 before and R_2 after passing through the die with a semi-angle φ_0. Image adapted from [164].

wire is coiled. This leads to the wire bending slightly after cooling. Depending on the application, any remnants of the graphite lubricant can be removed using brine prior to packaging or further processing. For more in-depth details on the wire drawing process, the reader is referred to [2, 32, 66, 165]. A schematic overview of the major steps involved in the fabrication process is shown in figure 5.3.

5.1.3 Evolution of the crystallographic texture during tungsten wire manufacturing

Following the process chain of tungsten wire manufacturing, one can trace the evolution of crystallographic texture. The first step that can influence the orientation of the material is pressing. As Zhou and co-workers [167] found, cold isostatic pressing can already lead to the development of a preferred orientation of crystallites. Other research [168] shows that sintered tungsten can also be untextured, i.e. the grains are randomly oriented. Thus, depending on the pressing technique, the sintered material can already develop certain albeit weak texture components. Leber et al. [169] report a pseudo $(111-112)$ $[\bar{1}10]$ cylindrical texture in swaged tungsten rods, i.e. a direction

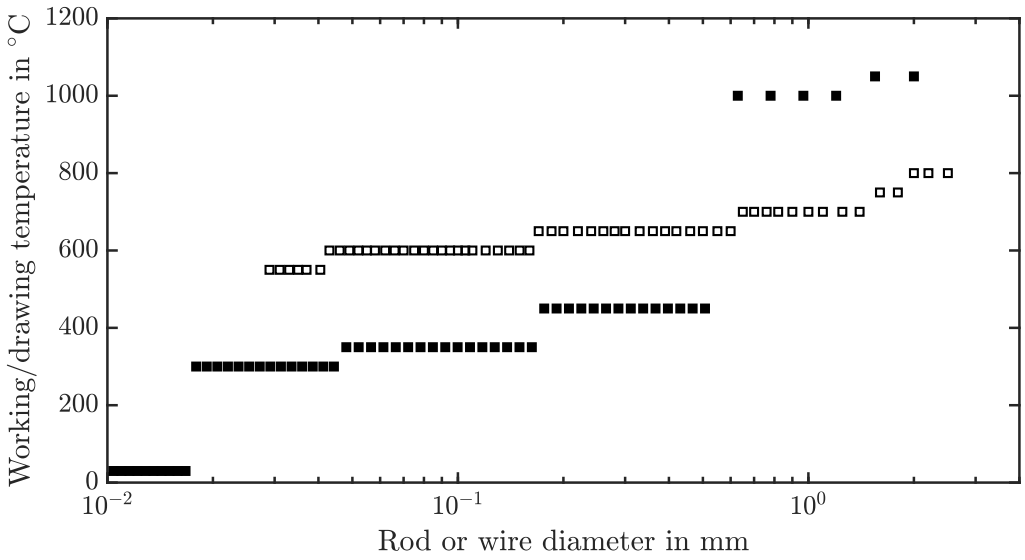

Figure 5.2: Working temperatures for rods and wires with different diameters during tungsten wire manufacturing (empty squares from [166]; filled squares from [2]).

between ⟨111⟩ and ⟨112⟩ is aligned with the radial direction of the swaged rod while the rod axis is parallel to $[\bar{1}10]$. Upon further deformation by swaging, the grains rotate so that the texture is best described by a $(112)\,[\bar{1}10]$ cylindrical texture. Grain rotation during wire drawing transforms the cylindrical texture into a ⟨110⟩ fibre texture [113, 170–172]. The characteristic appearance of the texture of a swaged rod and a ⟨110⟩ fibre texture in pole figures is shown in figure 5.4.

The reason for the formation and strengthening of the ⟨110⟩ fibre texture upon uniaxial tensile deformation was first explained by Hosford in 1964 [170]: Due to plastic anisotropy, grains in bcc materials tend to deform via plane-strain elongation rather than axisymmetric elongation during wire drawing. Van Houtte [174] was able to underpin Hosford's calculations using simulations employing the relaxed constraints model. A more recent study by Haus [175] identifies the texture of an as-drawn tungsten wire as cyclic $\{110\}\,\langle 110\rangle$ fibre texture, i.e. one set of ⟨110⟩ is aligned with the wire drawing axis while another one is aligned with the radial direction of the wire. The study by Yerra et al. [176] hints to a non-linear dependence of texture sharpness on the wire diameter: The texture sharpness passes through a maximum and then decreases if the diameter reduction during wire drawing increases. Since the mentioned study does not provide the exact wire diameters, the evolution of texture sharpness as a function of the wire diameter has so far not yet been fully characterised. Pink et al. [66] report that as the fibre texture sharpens, the alignment of ⟨110⟩ with the wire axis increases while the rotation of the grains around this axis gets more random, which partly objects to the findings of Haus, who investigated wires with a diameter of 150 µm. Browning et al. [177] and Nikolić and coworkers [178] investigated the lateral distribution of the preferred orientation over the whole wire cross-section and found that the ⟨110⟩ direction of grains in the wire centre is better aligned with the drawing axis compared with grains close to the wire surface. The reason for this deviation from a $\{110\}\,\langle 110\rangle$ fibre texture might lie in the friction between the wire surface and die during drawing [177]: Friction leads to the development of a multiaxial stress state in the near-surface region of the wire and thus the grains are not loaded by pure uniaxial tensile stress[2]. Thus, the deformation mechanisms and lattice rotation of these near-surface grains and thereby also their preferred orientation differs from the grains in the wire

[2]The deviatoric stress tensor in the wire centre comprises pure uniaxial stresses. The hydrostatic compressive stress resulting from the interaction of the workpiece with the drawing die can be neglected when discussing dislocation slip processes.

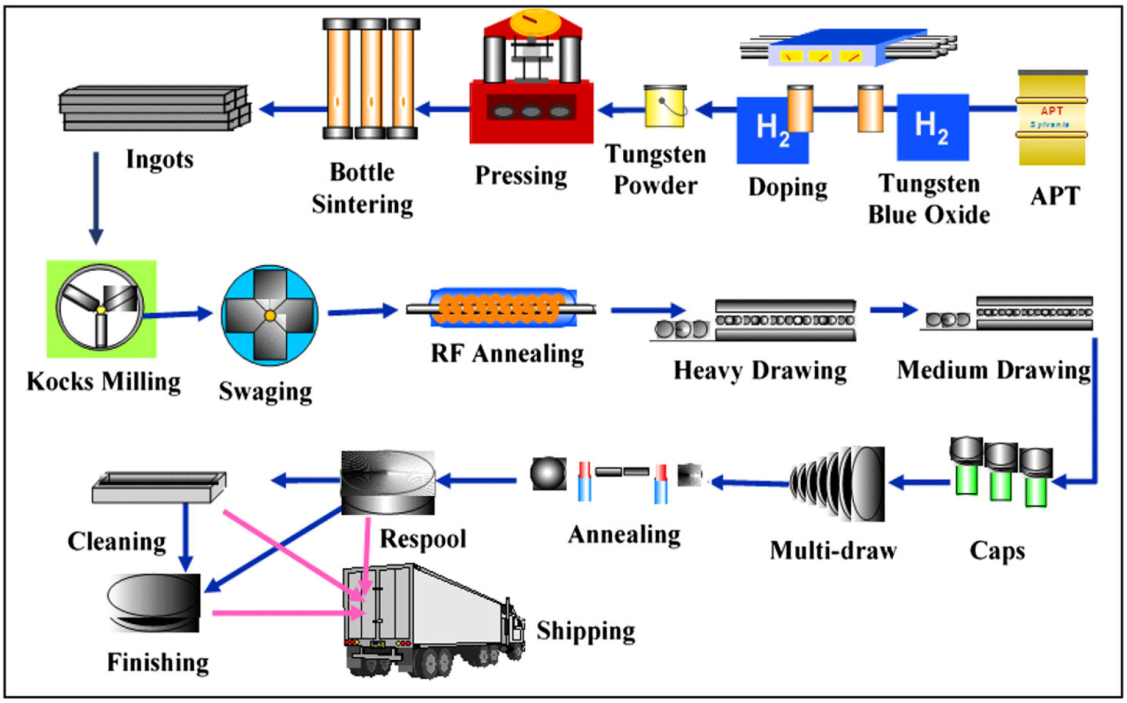

Figure 5.3: Steps in the manufacturing of drawn tungsten wire according to [154].

centre. Since the temperatures during wire drawing are lower than the temperatures necessary for recrystallisation ($T_{\mathrm{REX}} > 1600\,^{\circ}\mathrm{C}$ for wires with $d \leq 500\,\mu\mathrm{m}$ [73, 179, 180]), there are no reports of strong texture components in as-drawn wires that can be attributed to the development of a recrystallisation texture. If recrystallisation during the intermediate annealing steps would take place, the texture of as-drawn wires would also contain significant {531}, {320}, {430} or {421} components [181, 182]. The ⟨110⟩ fibre texture is very resistant to high-temperature annealing phenomena: Even after annealing at 2450 °C for 1 h, the ⟨110⟩ component is still dominant [183].

5.1.4 Evolution of the microstructure during tungsten wire manufacturing

The grains of sintered tungsten are usually equiaxed [168]. During thermo-mechanical working (swaging/Kocks milling), the grains follow the shape change of the workpiece and become elongated. This trend is even stronger during wire drawing: The strong deformation especially in very thin wires yields fibrous grains with a very high aspect ratio [66, 172, 184], see figure 5.5a. As another result of the deformation of the grains by plane strain elongation, they have to bend around a ⟨110⟩ in order to keep compatibility with their neighbouring grains [170, 171], see figure 5.5b. Formulated slightly more graphically, the shape of the initially equiaxed grains does not resemble a cigar after wire drawing, which would be the outcome of axisymmetric deformation, but takes after the form of plates that bend around one another due to deformation by plane-strain elongation [113]. If more than one of such grains is viewed in a transversal cross-section like the one shown in figure 5.5c, the grains appear curled. This grain curling has often been compared [170] to the sky structure in Vincent van Gogh's "The Starry Night" (1889).

The elongated grains found in heavily drawn tungsten wires can be described by a length that is accessible in longitudinal sections (LS) and a width that can be determined from both longitudinal sections and transversal cross-sections (TCS) samples. The grain width and its evolution during

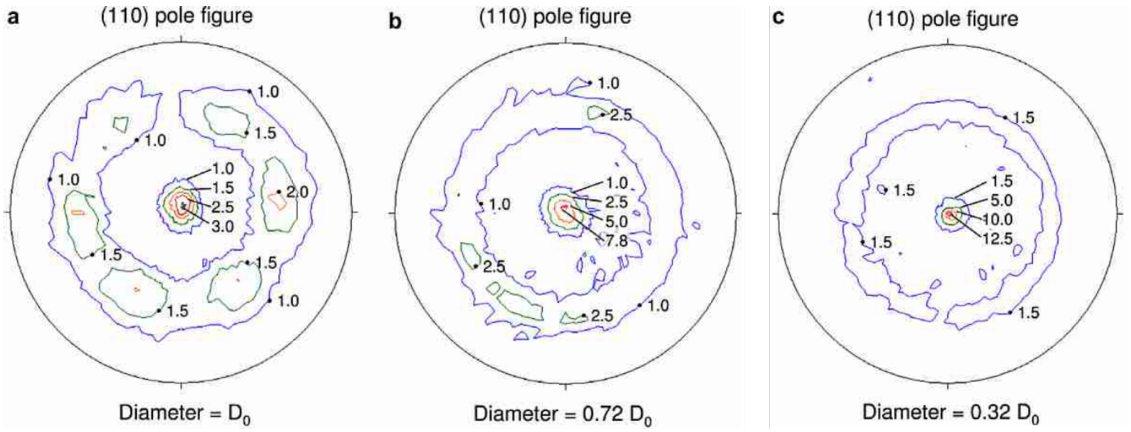

Figure 5.4: (110) pole figures of (a) a rolled and swaged tungsten rod, (b) a tungsten wire after 28 % and (c) after further 56 % reduction in wire drawing measured via neutron diffraction (from [173]). The contour lines join intensities of the same value.

the wire drawing process have been studied to great extent, while reports on the development of the grain length are scarce. Some literature values for the evolution of the grain width and other available microstructural features are shown in figure 5.6.

As illustrated in figure 5.6, the grain width decreases as the wire becomes thinner. The evolution of the grain length or its aspect ratio, i.e. the ratio between length and width, is less well studied. However, there is a relationship of both grain shape parameters with the ductile-to-brittle transition temperature: Seigle and Dickinson [34] as well as Eck [111] could show that T_{DBT} decreases with decreasing grain width. Similarly, Pink and Sedlatschek [190] report that an increase in grain aspect ratio also decreases the temperature of the ductile-to-brittle transition in recrystallised drawn molybdenum wires. In their study on molybdenum wires, Pink and Sedlatschek explain the lower transition temperatures in thinner wires with the complex path a crack has to take in a microstructure consisting of elongated grains, which increases the material's fracture toughness. They however conclude that the grain shape cannot be the only reason for the change in fracture behaviour[4], so that an all-encompassing, physically sound theory on why a smaller grain width or a larger grain aspect ratio have a beneficial effect on the DBT is still missing.

Since the plastic deformation during wire drawing is quite strong, the wires exhibit high dislocation densities. Some literature values are summarised in figure 5.6. Barna et al. [191] and Meieran and Thomas [172] report a strongly heterogeneous distribution of dislocations in different grains, i.e. some grains exhibit a high dislocation density while others are largely dislocation-free.

Since annealing phenomena are relevant for the microstructure evolution during wire drawing (intermediate annealing treatments, see 5.1.2), they are shortly summarised in the following: During recovery, which takes place at temperatures below 800 °C for tungsten wires, the dislocations generated during deformation form cell and subgrain structures [183, 192]. At higher temperatures, primary recrystallisation sets in. For tungsten wires, this means that the grain curling is lost and grains appear more circular in the transverse cross-section after primary recrystallisation. During primary recrystallisation, grain boundaries migrate until they reach the rows of potassium bubbles, which then pin the boundaries and inhibit further structural coarsening [183]. The grain elongation along the drawing axis is however not changed significantly due to the extension of bubble rows along the drawing axis. Since primary recrystallisation is retarded due to the presence

[4]Deriving a direct relationship between the grain length and the ductile-to-brittle transition from the comparison of recrystallised and as-drawn wires would anyway be challenging, since recrystallisation processes alter not only the grain length. Thus, T_{DBT} is influenced by many different variables and a shift of its value is difficult to be explained by only one individual parameter.

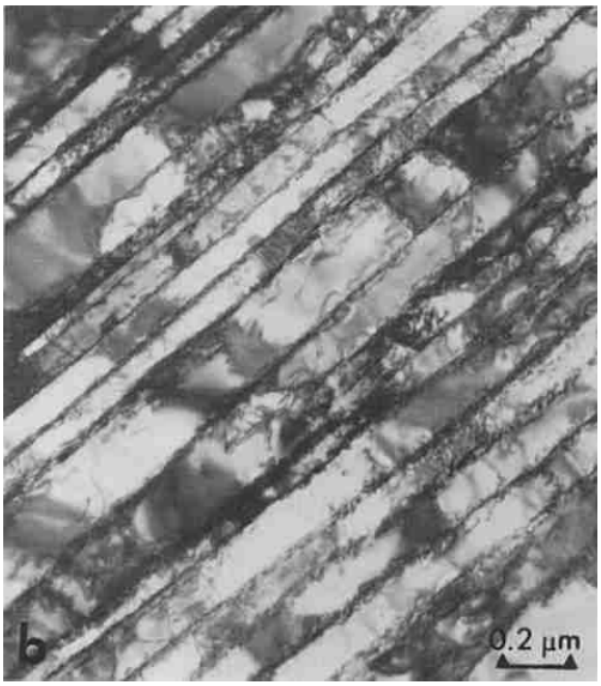

(a)

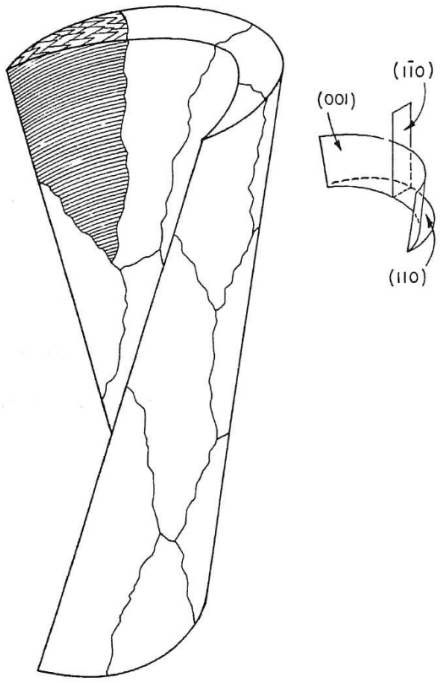

(b)

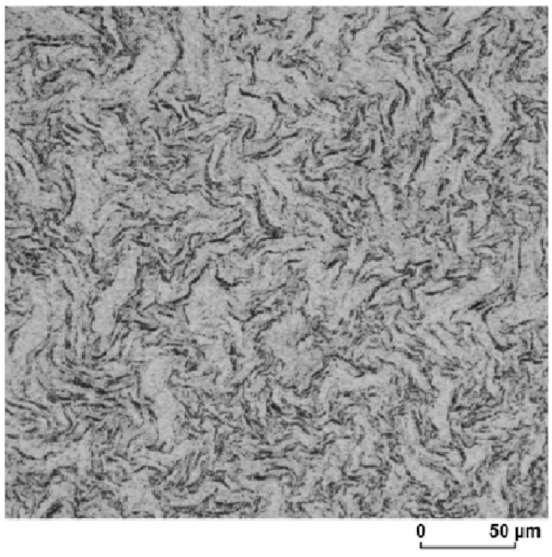

(c)

(d)

Figure 5.5: Microstructure of drawn tungsten wire: (a) Bright field TEM image acquired from a LS sample showing the grain structure of a 180 µm tungsten wire [179], (b) sketch of the bent shape of grains in thin drawn tungsten wires [172], (c) SE image of a transversal cross-section showing the curling of grain [185], (d) Simulation result of the deformation of grains during tungsten wire drawing illustrating the bending of grains around an axis parallel to the wire drawing axis [173].

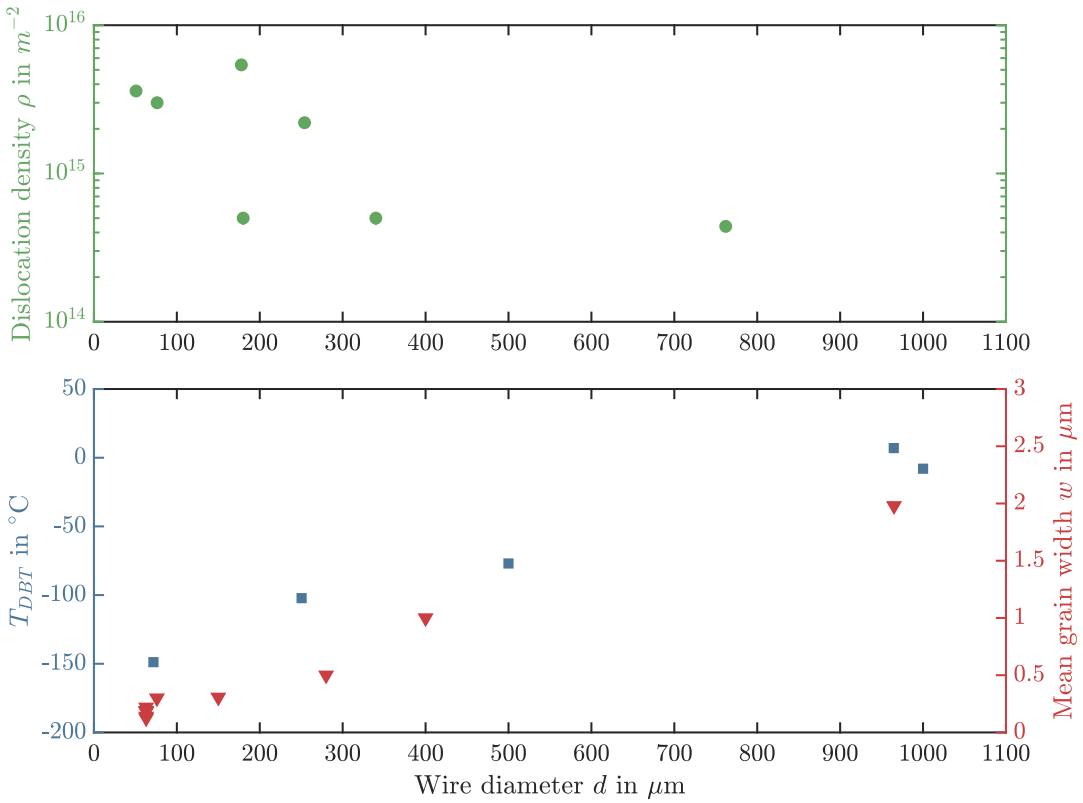

Figure 5.6: Microstructural evolution and ductility transition of drawn tungsten wires as a function of the wire diameter[3]: Dislocation density from TEM and XRD analyses (green, top) [186–188], width of elongated grains (bottom right) [34, 178, 184, 189] and ductile-to-brittle transition temperature T_{DBT} [34, 111].

of potassium bubbles, secondary recrystallisation leads to the exaggerated growth of individual grains with the aim of reducing the energy stored in the microstructure. The onset temperature for secondary recrystallisation is thereby a function of the wire diameter: While wires with a diameter of 500 µm show exaggerated grain growth at temperatures as low as 1700 °C, 150 µm thin wires show this phenomenon only above temperatures of 2250 °C [73, 179, 180].

5.1.5 Mechanical properties and deformation mechanisms of drawn tungsten wire

This section focuses on the low-temperature deformation mechanisms of tungsten wires – for creep deformation mechanisms and related properties, the reader is referred to [66, 193, 194].

The stress-strain curve of as-drawn doped tungsten wire with a diameter of 150 µm obtained in a room-temperature tensile test is shown in figure 5.7: In the as-fabricated state, the wire shows pronounced work hardening. Around the uniform strain, a stress plateau develops. As Riesch et al. [195] report, no visible necking develops during the stress plateau. The plateau is followed by a steep drop in stress, which is then related to the formation of a necking zone. This behaviour is explained based on the special microstructure of tungsten wires in the as-drawn state [196]: Assuming the grain boundaries lying non-parallel to the wire axis to fracture first when reaching the maximum stress, the transmission of shear forces via friction along the elongated gran boundaries parallel to the wire axis would prevent a catastrophic failure upon crack initiation. During the stress plateau, new cracks perpendicular to the drawing axis could

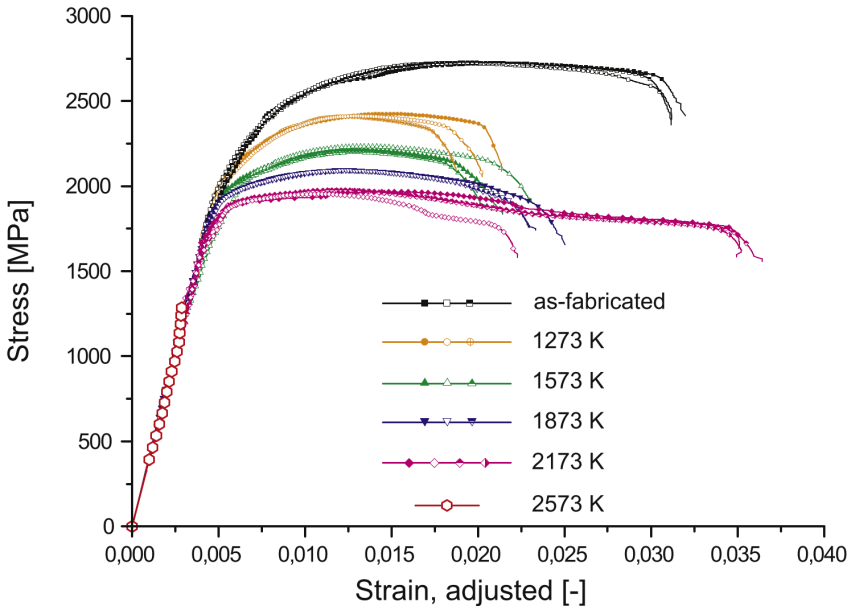

Figure 5.7: Engineering stress-strain curves of as-drawn (black curve) and annealed doped tungsten wires (coloured curves) with a diameter of 150 µm from [73]. The wires were annealed for a duration of 30 min.

form. Simultaneously, the grains could slide along their long boundaries. These processes would not decrease the stress significantly since the stressed cross-section would not change substantially and thus lead to the development of the plateau. Upon a certain true stress at which apparent necking commences, Riesch et al. [196] infer that cracks would also grow along the longitudinal grain boundaries parallel to the wire axis and the wire would split into bundles consisting of a multitude of grains, an effect already reported for example by Leber et al. in 1976 [33]. Until the final fracture, the bundles of grains neck down to almost 100 % reduction in area. This theory would match the commonly observed ductile fracture mode of tungsten wires, which is called fibrous fracture [33]. A representation of fibrous fracture is shown in figure 5.8.

The role of cohesive forces during the fracture of tungsten wires has been successfully modelled by Ren et al. [198]. Different theories on the deformation mechanisms governing the ductile deformation of tungsten wires at room temperatures can be found in literature. Boser [104] performed strain-rate jump tests on a wire with a diameter of 584 µm over a wide temperature range and found that the apparent activation volume corresponds to the kink-pair mechanism being rate-controlling during the deformation of tungsten wires [199]. Following this interpretation, the motion of screw dislocations controls the rate of plastic deformation [114]. In contrast to this result, Millner et al. [200] and Schultz [201] see grain boundary sliding, i.e. the sliding of grains along their mutual boundary during deformation, as the main mechanism governing the deformation of tungsten wires. So far, this contradiction has not been resolved yet so that the actual rate-controlling deformation mechanism remains unclear.

In order to investigate the influence of changes in the microstructure on the deformation mechanisms, two routes have been adopted so far: On the one hand, wires with different accumulated drawing strains were compared. On the other hand, a wire with a fixed diameter was annealed, and its deformation mechanism was investigated. The result of the latter is shown in figure 5.7: The recovery and primary recrystallisation processes taking place during annealing at intermediate temperatures ($T < 2300\,^{\circ}\mathrm{C}$) yields a decrease of work hardening and strength, while the ability of the wire to deform plastically is not hampered significantly. The decrease in work hardening rate

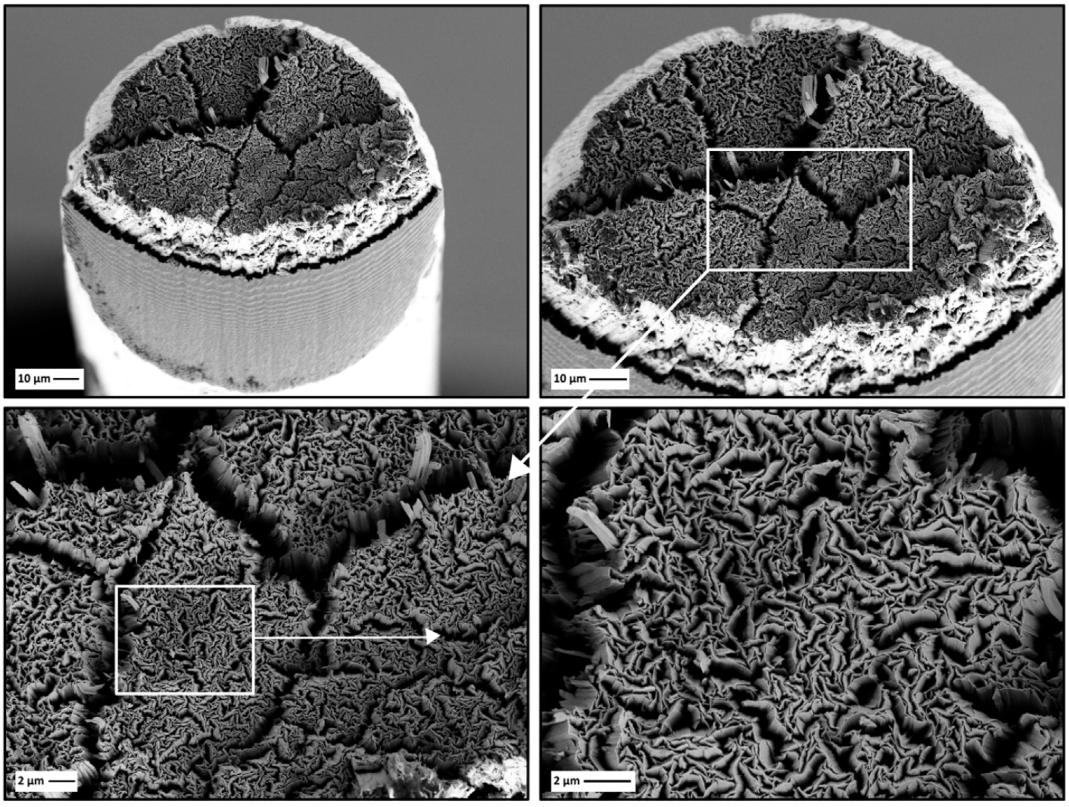

Figure 5.8: Topography of the fracture surface of a notched tungsten wire with a diameter of 150 µm broken at room temperature [197]. The insets show the fibre bundles consisting of a large number of grains that neck down very strongly prior to the macroscopic failure. The fibre bundles are separated by deep cracks running parallel to the drawing axis.

is probably linked to the decrease of the dislocation density [73]. Only if exaggerated grain growth sets in at very high annealing temperatures, the elongated, fine-grained microstructure and with it the ductile behaviour is lost, and the wire behaves in a brittle manner. The same behaviour has been shown by Zhao et al. [202] for pure tungsten wire, with the sole difference that the processes deteriorating the ductility set in at lower temperatures due to the lack of microstructure-stabilising potassium bubbles. High temperature tensile tests performed by Terentyev et al. [203] show that the deformation of tungsten wire ($d = 150\,\mu m$) annealed at 2300 °C for 30 min are different from the ones governing the deformation of as-drawn wire: While as-drawn wire reaches fracture strains around 2 % in the temperature range of 20 °C to 600 °C, annealed wire reaches a maximum fracture strain of 5 % around 300 °C and shows lower strains at higher temperatures. Terentyev and coworkers [203] explain this phenomenon by the nucleation of dislocations at the surface of the wire, which can then slip with considerable ease through the large, defect-free grains resulting from secondary recrystallisation. The deformation of as-drawn wire is superficially discussed by Terentyev et al. in terms of grain boundary strengthening and forest hardening.

Apart from annealing to change the microstructure and thus the deformation behaviour, wires with different diameters can be compared, as Leber et al. [33] did in terms of fracture behaviour. They found that there is a clear transition from brittle fracture by cleavage for wires with $d > 940\,\mu m$ to ductile, fibrous fracture for wires with diameters below 630 µm. This behaviour is clearly linked to the shift of the ductile-to-brittle transition temperature to lower temperatures

along with the decrease of the wire diameter in drawing, see figure 5.6. In addition to the fracture behaviour, the evolution of strength along with the accumulated drawing strain can be investigated when comparing wires with different diameters. By doing so, Riesch and coworkers [195] could confirm the assumption of Terentyev et al. [203] that grain boundary strengthening contributes to the high strength of the wires. Even though it has been studied if a tungsten wire with a certain accumulated drawing strain can deform plastically at a given temperature by determining its ductile-to-brittle transition temperature, the evolution of the extent of ductility (in the form of for example its uniform elongation, fracture strain or reduction in area) with the wire diameter has not yet been studied in detail.

5.2 Methods

5.2.1 Mechanical testing

5.2.1.1 Monotonous tests: Uniaxial tensile tests

Although an uniaxial tensile test appears to be one of the simplest mechanical test imaginable, many key parameters characterising the deformation of a material can be gained from it [204, 205]. Tensile tests are generally performed using tensile testing machines. A sketch of such a machine is shown in figure 5.9.

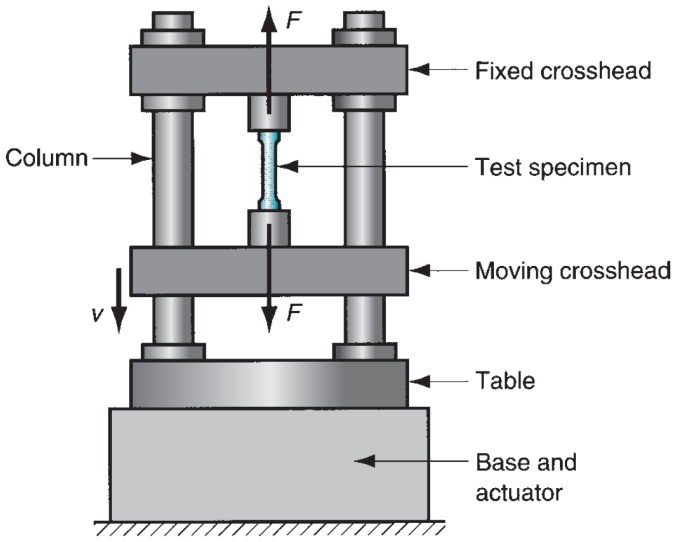

Figure 5.9: Sketch of a tensile testing machine (from [206]). Shown are the sample, the two crossheads as well as the table and base of the machine.

The main components of a tensile testing are the two crossheads between which the sample is fixed. In a simple uniaxial tensile test, one of the two crossheads is then moved with a constant crosshead velocity v (see figure 5.9). The force F acting in the sample is measured using a load cell which is connected in series to the sample and one of the two crossheads. The strain of the sample can be measured in various ways, for example using the displacement of the moving crosshead, special strain gauges, laser speckle interferometry or other optical techniques [204]. If the sample strain e is deduced from the displacement of the crosshead, the stiffness of the sample-machine assembly has to be taken into account. The engineering strain is defined as

$$e = \frac{\Delta l}{l_0} = \frac{l - l_0}{l_0} \tag{5.1}$$

where e : Engineering strain
l : Length of a line element
Δl : Incremental change in length of l
l_0 : Initial length of l

Using the force measured during the test, the engineering stress in the sample can be calculated:

$$R = \frac{F}{S_0} \tag{5.2}$$

where R : Engineering stress
F : Force acting in the sample
S_0 : Initial cross-sectional sample area.

Plotting engineering stress as a function of engineering strain yields the so-called *engineering stress-strain diagram*. From an engineering stress-strain curve, a number of key parameters characterising the mechanical properties of a material can be determined [205].

Fitting the elastic region of a stress-strain curve yields the Young's modulus E, which is characteristic for each material. If the sample is deformed above the elastic limit, its deformation becomes plastic, i.e. it remains if the sample is elastically unloaded. The point at which the transition from elastic to plastic deformation occurs, the so-called yield point, is often hard to distinguish. Thus, one commonly determines the stress at very small plastic strain, for instance 0.2 % as yield strength $R_{\mathrm{p0.2}}$. For very stiff materials with a high Young's modulus, yield strengths like $R_{\mathrm{p0.02}}$ or even $R_{\mathrm{p0.01}}$ at 0.02 % and 0.01 %, respectively, are reported [204]. The maximum stress reached in a tensile test is reported as ultimate tensile strength R_{m}. The corresponding strain, the so-called uniform elongation e_{u}, indicates the onset of non-uniform deformation since necking commences for $e > e_{\mathrm{u}}$. The end of necking and the fracture of the sample is described by the fracture strain e_{f} and the corresponding fracture stress R_{f}. An example of an engineering stress-strain curve including the major mechanical parameters is shown in figure 5.10.

In metal plasticity, the true strain ε is often preferred over the engineering strain, since it accounts for the influence of a strain path more accurately than the engineering strain [207]. It is defined as

$$\varepsilon = \int \frac{\delta l}{l} = \ln \frac{l}{l_0} = \ln (1 + e) \tag{5.3}$$

where l : Length of a line element
δl : Change in length of l
l_0 : Initial length of l
ε : True strain
e : Engineering strain

Presupposing volume conservation, an expression for the true stress

$$\sigma = \frac{F}{S} \tag{5.4}$$

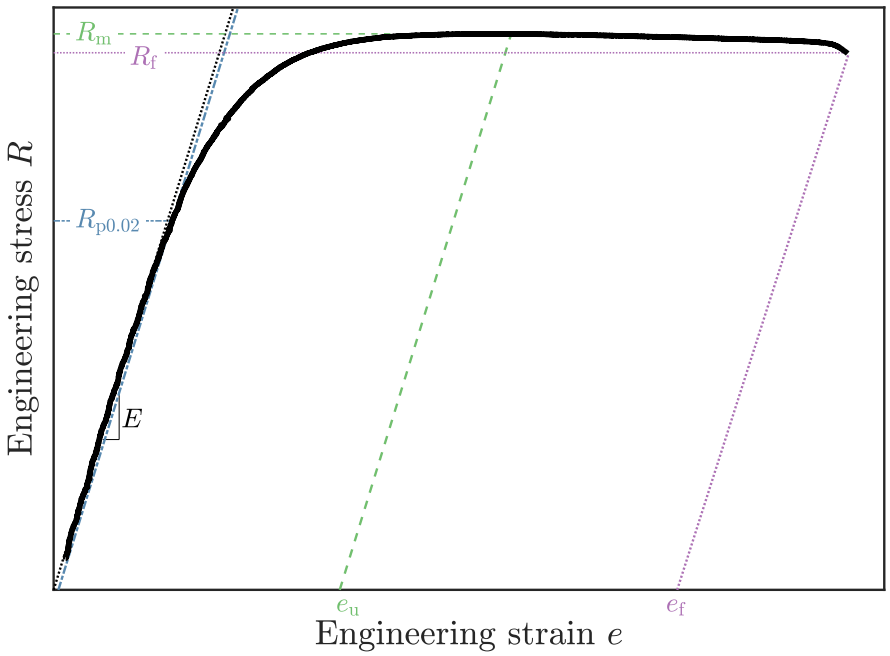

Figure 5.10: Engineering stress-strain diagram of a metallic sample. The key parameters Young's modulus E, 0.02 % yield strength $R_{\mathrm{p0.02}}$, ultimate tensile strength R_m, uniform elongation e_u, fracture strain e_f and fracture stress R_f are also indicated.

where σ : True stress
R : Force
S : Cross-sectional sample area

can be derived [207]:

$$\sigma = R\,(1 + e) \tag{5.5}$$

where σ : True stress
R : Engineering stress
e : Engineering strain.

Equations (5.3) and (5.5) are only valid for uniform elongation, i.e. it can only describe deformations without necking or other strain localisation phenomena. If necking effects shall be accounted for, the cross-sectional area of the whole sample has to be measured thoroughly throughout the test [204].

5.2.1.2 Transient mechanical tests

The basic assumption underlying transient mechanical tests is that the deformation mechanisms during a short transient (commonly around 30 s) are the same as the ones during a monotonous test such as a tensile test [80].

5.2.1.2.1 Strain-rate jump tests

Strain-rate jump tests are tests that allow for determining the strain-rate sensitivity and an apparent activation volume of a material [80] and can be performed using a standard tensile testing machine. The tests are performed by changing the crosshead velocity in the plastic region ($\sigma > \sigma_{\mathrm{Y}}$, where σ_{Y} is the true yield stress). The change in crosshead velocity translates into a change from an initial strain rate $\dot{\varepsilon}_1$ to a strain rate $\dot{\varepsilon}_2$ after the strain-rate change. The material's response to this transient is a jump in stress from σ_1 to σ_2. These parameters are used to calculate the strain-rate sensitivity

$$m = \frac{\ln \sigma_2 - \ln \sigma_1}{\ln \dot{\varepsilon}_2 - \ln \dot{\varepsilon}_1}. \tag{5.6}$$

where σ_1 : Stress prior to the strain-rate jump
σ_2 : Stress after the strain-rate jump
$\dot{\varepsilon}_1$: Strain rate prior to the strain-rate jump
$\dot{\varepsilon}_2$: Strain rate after the strain-rate jump

In addition to the strain-rate sensitivity, an apparent activation volume

$$V_{\mathrm{app}} = k_{\mathrm{B}}\, T\, \frac{\ln \dot{\varepsilon}_1 - \ln \dot{\varepsilon}_2}{\sigma_1 - \sigma_2} \tag{5.7}$$

where k_{B} : Boltzmann constant
T : Absolute temperature
σ_1 : Stress prior to the strain-rate jump
σ_2 : Stress after the strain-rate jump
$\dot{\varepsilon}_1$: Strain rate prior to the strain-rate jump
$\dot{\varepsilon}_2$: Strain rate after the strain-rate jump

can be determined from a strain-rate jump. The apparent activation volume is usually higher than the effective activation volume by a factor of 2 to 3 [208]. Several strain-rate jumps can be performed between the yield point and the maximum stress reached in the experiment. The temporal evolution of stress and strain (for a strain-rate jump test performed on a tungsten wire) is illustrated in figure 6.3 in chapter 6.

5.2.1.2.2 Repeated stress-relaxation experiments

In stress-relaxation experiments, the transient is created by stopping the moving crosshead. The material reacts to this change by relaxing the stored elastic stress. For most materials, including metals, this stress relaxation can be described by a logarithmic function [80]:

$$\Delta\sigma = \sigma\,(t) - \sigma\,(t=0) = -\frac{k_{\mathrm{B}}\, T}{V_{\mathrm{r}}} \ln\left(1 + \frac{t}{c_{\mathrm{r}}}\right), \tag{5.8}$$

where $\sigma\,(t)$: Stress at time t
k_{B} : Boltzmann constant
T : Absolute temperature
V_{r} : Apparent activation volume
t : Time
c_{r} : Time constant[5]

[5]The time constant can for example be used to evaluate the exhaustion of the mobile dislocation density during

Thus, single stress relaxations yield an apparent activation volume. A more detailed investigation of thermally activated dislocation mobility can be reached using repeated stress relaxation experiments [209]. In these experiments, the samples are given a fixed amount of time Δt to relax the stress. Then, it is reloaded to the stress right at the beginning of the relaxation, thereby completing the first relaxation cycle. Several relaxation cycles can be performed back to back. The temporal evolution of the stress during a RSRE is shown in figure 6.4 in chapter 6. Several ways of interpreting repeated stress relaxation experiments are available. Here, the method developed by Spätig et al. is presented [210]. This method involves determining $V_{\mathrm{r},1}$ during the first relaxation and the stress drops $\Delta\sigma_j\,(t = \Delta t)$ for the first and all subsequent relaxations. The maximum decay of the stress $\Delta\sigma_j$ during each relaxation j allows for calculating a correction term for the work-hardening occurring during the reloading

$$V_{\mathrm{h}} = \frac{k_{\mathrm{B}}\,T}{\sum_{j=1}^{N-1}\Delta\sigma_j}\ln\left[\frac{\exp\left(-\frac{\Delta\sigma_n V_{\mathrm{r},1}}{k_{\mathrm{B}}\,T}\right)-1}{\exp\left(-\frac{\Delta\sigma_1 V_{\mathrm{r},1}}{k_{\mathrm{B}}\,T}\right)-1}\right]. \tag{5.9}$$

where k_{B} : Boltzmann constant
T : Absolute temperature
$\Delta\sigma_j$: Maximum stress decay at the end of the j^{th} relaxation cycle
$V_{\mathrm{r},1}$: Apparent activation volume determined during the first relaxation cycle

The effective activation volume is then obtained as the difference between $V_{\mathrm{r},1}$ and V_{h}:

$$V_{\mathrm{eff}} = V_{\mathrm{r},1} - V_{\mathrm{h}} \tag{5.10}$$

where V_{eff} : Effective activation volume
$V_{\mathrm{r},1}$: Apparent activation volume determined during the first relaxation cycle
V_{h} : Apparent activation volume, describing the hardening during reloading of a repeated stress relaxation experiment

The strain-rate sensitivity is also accessible using the effective activation volume obtained from repeated stress relaxation experiments according to equation (4.8):

$$m = \frac{k_B\,T}{V_{\mathrm{eff}}\,\sigma_0}. \tag{5.11}$$

where k_{B} : Boltzmann constant
T : Absolute temperature
V_{eff} : Effective activation volume
σ_0 : Relaxation stress

5.2.2 Methods for microstructural characterisation

Similar to light microscopy, electron microscopy can be divided into techniques using transmitted (Transmission electron microscopy (TEM), see section 5.2.2.2) or reflected electrons (scanning electron microscopy (SEM), see section 5.2.2.1) for imaging. The main features, advantages, and drawbacks of these techniques as well as related techniques like electron backscattering diffraction (EBSD, section 5.2.2.1.3) and focused ion beams (FIB, section 5.2.2.1.4) will be discussed briefly in the following. X-ray diffraction as another important method of analysing crystalline materials will be reviewed in section 5.2.2.3.

relaxation experiments [80].

5.2.2.1 Scanning electron microscopy (SEM) and related techniques

5.2.2.1.1 Components of a SEM

The main components of an SEM are schematically shown in figure 5.11a.

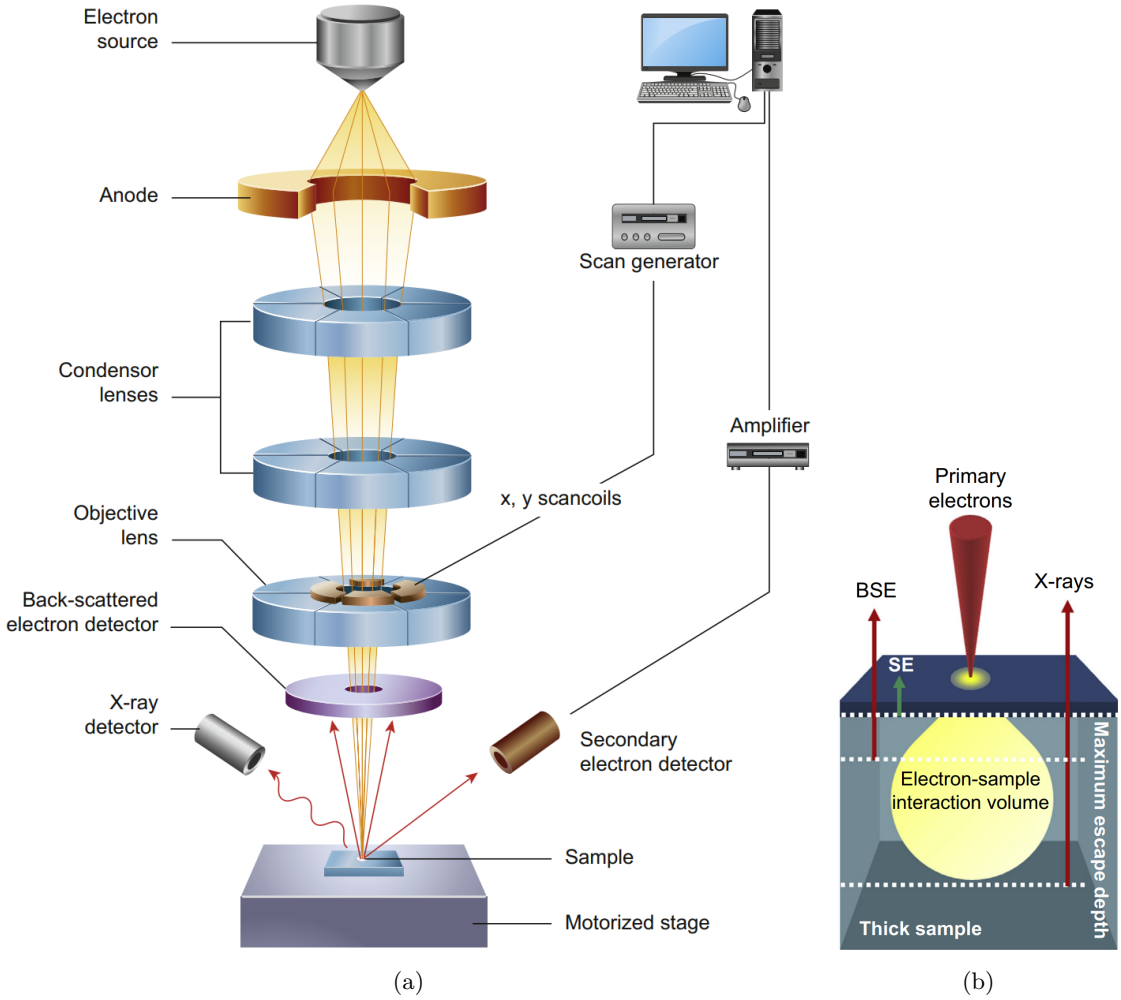

Figure 5.11: Main components (a) and signals (b) of a modern-day scanning electron microscope (from [211]).

In order to produce free electrons in the first place, modern-day scanning electron microscopes are equipped with electron guns utilizing the field enhanced thermionic emission principle. The so-called *Schottky effect* describes the enhanced emission of electrons from a conductive material under an external applied electrical field. The electrical field reduces the potential barrier, thereby allowing the electrons to tunnel through it [212]. Using a Wehnelt device, the free electrons are channelled, and an electron beam is formed[6]. By passing through an acceleration tube with an applied voltage U_A, the electrons are accelerated. The electron wavelength after acceleration is inversely proportional to the square root of the accelerating voltage U_A [213]. Accelerating voltages in common scanning electron microscopes rarely exceed 30 kV [214]. The electron beam current can be tailored, utilising apertures blocking a defined fraction of the beam. Using a series of electrical and electromagnetic coils, the electron beam is shaped and focused onto the sample surface. Both

[6]The electron gun and the Wehnelt cylinder are shown as one component called *Electron source* in figure 5.11.

the sample and the electron column are evacuated in order to reduce interference between residual gas atoms and the electron beam. The beam is scanned across the sample surface by applying a voltage to dedicated scanning coils. Combining a detected signal (see section 5.2.2.1.2) and the beam location at each point of time, an image can be constructed. The main signals that can be used for imaging and analysis in a SEM are shown in figure 5.11b. Note the pear-shaped form of the interaction volume generated by the primary electrons.

5.2.2.1.2 Main signals and their detection

The main (imaging) signals used in a modern-day SEM are backscattered electrons (BSE) and secondary electrons (SE). As the name suggests, backscattered electrons (BSE) are electrons from the initial beam's primary electrons (PE) that undergo elastic scattering at the crystal lattice and thus exhibit energies close to the energy of PE. The backscattering yield η is defined as the ratio between the intensity of BSE and PE [215]:

$$\eta = \frac{I_{\mathrm{BSE}}}{I_{\mathrm{PE}}} \tag{5.12}$$

where η : Backscattering yield
I_{BSE} : Intensity of backscattered electrons
I_{PE} : Intensity of primary electrons

Backscattered electrons are nowadays usually detected using solid state Si detectors [214] that are placed centred below the pole piece. The resolution of BSE is limited by their escape area, which is in turn linked to the accelerating voltage. In comparison to SE, the contrast of electron images using the BSE signal allows for reliably discerning regions with different chemical compositions and crystal orientations.

Secondary electrons are generated throughout the whole interaction volume in a depth of 0.5 nm to 50 nm [215]. Only those SE with energies higher than the work function Φ of the sample material

$$E_{\mathrm{SE}} > \Phi$$

can however escape the sample. The energy of secondary electrons is thus a continuum ranging from E_{PE} down to Φ. Similar to equation (5.12), the yield of secondary electrons can be defined as

$$\nu = \frac{I_{\mathrm{SE}}}{I_{\mathrm{PE}}} \tag{5.13}$$

where ν : Secondary electron yield
I_{SE} : Intensity of secondary electrons
I_{PE} : Intensity of primary electrons

Secondary electrons are usually detected using a so-called *Everhart-Thornley detector* (ETD) [216]. This type of detector features a metallic grid that can be biased positively or negatively, thereby increasing ν by attracting secondary electrons or enabling the detection of BSE and thus increasing η by repelling secondary electrons[7]. Electrons that pass the grid hit a scintillating layer

[7] Due to their high kinetic energy, the repulsion of BSE cannot be achieved efficiently with an ETD.

that allows for converting the electron signal into a photon signal. Using fibre optics, the electrons are guided to a photomultiplier that amplifies the initial signal. Due to the commonly utilized asymmetric geometry of beam, sample and ETD, SE images feature an unsurpassed topographic contrast [214].

Apart from secondary and backscattered electrons, the detection of characteristic X-rays (energy-dispersive X-ray spectroscopy (EDX) and wavelength-dispersive X-ray spectroscopy (WDX)) is used frequently for chemical sample analysis. For further information on these techniques, the reader is referred to [215] or [213]. Further detectable signals like Auger electrons or visible light (cathodoluminescence) are utilized for special applications, see [214].

5.2.2.1.3 Electron backscatter diffraction (EBSD)

Electron backscatter diffraction (EBSD) is the most commonly used technique in modern-day SEM to determine the crystal orientation and symmetry, as well as the phase of a crystallite or strain (fields) in the crystalline lattice [217].

5.2.2.1.3.1 Formation of electron backscatter patterns (EBSP)

As already discussed in section 5.2.2.1.2, one of the signals emerging from the surface of a sample illuminated by an electron beam are backscattered electrons. For SEM images making use of the BSE contrast, simply the number of BSE emerging from the scanned pixel is measured and converted into visual information. Additional information on the material can be gained if the BSE are detected in a different kind of way: If the material that is hit by the electron beam contains crystalline fractions, the backscattered electrons are also elastically scattered at the crystalline lattice. This is due to omnidirectional thermally diffuse scattering (TDS). There are always BSE that fulfil the Bragg equation [218]

$$n\,\lambda = 2\,d_{\mathrm{hkl}}\,\sin\theta_{\mathrm{B}} \tag{5.14}$$

where n : Diffraction order
λ : Wavelength of the diffracted wave
d_{hkl} : Distance of lattice planes with the Miller indices $\{hkl\}$
θ_B : Bragg angle

elastic scattering can occur. The trajectory of electrons elastically scattered at a given lattice plane is described by the surface of a cone, cf. figure 5.12a. For common SEM parameters, the Bragg angle is very low, i.e. the half apex angle of the cone $90° - \theta_{\mathrm{B}}$ is close to 90°. If the Kossel cone intersects a flat surface, for example a detector[8], a Kikuchi band [220] is formed (see figure 5.12b). The lines of the band appear parallel and have a spacing of $2\,\theta_{\mathrm{B}}$ [219]. Increasing the energy of the primary beam and thus decreasing the electron wavelength decreases the Kikuchi band width according to equation (5.14). The overlapping Kikuchi bands of the various lattice planes of a crystallite give rise to the Kikuchi pattern or Electron Backscatter Pattern (EBSP) (see figure 5.13).

[8]Modern-day EBSD detector consist of a phosphor screen intersected with a fast CCD camera that records the EBSP [219].

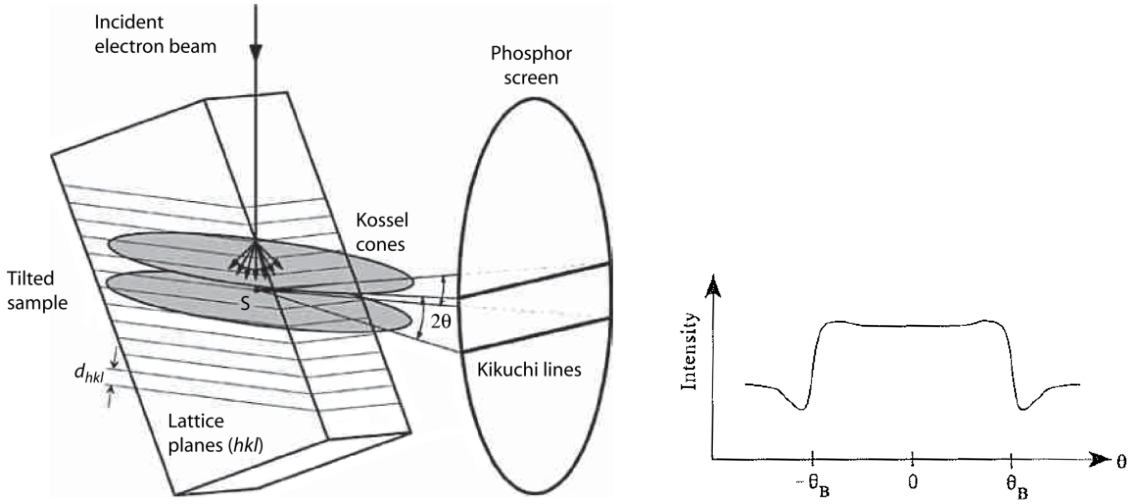

(a) (b)

Figure 5.12: Formation of EBSP in reflective geometry (a, from [219]) and angular intensity profile of an excess Kikuchi band (b, from [221]).

5.2.2.1.3.2 Identification and indexing of EBSP

Although there are more advanced methods available (see for example [222]), the standard indexing technique for EBSP [223] is based on a transformation of the EBSP into the accumulation space using the Hough [224] or the Radon transform [225]. The bands making up the EBSP appear as points after the transformation[9] and can be detected easily using computer algorithms. The result of the Radon transformation, which is described in more detail in [219] and [217] is shown in figure 5.13.

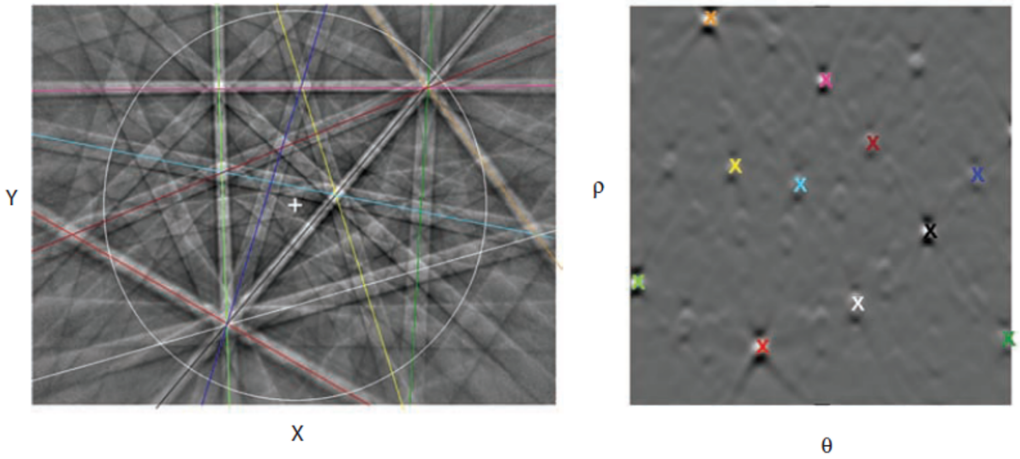

Figure 5.13: Electron backscatter pattern (left) and corresponding Hough transform (right). From the location of Hough peaks, the location of Kikuchi bands can be inferred and the EBSP can be indexed [217].

Once the bands in the EBSP are identified, the whole pattern is compared to simulated EBSP of the materials under consideration. The Kikuchi pattern can be indexed if a similar EBSP can

[9]The transformation is described as gray-tone weighted Hough transformation [219].

be found among the simulated patterns.

5.2.2.1.3.3 Microscope parameters for EBSD

In order to get indexable Kikuchi patterns, the microscope parameters have to be set with care [219]. In order to increase the backscattering yield η, the sample is tilted to angles between 60° to 80° relative to the incident beam. The accelerating voltage has to be tuned according to the aim of the EBSD investigation: Since a low accelerating voltage is linked to a small interaction volume, it should be chosen if a high spatial resolution, e.g. for the study of deformed or fine-grained material, is requested. High accelerating voltages are beneficial since they yield a higher efficiency of the phosphor screen. Furthermore, increasing the accelerating voltage increases the depth from which the diffracted BSE forming the EBSP emerge, and thus surface contamination affects the pattern quality less. In terms of the electron beam current, an overall lower current also reduces the size of the interaction volume and is hence beneficial for spatial resolution. As Humphreys and co-workers [226, 227] found, the effective resolution of EBSP is a non-linear function of the probe current and needs to be adjusted for each material individually. Another important parameters to be set for EBSD measurements is the spacing of measuring points, the so-called step size Δx, which needs to be adapted to the grain (or subgrain) size of the material to be investigated. In this context, it is also important to finely tune the exposure time, i.e. the duration for which the EBSP is recorded at each step, since it greatly influences the measurement duration.

5.2.2.1.3.4 The MTEX toolbox: A modern tool for the analysis of orientation maps

The MTEX toolbox[10] offers a free and convenient way to analyse orientation data obtained via various experimental methods (EBSD, Transmission Kikuchi Diffraction, neutron scattering, X-Ray diffraction, etc.) [228]. MTEX comes in the form of a MATLAB toolbox and comprises a multitude of functions for topics like grain analysis, analysis of crystallographic texture, analysis of geometrically necessary dislocation densities, phase transitions and others. MTEX makes use of a novel algorithm to calculate orientation distribution functions that is described in detail in [228].

5.2.2.1.4 Focused ion beam techniques

For the use in modern-day scanning electron microscopes, focused ion beam (FIB) techniques can be divided into three main fields of application: Structuring and preparation at nm scale, deposition of materials and FIB tomography [229]. There are currently three different methods for generating a beam of ions in FIB systems. The most commonly used FIB sources are so-called liquid metal ion sources (LMIS) [230]. These consist of a tungsten needle that is attached to a Ga reservoir. Due to ohmic heating, the tungsten needle heats up if a current is flowing through it. If the melting point of $T_{\mathrm{m,Ga}} = 29.5\,^{\circ}\mathrm{C}$ is reached, the molten metal wets the tip. Applying a high electric field to the tip leads to the ionisation and field emission of Ga^+ ions [230], see also section 5.2.2.1.1. Further ion sources are plasma sources, which normally produce a beam of Xe^+ ions and noble gas field emission sources, which produce beams of either He^+ or Ne^+. Once the ion beam is formed, it is accelerated using voltages typically in the range of 5 kV to 40 kV and subsequently shaped using quadrupole or octupole magnetic lenses [230]. If the ion beam hits the

[10] `https://mtex-toolbox.github.io/`

sample surface, the transfer of momentum leads to the ejection of atoms from the sample surface, i.e. the material is locally removed (FIB milling). During milling, the ion beam current and energy have to be monitored closely in order to achieve the desired removal rate. Furthermore, the orientation of the sample has to be taken into account since the milling process is crystal orientation dependent [215]. Using a suitable gaseous precursor, the focused ion beam can be used to deposit material on the sample surface. The precursor is thereby guided to the scanned region by means of a thin tube. Under ion irradiation, the precursor is cracked and an amorphous mixture of the constituents of the precursor gas and sputtered sample atoms[11] is deposited. In materials science, the combination of milling and deposition is used to prepare cross-sections of a material or to prepare thin lamellae for transmission electron microscopy, see section 5.2.2.2 [229]. In this context, the FIB-assisted deposition of Pt, W or C serves two different purposes: On the one hand, it protects the sample surface from irradiation damage caused by the impinging ions. On the other hand, it forms a continuous top layer on the region of interest and thus enables clean FIB-cut cross-sections since inhomogeneities (hardness/topology) lead to channelling of the ion beam which in turn leads to the so-called *curtaining* effect, i.e. a rough and undulating surface of the cut section [231].

5.2.2.2 Transmission electron microscopy (TEM)

Similar to light microscopy, electron microscopy can be performed in reflecting (SEM) and transmission geometry. The latter is summarised in the term transmission electron microscopy (TEM). Due to its higher energy, the interaction volume of an electron beam with a sample material in a TEM is smaller than the one of a SEM. Thus, TEM is better suited for smaller samples (particles, nanostructures, even rows of atoms) or the high-resolution investigation of a material's microstructure [211].

5.2.2.2.1 Components of a TEM

The components of a TEM are shown in figure 5.14a. Similar to a scanning electron microscope, transmission electron microscopes commonly feature a field emission electron source due to its low energy spread of the electron beam. In order to pass through the thin samples used in transmission electron microscopy, the electrons are commonly accelerated to energies of 200 keV to 300 keV [232]. After passing through the condenser lens, the electrons hit the sample. Then, the trajectory of the electron beam depends on the mode of operation (see section 5.2.2.2.2): The current flowing through the intermediate lens that is positioned between the selected area aperture and the projector lens (cf. figure 5.14a), decides whether the TEM is operated in imaging or diffraction mode. The detectors used in scanning transmission electron microscopy (STEM, see section 5.2.2.2.3) are positioned below the projector lens. Finally, either direct observation of the image or diffraction pattern is possible using a viewing screen or CCD camera. If both the viewing screen and the camera are retracted, electron energy loss spectroscopy (EELS) can be performed [232]. EELS makes use of the inelastic scattering of electrons in the sample by quantifying their energy loss and provides information on the thickness, composition, bonding structure and electrical properties of a sample [233]. The detector used for the other major analytical tool in a TEM, X-ray spectroscopy, sits at approximately the same height as the sample. The main signals that are generated when a focused electron beam hits a thin sample, as is the case of TEM is shown in figure 5.14b.

[11] so-called re-deposited atoms

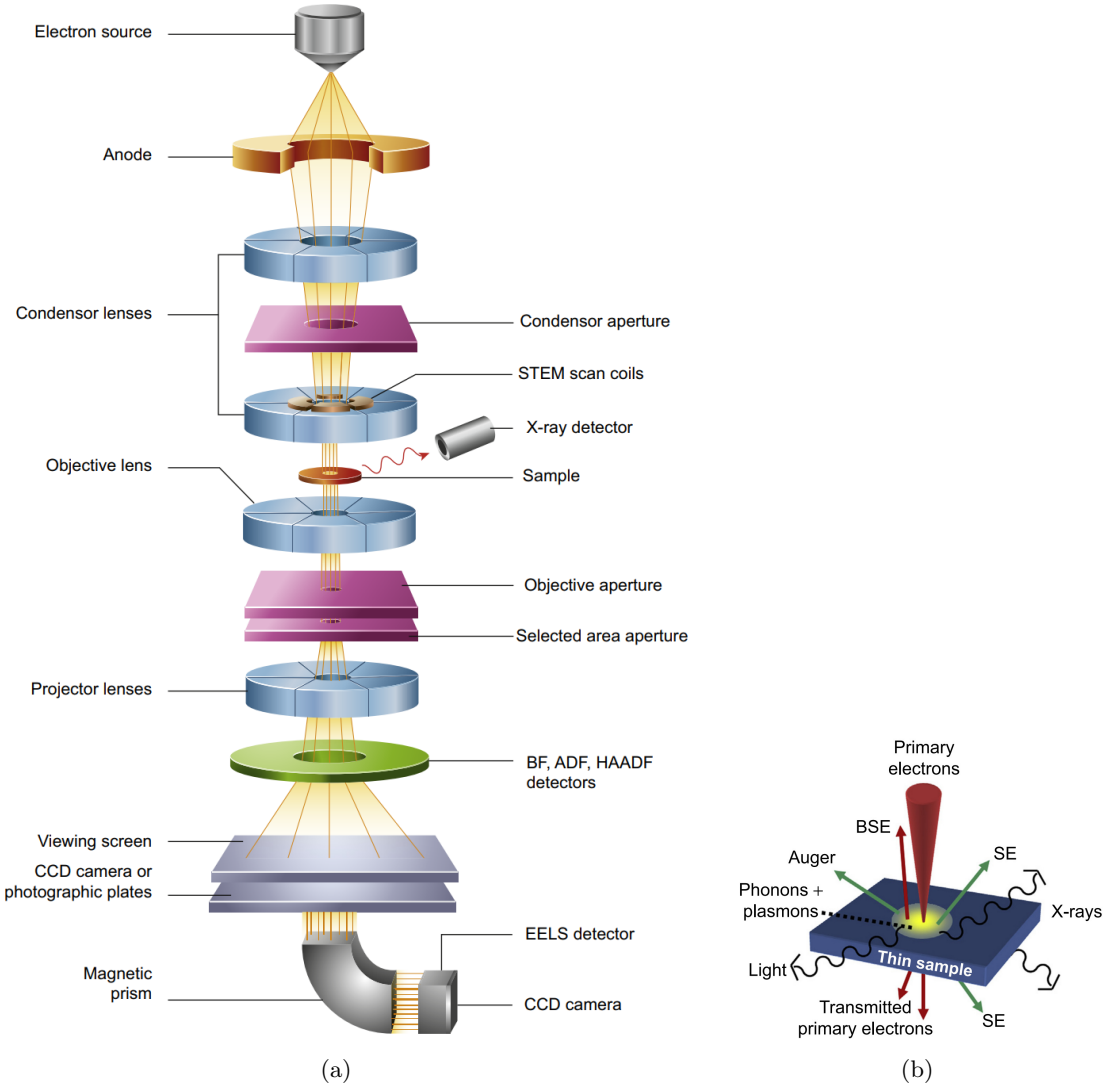

(a) (b)

Figure 5.14: Main components of a modern-day transmission electron microscope (a) and an overview over signals that can be generated upon the interaction of an electron beam with a thin, electron-transparent material sample that is used for transmission electron microscopy (b) (from [211]).

5.2.2.2.2 Imaging modes

Apart from scanning transmission electron microscopy, which is discussed in section 5.2.2.2.3, the main modes of operation in conventional TEM are imaging or diffraction, see figure 5.15.

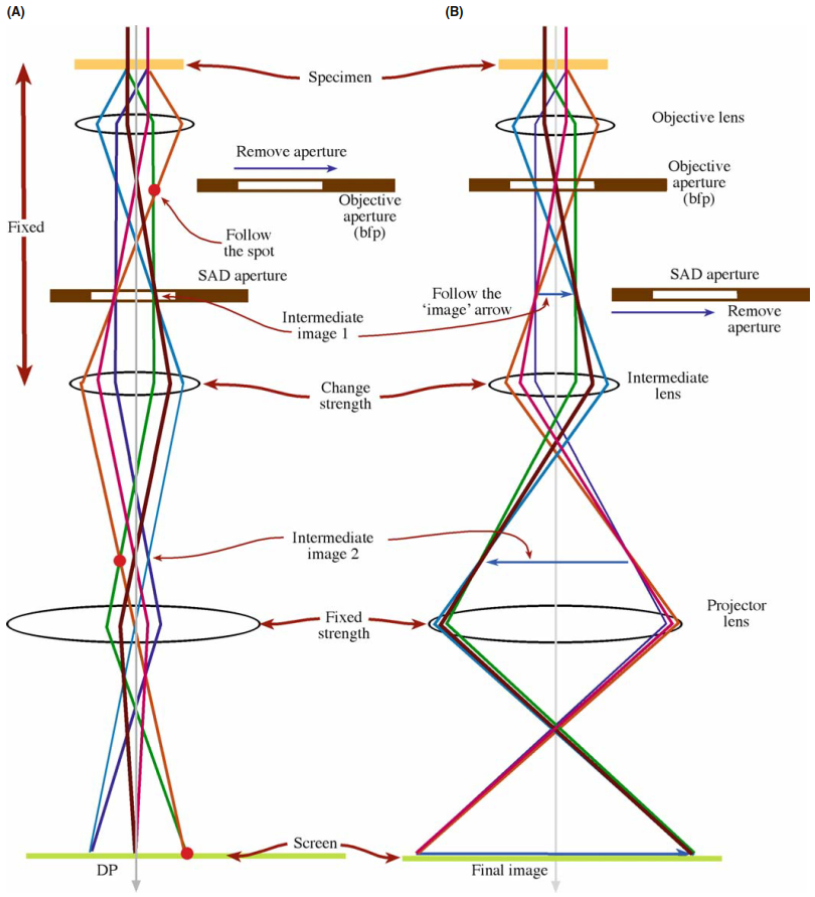

Figure 5.15: The two modes of operation in conventional TEM: Diffraction mode (left) and imaging mode (right, from [232]).

In imaging mode, the first intermediate image is magnified on the screen or CCD camera. In diffraction mode, the first diffraction pattern formed by electrons that are scattered at the crystalline lattice of the sample can be imaged. The area forming the diffracted image can be restricted by blocking the diffracted beams from other regions using the selected area aperture [211]. This is, for example, useful, if precipitates in a matrix shall be investigated. The final image can either be formed by the transmitted (BF, bright field imaging) or a selected diffracted beam (DF, dark field imaging). Thus, areas fulfilling the Bragg equation (see (5.14)) appear dark in BF imaging and bright in DF imaging [232].

5.2.2.2.3 Scanning transmission electron microscopy

In contrast to conventional transmission electron microscopy (CTEM), where a spread electron beam illuminates the sample, a (convergent) focused electron beam is scanned over the sample in scanning transmission electron microscopy (STEM) [211]. Due to the nature of their formation, STEM images are a superposition of parallel beam CTEM images. The high convergence of the beam yields a low interaction volume and in turn a higher resolution of the STEM images

compared to CTEM images. Analytical methods like EELS or EDX spectroscopy (see section 5.2.2.2.1) can be performed simultaneously to STEM imaging. A segmented annular detector used in STEM imaging is shown exemplarily in figure 5.14a. Different segments of the annular detector are suitable for different purposes: The high angle annular dark field (HAADF) detector with the highest acceptance angle[12] is for example well suited for defect analysis since electrons diffracted by thermally diffuse scattering (see section 5.2.2.1.3) reach the angular range it covers [232].

5.2.2.2.4 Imaging of crystal defects

Crystal defects like dislocations or grain boundaries can be imaged in TEM due to their nature of locally distorting the crystalline lattice. This is illustrated exemplarily in figure 5.16

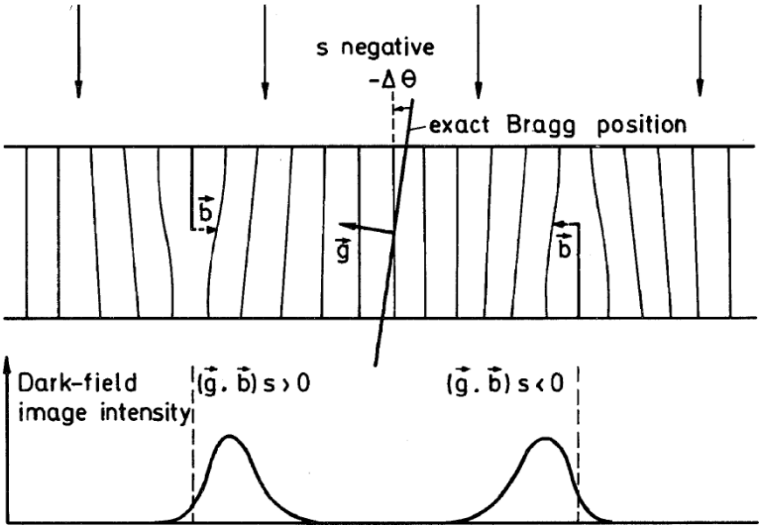

Figure 5.16: Contrast mechanisms in dark field mode for two dislocations in an otherwise perfect crystal lattice [234]: Due to the strain field surrounding the dislocations, they appear bright if the scattered electrons are used for imaging. $\vec{g}$ represents the diffraction vector, $\vec{b}$ the Burgers vector of the dislocation and $\vec{s}$ the excitation error.

In BF TEM, the lattice in which a dislocation is embedded fulfils the Bragg equation and appears bright while the dislocation does not fulfil the equation, thus appearing dark and vice versa in DF TEM [235]. For techniques to determine the Burgers vector of a dislocation in TEM and advanced methods like weak beam dark field, the reader is referred to [234]. The contrast mechanisms for imaging grain boundaries are very similar to the ones of dislocations, since also planar defects like grain boundaries represent a distortion of the crystalline lattice and can be imaged accordingly. While low-angle grain boundaries which are accumulations of multiple dislocations might be analysed using the techniques used for dislocations given their misorientation angle is low enough, high-angle grain boundaries stand out in TEM images since the grains that form the grain boundary have different orientations to the primary beam and are thus discernible due to different contrast both in CTEM (BF/DF) and STEM.

5.2.2.3 Structural analysis using X-ray diffractograms

X-ray diffraction is a versatile method for the analysis of materials. In contrast to (electron) microscopy, large volumes can be investigated with ease with X-ray techniques. Among other aspects

[12]The acceptance angle is enclosed by the primary transmitted and the diffracted beam arriving at the detector.

like crystallinity, phase constitution, crystallographic texture, crystallite size, residual strain and defect structure of a material can be assessed using X-rays [236]. The following paragraphs will focus on the most commonly used technique for the analysis of powders or polycrystalline samples, namely the acquisition of diffractograms in Bragg-Brentano geometry, and how the acquired data are evaluated in order to analyse the microstructure defect structure of the investigated samples. For further techniques, the reader is referred to [236, 237].

5.2.2.3.1 Hardware

X-rays are generated by accelerating an electron beam onto a cathode in an X-ray tube. Upon impact of the beam on the (water-cooled) cathode, electromagnetic radiation is emitted [236]. The emitted radiation can be subdivided into characteristic X-rays and bremsstrahlung. Bremsstrahlung is generated due to the deceleration of the electrons in the cathode surface, and thus forms a spectrum of energies. Characteristic X-rays are generated if an inner-shell electron of a nucleus of the cathode material is knocked out of the atom and an electron from a higher shell takes its place. The energy difference between the two shell positions is emitted as a photon, with the wavelength

$$\lambda = \frac{hc}{\Delta E} \tag{5.15}$$

where λ : Photon wavelength
ΔE : Energy difference between the shell where an electron is knocked-out and the outer shell from which an electron fills the hole
h : Planck's constant
c : Velocity of light in vacuum

Thus, as the name suggests, characteristic X-rays are distinctive for a given cathode material. The most common cathode material is copper [238]. Its most energetic characteristic lines possess wavelengths of around 1.54 Å. For the study of polycrystalline samples or powder, the beam emitted from an X-ray source has to be limited to the characteristic lines by using monochromators [236]. Beam shaping is commonly performed using collimators such as Soller slits, which reduce the beam divergence [238]. The scattering of X-rays on the crystalline lattice of the sample follows the famous Bragg equation, see equation (5.14) [218]. The scattered beams can be collimated and shaped similar to the incident X-rays, see figure 5.17a. Point (0D), line (1D) or area detectors (2D) can be used to convert the diffracted beam into an electric signal. Different detectors like scintillation counters, proportional counters or solid-state (semiconductor) detectors can be used depending on the geometry of the goniometer and the purpose of the analysis [238].

The finite angular resolution of the diffractometer contributes to the broadening of diffraction peaks in addition to the microstructural effects (see section 5.2.2.3.3) that are for example investigated in the Williamson-Hall [239] or Warren-Averbach analysis [240]. The convolution of the mentioned effects can be described as follows [237]:

$$I(2\theta) = \int_{+\infty}^{-\infty} I_{\text{inst}}(\psi)\; I_{\text{sample}}(2\theta - \psi)\; d\psi \tag{5.16}$$

where $I(2\theta)$: Total measured diffracted intensity at the diffraction angle 2θ
2θ : Diffraction angle
$I_{\text{inst}}(\psi)$: Diffracted intensity related to the used diffractometer

ψ : Auxiliary variable covering all possible ways the diffractometer can influence the diffracted intensity

$I_{\text{sample}}(2\theta - \psi)$: Diffracted intensity related to the sample's microstructure

In order to determine $I_{\text{sample}}(2\theta - \psi)$, the measured data has to be deconvoluted. This can be mathematically either very complex or relatively easy, depending on the shape of the measured peaks. If the peaks are described sufficiently well by a Gaussian or a Lorentzian distribution, the deconvolution of the measured peak breadth[13] is given as [241]

$$B_{\text{tot}}^{\text{n}} = B_{\text{inst}}^{\text{n}} + B_{\text{sample}}^{\text{n}} \tag{5.17}$$

where

B_{tot} : Total peak breadth (FWHM or integral breadth)

B_{inst} : Peak breadth (FWHM or integral breadth) caused by the diffractometer

B_{sample} : Peak breadth (FWHM or integral breadth) caused by the sample's microstructure

$n = \begin{cases} 1: & \text{Lorentzian} \\ 2: & \text{Gaussian} \end{cases}$: Exponent depending on the peak shape

5.2.2.3.2 Bragg-Brentano geometry

The Bragg-Brentano geometry is a focusing geometry (in contrast to parallel beam geometries) where the X-ray source and detector move on a circle that has the sample in its centre, see figure 5.17a. It is most suited for the study of polycrystalline or powder samples, since it uses monochromatic X-ray [238]. The Bragg-Brentano geometry is characterised by a high intensity and a low measuring time but also comes with a high beam divergence and a high angular error. Several systematic errors that need to be taken into account for this kind of geometry are listed in [236].

In Bragg-Brentano geometry, only those lattice planes that have their plane normal symmetric between incident and scattered beam contribute to the scattered intensity, see figure 5.17b. The Bragg-Brentano geometry is mainly used to acquire diffractograms by scanning a certain angular range $\Delta\theta$. A schematic example of a diffractogram is shown in figure 5.17c. Amorphous fraction in the sample manifest in a higher background of the diffractogram. If the sample contains crystalline regions, the diffractogram features peaks at the Bragg angle, see equation (5.14). If the crystal structure of the crystalline regions is known, the position of the peaks can be calculated using

$$2\theta_{\text{theor}} = 2 \arcsin\left(\frac{n\lambda}{2\, d_{\text{hkl}}}\right) \tag{5.18}$$

where

θ_{theor} : Theoretical peak position

n : Diffraction order

λ : Wavelength of the X-ray photons

d_{hkl} : Lattice spacing of the lattice with the Miller indices h, k and l (see for example equation 3.14 in [236])

h, k, l : Miller indices of the diffracting plane

Due to kinematic scattering, some Bragg reflections do not show up in a certain crystal struc-

[13] In crystallography, the width of a peak is denoted as *breadth*.

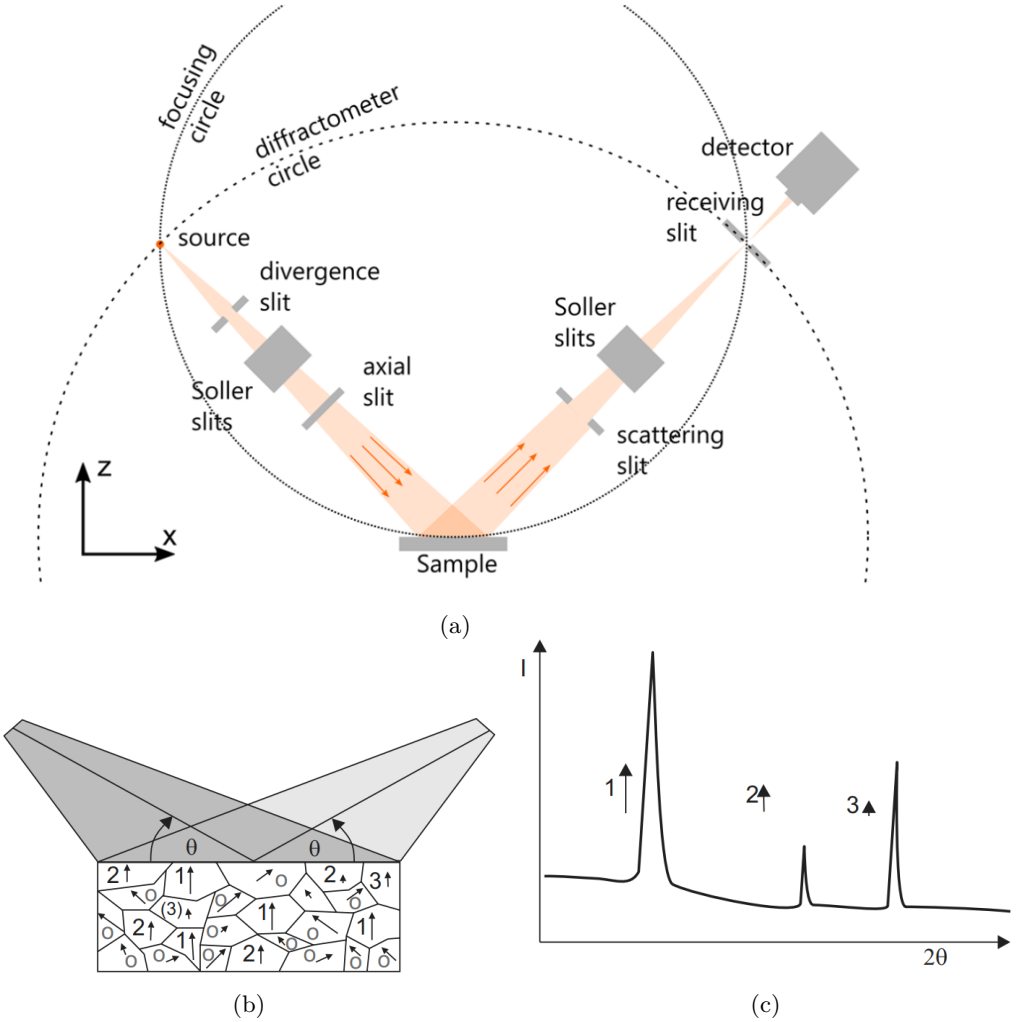

Figure 5.17: Bragg-Brentano geometry: (a) General positions of X-ray source, sample, and detector [238]. (b) Scheme showing lattice planes whose normal vectors are symmetric between incident and scattered beam and who thus contribute to the scattered intensity (c). The length of the arrow next to the group of lattice planes is a measure of their lattice spacing d_{hkl} [236].

ture. The corresponding rules for cubic crystal structures are shown in table 5.1.

The presence of a crystallographic texture strongly influences the outcome of a scan in Bragg-Brentano geometry, since it affects the height of peaks and can also lead to the vanishing of certain Bragg peaks [236]. Measuring the sample in different orientations can thus be used to quantify the texture. For more information on techniques to determine a crystallographic texture, see [219, 236, 242].

5.2.2.3.3 The conventional and modified Williamson-Hall method

The diffraction peaks in a diffractogram broaden due to the presence of small crystallites and/or the presence of lattice strain [243]. Since the effect of size broadening is diffraction-order independent and the effect of strain broadening is diffraction order-dependent [244], the influence of both effects can be disentangled and used to study the microstructure of a material. Two main methods are used for this purpose: The Warren-Averbach method [240] uses a Fourier transform

Table 5.1: Allowed and forbidden Bragg reflexes for cubic primitive, face- and body-centered crystals [236].

Crystal structure	Forbidden reflexes	Allowed reflexes
cubic primitive (cp)	all	none
face-centered cubic (fcc)	h, k, l are mixed odd and even	h, k and l are all odd or all even
body-centered cubic (bcc)	$(h+k+l)$ is odd	$(h+k+l)$ is even

of the broadened peak to study the effects mentioned while the Williamson-Hall method [239] relies on the analysis of the breadth $\Delta\theta$ of the broadened peak which can be expressed as the full width at half maximum (FWHM) or the integral breadth B. In the conventional Williamson-Hall method, the effects of strain and crystallite size are summed up linearly. In order to determine their magnitude, the experimentally determined peak breadth $\Delta\theta$ is plotted as a function of the diffraction angle [237, 243]:

$$\Delta K = \frac{2\cos(\theta)\Delta\theta}{\lambda} = \frac{\alpha}{D} + \sqrt{\langle\varepsilon^2\rangle}K \tag{5.19}$$

where
θ : Diffraction angle
$\Delta\theta$: Broadening of the Bragg reflection
λ : Wavelength of the X-ray photons
$\alpha = \begin{cases} 0.9: & \text{Integral breadth} \\ 1: & \text{FWHM} \end{cases}$: Constant
D : Size of coherently scattering domains
$\langle\varepsilon^2\rangle$: Mean square strain
$K = \frac{2\sin\theta}{\lambda}$: Inverse lattice spacing (cf. equation (5.14))

If the strain in the sample and the crystalline shape are isotropic, the peak breadths of different lattice planes should follow a straight line in a plot of ΔK vs. $\sin\theta$. The crystallite size can then be read from the intercept of the ordinate and the linear function fitted to the experimental data [237], see figure 5.18a.

In the case of anisotropically shaped grains or anisotropic strain, the Williamson-Hall method has to be modified in order to reliably separate the effects of strain and crystallite size [244]. The contribution of strain to peak broadening can be evaluated for different crystal defects like for example dislocations. In this context, the mean square strain reads as [237]

$$\langle\varepsilon^2\rangle = \frac{\rho b^2 \bar{C}_{\mathrm{hkl}}}{4\pi} M_{\mathrm{W}}^2 \tag{5.20}$$

where $\langle\varepsilon^2\rangle$: Mean square strain
ρ : Dislocation density
b : Burgers vector
$\bar{C}_{\mathrm{hkl}}$: Average contrast factor for the reflection associated with the Miller indices h, k and l
M_{W} : Wilkens factor

The Wilkens factor M_{W} in equation (5.20) characterises the arrangement of dislocations and their distribution in a material [245]. In a first-order approximation, it can be defined as [246]

$$M_{\mathrm{W}} = R_{\mathrm{e}} \sqrt{\rho} = \sqrt{\frac{N}{\pi}} \tag{5.21}$$

where M_{W} : Wilkens factor
R_{e} : Arrangement parameter
ρ : Dislocation density
N : Number of restricted randomly distributed dislocations intersecting an area $R_{\mathrm{e}}^2\,\pi$

The arrangement parameter R_{e} is the outer cut-off radius of dislocations and – depending on its definition – also a function of the dislocation density [241]. Following the derivation of Wilkens [245, 246], the lower bound for the Wilkens factor is found for a dislocation dipole consisting of two dislocations with opposite sign intersecting the area $R_{\mathrm{e}}^2\,\pi$:

$$\min\{M_{\mathrm{W}}\} = \sqrt{\frac{2}{\pi}} \approx 0.80.$$

The Wilkens factor can only be determined accurately by Fourier analysis of the diffraction peaks [247].

The anisotropy of strain is incorporated into the analysis by means of the average contrast factor, $\bar{C}_{\mathrm{hkl}}$, which can be calculated based on the crystallography and elastic constants of the investigated material. For untextured cubic crystals, the mean contrast factor can be calculated using [248]

$$\bar{C}_{\mathrm{hkl}} = \bar{C}_{\mathrm{h00}}\,\left(1 - q\,H^2\right) \tag{5.22}$$

where $\bar{C}_{\mathrm{hkl}}$: Average contrast factor for the reflection associated with the Miller indices h, k and l
$\bar{C}_{\mathrm{h00}}$: Average contrast factor for the $(h00)$ reflections
q : Constant depending on the elastic constants of the crystal and the character (edge/screw/mixed) of the dislocation population
H^2 : Cubic invariant

The cubic invariant in equation (5.22) is defined by the Miller indices of the respective reflection according to [249]

$$H^2 = \frac{h^2k^2 + h^2l^2 + k^2l^2}{\left(h^2 + k^2 + l^2\right)^2} \tag{5.23}$$

where H^2 : Cubic invariant
h, k, l : Miller indices of the respective reflection

Interpreting the strain contribution to diffraction line broadening as a result of the dislocation content and arrangement in the crystal, the modified Williamson-Hall plot can be computed using the following equation[14] [250]:

[14] Higher-order terms of the modified Williamson-Hall equation are not considered in this notation. The all-encompassing approach can be found for example in [244, 249, 250].

$$\Delta K = \frac{2\cos(\theta)\Delta\theta}{\lambda} = \frac{\alpha}{D} + \sqrt{\frac{\pi M_{\mathrm{W}}^2 b^2 \rho}{2}}\sqrt{\bar{C}_{hkl}}K \tag{5.24}$$

where

θ : Diffraction angle

$\Delta\theta$: Broadening of the Bragg reflection

λ : Wavelength of the X-ray photons

$\alpha = \begin{cases} 0.9: & \text{Integral breadth} \\ 1: & \text{FWHM} \end{cases}$: Constant

D : Size of coherently scattering domains

M_{W} : Wilkens factor, characterising the arrangement of dislocations in the crystal

b : Burgers vector of the dislocations

ρ : Dislocation density

$\bar{C}_{\mathrm{hkl}}$: Average contrast factor for the reflection associated with the Miller indices h, k and l

$K = \frac{2\sin\theta}{\lambda}$: Inverse lattice spacing (cf. equation (5.14))

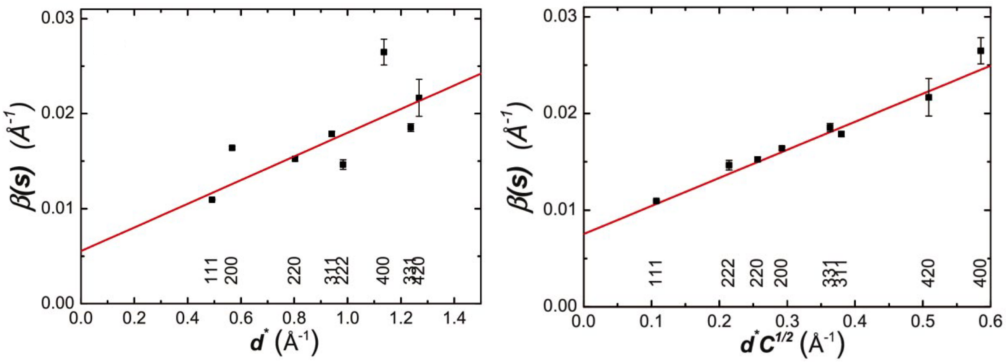

(a) (b)

Figure 5.18: Conventional (a) and modified Williamson-Hall plot (b) for a ball-milled Nickel powder [251]. In both plots, the integral breadth is used as a measure for the peak broadening.

In a modified Williamson-Hall plot, ΔK is plotted vs. $\sqrt{\bar{C}_{\mathrm{hkl}}}K$ and the experimental data is fitted with a straight line, see figure 5.18b for an example. From the intercept with the ordinate and the slope of the straight line, the size of coherently scattering domains D and ρM_{W}^2 is obtained, respectively [237]. In order to disentangle the dislocation density from the Wilkens factor, asymptotic Fourier analysis has to be employed [245, 247, 252]. Thus, the dislocation density cannot be obtained by merely performing the modified Williamson-Hall procedure [247].

5.2.3 Selected methods for quantifying the geometry and size of grains

5.2.3.1 Principal Component Analysis (PCA)

Principal Component Analysis (PCA) is a technique to reduce the dimensionality of large datasets, making them easier to interpret and at the same time preventing the loss of information [253]. In a metallographical context, PCA can for example be used to extract the shape of a grain based on orientation data [254]. A generalised example of this two-dimensional case is illustrated in the

following:

If the 2D-object object that shall be analysed can be described by two vectors $\vec{x}$ and $\vec{y}$ which contain the x and y coordinates of the object, the first step of the analysis is to centre the vectors by subtracting the arithmetic mean of all x or y components of the vector:

$$\begin{pmatrix} \vec{x_c} \\ \vec{y_c} \end{pmatrix} = \begin{pmatrix} \vec{x} - \frac{1}{N}\sum_{i=1}^{N} x_i \\ \vec{y} - \frac{1}{N}\sum_{i=1}^{N} y_i \end{pmatrix} \tag{5.25}$$

where $\vec{x_c}$: Centred $\vec{x}$ vector
$\vec{y_c}$: Centred $\vec{y}$ vector
$\vec{x}$: Vector containing all $i = 1 \dots N$ x values of the pixels belonging to the 2D object
$\vec{y}$: Vector containing all $i = 1 \dots N$ y values of the pixels belonging to the 2D object

Then, the 2$^{\text{nd}}$ order of mass is calculated by determining the eigenvalues (Λ_1,Λ_2) and eigenvectors of the matrix

$$P = \begin{pmatrix} \vec{x_c} \cdot \vec{x_c} & \vec{x_c} \cdot \vec{y_c} \\ \vec{y_c} \cdot \vec{x_c} & \vec{y_c} \cdot \vec{y_c} \end{pmatrix}.$$

so that

$$V^{-1} P V = \begin{pmatrix} \Lambda_1 & 0 \\ 0 & \Lambda_2 \end{pmatrix},$$

where V is the matrix of eigenvectors. The principal components PC_1 and PC_2 of the 2D object are then given as square-roots of the eigenvalues Λ_1 and Λ_2, respectively. The PCA of a 2D object is illustrated in figure 5.19.

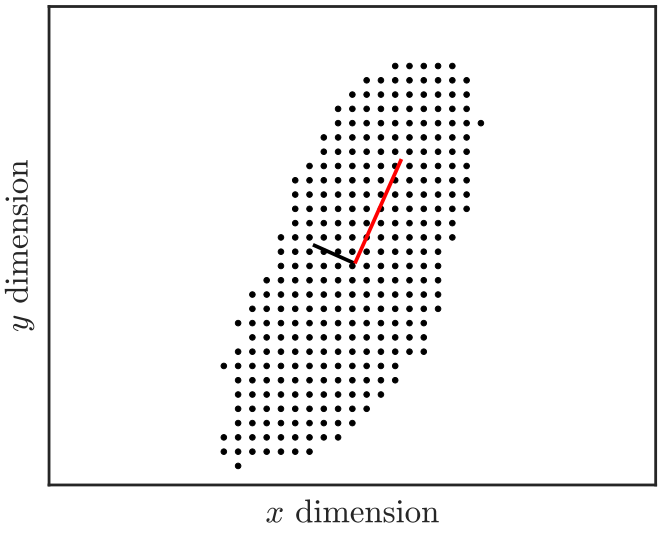

Figure 5.19: Two-dimensional object represented by black dots. Using the x and y coordinates of the points representing the object, its principal components can be determined. The eigenvectors are exemplarily drawn as red and black lines starting in the object's centre of mass.

For a more general treatment and the application of PCA to higher dimensional datasets, the reader is referred to [253, 255].

5.2.3.2 Line Intersection Method (LIM)

The perhaps most straightforward way to determine the grain size (distribution) of a polycrystalline material is to apply the line intersection method (LIM) [256]. The main prerequisite for this method are images of the grain structure or microstructure of the material, respectively. These can be taken both from metallographically prepared cross-sections that are imaged using light or scanning/transmission electron microscopy.

In order to determine the grain size of a material, parallel lines with a constant spacing are drawn on top of a microstructure image, see figure 5.20. The best description of the size of practically equiaxed grains is achieved if the lines are drawn and evaluated under different angles. The orientation of the lines has to be adjusted to the individual grain morphology, especially for anisotropic or irregularly shaped grains. For each drawn line, the number of intersections between the line and the grain boundaries[15] are counted.

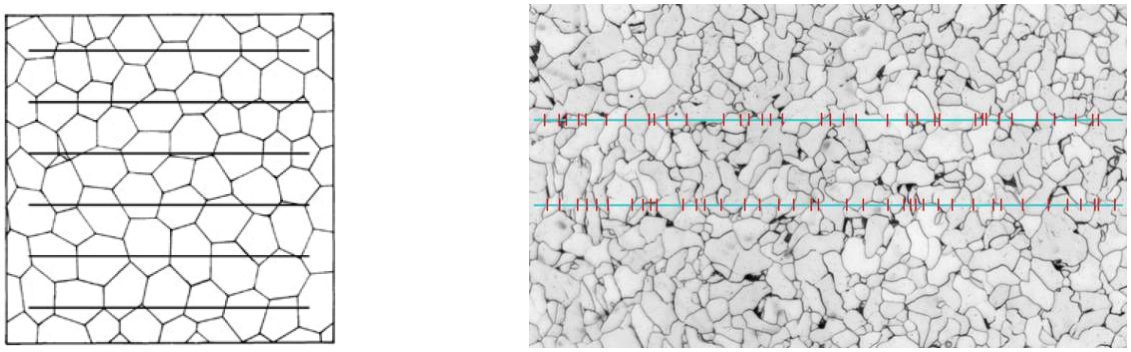

(a) (b)

Figure 5.20: Scheme of the parallel, equidistant lines drawn on top of the image of a microstructure in order to perform the line intersection method (a, from [256]) and a practical example in which the red vertical lines represent the intersection points of the imaginary lines with grain boundaries (b, ©SCHÜTZ+LICHT Prüftechnik GmbH).

Using the initial length L_M and the number of intersected grain boundaries P_M or intersected grains P_K, the chord length l can be determined following

$$l = \frac{L_M}{P_M} = \frac{L_M}{P_K - 1} \tag{5.26}$$

where L_M : Length of the line drawn for LIM
P_M : Number of grain boundaries cut by the line with a length L_M
P_K : Number of grains cut by the line with a length L_M

From the mean chord length $\langle l \rangle$, the grain boundary area per volume is given for microstructures consisting of equiaxed grains as [258]

$$A_K = \frac{2}{\langle l \rangle} \tag{5.27}$$

where A_K : Grain boundary area per volume
$\langle l \rangle$: Mean chord length as measure for the grain size

Internationally, the line intersection method is standardised in DIN EN ISO 643 [259].

[15] Alternatively, the number of intersected grains can be counted, see [257].

Chapter 6

Experimental characterisation of a unique tungsten wire series

6.1 Tungsten wire series

The material investigated in this study was drawn, K-doped tungsten wire manufactured by OSRAM GmbH, Schwabmünchen, following the procedure outlined in section 5.1.2. Starting with a thermo-mechanically treated rod of 3.6 mm diameter, wire drawing was performed at different temperatures. After a certain number of drawing steps, a sufficient length of wire was stored for characterisation. The remaining wire was subsequently drawn down to thinner diameters. As described in section 5.1.2, the wire drawing temperature decreased with decreasing wire diameter. The advantage of the chosen approach is that the chemical composition of the wire series is comparable since all wires are drawn from the same sintered rod[1]. Thus, any differences in the mechanical behaviour can be related to deformation induced changes to the microstructure and texture of the wire. Together with the wire, the manufacturer also supplied a chemical analysis based on glow discharge mass spectroscopy (GD-MS) of the sintered rod. The results of this study are shown in table 6.1.

Table 6.1: Composition of the sintered rod representing the starting point of the wire series investigated in this study. The element concentrations were measured using glow discharge mass spectroscopy (GD-MS). The column for potassium is highlighted since GD-MS is not the ideal method to measure the potassium content. The manufacturer however guarantees a potassium concentration above 75 wt. ppm.

Element	Al	Cr	Fe	K	Mo	Nb	Ni	Si	Ti	V
Content in wt. ppm	10.1 ±0.2	2.1 ±0.1	8.1 ±0.2	67.1 ±4.6	0.6 ±0.1	0.6 ±0.1	1.5 ±0.1	0.1 ±0.1	0.1 ±0.1	0.5 ±0.1

In order to make the results of the study presented here also comparable with other materials such as rolled plates or severely plastically deformed materials, we define the (logarithmic) strain accumulated during wire drawing as

$$\varphi = 2 \ln \frac{d_0}{d} \tag{6.1}$$

where φ : Accumulated drawing strain

[1]The chemical changes during wire drawing are assumed to be negligible, see section 5.1.2.

$d_0 = 3.6\,\mathrm{mm}$: Initial diameter of the rod representing the starting point of wire drawing
d : Wire diameter

The accumulated drawing strain is defined under the assumption that the cross-section of each wire is perfectly circular. The wire diameters and corresponding accumulated drawing strains φ of the materials used in this study are listed in table 6.2.

Table 6.2: Diameters and accumulated drawing strains of the tungsten wires and the tungsten rod investigated.

Wire diameter d in µm	3600	2800	1750	950	490	150	41	16
Accumulated drawing strain φ	0	0.5	1.4	2.7	4.0	6.4	9.0	10.8

After drawing, some remnants of the graphite lubricant remain on the wire surface. Wires with $d \leq 150\,\mu\mathrm{m}$ were cleaned before shipping. The other wires were not treated before shipping.

6.2 Mechanical testing

6.2.1 Sample preparation for mechanical testing

Thin wires ($d \leq 150\,\mu\mathrm{m}$) were prepared for mechanical testing following the procedure developed by Riesch et al. and described e.g. in [73]: First, a wire specimen with a length of 70 mm is cut from the spool using wire cutters. In order to ensure that the specimen fractures in the measuring zone, its ends are covered with an epoxy glue (*UHU© Endfest 300*), thus leaving a free length of 30 mm. Several wires were glued at the same time. After a curing time of 24 h the individual wire specimens were cut to size for tensile tests.
The surface of thick wires ($d \geq 490\,\mu\mathrm{m}$) has to be cleaned from any remnants of graphite lubricant in order to prevent slipping during the mechanical tests. Therefore, wires with a diameter $d \geq 490\,\mu\mathrm{m}$ were cut to a suitable length and then immersed in a 2 M NaOH solution for a duration of 90 min, which leads to the detachment of the graphite from the surface, from which it can then be wiped off easily.

6.2.2 Tensile testing setups

6.2.2.1 Thin wires ($d \leq 150\,\mu\mathrm{m}$)

For tensile testing, the glued ends of a wire specimen are clamped into the upper and lower crossheads of a universal testing machine. Prior to the mechanical test, the position of the wire is aligned with the load axis using an x-y-table, thereby ensuring that the sample is stressed by pure uniaxial tensile stress. An image of the used setup is shown in figure 6.1.

6.2.2.2 Thick wires ($d \geq 490\,\mu\mathrm{m}$)

For testing thick wires ($d \geq 490\,\mu\mathrm{m}$) a custom-made clamping assembly (cf. figure 6.2) was developed in order to ensure a suitable clamping force and to prevent slipping. The assembly is made up of two half-cylinders the wire sample is guided across, while the ends of the wire specimen are fixed using a washer and a screw. The half-cylinders can be moved along a direction perpendicular to the tensile direction. Pure unidirectional tensile stress in the specimens is achieved if the wire is aligned with the axes of force transmission. The friction between the wire specimen and the lateral surface of the half-cylinders results in the maximum stress acting in the free length of the wire, while the residual parts of the sample are loaded with lower normal stresses.

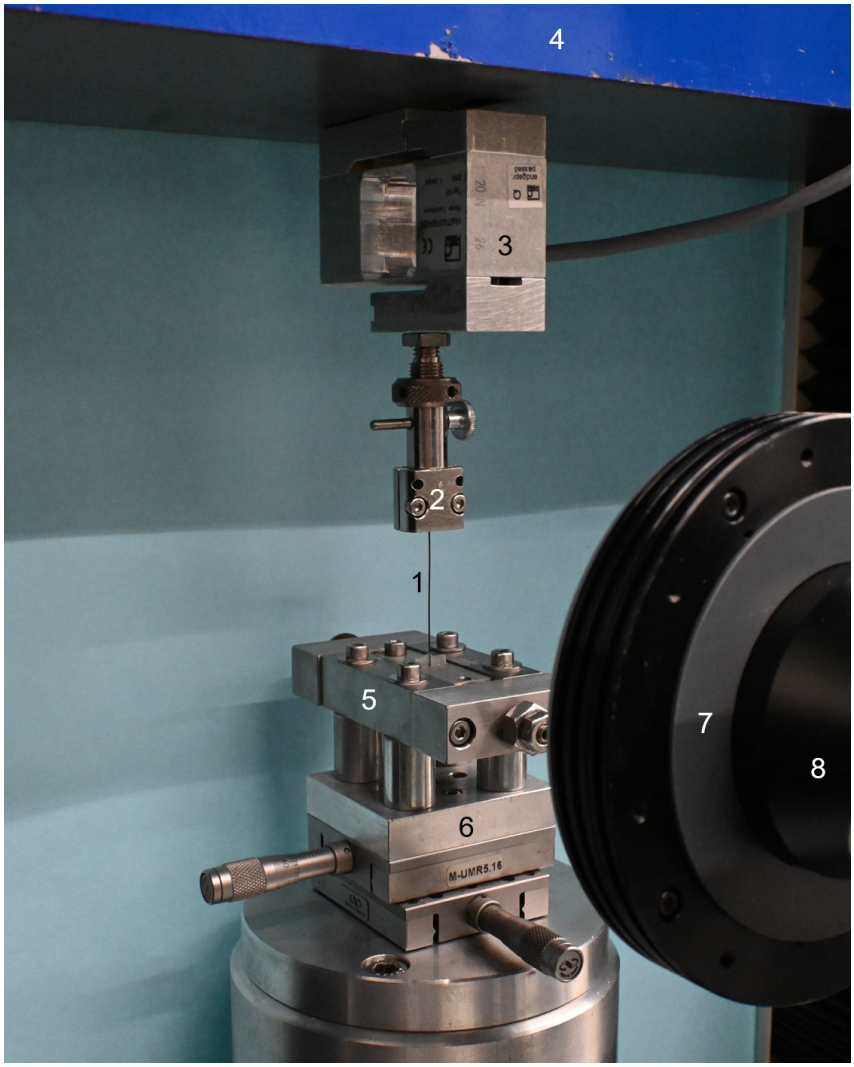

Figure 6.1: Image of the setup used for testing tungsten wires with diameters $d \leq 150\,\mu m$. Numbers mark the main components of the tensile testing setup: (1) uniaxially stressed wire specimen, (2) upper clamp, (3) load cell, (4) upper (moving) crosshead, (5) lower clamp, (6) x-y-table, (7) ring light, (8) telecentric lens mounted on a CCD camera chip.

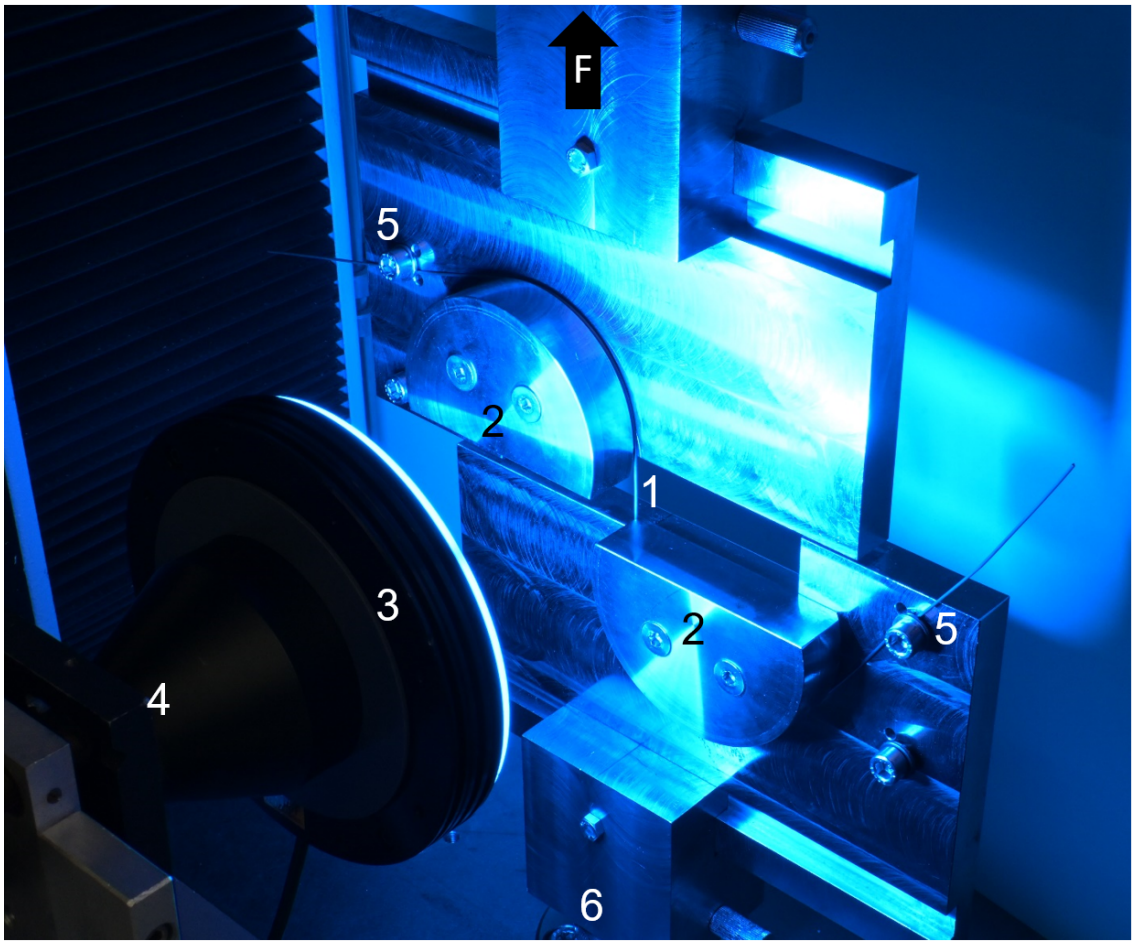

Figure 6.2: Image of the setup used for testing tungsten wires with diameters $d \geq 490\,\mu m$. Numbers mark the main components of the tensile testing setup: (1) free, uniaxially stressed wire length, (2) half-cylinders, (3) ring light, (4) telecentric lens mounted on a CCD camera chip, (5) wire clamps, (6) lower, fixed crosshead. The black arrow indicates the direction of loading.

6.2.3 Conduct of mechanical tests

Tensile tests were performed using a TIRAtest® 2820 universal testing machine at room temperature. Load cells with different maximum loads (20 N for $d < 150\,\mu m$, 200 N for $d = 150\,\mu m$ and 5 kN for $d > 150\,\mu m$) were used to measure the force acting in the sample. During the mechanical tests, the sample surface was recorded using a camera system consisting of a CMOS image sensor (*Toshiba® DU657M*) and a telecentric lens (*Opto Engineering® TC110-08/C*). The telecentric lens was used to in order to eliminate perspective (parallax) errors [260, 261].

6.2.3.1 Monotonous uniaxial tensile tests

Monotonous tests were performed by deforming the sample with a constant crosshead velocity $\dot{x}$ until fracture.

6.2.3.2 Strain-rate jump tests

For strain-rate jump tests, the sample was deformed with constant crosshead velocity to a stress above the yield point, which is roughly identifiable from the deviation of the force-displacement curve from a linear course or can for example be determined in monotonous uniaxial tensile tests. At stresses $R > R_{p0.02}$, the crosshead velocity was manually changed. Since only strain-rate jumps from a higher to a lower strain rate could be unequivocally evaluated, the crosshead velocity, which is proportional to the strain rate, was alternated in a way that every increase of $\dot{x}$ followed a decrease and vice versa. The test ended with the fracture of the sample.

The evolution of true strain and stress during a SRJT is illustrated in figure 6.3.

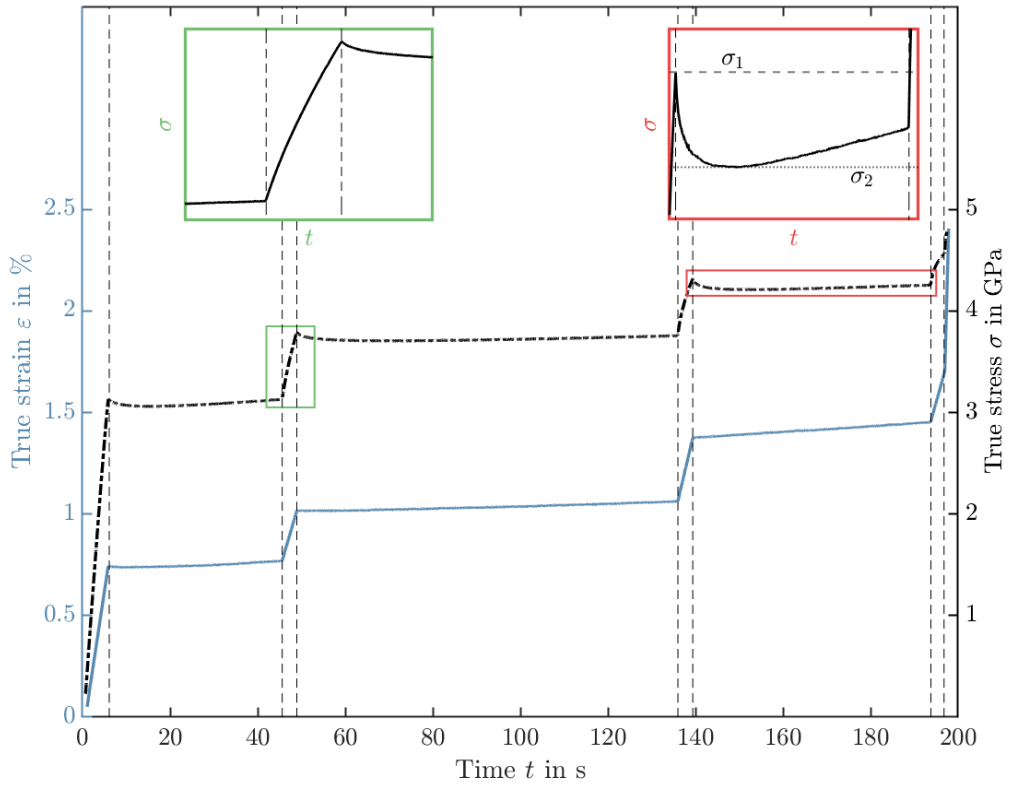

Figure 6.3: Temporal evolution of true strain (left y-axis) and stress (right y-axis) during a strain-rate jump test performed on a tungsten wire with a diameter of 16 μm. Dashed vertical lines mark the times at which a strain-rate jump was performed. The two zoomed insets show jumps from low to high (green, left side) and from high to low strain rate (red, right side).

Since the effective activation volume V_{eff} was also measured in repeated stress relaxation experiments, the apparent activation volume from strain-rate jump tests was not used for subsequent evaluation. The evolution of the apparent activation volume and the reasons for basing the analysis on the effective activation volume can be found in appendix B.1.5.

Since the equations for calculating σ and ε are only valid up to the point of ultimate tensile strength, no strain-rate jumps were performed between R_m and fracture of the sample. Only jumps from a higher to a lower strain rate were considered for determining the strain-rate sensitivity since for these jumps, the determination of σ_1 and σ_2 is more accurate than for jumps from a low to

a higher strain rate. The right inset (red) in figure 6.3 illustrates the determination of the stress before and after the strain-rate jump: The stress in the moment of the jump was taken as σ_1, while σ_2 was allocated to the lowest stress after the jump and prior to the next jump. The influence of the magnitude of the ratio $\dot{\varepsilon}_1/\dot{\varepsilon}_2$ on m was investigated but found to be insignificant, as long as

$$\frac{\dot{\varepsilon}_1}{\dot{\varepsilon}_2} > 2.$$

was satisfied. This value was then used as a lower boundary.

6.2.3.3 Repeated stress relaxation experiments

Each repeated stress relaxation experiment performed in the course of this study is characterised by four variables: The target load F_{RELAX}, the crosshead velocity $\dot{x}$, the number of relaxation cycles N_{RELAX} and the relaxation time t_{RELAX}. The sample was deformed above the yield point at a constant crosshead velocity $\dot{x}$ until the previously set target load F_{RELAX} was reached. Then, the movement of the crosshead was stopped for a duration of t_{RELAX}. Then, since the load has dropped during t_{RELAX}, the sample was reloaded to F_{RELAX}. This concluded the first relaxation cycle and was repeated N_{RELAX}-times. Following the suggestions given in [80], $t_{\mathrm{RELAX}} = 30\,\mathrm{s}$ and $N_{\mathrm{RELAX}} \in [4; 6]$ was used. The upper bound of the crosshead velocity was set differently for each wire diameter, e.g. $\dot{x} = 20\,\mu\mathrm{m\,s^{-1}}$ for $d = 150\,\mu\mathrm{m}$ and $\dot{x} = 150\,\mu\mathrm{m\,s^{-1}}$ for $d = 950\,\mu\mathrm{m}$. Higher crosshead velocities than the ones mentioned lead to an overshoot, i.e. the crosshead could not be stopped reliably at F_{RELAX}, and were thus avoided. After the last relaxation cycle was finished, the sample was deformed with a constant crosshead velocity $\dot{x}$, similarly as in a monotonous test until fracture. The temporal evolution of the stress during a RSRE is shown exemplarily in figure 6.4.

Several stress relaxation experiments at different forces F_{RELAX} were conducted for each wire type to probe the stress dependence of the effective activation volume and the strain-rate sensitivity.

6.2.4 Determination and alignment of local strain and stress

The first step in evaluating each mechanical test was to correlate the force or stress to the corresponding strain during the test, respectively. For this purpose, a custom LabView program written in-house [195] was used. The program allows tracking specific regions on the surface of the sample during the mechanical test in order to determine the strain between these regions. As a first step for determining the local strain, regions of interest (ROI) were defined. An example of the location of the ROI on a sample is shown in figure 6.5.

For the mechanical tests treated in this work, the strain between two regions at the top and the bottom of the sample was determined in order to maximise the gauge length. The LabView program finds the location of the ROI in each image that was recorded during the mechanical test. This yields a 2D temporal evolution of the region's location that can be described by a x- ($x_{\mathrm{i}}(t)$) and a y-position ($y_{\mathrm{i}}(t)$). The distance $L(t)$ between the two regions $i \in [1; 2]$ is then given using the Pythagorean theorem:

$$L(t) = K\sqrt{\left(y_2(t) - y_1(t)\right)^2 + \left(x_2(t) - x_1(t)\right)^2} \tag{6.2}$$

where $L(t)$: Distance between ROI 1 and ROI 2 at time t
K : Calibration constant relating px to m
$y_i(t)$: y position of ROI i at time t

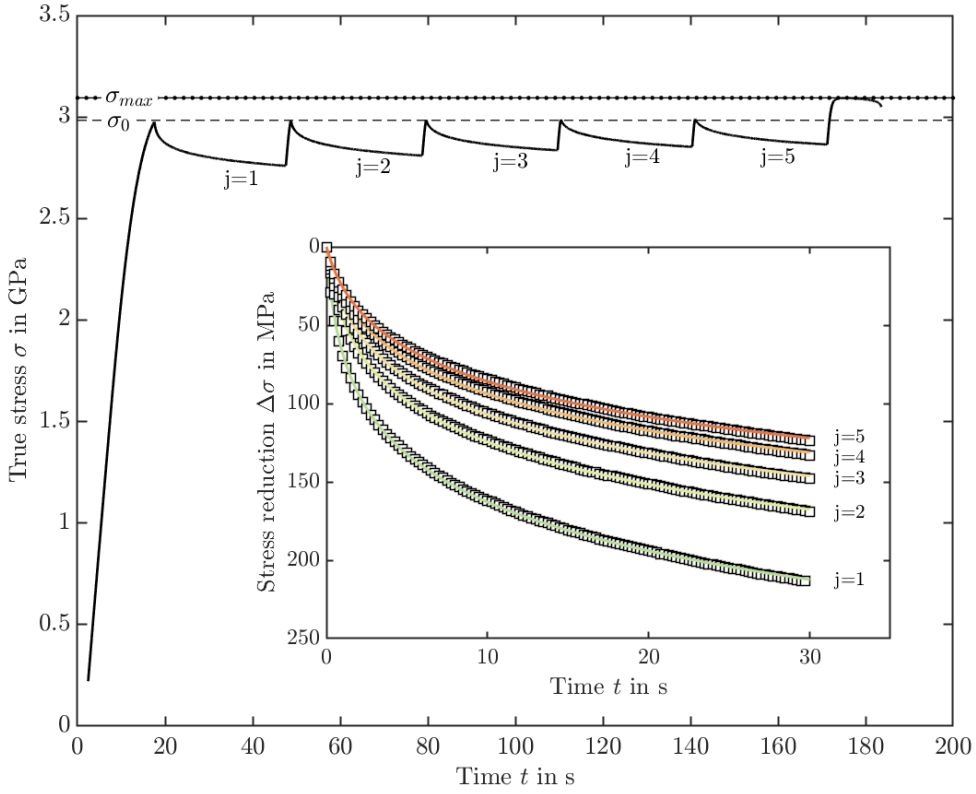

Figure 6.4: Temporal stress evolution during a repeated stress relaxation experiment performed on a drawn tungsten wire with a diameter of 150 µm at room temperature. The inset shows the temporal stress decay $\Delta\sigma$ during the five relaxation cycles performed. For better visibility, only every fifth measured data point is drawn. The dashed lines represent the fitted stress decays following equation (5.8).

$x_i\,(t)$: x position of ROI i at time t.

In order to determine the calibration constant K, images of objects with a known distance were evaluated and the number of pixel separating the objects was determined. This yielded a value of the calibration constant for the chosen camera lens of

$$K = (7.304 \pm 0.003)\,\mathrm{px\,\mu m^{-1}}.$$

The (engineering) strain is then determined using equation (5.1):

$$e\,(t) = \frac{L\,(t) - L\,(t=0)}{L\,(t=0)} \tag{6.3}$$

Figure 6.5: Image of a tungsten wire with a diameter of 150 µm during a mechanical test. The regions of interest that were tracked are indicated by red circles.

where $e(t)$: Engineering strain at time t
$L(t)$: Distance between ROI 1 and ROI 2 at time t
$L(t=0)$: Distance between ROI 1 and ROI 2 at time $t=0$.

An example of the temporal evolution of the engineering strain determined during a monotonous tensile test on a tungsten wire with a diameter of 16 µm is shown in figure 6.6.

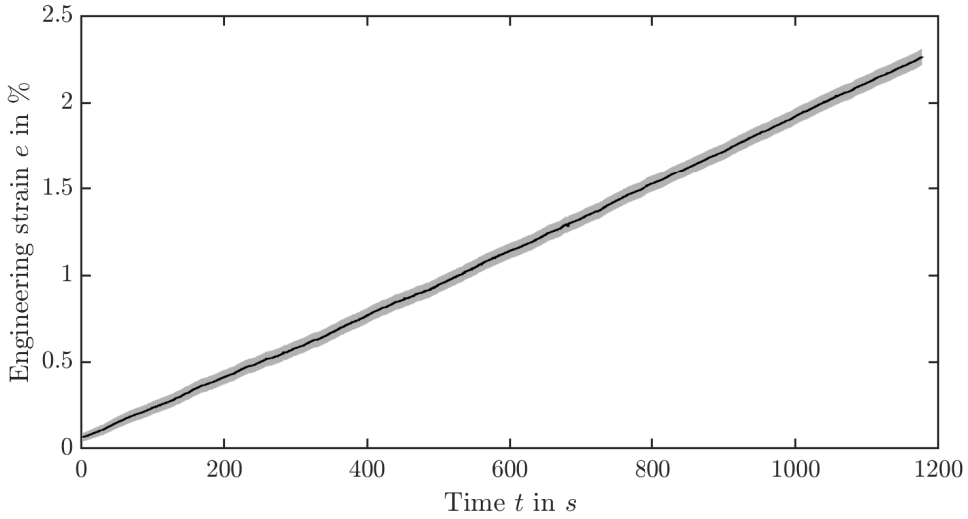

Figure 6.6: Engineering strain as a function of time measured during an uniaxial tensile test performed on a tungsten wire with a diameter of 16 µm using a crosshead velocity of $1\,\mu m\,s^{-1}$. The shaded region denotes the realm of uncertainty of both engineering strain and time.

From the load-displacement curve that is recorded during the mechanical test, the stress can be determined following equation (5.2):

$$R(t) = \frac{4\,F(t)}{\pi\,d^2} \tag{6.4}$$

where $R(t)$: Engineering stress at time t
$F(t)$: Load at time t
d : Wire diameter

Equation (6.4) assumes that the wire cross-section can be approximated as a perfect circle with diameter d.

After calculating the strain, it was necessary to align the strain and stress signal, since the measurements were usually not started at the same time. The moment of rupture was used for alignment since it can be unambiguously identified in both signals: In the stress signal, it appears as a strong stress drop while it concurrently appears as a strong strain jump or can directly be seen from the camera images. For aligning, the time signal was shifted by a manually determined amount t_{shift}. Furthermore, since the acquisition frequencies of the camera chip ($f_{\mathrm{e}} = 20\,\mathrm{Hz}$) and the load cell ($f_{\mathrm{F}} = 50\,\mathrm{Hz}$) were different, interpolation was needed in order to know stress and strain at the same point in time. Therefore, at each point in time t_{e} for which the strain was measured, the corresponding stress was determined by linearly interpolating between the two stresses $R(t_{\mathrm{R}} = t_{\mathrm{i}})$ and $R(t_{\mathrm{R}} = t_{\mathrm{i+1}})$ at the time points $t_{\mathrm{R,i}}$ and $t_{\mathrm{R,i+1}}$, for which $t_{\mathrm{R,i}} < t_{\mathrm{e,j}} < t_{\mathrm{R,i+1}}$ was valid[2].

[2]Due to the specific sampling frequency, more data points would have to be calculated by interpolation when

Mathematically, the interpolation can be described as follows:

$$R\left(t = t_{\mathrm{e,j}}\right) = \frac{t_{\mathrm{e,j}} - t_{\mathrm{R,i}}}{t_{\mathrm{R,i+1}} - t_{\mathrm{R,i}}} \left[R\left(t_{\mathrm{R,i+1}}\right) - R\left(t_{\mathrm{R,i}}\right)\right] + R\left(t_{\mathrm{R}} = t_{\mathrm{i}}\right) \tag{6.5}$$

where $R\left(t = t_{\mathrm{e,j}}\right)$: Interpolated stress at time $t_{e,j}$
$t_{e,j}$: Time, at which strain ε_{j} is measured
$t_{\mathrm{R,i}}$: Next lower point in time, at which $R\left(t_{\mathrm{R,i}}\right)$ is measured
$t_{\mathrm{R,i+1}}$: Next higher point in time, at which $R\left(t_{\mathrm{R,i+1}}\right)$ is measured

The procedure is illustrated in figure 6.7.

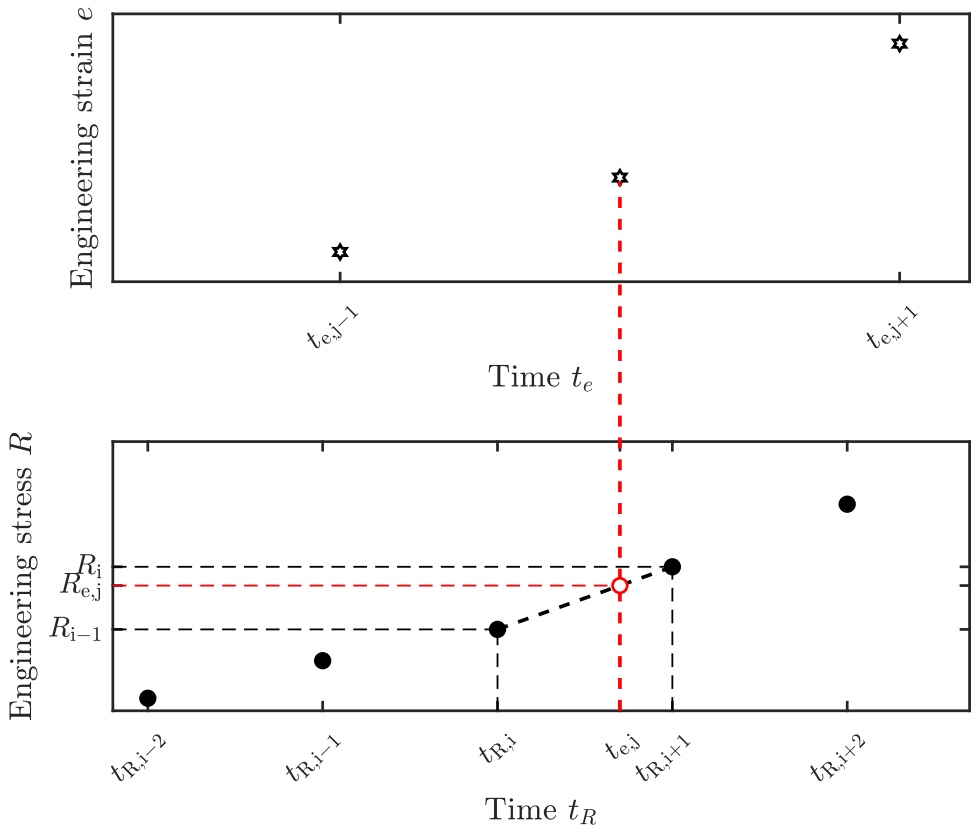

Figure 6.7: Illustration of the linear interpolation method used to align the (engineering) stress and strain measured during a mechanical test. The outcome of the procedure is a triple of data points $(t \mid e \mid R)$ which can then be used to analyse the mechanical behaviour of the investigated sample.

Using the procedure outlined above, stress-strain diagrams can be drawn and subsequently evaluated.

During evaluation of the mechanical tests, slight variations in the apparent Young's modulus of the wires were detected. A statistical analysis of the scatter of the measured elastic moduli

interpolating the strain instead of the stress. Hence, in order not to overstress the validity of the linear interpolation, interpolation of the stress was chosen.

can be found in appendix B.1.2. Since all wires consist of tungsten with only small amounts of impurity, these variations are not physically justified and the measured Young's modulus has to match the theoretical value determined for pure tungsten at room temperature. Thus, the elastic strain measured in each test was adjusted in a way that the slope in the elastic region matches the theoretical value in order to ensure comparability. Therefore, the measured Young's modulus E_{meas} was determined by fitting a linear function to the elastic region of the tensile test. The elastic region was determined individually for each test. The correction of the strain was performed as follows:

$$e_{\mathrm{corr}}(t) = \frac{E_{\mathrm{app}}}{E_{\mathrm{W}}}\, e(t) \tag{6.6}$$

where
$e_{\mathrm{corr}}(t)$: Corrected engineering strain
E_{app} : Experimentally determined Young's modulus
$E_{\mathrm{W}} = 410\,\mathrm{GPa}$: Theoretical Young's modulus at $T = 300\,\mathrm{K}$ [262]
$e(t)$: Engineering strain

In a subsequent step, the stress-strain curves were shifted so that the extrapolation of the elastic straight crosses the origin of the coordinate system[3], since it is assumed that $R = 0$ for $e = 0$. After all these corrections were implemented, the true stress and strain were determined according to equations (5.5) and (5.3).

6.3 Microstructural characterisation

Different cross-sections of the wires investigated in this study were prepared in order to study their microstructure using EBSD and XRD. For longitudinal sections (LS), the wire was embedded in a way that its drawing axis is contained in the surface of the embedding. In the case of a transversal cross-section (TCS) the axis was parallel to the surface normal of the embedding. Examples are shown in figure 6.8.

6.3.1 Sample preparation

6.3.1.1 Thick wires ($d \geq 150\,\mu\mathrm{m}$)

6.3.1.1.1 Cutting, mounting & embedding

Since wires are a continuous product, smaller sections had to be cut in order to allow for analysis. This was either done using wire cutting clippers in the case of thin wires or a diamond wire saw (*well® Precision Diamond Wire Saw 3242*) in the case of thick wires. For LS samples, the wire pieces were aligned parallel and embedded. For TCS, the wire pieces were either attached to an aluminium or steel cuboid for support using spot welding, Ag conductive resin or Cu tape or put upright using steel springs (see TCS sample in figure 6.8). The mounting in TCS was always performed with the goal to align the wire drawing axis with the surface normal of the embedding.

Since the embedded samples had to be electrically conductive for electron microscopic analysis, either a resolvable (*Kulzer® Technovit 5071™*) or conductive embedding (*Buehler Duroplast Black™*) was used. For the latter, hot-embedding at a temperature of 180 °C and a pressure of 80 bar was performed using a *Buehler® OPAL 450™* embedding machine.

[3]The thus corrected engineering strain is still denoted $e(t)$.

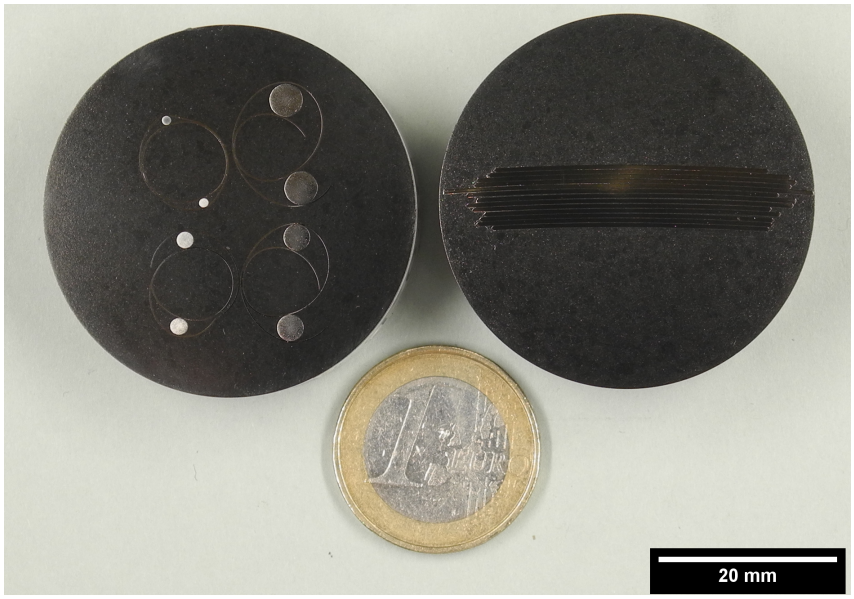

Figure 6.8: Examples for the two types of metallographical samples prepared for microstructural characterisation of tungsten wires: Longitudinal cross-section containing a bundle of wires with the same diameter (LS, left) and transversal cross-section containing four sets à two wires of the same diameter (TCS, right).

6.3.1.1.2 Metallographical grinding and polishing

Grinding and polishing was performed both by hand and using a *Buehler® Phoenix 4000™* automatic grinding and polishing machine. The grit sizes of grinding paper used were P600, P1200, P2500 and P4000. Grinding with a certain grit size was finished once the grinding grooves from the next coarser paper were removed. Subsequent to grinding, the samples were polished using diamond suspensions with 3 µm (*Kulzer® BioDiamant Liquid Orange*) and 1 µm particle size (*Kulzer® BioDiamant Liquid Red*). Polishing was performed for a duration of 15 min to 20 min. Final polishing was performed using a *Buehler® VibroMet 2™* vibrational polisher. There, the samples were polished using a fine SiO_2 particle suspension (particle size: 20 nm). The duration of the final polishing step varied between 5 h and more than 70 h depending on the sample area to be polished. The polishing progress was checked periodically using a light microscope. In order to get rid of any remnants from the SiO_2 particle suspension, the sample was cleaned using a soft tissue on the automatic grinding/polishing machine that was soaked with running water and detergent. If a resolvable embedding was used, this had to be dissolved overnight using acetone. After dissolving the embedding material, a final cleaning of the surface using isopropyl alcohol was conducted.

6.3.1.2 Thin wires ($d \leq 41$ µm)

Thin wires could not be prepared using metallographical techniques, but had to be prepared using Focused Ion Beam (FIB) techniques. Wires with a diameter of 16 µm were additionally electroplated with a Pt layer to improve their handling. Therefore, they were glued across a small hole (diameter: 6 mm) that was punched into a Kapton™ foil and afterwards immersed in a beaker filled with *Jentner® Platinum Bath JE18™*. By applying a voltage of 1.7 V between the sample and a counter-electrode, the free wire section is coated with a homogeneous layer of platinum. Electroplating for a duration of 30 min resulted in a radial thickness of the platinum

layer of (6.1 ± 0.3) µm yielding a sample thickness of around 30 µm. Both the electroplated samples prepared from a wire with a diameter of 16 µm and cut specimens of as-drawn wires with a diameter of 41 µm were glued to a steel or Al support using conductive Ag paint and Cu tape in order to prepare them for the FIB preparation routine.

6.3.2 Electron microscopy

The majority of electron microscopic analyses were performed using a *ThermoFisher FEI Helios NanoLab 600*. Additional measurements for the thinnest wire (16 µm) were performed on a *Zeiss Crossbeam 540* using an *Oxford NordlysNano* EBSD detector. Sample preparation for (S)TEM lamellae was carried out using a *Hitachi NB 5000*. All scanning electron microscopes are equipped with a FEG electron source and an Ga^+ ion source.

6.3.2.1 Acquisition of secondary and backscattered electron images

Secondary (SE) and backscattered electrons (BSE) were used to qualitatively investigate the microstructure of the prepared tungsten wires. BSE and SE images were acquired using an acceleration voltage of 5 kV and a beam current of 0.69 nA.

6.3.2.2 Preparation of cross-sections and TEM lamellae using Focused Ion Beam (FIB) techniques

As mentioned before, the preparation of longitudinal cross-sections and transversal sections by means of a Focused Ion Beam (FIB) was necessary in order to study the microstructure of thin wires ($d \leq 41$ µm) using SEM, TEM and EBSD. The preparation of the wire specimens was performed according to the procedure described in section 6.3.1.2. Prior to FIB cross-sectioning, the sample surface was coated with a platinum layer in order to reduce the curtaining effect. Then, cross-sectioning steps performed on samples for SEM and EBSD analyses were performed with an Ga^+ ion beam (acceleration voltage: 30 kV). The ion beam current was reduced systematically from initially 21 nA to 0.46 nA in the final step. By doing so, the surface quality could be enhanced, which was beneficial for all subsequent analyses. Prior to TEM analysis, the surface of the pre-cut lamella with a thickness of roughly 150 nm was polished using a gentle Ar^+ ion beam (beam energy: 0.5 eV to 1 eV) using a *Gentle Mill 2HI Technoorg LINDA* ion polisher until the lamella exhibited a smooth surface and a thickness of roughly 80 nm to 100 nm.

6.3.2.3 Acquisition of orientation maps using EBSD

All EBSD measurements for wires with $\varphi \leq 9.0$ were performed at the *ThermoFisher FEI Helios NanoLab 660* using the *Oxford Instruments® Symmetry* EBSD detector. EBSD measurements were performed at an angle of 57° between sample surface and electron beam. The accelerating voltage and the beam current were varied in the range of 10 kV to 30 kV and 1.4 nA to 5.5 nA, respectively, in order to achieve the best indexing rate. Similarly, the step size of the EBSD measurement was chosen as a compromise between a high spatial resolution of the orientation map and a reasonable measurement duration, and thus ranged from 5 nm to 4.5 µm.

6.3.3 Acquisition of X-ray diffractograms

On a *Seifert-FPM RD7* goniometer situated at the Institute of Materials Science at TU Bergakademie Freiberg, X-ray diffractograms of the LS samples that were already analysed using EBSD and SEM were recorded in Bragg-Brentano geometry. An X-ray source ($U = 40$ kV | $I = 30$ mA) with a Cu cathode emitting $Cu - K_\alpha$ radiation with a wavelength of 1.5406 Å was

used to scan the angle range $2\theta \in [18°; 150°]$ with a step size of 0.02° and an exposure time of 12 s. The size of the beam was adjusted using a slit system. The diffracted peak passed antiscatter and receiving slit before entering a secondary graphite monochromator to remove unwanted radiation components from the measured signal. The scattered photons were counted by a proportional counter. For wires with $\varphi \leq 4.0$, the longitudinal sections prepared for EBSD orientation map acquisition could be used for measuring the XRD diffractograms. Wires with diameters of 150 µm or 41 µm were wound around a circumferential recess in an Al block. They were then embedded using a transparent resin (*Araldite® DBF Harz*) and subsequently metallographically prepared in the same manner as described in section 6.3.1.1.2. The thinnest wire could not be prepared by either of the methods described, and was thus not analysed using XRD. In order to determine the instrumental contribution to line broadening, the *Standard Reference Material® 660c* issued by the National Institute of Standards & Technology (NIST) consisting of a coarse grained LaB_6 powder was measured using the same instrument settings used for the analysis of the tungsten wires.

6.3.4 Acquisition of STEM images

STEM images of the FIB-cut lamellae were acquired using a *Thermo Fisher FEI Spectra S/TEM* operating at a voltage of 200 kV. The images were recorded using bright field (BF), dark field (DF) and high-angle annular dark field (HAADF) detectors.

Chapter 7

Results

7.1 Mechanical behaviour and deformation mechanisms

Monotonous and transient mechanical tests at room temperature could only be performed on wires with diameters $d \leq 950\,\mu m$ ($\varphi \geq 2.7$). Wires with larger diameters or lower accumulated drawing strains, respectively, exhibited brittle behaviour at ambient temperature.

A comprehensive list containing the number of successful mechanical tests for each ductile wire and the respective test type can be found in appendix B.1.1.

7.1.1 Stress-strain characteristics

In order to show the dependence of the stress-strain characteristics on the (true) strain rate $\dot{\varepsilon}$, the strain rate was determined from the temporal evolution of the true strain (see figure 6.6). The resulting engineering and true stress-strain curves for different strain rates are shown in figure 7.1 and 7.2, respectively.

The most striking difference between the engineering and the true stress-strain curves is that, especially for the two thicker wires ($d \leq 490\,\mu m$) investigated, the engineering strain reaches very high values of over 9 %, while the true strain doesn't exceed values of 3 %. The engineering strain of the two thickest wires is comparable, while it is less than 4 % for the next thinnest wire ($d = 150\,\mu m$) and then stagnates at values of 2 % to 3 %. Some engineering stress-strain curves of the two thickest wires $\varphi \leq 4.0$ show stress decays prior to fracture that have a positive slope in contrast to the majority of necking-induced stress decrease observed for the other wires, which has a negative slope. The strain-rate dependence of the maximum strain for the thickest wire ($d = 950\,\mu m$) is very pronounced: While wires tested with low strain rates show overall larger maximum strains prior to fracture, wires tested at high crosshead velocity, i.e. high strain rate, show strongly diminished maximum strains. This trend is not seen in the stress-strain curves of the other wires. It is also noteworthy that the maximum strain reached in uniaxial tensile tests of thick wires ($d \geq 490\,\mu m$) shows a strong scatter, while the scatter for thinner wires is comparatively small. The true strain of the investigated tungsten wires reaches values around 1.5 % to 3 %. It shows a pronounced strain-rate dependence for thicker wires, especially those with a diameter of 150 µm whereas this trend is almost lost for the two thinnest wires due to the high scatter. A trend that is apparent for both engineering and true stress is that wires with a higher accumulated drawing strain reach higher stresses at constant strain rate. On the other hand, higher strain rates yield overall higher maximum stresses for a given wire diameter. Here again, a significant scatter is observable. Qualitatively, the shape of the true stress-strain curve, which is linked to the work hardening behaviour of the wires, appears to be very similar for all

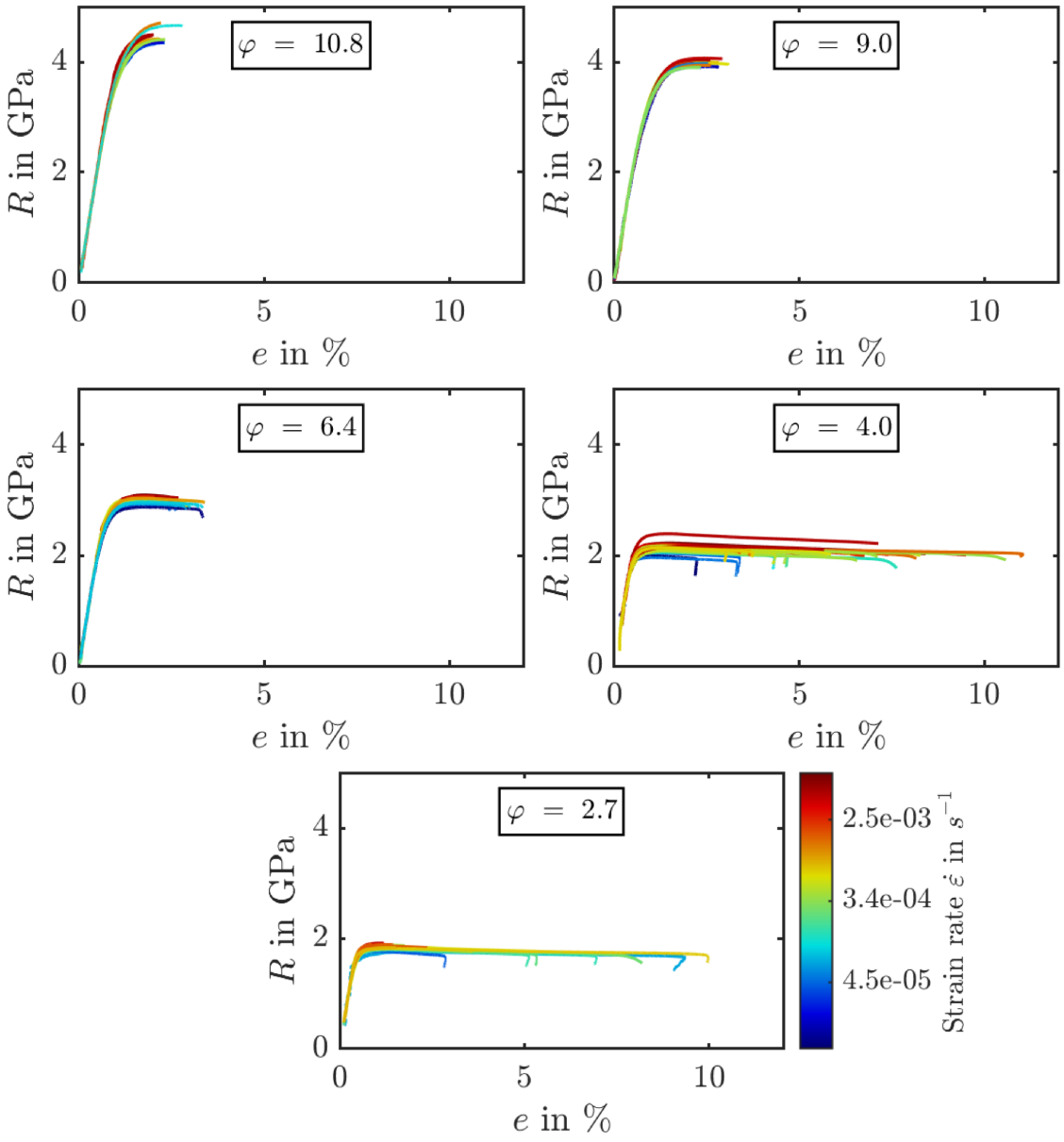

Figure 7.1: Engineering stress R vs engineering strain e of tungsten wires with diameters between 950 µm and 16 µm. The colour-coding of the strain rate shown next to the stress-strain diagram of the thinnest wire also applies to all other diagrams.

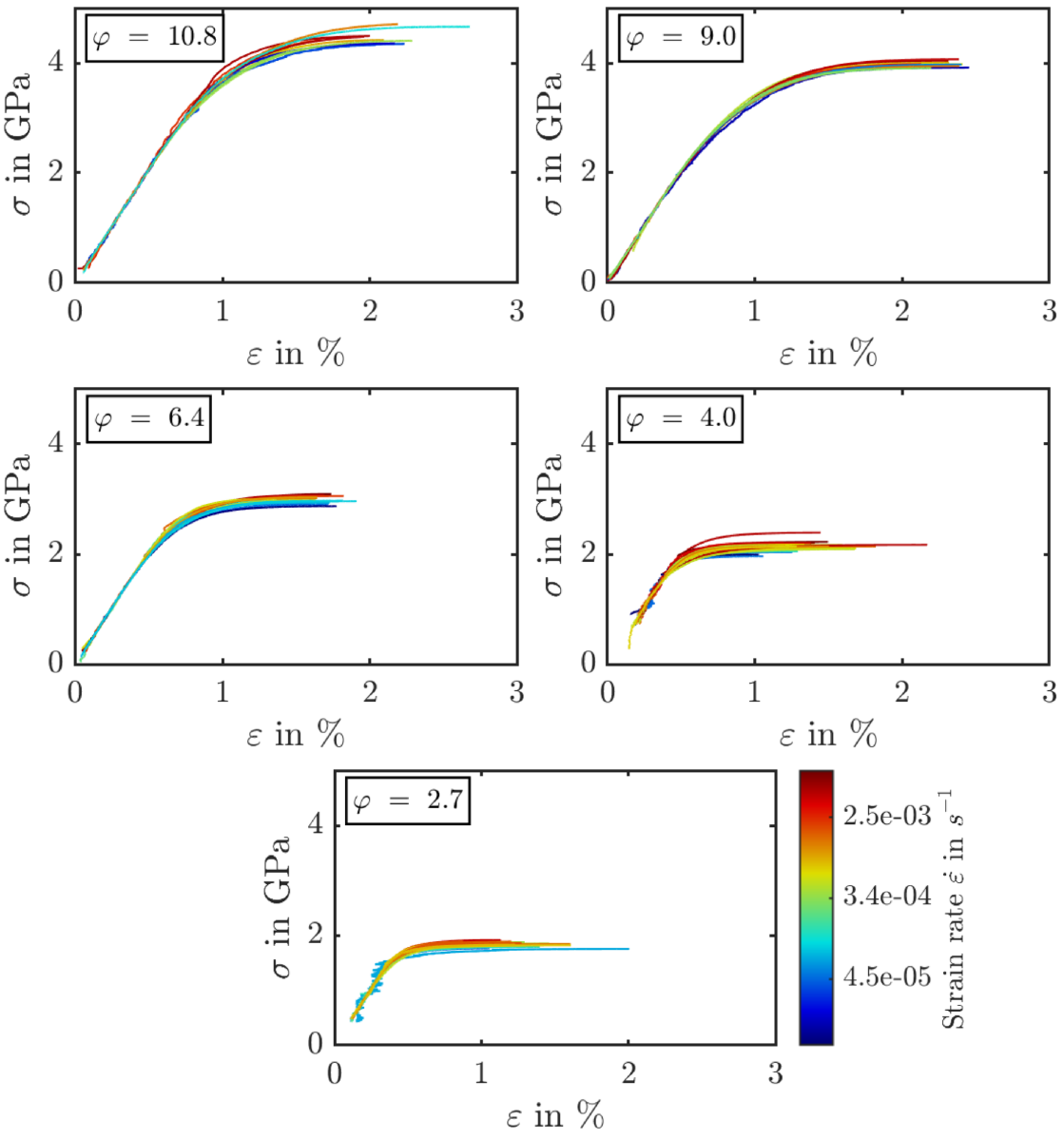

Figure 7.2: True stress σ vs. true strain ε of tungsten wires with diameters between 950 µm and 16 µm. The colour-coding of the strain rate shown next to the stress-strain diagram of the thinnest wire also applies to all other diagrams.

specimens tested.

7.1.2 Effective activation volume

Figure 7.3 shows the evolution of the effective activation volume measured in stress relaxation experiments (see section 5.2.1.2.2 for details on the determination of V_{eff}) as a function of relaxation stress σ_0 and wire diameter d.

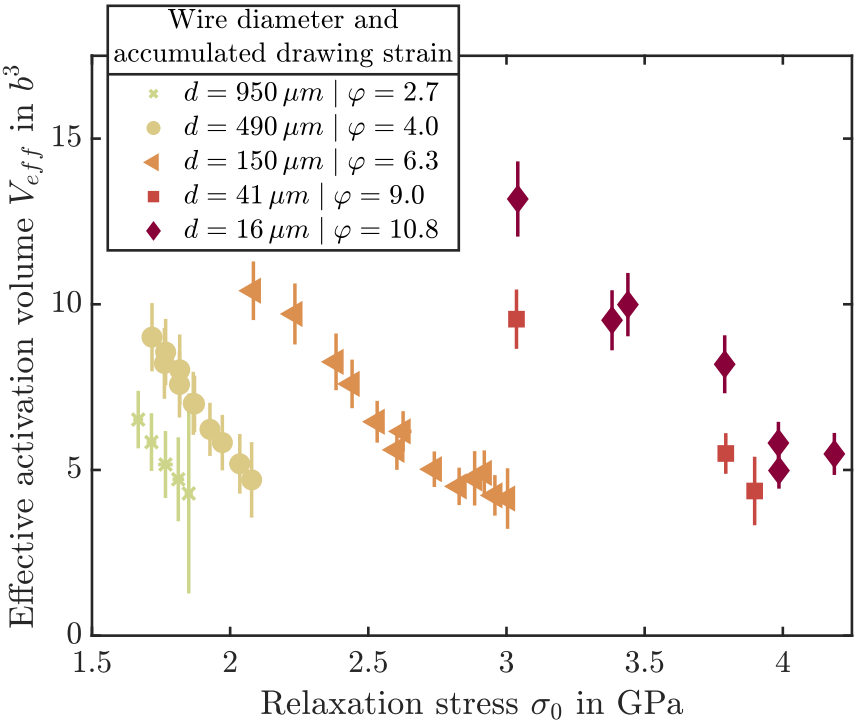

Figure 7.3: Effective activation volume determined in room temperature repeated stress relaxation experiments as a function of relaxation stress σ_0 for the five wire diameters that show ductile behaviour.

All effective activation volumes measured for the five different tungsten wires lie between $3\,\text{b}^3$ and $14\,\text{b}^3$. All wires show a monotonous decrease of V_{eff} with increasing relaxation stress, with only a very little number of outliers for wires with $\varphi = 6.4$ and $\varphi = 10.8$. As explained in section 5.2.1.2.2, the effective activation volume can only be measured for stresses between the yield and the ultimate tensile strength and $0 \leq \varepsilon_{\text{pl}} \leq \varepsilon_{\text{u}}$. Thus, the shift of the stress regions in which V_{eff} was probed, towards higher relaxation stresses for thinner wires already hints at the evolution of the yield and ultimate tensile strength with the accumulated drawing strain. A more thorough analysis of this relationship is discussed in section 8.1.

7.1.3 Strain-rate sensitivity

The strain-rate sensitivity of the wires that exhibited sufficient plastic deformation at room temperature were determined both in repeated stress relaxation experiments and strain-rate jump tests. The results are shown in figure 7.4.

The first observation that can be made upon comparing the results of RSRE and SRJT is that the strain-rate sensitivities measured in both experiments line up well. The obtained strain-rate sensitivities of drawn tungsten wires at room temperature are of the order of $5 \cdot 10^{-4}$ to $7 \cdot 10^{-2}$.

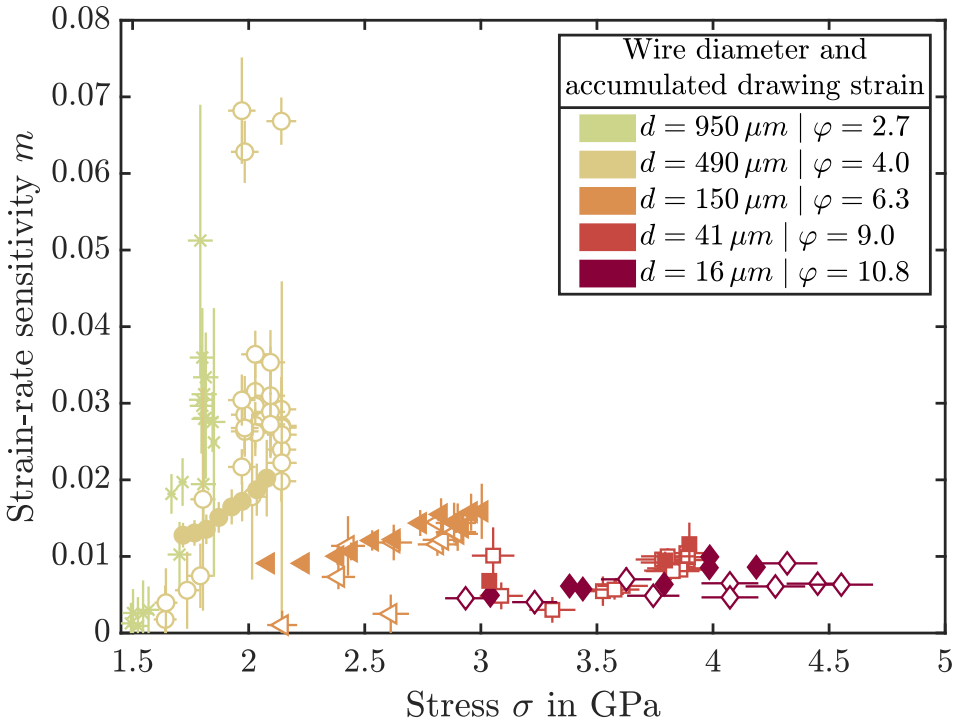

Figure 7.4: Strain-rate sensitivities from repeated stress relaxation experiments (filled symbols) and from strain-rate jump tests (empty symbols) as a function of the relaxation stress σ_0 and jump stress σ_1, respectively.

Wires having accumulated a higher drawing strain show overall lower strain-rate sensitivities. For wires with the same diameter, tests at higher stresses yield higher stain-rate sensitivities. Similar as for the effective activation volume, the stress range in which the strain-rate sensitivity was determined is shifted to higher stresses for thinner wires.

7.2 Microstructure

7.2.1 Conventional scanning electron microscopy

Since orientation maps contain a greater wealth of information and are by definition more quantitative in nature, the results from conventional electron microscopy, i.e. BSE or SE images at this point are not used to examine the evolution of the microstructure of the drawn tungsten wires. During the SEM investigations, it was however found that all wires seem to contain pores. A selection of SE images illustrating this feature are shown in figure 7.5.

A comparison of the secondary electron images shown in figure 7.5 reveals that all wires contain pores, but the number and arrangement of pores seems to vary. In wires with $\varphi \leq 2.7$, pores are both found in the grain interior and at the grain boundaries. In wires with accumulated drawing strains of $4.0 \leq \varphi \leq 6.4$, the pores are predominantly situated at grain boundaries and also their shape is different from the ones found in thicker wires: While the pores are initially circular, they appear crescent-shaped after a higher deformation in wire drawing. For the two thinnest wires investigated ($\varphi \geq 9.0$), the pores are strongly concentrated in the wire centre. Very small pores are present in the near-surface area of these wires. The pores in these wires are again found at grain boundaries and their shape is a function of their size: Small pores appear circular, while larger ones are again crescent-shaped. For $\varphi < 9.0$, the pores seem to decrease in size along with

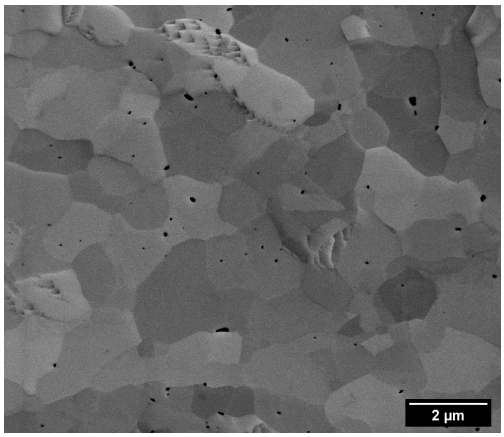

(a) $d = 3600\,\mu\text{m}$ | $\varphi = 0.0$

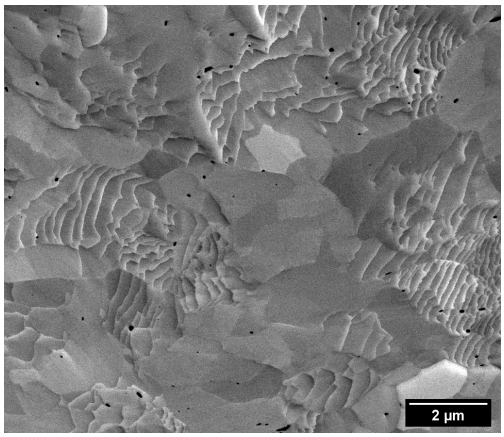

(b) $d = 2800\,\mu\text{m}$ | $\varphi = 0.5$

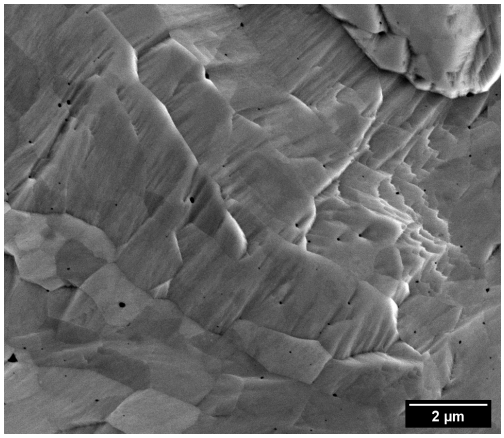

(c) $d = 1750\,\mu\text{m}$ | $\varphi = 1.4$

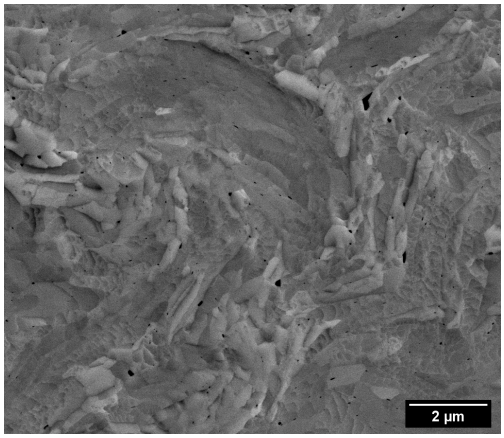

(d) $d = 950\,\mu\text{m}$ | $\varphi = 2.7$

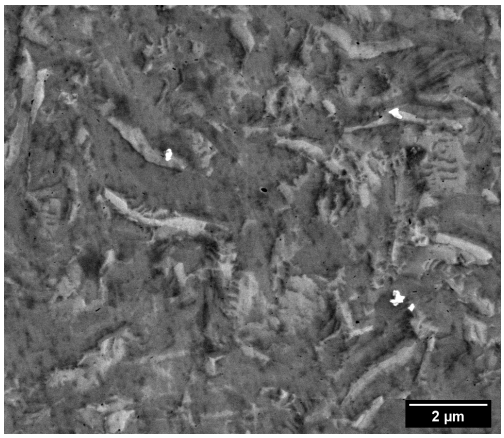

(e) $d = 490\,\mu\text{m}$ | $\varphi = 4.0$

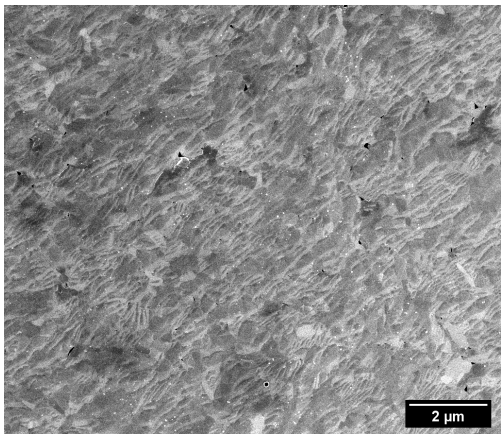

(f) $d = 150\,\mu\text{m}$ | $\varphi = 6.4$

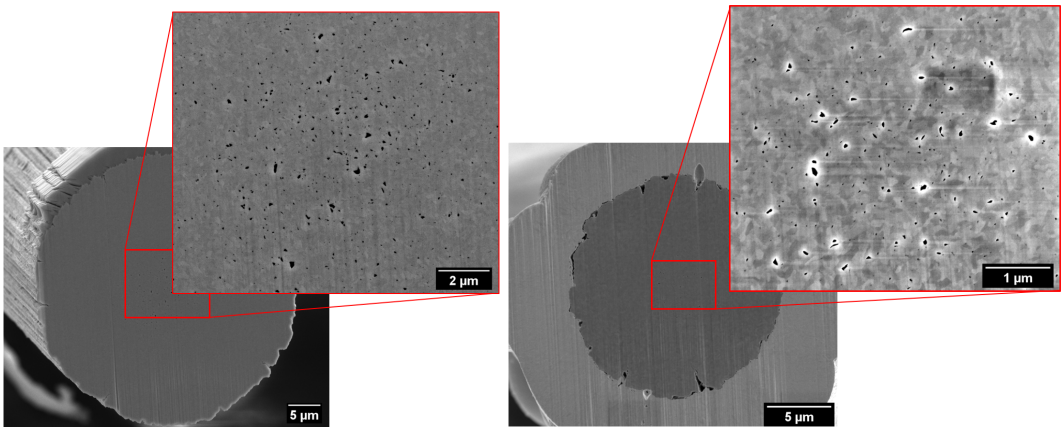

(g) $d = 41\,\mu m$ | $\varphi = 9.0$ (h) $d = 16\,\mu m$ | $\varphi = 10.8$

Figure 7.5: Secondary electron images acquired from the central region of transversal cross-sections of all wires investigated in this study. Note the black spots in each image. In the case of the thinnest wires (subfigures g and f) the image at the upper right part of the image is a zoomed cutout of the corresponding image below in order to increase visibility.

the qualitative decrease of grain size observed in figure 7.8. Pores could also be observed in STEM images, see appendix B.2.4. Theories on the origin of the pores in wires with different accumulated drawing strain will be discussed in section 8.4.1.

7.2.2 Scanning transmission electron microscopy

Two exemplary images acquired using scanning transmission electron microscopy are shown in figure 7.6. They reveal the fine-grained microstructure (mean grain width in the realm of approximately 100 nm) of the thinnest tungsten wire investigated in the course of this study. The micrograph taken with the HAADF detector (figure 7.6a) highlights the grain boundaries and reveals the bent shape of the grains. Especially in the high-magnification image (figure 7.6b), the internal (defect) structure of grains is observable. Individual dislocation lines are not visible in the grains, which might be either due to a too high thickness of the lamella or the superposition of FIB-induced damage and the pristine defect structure of the wire. The red arrow points to a pore between three grains. A higher magnification image of the lamella shown in the appendix (see section B.2.4) gives another impression of the porosity in the microstructure of the thinnest tungsten wire investigated in the course of this study. A quantification of the grain width from micrographs like the ones shown in figure 7.6 will be presented and discussed in section 8.4.2.2.

7.2.3 Orientation maps acquired using Electron Backscatter Diffraction

An overview of the number of orientation maps acquired from the wire edge or centre (for a definition, see section 8.3.2) of LS/TCS samples for a given wire diameter is shown in section B.2.1 of the appendix.

7.2.3.1 Transversal cross-section

7.2.3.1.1 Total wire cross-section

Orientation maps covering the whole wire are shown in figure 7.7. Due to their size, the cross-section of the tungsten rod ($\varphi = 0$) and the wire representing the first drawing stage ($\varphi = 0.5$)

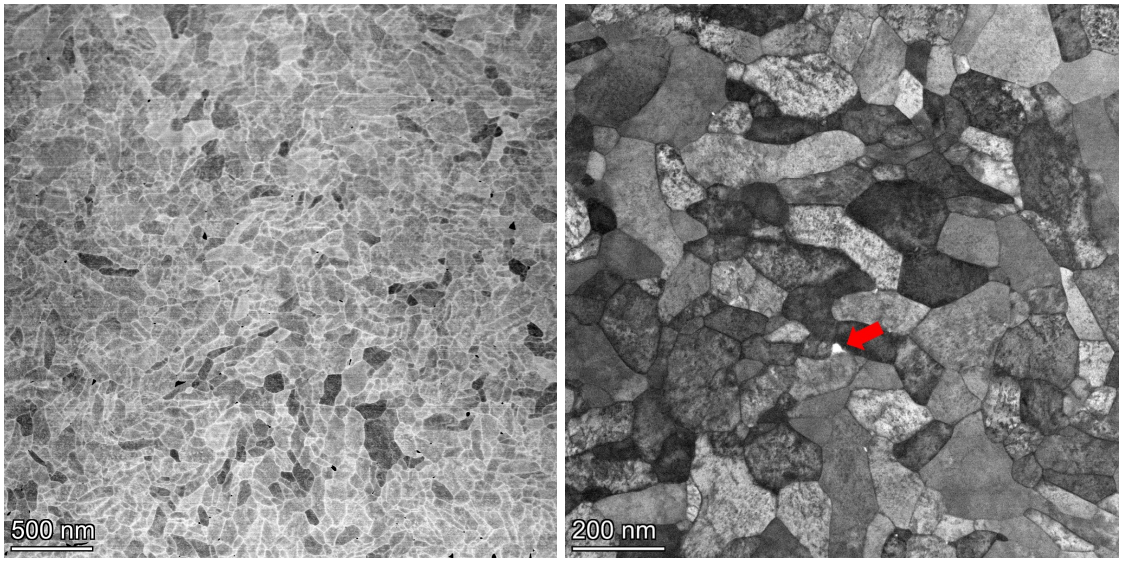

(a) Low magnification, high angle annular dark field detector.

(b) High magnification, dark field detector.

Figure 7.6: Scanning transmission electron micrographs acquired from a (transversal) lamella cut from a tungsten wire with a diameter of 16 µm using FIB techniques.

could not be mapped using a single orientation map but had to be composed of nine[1] or four single maps, respectively. The orientation map of the wire with a diameter of 2.8 mm shows a comparably bad indexing rate. Similarly, also the top part of the wire with a diameter of 150 µm is badly indexed.

Following the evolution of the orientation in the transversal cross-section, one finds that up to $\varphi = 0.5$ there is no clear difference between edge and centre of the wire, but it is apparent that more and more regions all over the wire rotate towards ⟨110⟩. For wires with $\varphi \geq 1.4$, a clear demarcation between edge and centre begins to show: The wire centre rotates disproportionately strong towards ⟨110⟩ (see $\varphi = 2.7$), while the edge does not undergo a significant change in orientation. This trend holds for $\varphi = 4.0$ where it also appears as if the region with a strong orientation towards ⟨110⟩ is spreading further to the wire edge. For even thinner wires, the misalignment angle between the wire axis and ⟨110⟩ in the centre region seems to become even lower. Simultaneously, the wire region close to the wire surface starts to deviate stronger from ⟨110⟩. Thus, the thinnest wire shown in figure 7.7 is characterised by a very sharp ⟨110⟩ region in the wire centre and an edge region where the orientation can be described by high-(Miller)-indexed directions.

7.2.3.1.2 Detail

Figure 7.8 shows representative orientation maps acquired from TCS samples of the tungsten wires with $d \geq 41$ µm.

Similar to the orientation maps acquired from the whole wire cross-section (see figure 7.7), some interesting trends can be observed if the orientation of crystallites in a smaller region of the cross-section is investigated. Since the detailed maps have the same horizontal and vertical size, the most apparent trend is the decrease of the mean grain size from the wire rod to the

[1] As figure 7.7 shows, one out of the envisioned eight maps was not measured. The texture can however still be investigated from the orientation data of the tungsten rod due to its radial symmetry. The same is true for the rather low indexing rate achieved when mapping the orientation of the first drawing stage ($\varphi = 0.5$).

Figure 7.7: Representative orientation maps acquired from TCS samples capturing a whole wire. Similar to figure 7.8 white pixels represent measurement positions where the EBSD software could not index the corresponding EBSP. The crystallographic orientations are coloured according to the sample z-direction, which coincides with the wire drawing axis. The respective colour key for the space group $m\bar{3}m$ is shown in the lower right corner of the figure.

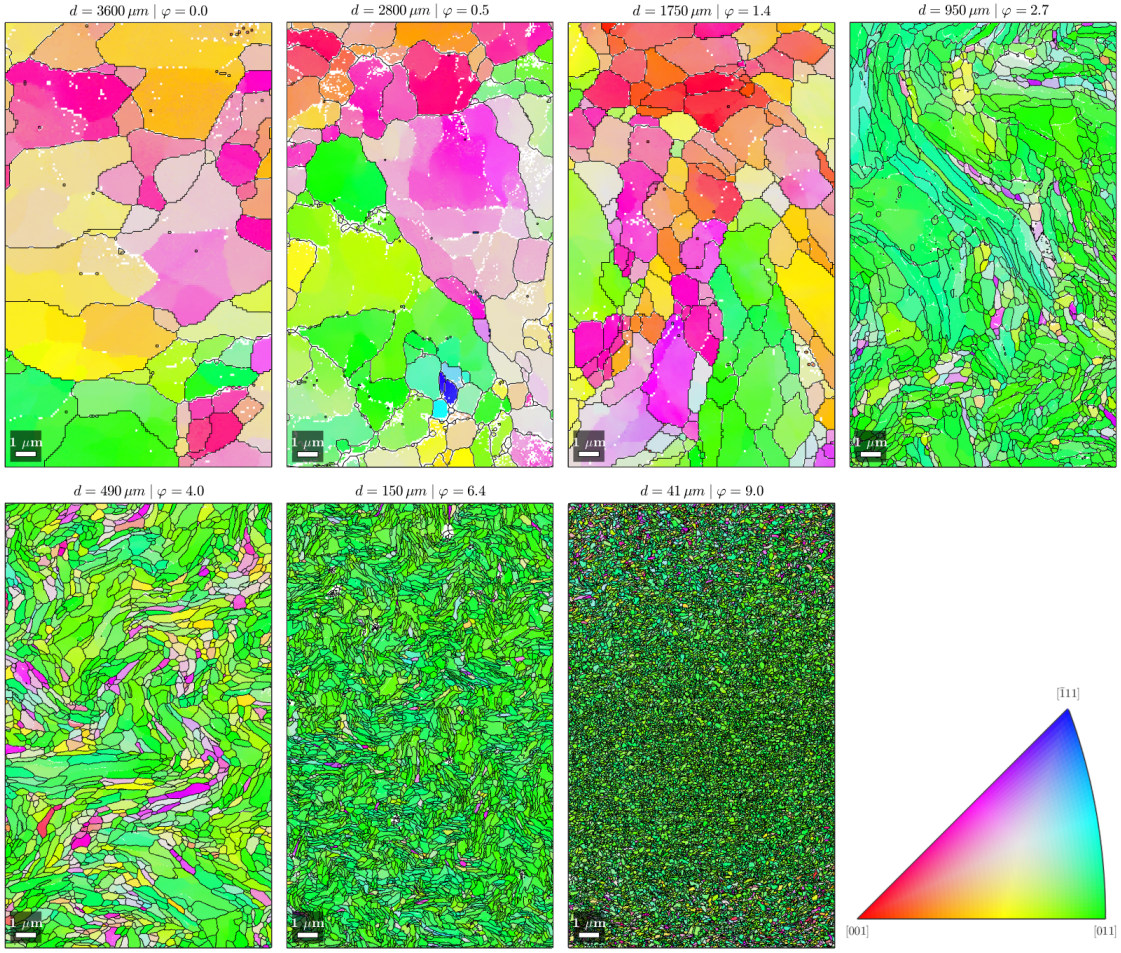

Figure 7.8: Detailed orientation maps acquired from the centre of TCS samples. All orientation maps have the same size in order to illustrate the evolution of the grain structure with increasing accumulated drawing strain. The black lines represent grain boundaries that were calculated with a minimum misorientation angle of 2°. White pixels represent measurement positions where the corresponding Kikuchi pattern could not be indexed. The crystallographic orientations are coloured according to the sample z-direction, which coincides with the wire drawing axis. The respective color key for the space group m$\bar{3}$m is shown in the lower right corner of the figure.

heavily drawn wires. The grains in thicker wires, especially the rod and the wire after the first drawing step also reveal a kind of subgrain structure, which can be seen from the regions of similar orientation that are sharply separated from each other. In accordance with the observations stated in section 7.2.3.1.1, the number of grains aligned with an orientation close to ⟨110⟩ is increasing with increasing accumulated drawing strain.

7.2.3.2 Longitudinal section

Detailed orientation maps acquired from longitudinal sections of drawn tungsten wires are shown in figure 7.9. The comparison showcases that the microstructural changes that are apparent from transversal orientation maps (figure 7.8) can also be seen in longitudinal orientation maps. Primarily, the decrease of grain thickness with increasing accumulated drawing strain is apparent. Concurrently, the transformation of the grains with an initially low aspect ratio into strongly elongated grains can be retraced. Starting from $\varphi = 6.4$, grains that run from one end of the orientation map to the other are visible. Apart from their length, also the shape of the grains is changing: While grains appear slightly bent in thicker wires, they are almost straight in thinner ones. The conclusion from figure 7.8 that the grain width, i.e. in the case of longitudinal sections the width of the grains perpendicular to the wire drawing axis, decreases, can also be drawn from figure 7.9. Results on the evolution of grain length and aspect ratio can be found in section 8.4.2.4.

7.2.4 Results from X-ray diffraction studies

The primary result of the X-ray diffraction analyses are the diffractograms shown in figure 7.10. All diffractograms show the diffraction peaks for polycrystalline tungsten that are expected from theory (see equation (5.18)). Additionally, there is a peak at an angle of 26° for all samples that were embedded in the conductive embedding. This peak correlates well with the 002 peak found in graphite samples, see for example [263], and is thus most likely caused by the graphite admixture to the embedding material. The samples containing the thinnest wires ($\varphi = 6.4$ and $\varphi = 9.0$) show distinct peaks at diffraction angles of 38°, 44.5°, 64.7°, 77.7° and 98.4°. There is no clear correlation between the height of the tungsten peaks and the accumulated drawing strain of the respective wire[2].

[2] An in-depth analysis of this relationship can be found in appendix B.2.5.

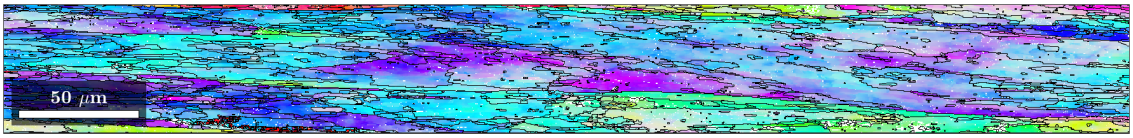

(a) $d = 3600\,\mu\text{m}$ | $\varphi = 0.0$

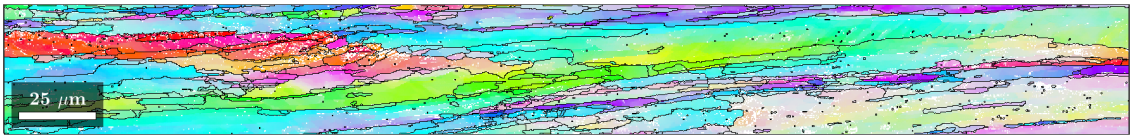

(b) $d = 2800\,\mu\text{m}$ | $\varphi = 0.5$

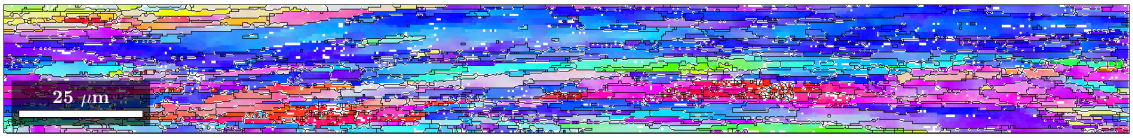

(c) $d = 1750\,\mu\text{m}$ | $\varphi = 1.4$

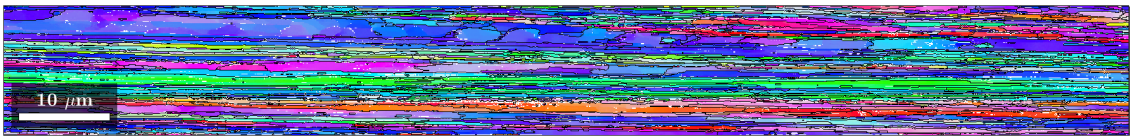

(d) $d = 950\,\mu\text{m}$ | $\varphi = 2.7$

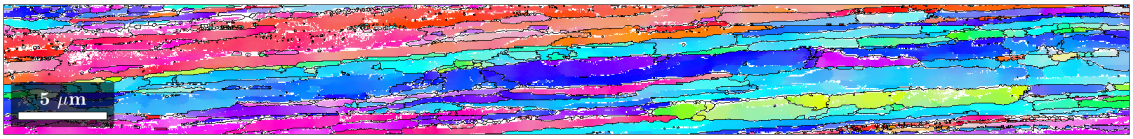

(e) $d = 490\,\mu\text{m}$ | $\varphi = 4.0$

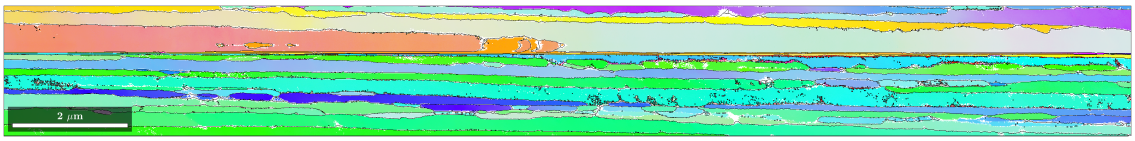

(f) $d = 150\,\mu\text{m}$ | $\varphi = 6.4$

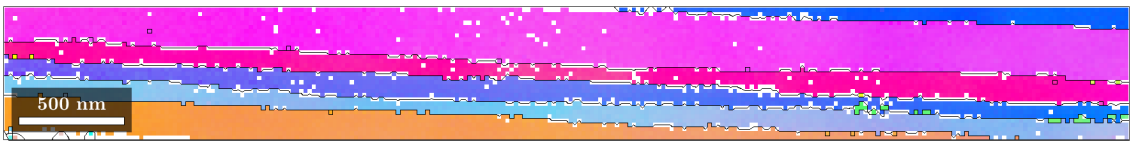

(g) $d = 41\,\mu\text{m}$ | $\varphi = 9.0$

Figure 7.9: Detailed orientation maps acquired from longitudinal sections of different tungsten wires. The wire diameter and the respective accumulated drawing strain is indicated below each subfigure. Grain boundaries are drawn as black lines, while non-indexed pixels are white. The cutouts are chosen in a way that all figures possess the same aspect ratio (width/height); note the different scale bars. The crystallographic orientations are coloured according to the sample z-direction. The associated colour key can be found in figures 7.8 and 7.7.

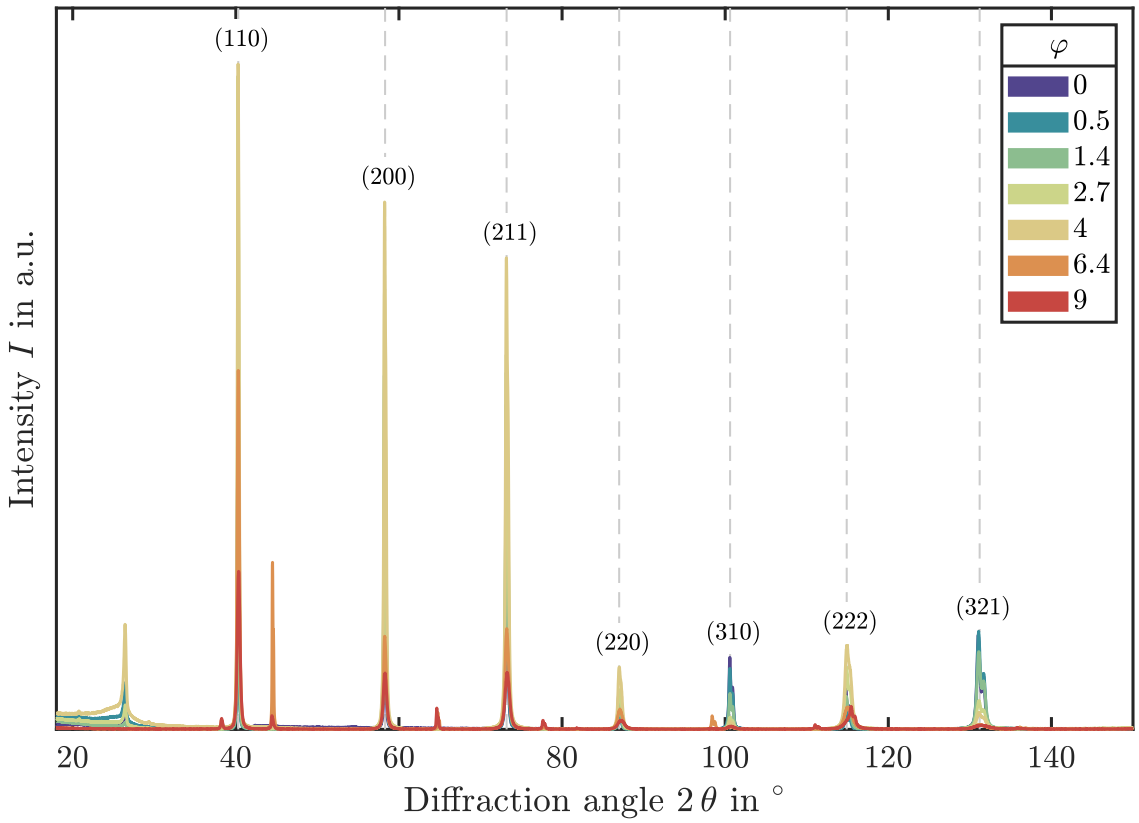

Figure 7.10: X-ray diffractograms of seven tungsten wire specimens with diameters $d \geq 41\,\mu\text{m}$ investigated in this study. The grey lines indicate the theoretical positions of the diffraction peaks calculated according to equation (5.18).

Chapter 8

Discussion

8.1 Key mechanical properties

The discussion of the stress-strain characteristics of drawn tungsten wires determined in uniaxial tensile tests will be limited to the strain region $e \leq e_u$, i.e. up to the uniform elongation of the wires. This has the two following reasons:

- One of the aims of the mechanical tests was to investigate the ductility of the wires. Ductility can be defined as the ability of a material to show plastic deformation prior to failure [107]. In other words, ductile materials reach a non-zero plastic strain when deformed. The uniform elongation regime thereby contains information on the strain-hardening behaviour and the extent to which a material can be deformed plastically without showing plastic instabilities. The extent of uniform plastic deformation is used as a measure of ductility. Furthermore, as shown by Leber and co-workers [33], Millner et al. [200] and Riesch et al. [73, 196], the necking behaviour of tungsten wires, which can be described as diffuse necking [264], is very complex.
- As already mentioned, the equations for determining the true stress and strain (equations (5.3) and (5.5)) presented in section 5.2.1.1 are only valid for $e \leq e_u$. Since the measurement of the spatially resolved evolution of the cross-sectional area $S(t)$ was beyond the scope of this work, the true stress and strain was not accessible for $e > e_u$. Thus, the following discussion is limited to the uniform elongation regime.

Since only the strain region $e \leq e_u$ is investigated further, effects like the necking-related stress decays found for the thicker wires prior to fracture are not discussed further. The reason for this behaviour is that the necking region was located outside the measuring length (see section 6.2.4). During necking, the plastic deformation and the sample elongation is focused on a finite length of the sample. Consequently, the stress in the rest of the sample is relieved following Hooke's law. Up until e_u, the deformation is uniformly distributed over the whole sample length and strain localisation does not occur. Hence, when only analysing $e \leq e_u$, the test can be seen as valid.

Due to tungsten's high Young's modulus [262], the stress at 0.02 % plastic strain is reported as yield strength $R_{p0.02}$ (see section 5.2.1.1). Since repeated stress relaxation experiments and strain-rate jump tests represent standard monotonous tensile tests until the first stress relaxation or strain-rate jump is performed, the yield strength measured in these experiments is also reported. The yield strengths determined this way as well as the ultimate tensile strength R_m and the uniform elongation e_u as a measure of ductility are shown in figure 8.1 as a function of the applied strain rate.

As shown in figures 7.2 and 7.1 and already reported for example by Schmidt et al. [265],

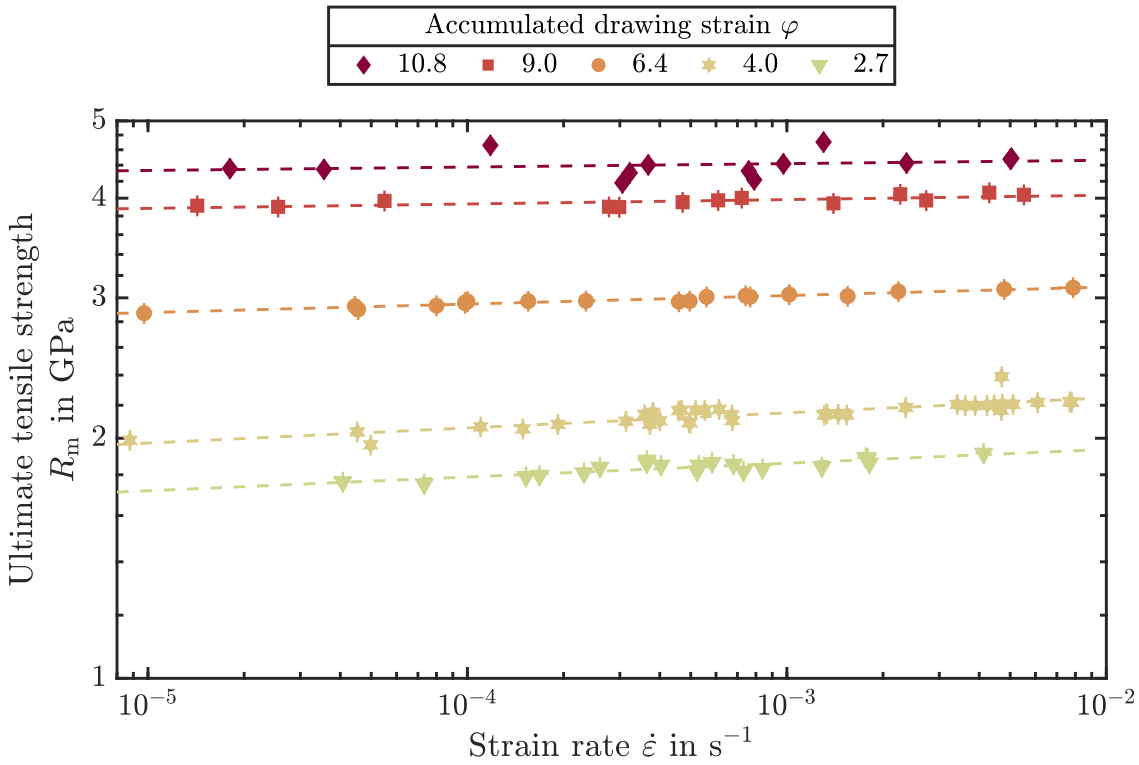
Accumulated drawing strain φ
10.8
9.0
6.4
4.0
2.7
Ultimate tensile strength
R_m in GPa
5
4
3
2
1
10^{-5}
10^{-4}
10^{-3}
10^{-2}
Strain rate $\dot{\varepsilon}$ in s^{-1}

(a)

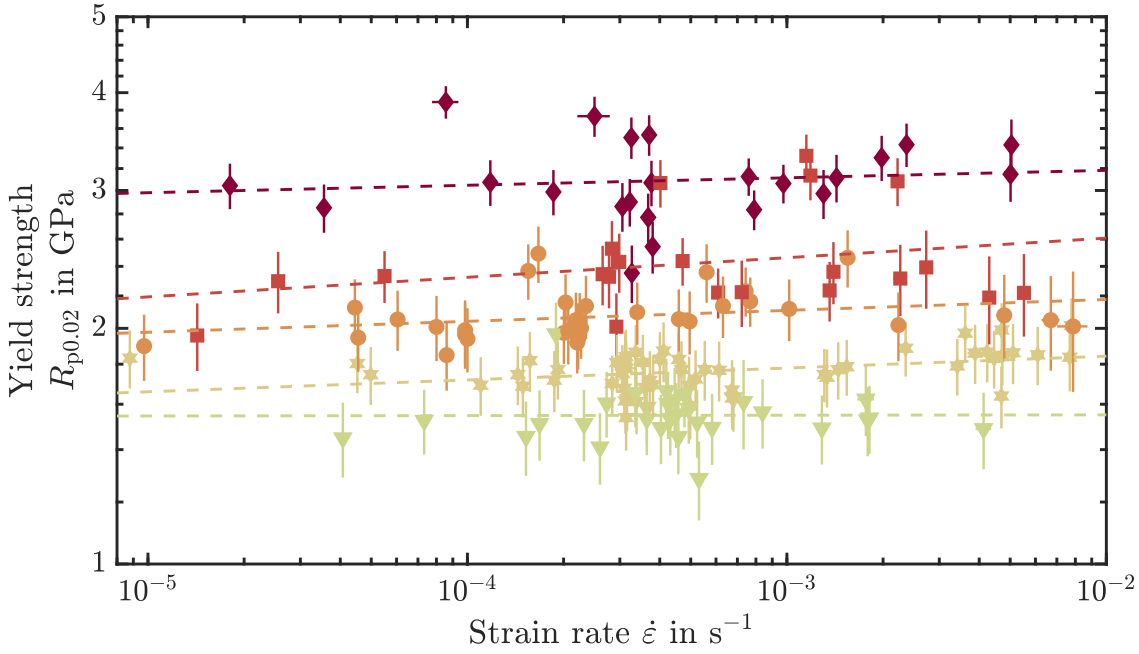
Yield strength
$R_{p0.02}$ in GPa
5
4
3
2
1
10^{-5}
10^{-4}
10^{-3}
10^{-2}
Strain rate $\dot{\varepsilon}$ in s^{-1}

(b)

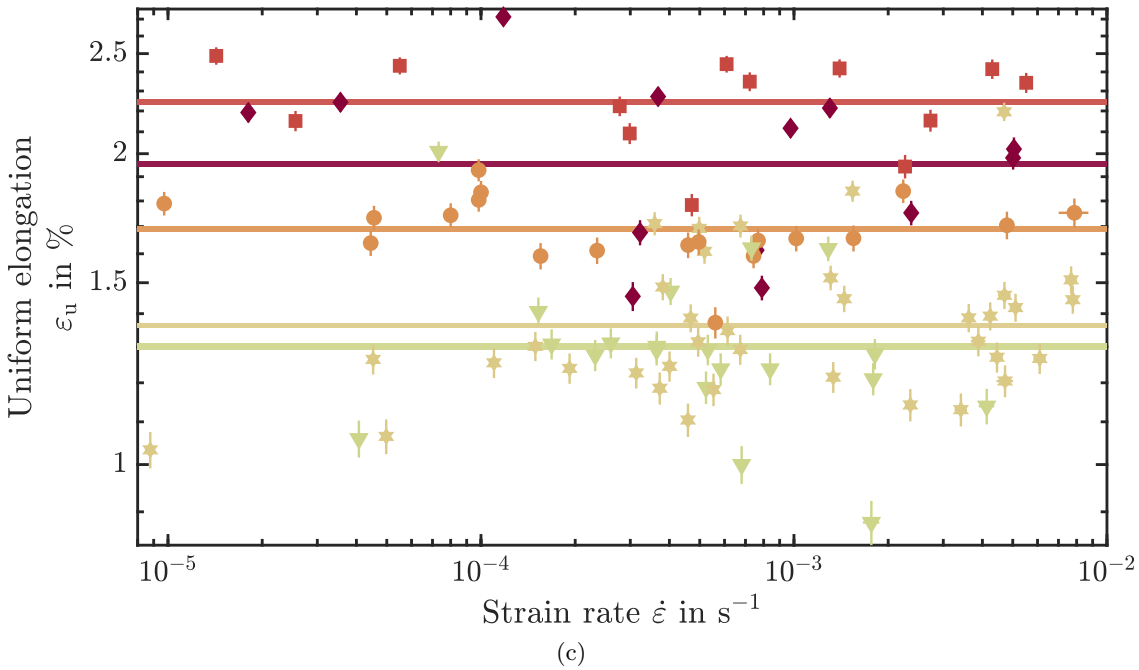

(c)

Figure 8.1: Strain rate dependence of the ultimate tensile strength R_m (a), the yield strength $R_{p0.02}$ (b) and the uniform elongation ε_u (c) of tungsten wires. The yield strength was extracted from strain-rate jump tests, uniaxial tensile tests and repeated stress relaxation experiments, while the ultimate tensile strength and uniform elongation were determined from uniaxial tensile tests. The dashed lines in subfigures (a) and (b) are fits to the experimental data following equation (8.1). The horizontal lines in subfigure (c) represent the mean uniform elongation for each wire diameter. The thickness of the horizontal line illustrates the uncertainty associated with the mean uniform elongation. The assignment of the accumulated drawing strain of each wire to the colours used is shown in the legend on top of subfigure (a).

the strength (both in form of the yield and the ultimate tensile strength) of tungsten wires increases with increasing accumulated drawing strain (see [195] for an overview over the available literature). Figure 8.1 clearly shows that tungsten wires evade the strength-ductility trade-off [107] since thinner wires exhibit not only higher strength but also an enhanced uniform elongation when compared to thicker wires. The origin of this behaviour will be discussed in section 8.6.1. Since determining the yield strength is linked to uncertainties in both stress and strain, while the uncertainty of the ultimate tensile strength is only influenced by uncertainty in the stress, the scatter of the yield strength is higher than the one of the ultimate tensile strength. From the apparent plastic deformation observed in room-temperature tensile tests, it can also be concluded that the ductile-to-brittle transition temperature of all wires with $\varphi \geq 2.7$ lies below room temperature. This is in line with findings from literature [34, 111].

Using a power law for the strain-rate dependence of the strength[1]

$$\sigma = K\,\dot{\varepsilon}^{n}, \tag{8.1}$$

where σ : True stress
K : Coefficient

[1]Note the resemblance to Hollomon's [266] and Ludwik's [267] expressions for the strain-hardening of metals.

$\dot{\varepsilon}$: Strain rate
n : Strain-rate sensitivity,

the strain-rate sensitivity n can be estimated from the strain-rate dependence of the yield and ultimate tensile strength. The results of this evaluation are plotted in figure 8.2 alongside the stain-rate sensitivities obtained from strain-rate jump and repeated stress relaxation experiments (see figure 7.4).

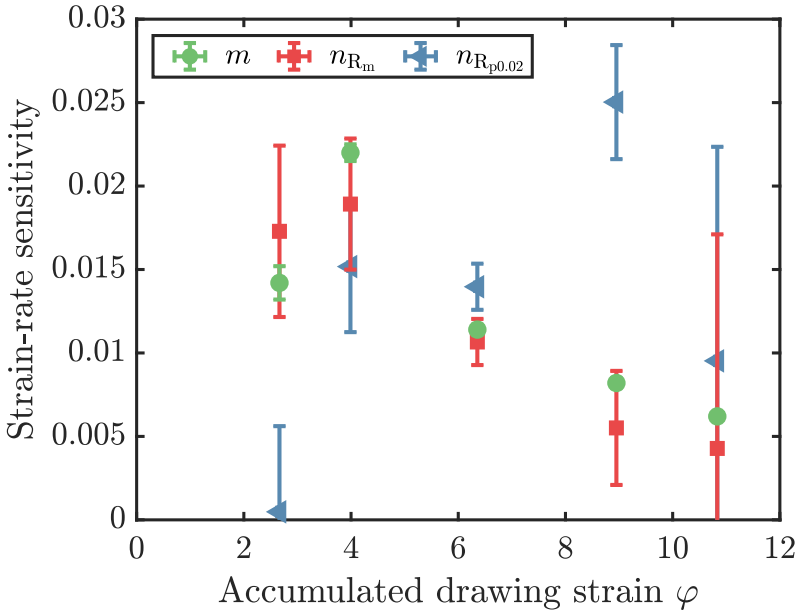

Figure 8.2: Strain-rate sensitivities of tungsten wires at room temperature determined from strain-rate jump experiments (green circles) as well as the strain-rate dependence of the yield strength (blue triangles) and the ultimate tensile strength (red squares) using equation (8.1).

The strain-rate sensitivity determined from the yield strength $n_{R_{p0.02}}$ does not show any clear trend associated with the accumulated drawing strain but stands out due to its strong variation. This is probably due to the higher variation of the strain-rate dependence of the yield stress when compared for example to the ultimate tensile stress. n_{R_m} in contrast, lines up very well with the strain-rate sensitivity determined from transient mechanical tests. As a consequence, m and n_{R_m} show the same trend: After a plateau for $\varphi \leq 4.0$, a decrease in strain-rate sensitivity with increasing φ is observed. The reason for this trend is discussed in section 8.6.

8.2 Modelling of the strain hardening behaviour

Using the theoretical considerations discussed in section 4.2.2.1, the evolution of true stress σ vs. true plastic strain ε_{pl} was modelled. For this, equation (4.21) was slightly adjusted in order to incorporate an internal stress. Thus, instead of using the true stress, an effective stress

$$\sigma_{eff} = \sigma - \sigma_i \tag{8.2}$$

where σ_{eff} : True effective stress
σ : True stress
σ_i : Internal stress

was used (see [268] for a treatment of the internal stress). Accordingly, the initial stress [130] introduced in equation (4.21) was modified:

$$\sigma_{\mathrm{eff},0} = \sigma_{\mathrm{y}} - \sigma_{\mathrm{i}} \tag{8.3}$$

where $\sigma_{\mathrm{eff},0}$: Initial effective true stress
σ_{y} : True yield stress
σ_{i} : Internal stress

With these adaptions, equation (4.21) reads as

$$\varepsilon_{\mathrm{pl}} = \frac{\sigma_\infty}{\theta_0} \frac{1}{\sigma^+ - \sigma^-} \left[\sigma^- \ln\left(\frac{\sigma_{\mathrm{eff}} - \sigma^-}{\sigma_{\mathrm{eff},0} - \sigma^-} \right) - \sigma^+ \ln\left(\frac{\sigma_{\mathrm{eff}} - \sigma^+}{\sigma_{\mathrm{eff},0} - \sigma^+} \right) \right]. \tag{8.4}$$

where $\varepsilon_{\mathrm{pl}}$: True plastic strain
σ_∞ : Saturation stress
θ_0 : Initial work-hardening rate
$\sigma^\pm = \frac{\sigma_\infty}{2} \pm \sqrt{\frac{\sigma_\infty^2}{4} - \sigma_\infty \sigma_{\mathrm{D}}}$: Auxiliary stresses
$\sigma_{\mathrm{eff},0}$: Initial effective true stress
σ_{eff} : True effective stress

The evolution of true plastic strain vs. true stress can be modelled using the four free variables of equation (8.4), namely the annihilation length y_{a}, the spacing between fixed obstacles λ_f, the coefficient β describing the accumulation of dislocations at forest dislocations and the internal stress σ_{i}. A Taylor factor of $M_{\mathrm{T}} = \sqrt{6}$ for textured tungsten wires with $\langle 111 \rangle \{110\}$ slip [113] and an interaction coefficient for dislocations of $\alpha = 0.5$ [117] was used during fitting.

The fitting procedure was performed in a two-step manner: In a first step, physically sound limits for the four fitting variables were defined. These are listed in table 8.1.

Table 8.1: Physical limits of the variables used during fitting of the modified Breuer model to the experimentally determined stress-strain curves.

Fitting variable		Lower boundary	Upper boundary
Parameter β		0.01	7
Annihilation length y_{a}		$50\,b$	$350\,b$
Internal stress σ_{i}		1 GPa	σ_{y}
spacing between fixed obstacles λ_{f}	$\varphi = 2.7$	250 nm	1.7 µm
	$\varphi = 4.0$	200 nm	1.15 µm
	$\varphi = 6.4$	80 nm	480 nm
	$\varphi = 9.0$	30 nm	180 nm
	$\varphi = 10.8$	30 nm	172 nm

The choice of the upper and lower boundaries of β and y_{a} were based on the considerations by Kocks and Mecking [127] as well as Essmann and co-workers [129, 269]. Since the internal stress cannot surmount the true yield strength, σ_{y} was chosen as an upper boundary for σ_{i}. The upper and lower bound for the spacing between fixed obstacles were selected according to the grain size obtained from the microstructural analysis.

The four fitting variables span a four-dimensional space. This space was probed at $45^4 = 4100625$ positions by calculating the theoretical evolution of plastic strain $\varepsilon_{\mathrm{pl,theor}}$ using the experimental true stress and the values of the fitting variables at the selected point. The agreement between the modelled and experimental evolution of the plastic strain was evaluated using an arbitrarily estimated evolution of the uncertainty of the true plastic strain as a weighing factor. The uncertainty is given by

$$\Delta\varepsilon_{\mathrm{pl}} = 0.08 + 0.05\,\varepsilon_{\mathrm{pl}}. \tag{8.5}$$

where $\Delta\varepsilon_{\mathrm{pl}}$: Uncertainty of the true plastic strain
$\varepsilon_{\mathrm{pl}}$: True plastic strain

Using this definition, the agreement between model and experimental data is quantified using the χ^2-test [270, p. 778]:

$$\chi^2 = \sum_{k=1}^{N} \left(\frac{\varepsilon_{\mathrm{pl,k}} - \varepsilon_{\mathrm{mod,k}}\left(\beta_{\mathrm{j}}, y_{\mathrm{j}}, \sigma_{\mathrm{i,j}}, \lambda_{\mathrm{j}}\right)}{\Delta\varepsilon_{\mathrm{pl,k}}} \right)^2 \tag{8.6}$$

where $\varepsilon_{\mathrm{pl,k}}$: Experimental true plastic strain
$\varepsilon_{\mathrm{mod,k}}\left(\beta_{\mathrm{j}}, y_{\mathrm{j}}, \sigma_{\mathrm{i,j}}, \lambda_{\mathrm{j}}\right)$: Calculated true plastic strain
$\Delta\varepsilon_{\mathrm{pl}}$: Empirical uncertainty of the true plastic strain (see equation (8.5))

The set of variables (quadruplet $(\beta_{\mathrm{j}}, y_{\mathrm{a,j}}, \sigma_{\mathrm{i,j}}, \lambda_{\mathrm{f,k}})$) with the lowest χ^2 was interpreted as best fit. Following this first rough fitting procedure, the fit result was refined using the `fmincon` function of MATLAB. This function can be used to perform a constrained nonlinear optimization [271]. In the present case, it was used to fine-tune the results of the first fitting. The result of the best fit in the first fitting step $(\beta_{\mathrm{best}}, y_{\mathrm{a,best}}, \sigma_{\mathrm{i,best}}, \lambda_{\mathrm{f,best}})$ was used as starting point for the second fitting procedure. The constraints chosen for the second fit were the same as used for the first fit (see table 8.1). The result of the modelling of the strain-hardening behaviour are shown in figure 8.3.

Upon comparing the experimentally determined and modelled evolution of stress and strain, a very good agreement (coefficient of determination $R^2 \geq 98\%$ for all measurements) is observed. The dependence of the fitting variables on strain rate and the accumulated drawing strain is shown in figure 8.4.

As apparent from figure 8.4 and quantified in table B.2 in section B.1.4 of the appendix, the fitting variables do not exhibit[2] a significant strain-rate dependence[3]. Hence, mean values can be used to characterise the strain hardening behaviour of the investigated tungsten wires. The mean values are summarised in table 8.2.

8.2.1 Recovery of dislocations

The average annihilation lengths y_{a} for wires with different accumulated drawing strain are listed in table 8.2 (page 93). The annihilation length is increasing with the accumulated drawing strain until it reaches its maximum around $205\,b$ at $\varphi = 6.4$. For even higher accumulated drawing strains, y_{a} decreases again monotonically. Using the findings of investigations by Essmann & Rapp [269] and Essmann and Mughrabi [129], the character of the dislocations that are mainly responsible for annihilation during work hardening can be deduced: Comparing neutron-irradiated and unirradiated copper specimens, Essmann and Rapp [269] found that the critical distance for the annihilation of edge dislocations is roughly $6\,b$. For screw dislocations in Cu, Essmann & Mughrabi [129] obtained annihilation lengths in the range of 195 to $1950\,b$. Thus, the annihilation lengths ranging from 100 to $200\,b$ found in the present study indicate that the recovery of dislocations is most likely achieved by annihilation following the cross-slip of screw dislocation (segments) as predicted for low temperature deformation [128, 272, 273].

[2] This means that either the value of n is close to zero or the uncertainty is significantly larger than the value itself, see table B.2.

[3] The low strain-rate sensitivity of the annihilation length will be discussed in section 8.2.1.

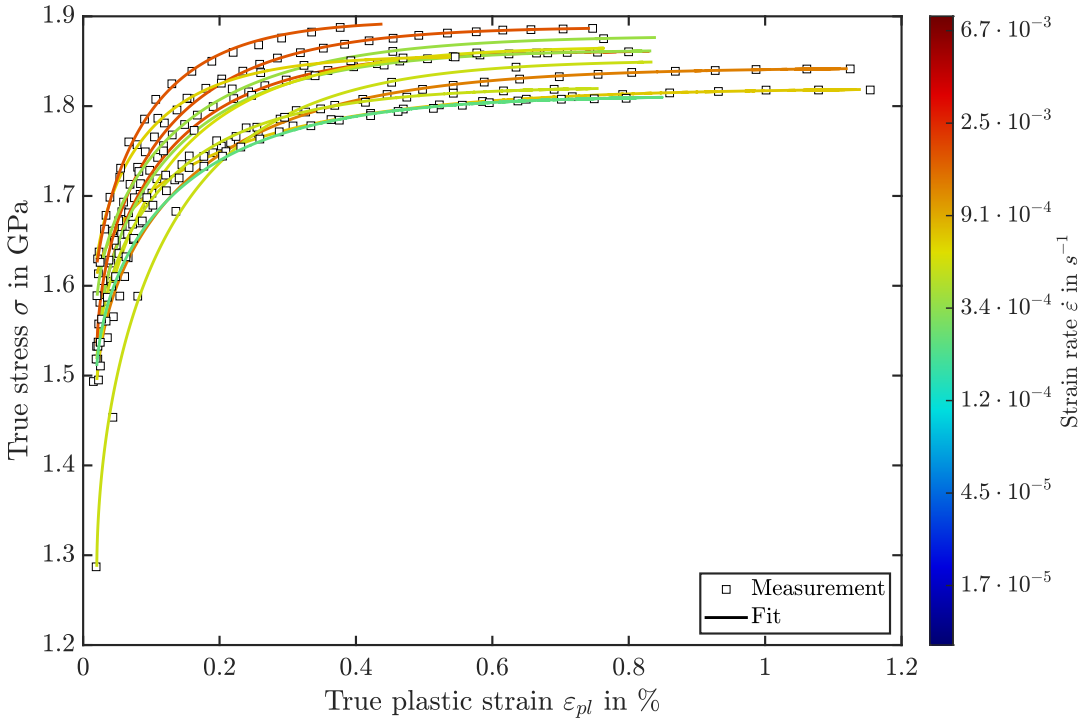

(a) $\varphi = 2.7$

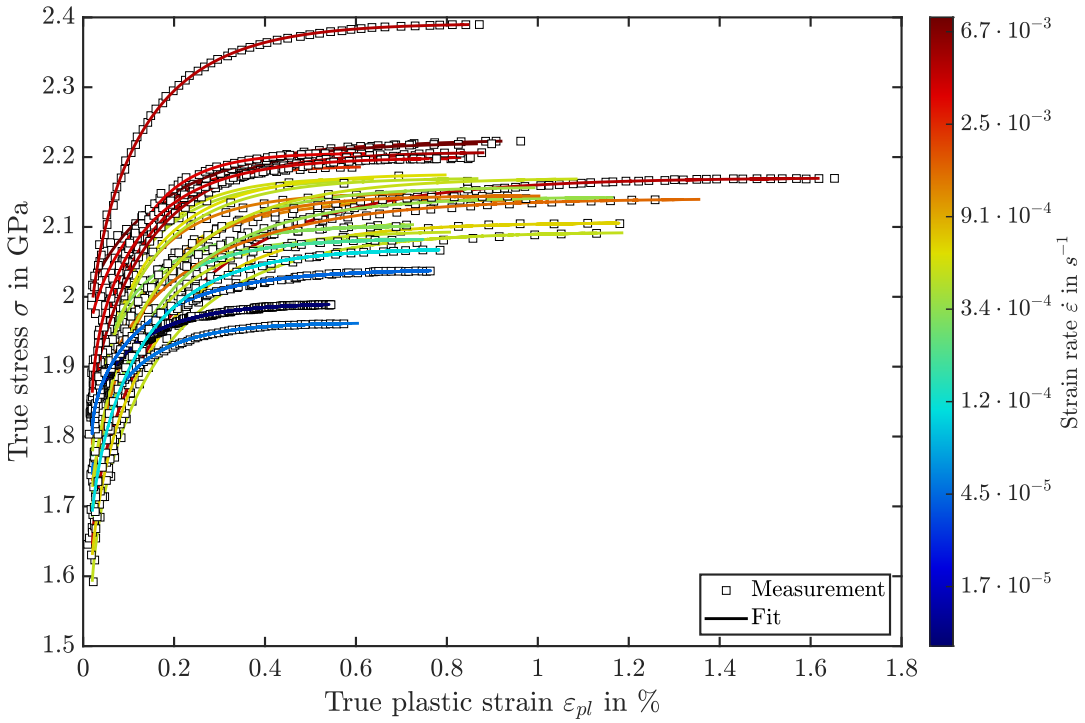

(b) $\varphi = 4.0$

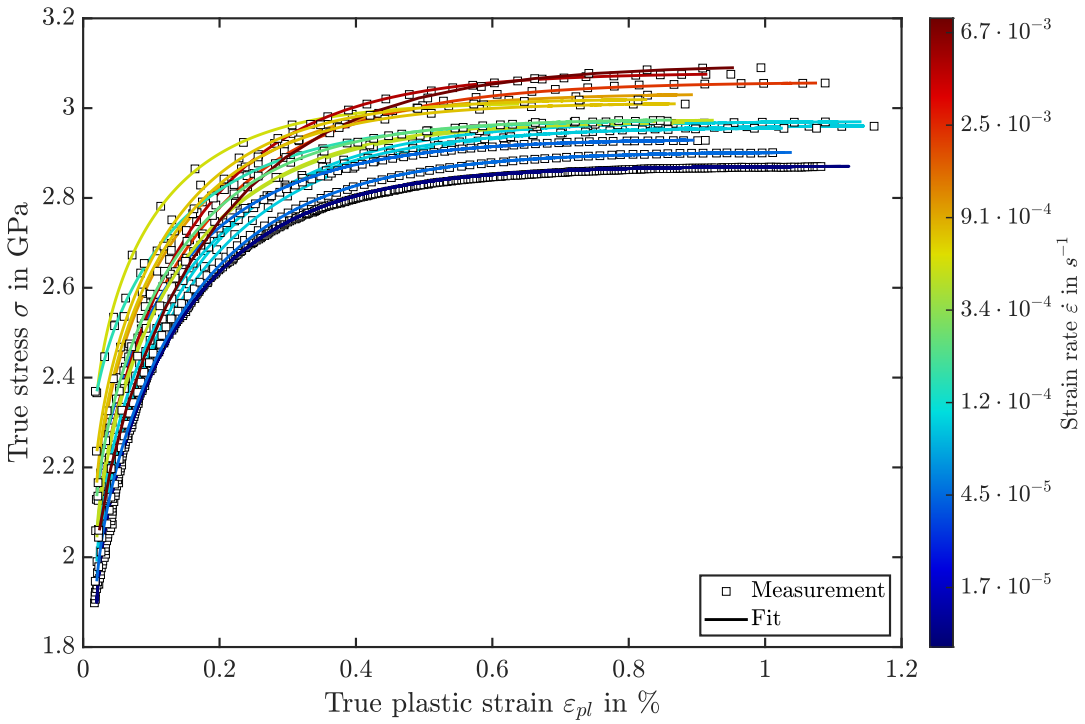

(c) $\varphi = 6.4$

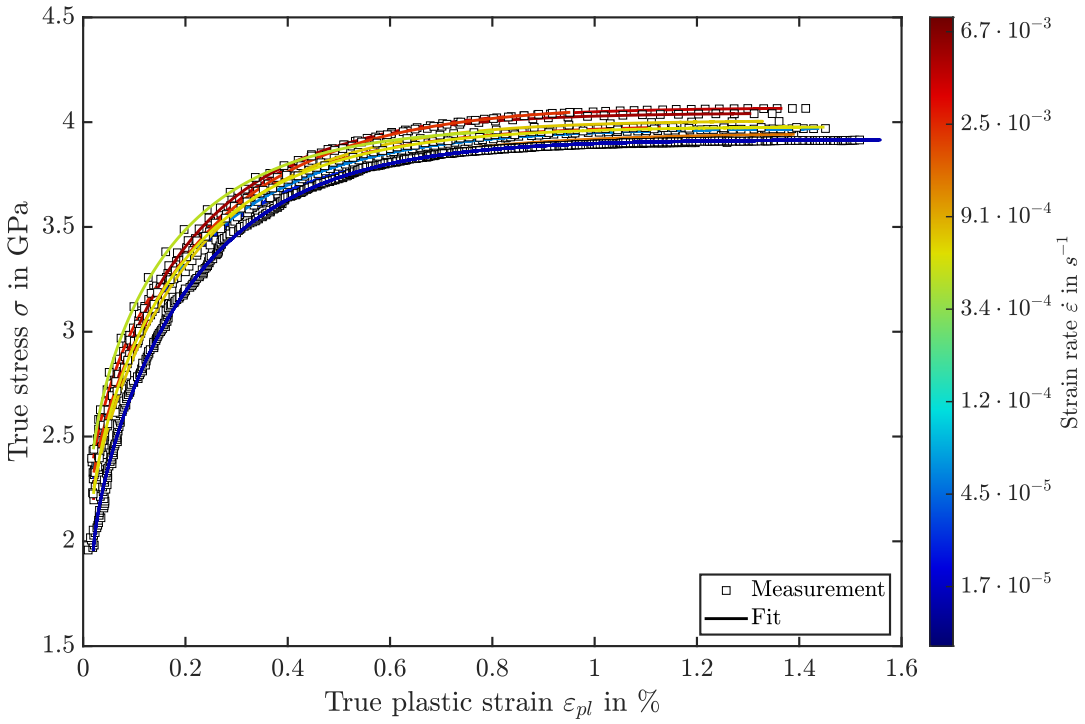

(d) $\varphi = 9.0$

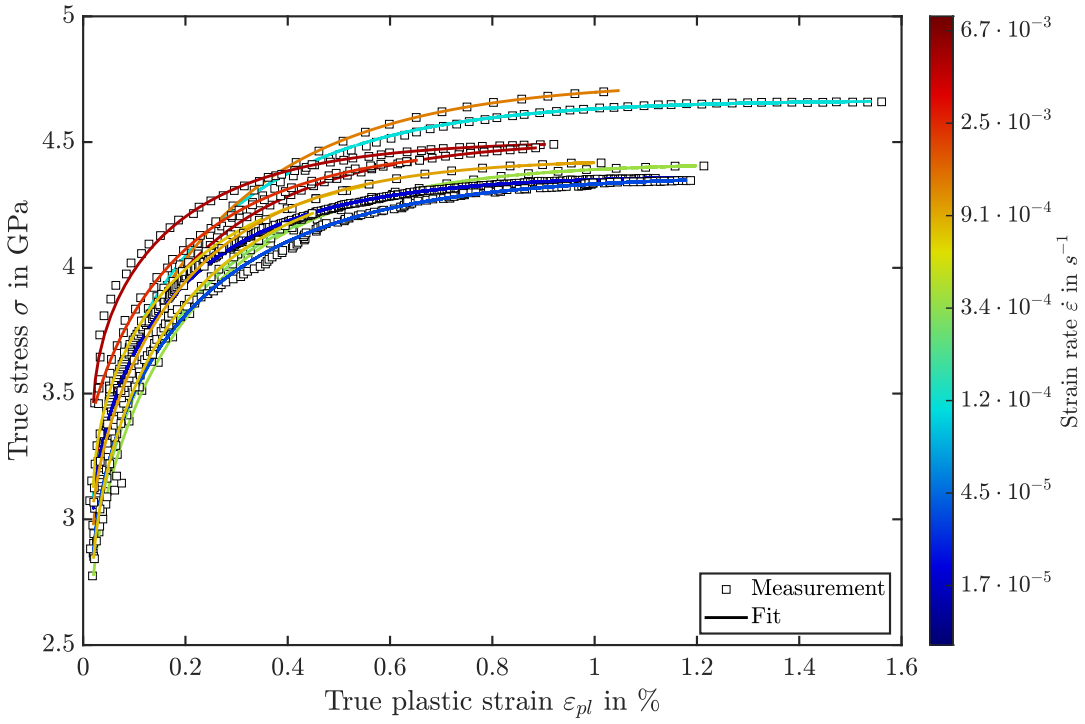

(e) $\varphi = 10.8$

Figure 8.3: True stress vs. true plastic strain for drawn tungsten wires with diameters ranging from 0.95 mm to 16 µm. The experimental data are plotted as empty squares with a black edge while the corresponding fit using the modified Kocks-Mecking model is plotted as a coloured line, where the line colour reveals the strain rate used during testing (see colour key to the right side of the figure). Note that the number of points shown for the measurements (black empty squares) was set to a constant value regardless of the strain rate of the respective tensile test, in order to improve visibility.

Table 8.2: Mean values of the variables characterising the evolution of the strain hardening behaviour of drawn tungsten wires with different accumulated drawing strains φ. The listed variables are the coefficient β, the spacing between fixed obstacles λ_f, the annihilation length y_a, the steady-state dislocation density ρ_ss, the initial dislocation density ρ_0, the prevailing accumulation mechanism characterised by the ratio $\upsilon = {k_0}/{\left(k_0 + k_1\sqrt{\rho_\mathrm{ss}}\right)}$ (see equation (8.10)) and the ratio of the mean spacing between fixed obstacles and forest dislocations, $\lambda_\mathrm{f}\sqrt{\rho_\mathrm{ss}}$, in the steady state condition.

φ	2.7	4.0	6.4	9.0	10.8
β	18.35 ± 6.19	7.82 ± 1.69	0.74 ± 0.09	0.47 ± 0.06	2.65 ± 1.09
σ_i in GPa	1.49 ± 0.02	1.72 ± 0.02	2.00 ± 0.03	2.09 ± 0.03	2.87 ± 0.07
λ_f in nm	332.0 ± 62.6	343.4 ± 58.9	70.7 ± 3.1	38.9 ± 5.8	32.4 ± 3.6
y_a in b	151.3 ± 11.6	176.3 ± 9.4	205.2 ± 4.6	153.6 ± 6.7	111.5 ± 6.0
ρ_ss in $1 \cdot 10^{15}\,\mathrm{m}^{-2}$	0.06 ± 0.01	0.08 ± 0.01	0.42 ± 0.02	1.52 ± 0.04	1.10 ± 0.08
ρ_0 in $1 \cdot 10^{13}\,\mathrm{m}^{-2}$	0.06 ± 0.01	0.06 ± 0.01	0.18 ± 0.01	4.35 ± 0.10	1.65 ± 0.04
$\upsilon = \frac{k_0}{k_0 + k_1\sqrt{\rho_\mathrm{ss}}}$	0.82 ± 0.03	0.65 ± 0.04	0.34 ± 0.03	0.27 ± 0.04	0.57 ± 0.07
$\lambda_\mathrm{f}\sqrt{\rho_\mathrm{ss}}$	2.23 ± 0.26	2.49 ± 0.29	1.45 ± 0.09	1.52 ± 0.23	1.03 ± 0.10

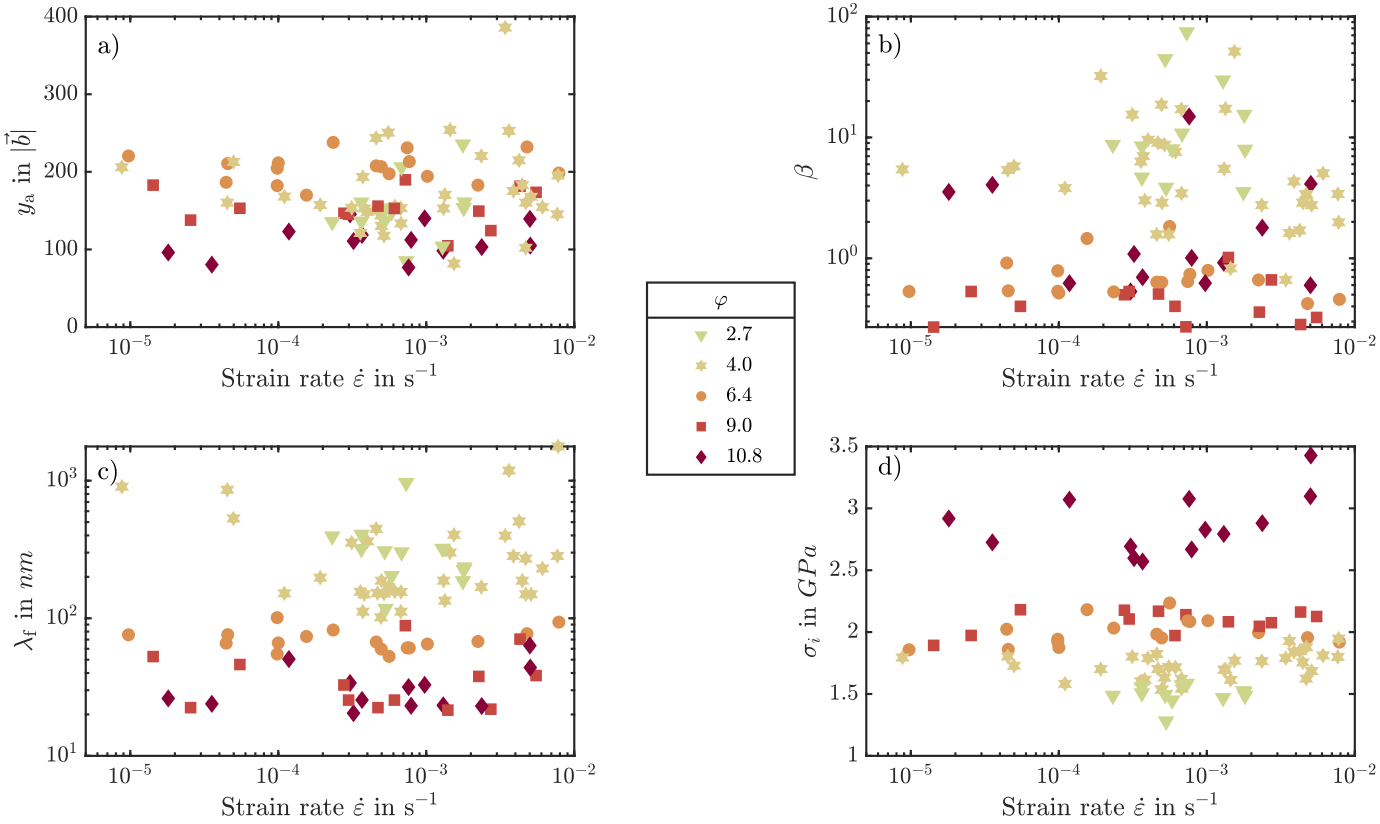

Figure 8.4: Dependence of the annihilation length y_a (a), the coefficient β (b), the spacing between fixed obstacles λ_f (c) and the internal stress σ_i (d) on the strain rate $\dot{\varepsilon}$ extracted from fits of the modified Kocks-Mecking model to experimental true stress-true plastic strain curves (see figure 8.3).

As explained in section 4.2.2.1.2, literature (see e.g. [128, 274]) predicts a pronounced strain-rate sensitivity of the recovery coefficient k_2, see equation (4.17). See equation (4.18) for the conversion factor between k_2 and y_a. The true strain-rate sensitivity n' characterising the strain-rate dependence of the recovery coefficient is the sum of the instantaneous strain-rate sensitivity m and the strain-rate exponent n of the saturation stress σ_∞ [275]:

$$n' = n - m \tag{8.7}$$

where n' : Strain-rate sensitivity of the recovery coefficient (see equation (4.17))
$n = \frac{d \ln \sigma_\infty}{\partial \ln \dot{\varepsilon}_{\mathrm{pl}}}$: Strain-rate exponent of the saturation stress (see equation (4.6)
m : Instantaneous strain-rate sensitivity

The instantaneous strain-rate sensitivity can be determined in strain-rate jump experiments (see figure 8.2 and section 7.1.3). The strain-rate exponent of the saturation stress was determined by applying equation (8.1) to the saturation stress. A plot of σ_∞ as a function of the plastic strain rate can be found in section B.1.4 in the appendix. The resulting values for n' and n are listed in table 8.3.

Table 8.3: Measured and calculated strain-rate sensitivity of the recovery coefficient. The calculated values for n' are the sum of the instantaneous strain-rate sensitivity (from strain-rate jump experiments) and the strain-rate sensitivities extracted from the evolution of σ_∞ and the ultimate tensile strength.

φ	n'	m	$n_{\sigma_\infty} = \frac{\partial \ln \sigma_\infty}{\partial \ln \dot{\varepsilon}_{\mathrm{pl}}}$	$n_{\mathrm{R_m}} = \frac{\partial \ln R_{\mathrm{m}}}{\partial \ln \dot{\varepsilon}_{\mathrm{pl}}}$	$n'_{\sigma_\infty} = n_{\sigma_\infty} - m$	$n'_{\mathrm{R_m}} = n_{\mathrm{R_m}} - m$
2.7	-0.078 ± 0.268	0.014 ± 0.001	-0.186 ± 0.783	0.017 ± 0.005	-0.200 ± 0.842	0.003 ± 0.001
4.0	-0.006 ± 0.065	0.022 ± 0.001	0.195 ± 0.165	0.019 ± 0.004	0.173 ± 0.147	-0.003 ± 0.001
6.4	-0.003 ± 0.029	0.011 ± 0.001	0.022 ± 0.106	0.011 ± 0.001	0.011 ± 0.053	0.001 ± 0.001
9.0	0.007 ± 0.057	0.008 ± 0.001	-0.006 ± 0.080	0.006 ± 0.003	-0.014 ± 0.187	-0.002 ± 0.001
10.8	-0.034 ± 0.007	0.006 ± 0.001	0.054 ± 0.329	0.004 ± 0.013	0.048 ± 0.293	-0.002 ± 0.007

As the results in table 8.3 show, the strain-rate sensitivity calculated from the strain-rate dependence of the saturation stress are not reliable due to their high variation, which translates into a high level of uncertainty. Using the ultimate tensile strength as a proxy, the expected strain-rate sensitivity of the recovery coefficient can be estimated. The low values of $|n'_{\mathrm{R_m}}| \leq 0.03$ demonstrate that a low strain-rate sensitivity of the recovery coefficient could be expected in the first place[4]. This result can be seen as a sanity check for the strain hardening modelling. A derivation explaining why the ultimate tensile strength can be used as proxy for σ_∞ is also given in section B.1.4 of the appendix.

8.2.2 Internal stresses

As shown in table 8.2, the mean internal stress in the tungsten wires increases monotonically with increasing accumulated drawing strain. Upon comparison, one finds that the mean internal stress reaches values of 86 % to 97 % of the respective true yield stress σ_y, which are very high values[5]. According to Follansbee [276] and Kocks & Mecking [119], the internal stress can have its origin in friction stresses, back stresses and Orowan stresses or can be caused by secondary particles and/or impurities. Due to the similar impurity content in the wires contained in the investigated wire series, the influence of different impurity levels on the internal stress can be neglected. The arrangement and number of potassium bubbles however changes due to the wire drawing process:

[4] Note that $n'_{\mathrm{R_m}}$ is illustrated graphically as the difference between $n_{\mathrm{R_m}}$ and m in figure 8.2.
[5] The high values of σ_i when compared to the yield strength will be discussed again in the following section.

The potassium-filled reservoirs get elongated during deformation and dynamically decompose into strings of bubbles [152]. Thus, wires with a higher accumulated drawing strain contain more but smaller and more finely distributed bubbles. Hence, it can be expected that the interaction between dislocations and potassium bubbles is more pronounced in wires with a higher accumulated drawing strain. Furthermore, the athermal stress component (see equation (4.3)) is expected to increase with increasing accumulated drawing strain (see section 8.6) due to the decrease in grain width (see section 8.4.2.2). Thus, the increase of the athermal stress additionally increases the internal stress, which is in line with its evolution with φ (see section 8.6). Hence, the increase in internal stress with φ can be explained when considering the distribution of potassium bubbles and the athermal stress component. Based on the current model, it is however very difficult to assess which process is most significant for the increase of the internal stress. Some ideas on a systematic study of the internal stress will therefore be discussed in section 10.

8.2.3 Evolution of the dislocation density during cold working

As discussed in section 4.2.2.1, the Kocks-Mecking model assumes that the flow stress evolves from an initial value towards a certain saturation value [119]. Accordingly, the dislocation densities corresponding to these two conditions can be determined using the results of the strain hardening analysis. On the one hand, the steady-state value of the dislocation density,

$$\rho_{\mathrm{ss}} = \lim_{\sigma \to \sigma^{+}} \rho = \lim_{\varepsilon_{\mathrm{pl}} \to \infty} \rho$$

can be calculated using the evolution equation introduced in section 4.2.2.1 (cf. equation (4.16)):

$$\frac{\partial \rho}{\partial \varepsilon} = 0 \iff k_0 + k_1 \sqrt{\rho} - k_2 \rho = 0.$$

Solving for the steady-state dislocation density yields the following expression for the steady-state dislocation density

$$\rho_{\mathrm{ss}} = \frac{k_1 + \sqrt{k_1^2 + 4\, k_0\, k_2}}{2\, k_0} \tag{8.8}$$

where ρ_{ss} : Steady-state dislocation density
k_0 : Coefficient characterising the storage of dislocations at fixed obstacles
k_1 : Coefficient characterising the storage of dislocations at movable obstacles
k_2 : Recovery coefficient

The steady-state dislocation density calculated for every tensile test performed on a drawn tungsten wire in the course of this study is shown in figure 8.5.

Judging from equation (8.8), the steady-state dislocation density should depend slightly weaker on the strain rate as the recovery coefficient. Since it was however already explained why k_2 has no or a very low strain-rate sensitivity (see section 8.2.1), it is not surprising that the steady-state dislocation density does not show a significant strain-rate sensitivity.
Besides the steady-state dislocation density, the dislocation density at the beginning of strain hardening, i.e. at $\sigma = \sigma_{\mathrm{y}}$, ρ_0, is accessible. Using equation (4.13), it can be determined as follows:

$$\rho_0 = \left(\frac{\sigma_{\mathrm{y}} - \sigma_{\mathrm{i}}}{M_{\mathrm{T}}\, \alpha\, \mu\, b} \right)^2 \tag{8.9}$$

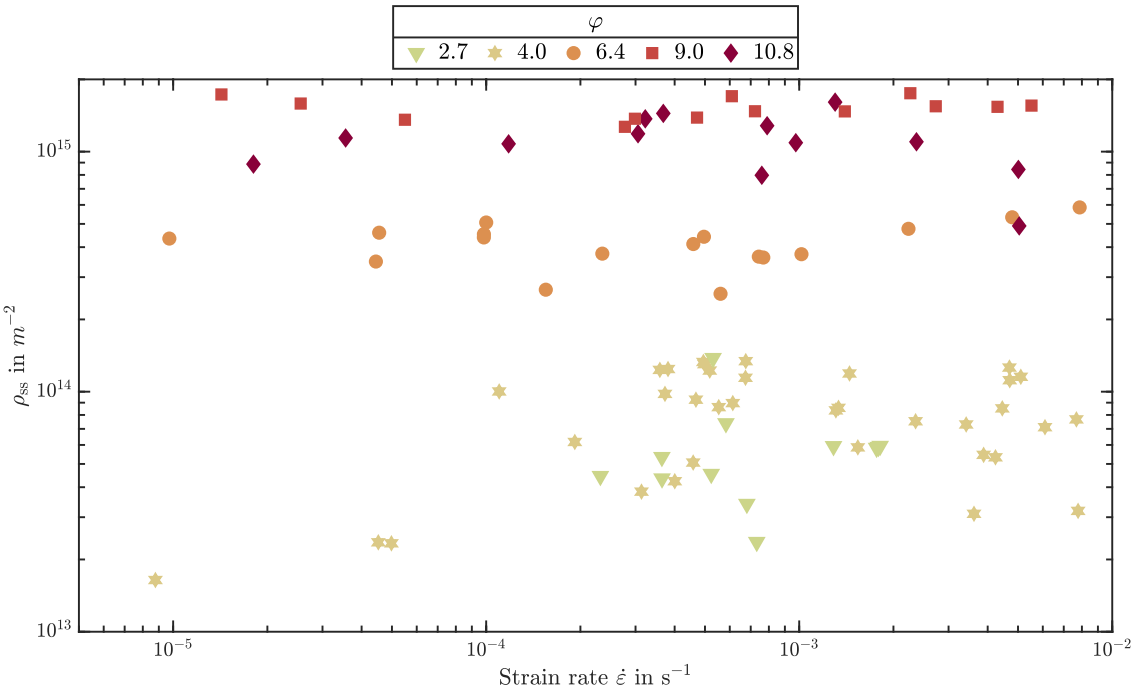

Figure 8.5: Steady-state dislocation density as a function of the strain rate for drawn tungsten wires with different accumulated drawing strain. Note that the uncertainty of ρ_{ss} is smaller than the size of the symbols.

where
ρ_0 : Initial dislocation density
σ_y : True yield stress
σ_i : Internal stress
$M_T = \sqrt{6}$: Taylor factor
α : Interaction coefficient
μ : Shear modulus
b : Norm of the Burgers vector

The mean initial dislocation density is plotted alongside the mean steady-state dislocation density in figure 8.6.

It is apparent from figures 8.5 and 8.6, that both the initial and the steady-state dislocation density increase with increasing accumulated drawing strain, up to a value of $\varphi = 9.0$. Both variables decrease if φ increases further. As a sanity check, the initial dislocation density can be compared to the redundant dislocation densities[6] obtained from XRD measurements (see section 7.2.4). Upon comparing, it turns out that $M_W^2\,\rho$ is two to three orders of magnitude higher than the initial dislocation density, although the values should be quite similar since there should be no significant difference[7] in ρ between the unstressed sample that was analysed using XRD and the stressed sample at the end of the elastic regime[8], i.e. at $\sigma = \sigma_y$. Thus, it can be concluded, that the internal stresses obtained from the modelling attempts turn out to be too high and the initial dislocation density is underestimated. This effect could not be suppressed during fitting, since no physically sound reason was found to decrease the upper limit (σ_y) for the internal stress.

[6]For the sake of comparison, the Wilkens factor was assumed to be $M_W \approx 1$.
[7]Since M_W does not vary by two orders of magnitude, it can also not explain the observed discrepancies.
[8]It can be assumed that the dislocation density changes for $\varepsilon_{pl} > 0$, i.e. at stresses above the true yield strength.

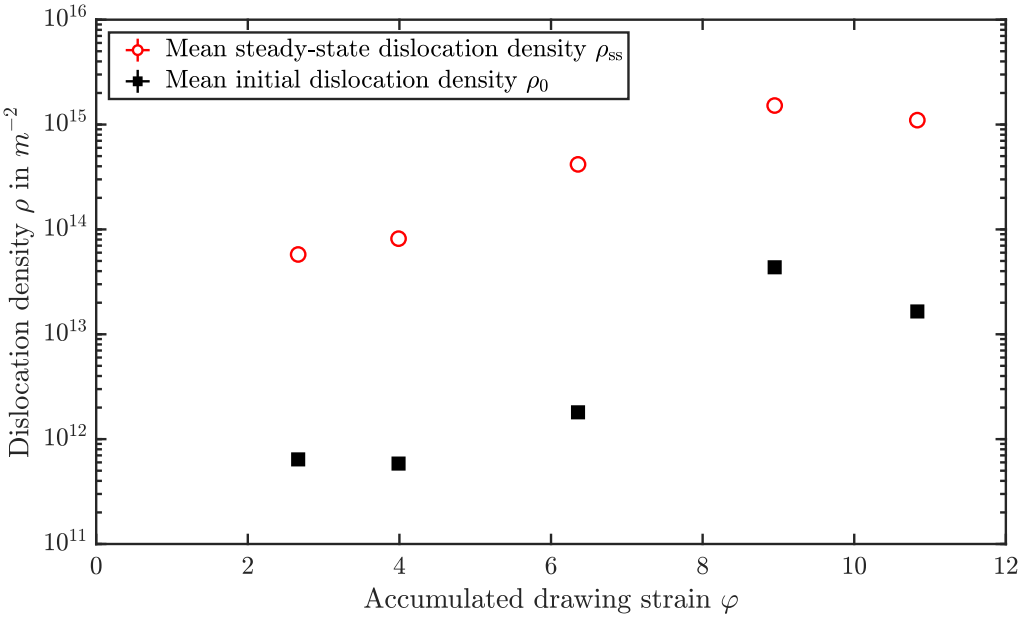

Figure 8.6: Mean steady-state dislocation density ρ_{ss} (red empty circles) and initial dislocation density ρ_0 (black squares) as a function of the accumulated drawing strain of drawn tungsten wires. Note that the uncertainty of the values is low enough to be hidden by the symbols.

8.2.4 Accumulation of dislocations

As discussed in section 4.2.2.1, the Kocks-Mecking model incorporates two different obstacles for dislocations, namely forest dislocations and fixed obstacles like grain boundaries or secondary particles. The mean spacing between fixed obstacles is shown in figure 8.7.

It is apparent that the mean spacing between fixed obstacles is roughly equal for the two wires with the largest diameters, and decreases monotonically if the accumulated drawing strain increases further. Recalling the microstructure of tungsten wires (see section 5.1.4), the two potential fixed obstacles in tungsten wire are grain boundaries and potassium bubbles. According to literature [23, 152, 277], K bubbles are found predominantly at grain boundaries or in the grain interior. Thus, if potassium bubbles located in the grain interior would additionally contribute to the accumulation of dislocations, the mean spacing between fixed obstacles λ_f would be lower than the grain width. Figure 8.7 however reveals, that the spacings between fixed obstacles line up well with the mean grain width. The only exception is the wire with $\varphi = 4.0$, which shows a spacing between fixed obstacles that is roughly 1.6 to 2.2 times higher than the mean grain width determined in the wire centre and edge, respectively. As considerations on the relation between the mean free path of dislocations and the grain width in the appendix (see section B.2.3) show, the factor between λ_f and $\langle w \rangle$ can be explained by the geometry of slip. Thus, it can be concluded that the main fixed obstacles which contribute to dislocation accumulation during work hardening in tungsten wires are grain boundaries and that potassium bubbles mainly add to the increase of the internal stress σ_i (see section 8.2.2).

The accumulation of dislocations at forest dislocations can be analysed using the mean values listed in table 8.2: β can be interpreted as the number of forest dislocations a dislocation can cross before it is stored at a forest dislocation. In this framework, the decrease of β with increasing accumulated drawing strain can be understood: While up to 24 dislocations can be crossed by a

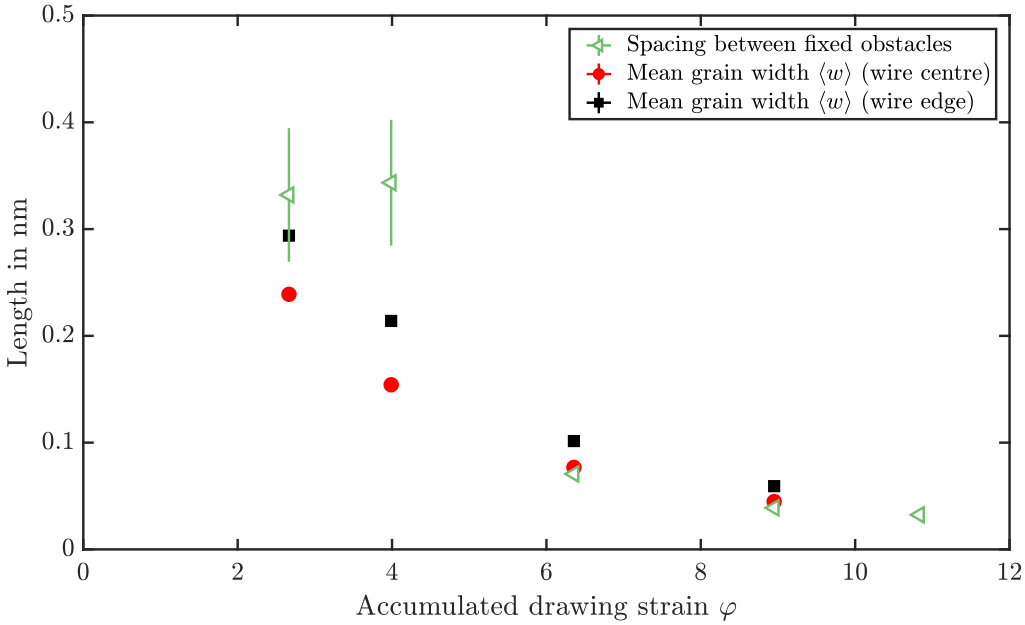

Figure 8.7: Mean spacing between fixed obstacles λ_f in tungsten wires with different accumulated drawing strains determined from tensile tests at room temperature (green triangles). For comparison, the mean grain width determined from individual EBSD orientation maps located in the centre and edge region of the wires are drawn as red and black circles alongside λ_f, respectively. The errors bars are hid by the symbols due to the low level of uncertainty.

dislocation in the thickest wire investigated, this number drops to less than 1 at $\varphi > 4.0$. This trend is most likely linked to a change in the arrangement of forest dislocations with increasing accumulated drawing strain. The reason for the increase of β for the thinnest wire investigated, and its implications will be discussed in section 8.7.1.2.

The prevailing storage process for dislocations can be identified by comparing the storage at fixed obstacles (parameter: k_0) and the storage at (forest) dislocations (parameter: $k_1\sqrt{\rho}$). As an approximation for large strains ($\varepsilon_{pl} \to \infty$), for which $\rho = \rho_{ss}$, the ratio

$$\upsilon = \frac{k_0}{k_0 + k_1\sqrt{\rho_{ss}}} \tag{8.10}$$

where υ : Dimensionless parameter characterising the fraction of dislocations stored at fixed obstacles during work hardening
k_0 : Coefficient characterising the storage of dislocations at fixed obstacles
k_1 : Coefficient characterising the storage of dislocations at forest dislocations
ρ_{ss} : Steady-state dislocation density

can be used to investigate the prevalent storage mechanism. If storage is dominated by the fixed obstacles and $k_0 \gg k_1\sqrt{\rho_{ss}}$, υ approaches 1. If $k_0 \ll k_1\sqrt{\rho_{ss}}$, υ approaches 0 and the storage is dominated by the accumulation of dislocations at forest dislocations. The mean values of υ listed in table 8.2 show a clear trend up to an accumulated drawing strain of $\varphi = 9.0$: For thick wires, the storage is dominated by the accumulation at fixed obstacles, i.e. grain boundaries. The higher the accumulated drawing strain (and the dislocation density) becomes, the more the significance

of storage at forest dislocations increases. For the thinnest wire, both accumulation mechanisms seem to balance. The discontinuation of the trend by the thinnest wire is also reflected in the evolution of other variables characterising the strain hardening behaviour of this wire. The ratio of the mean distance between fixed obstacles λ_f and the mean spacing between dislocations at $\rho = \rho_{ss}$, $\lambda\,{\rho_{ss}}^{-0.5}$, is also listed in table 8.2. The evolution of the mentioned ratio is in line with the other findings on the strain hardening behaviour: The spacing between fixed obstacles, in the case of tungsten wires mainly grain boundaries, is larger than the spacing of dislocations in thick wires and decreases with increasing accumulated drawing strain until the spacing of dislocations and fixed obstacles is roughly equal in the thinnest wire. This trend is linked to the increase in dislocation density with increasing accumulated drawing strain.

8.2.5 Prediction of the necking strain

Up to $\varepsilon \leq \varepsilon_u$, the deformation in a sample stressed by uniaxial tension is uniform. At $\varepsilon = \varepsilon_u$, plastic instabilities develop, i.e. the plastic deformation concentrates in a small region of the sample, the so-called *necking region*. The strain at which plastic instability sets in can be predicted, if the strain hardening behaviour is known. The historically first necking criterion was developed by Considère [278]:

$$\frac{\partial \sigma}{\partial \varepsilon} = \sigma \tag{8.11}$$

where σ : True stress
ε : True strain

Incorporating the strain-rate sensitivity, Hart [279] derived a modified criterion to predict plastic instability of strain-rate sensitive materials ($m \neq 0$):

$$\frac{\partial \sigma}{\partial \varepsilon} = \sigma\,(1 - m) \tag{8.12}$$

where σ : True stress
ε : True strain
m : Strain-rate sensitivity

Following the considerations of Yasnikov et al. [280], the strain hardening model is used to predict the necking strain $\varepsilon_{N,pred}$: Since equation (8.4) is monotonous, positive and differentiable with respect to the stress σ, the strain-hardening rate is accessible via:

$$\theta = \sigma'(\varepsilon) = \frac{1}{\varepsilon'(\sigma)} \tag{8.13}$$

where θ : Strain-hardening rate
σ : True stress
ε : True strain

With this, the equations (8.11) and (8.12) can be inverted as follows:

$$\frac{\partial \varepsilon}{\partial \sigma} = \begin{cases} \frac{1}{\sigma} & \text{Considère criterion} \\ \frac{1}{\sigma\,(1-m)} & \text{Hart criterion} \end{cases} \tag{8.14}$$

where σ : True stress
ε : True strain
m : Strain-rate sensitivity

Thus, upon differentiating equation (8.4) with respect to σ and plotting it as a function of $\varepsilon_{\mathrm{pl}}$, the intersection of $\partial\varepsilon_{\mathrm{pl}}/\partial\sigma$ and $1/\sigma$ (Considère criterion) or $1/\sigma\,(1-m)$ (Hart criterion) yields the (plastic) necking strain and hence the necking stress. The outlined procedure is exemplarily illustrated in figure 8.8. The predicted and experimentally measured necking strains are compared in figure 8.9. As the figure illustrates, the model underestimates the experimentally determined uniform elongations. Fitting a linear function to the data set reveals that the predicted uniform elongations in average take values of 73 % of $\varepsilon_{\mathrm{u,exp}}$. This kind of underestimation is also found in literature [280, 281] and points to the fact that there is still room for optimising the strain hardening model. Note that due to the low strain-rate sensitivity of the tungsten wires (see figure 8.2), the differences between the Hart and the Considère criterion are marginal. The discussion of the influence of the variables of the used KM model in section 8.7.1.2 shows how the microstructure-informed nature of the applied strain hardening model can explain the evolution of the uniform elongation of drawn tungsten wires with accumulated drawing strain (see figure 8.1).

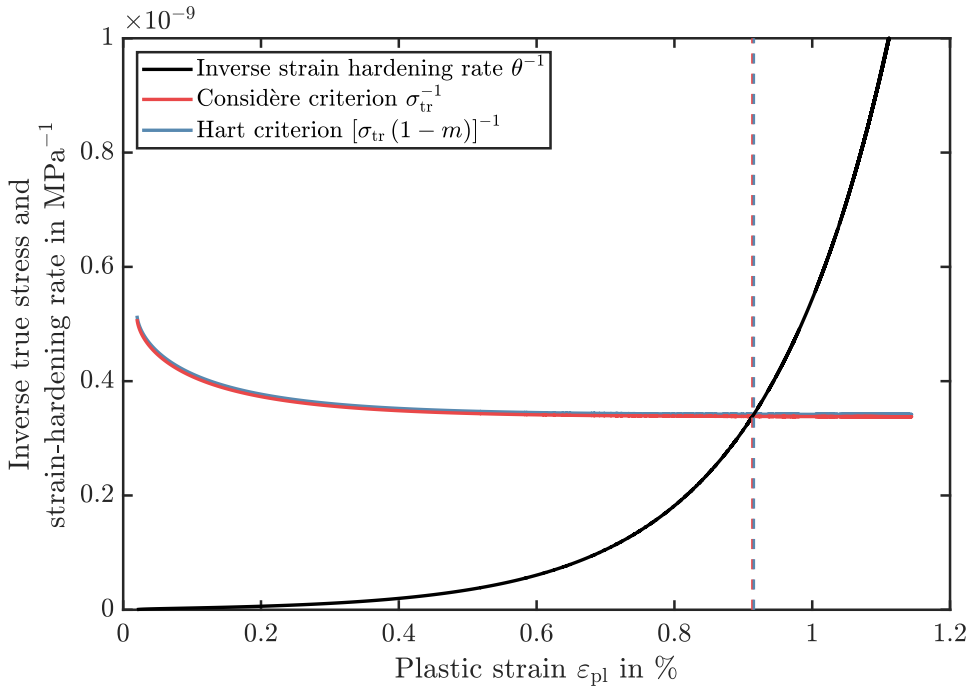

Figure 8.8: Procedure to predict the necking strain based on equation (8.4): The necking strain follows from the intersection of the inverse strain hardening rate (black line) and the inverse of the true stress for the Considère criterion (red line) or the inverse of true stress multiplied by $(1-m)$ for the Hart criterion (blue line). The predicted uniform elongations are drawn as dashed vertical lines. The experimental data were extracted from the uniaxial tensile test performed on a drawn tungsten wire with a diameter of 950 µm at a strain rate of $2.3 \cdot 10^{-4}\,\mathrm{s}^{-1}$.

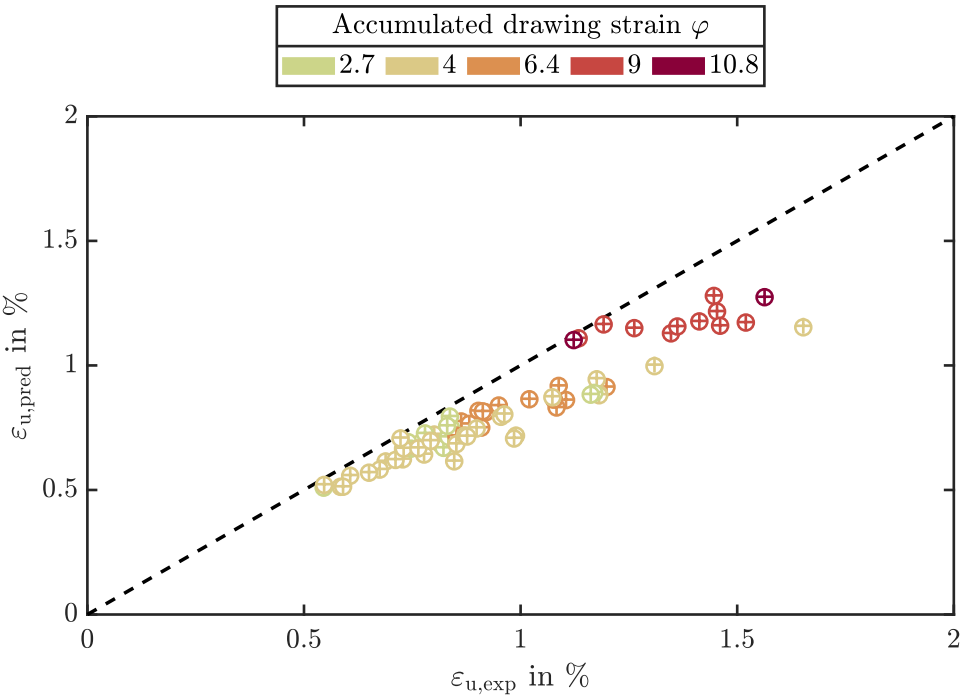

Figure 8.9: Comparison of the predicted (ordinate) and experimentally measured uniform elongation ε_u (abscissa). Uniform elongations predicted by the Hart criterion are drawn as circles, while those predicted by the Considère criterion are drawn as crosses. A line passing through the origin of the coordinate system with slope 1 is drawn in order to illustrate a potentially perfect agreement between $\varepsilon_{u,exp}$ and $\varepsilon_{u,pred}$. The link between the symbol colour and the accumulated drawing strain of the wire can be found in the legend.

8.2.6 Concluding remarks concerning the strain hardening behaviour of drawn tungsten wires

The agreement between modelled and experimentally determined stress-strain curves (and work hardening behaviour) of tungsten wires with $2.7 \leq \varphi \leq 10.8$ was found to be excellent (see figure 8.3). Thus, although there are some minor inconsistencies which call for a future optimisation of the used model, the conclusions drawn from the evolution of the individual microstructure-informed variables are robust. The work hardening behaviour can be summarized as follows:

- Recovery takes place by annihilation of screw dislocation segments, facilitated by cross-slip.
- The distance of fixed obstacles at which dislocation storage occurs decreases with increasing accumulated drawing strain. This trend is shared with the mean grain width, indicating that fixed obstacles for dislocation storage are mainly grain boundaries.
- With increasing accumulated drawing strain, the storage of dislocations at forest dislocations gains importance and prevails over the storage at fixed obstacles. This trend can be linked with the increase of dislocation density with increasing accumulated drawing strain.

Furthermore, it could be shown that the applied strain hardening model can be used to predict the necking strain with acceptable accuracy. A specific observation, namely the disruption of trends observed for some averaged variables by the thinnest wire investigated ($\varphi = 10.8$), calls for a separate assessment. Two possible explanations can be discussed for the mentioned phenomenon: On the one hand, the non-continuation of trends could be due to the high scatter in the stress-strain curves (see figures 7.2 and 8.3) for the thinnest wire. On the other hand, the observed anomalies

could point to the fact that the work hardening in the respective wire does really deviate from the one of the thicker wires. In this case, the strain hardening in the thinnest wire is characterised by a storage of dislocations that is again more strongly dominated by the accumulation at fixed obstacles when compared to thicker wires and a higher number of dislocations that can be crossed before the dislocation is stored (cf. table 8.2). Since the most strongly cold-worked wire was not investigated using XRD, its redundant dislocation density and the evolution of $\rho_{\mathrm{red}} M_{\mathrm{W}}^2$ are not known. Thus, since the dislocation density influences many values characterising the work hardening behaviour (ρ_{ss}, υ) significantly, its measurement would help to decide whether the peculiar behaviour of the thin wires is due to different deformation mechanism or is an artefact of the sensitive nature of these wires. A study of the strain hardening behaviour of the thinnest wires after different annealing treatments which slightly alter the wires' microstructure could help to understand better the work hardening of wires with a diameter of 16 µm. The behaviour of the thinnest wire is however intrinsically sound since the prediction of the necking strain based on the results of the strain hardening model agrees with the experimentally determined values, see section 8.7.1.2.

8.3 Evolution of crystallographic texture

8.3.1 Misalignment correction applied to TCS orientation maps

Any misalignment of the TCS sample in the SEM or embedding can be spotted and corrected using the strong ⟨110⟩ fibre texture component of the drawn tungsten wires. In a 110 pole figure with the normal direction parallel to the wire axis, the ⟨110⟩ fibre texture shows up in the form of a strong centre peak and an additional circular ring in a certain radial distance from the centre. If the drawing axis $\overrightarrow{D}$ and the $\overrightarrow{z}$ direction of the orientation map coincide, the peak in the 110 pole figure is perfectly centred (see right pole figure in figure 8.10) and no misalignment correction is needed. In the case of a slight misalignment of the sample in the SEM and/or the embedding, the peak is off-centre (see left pole figure in figure 8.10). Using rotations of the measured orientations around the $\overrightarrow{x}$ and $\overrightarrow{y}$ axis, the peak can be brought to the centre. Thus, all orientation maps acquired from TCS samples using EBSD were corrected for any misalignments using the aforementioned procedure.

8.3.2 Qualitative assessment

The qualitative evolution of the crystallographic texture can be monitored using pole figures. Since the deformation during wire drawing is radially heterogeneous, the orientation data used as basis for the pole figures were subdivided:

$$\begin{aligned} \text{Wire centre}: &\quad r \leq 0.4\, r_{\mathrm{W}} \\ \text{Wire edge}: &\quad r > 0.4\, r_{\mathrm{W}}. \end{aligned}$$

Here, r is the distance of a pixel from the wire centre and $r_{\mathrm{W}} = 0.5\, d$ is the wire radius. The choice of $0.4\, r_{\mathrm{W}}$ as limit is justified in section 8.3.3. The 110 pole figures calculated from the edge and centre region of drawn tungsten wires are shown in figures 8.11 and 8.12, respectively.

Initially focusing on the pole figures calculated from orientations determined from the central wire regions, one finds the expected pronounced centre peak that is characteristic for the ⟨110⟩ fibre texture. With increasing accumulated drawing strain, the width of the centre peak decreases while its pole density increases. The circular ring surrounding the centre peak constricts simultaneously.

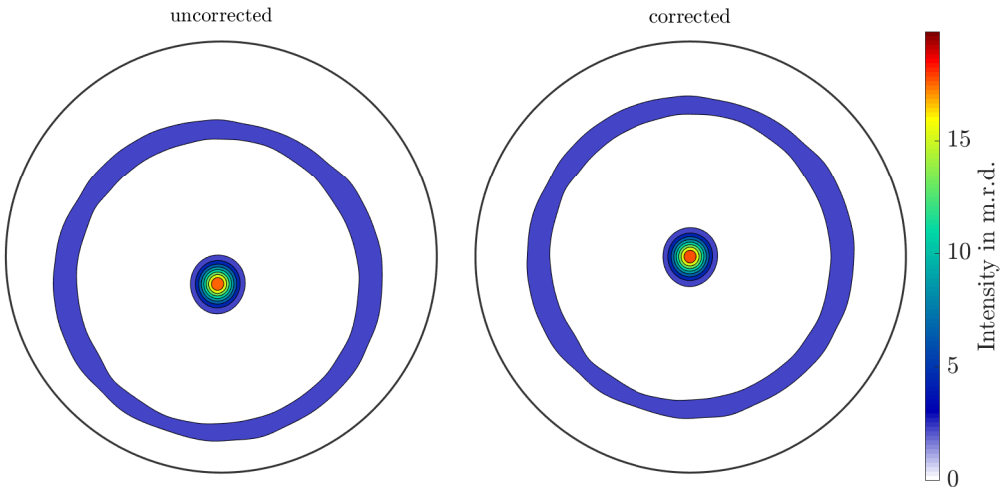

Figure 8.10: Comparison of 110 pole figures calculated from orientations uncorrected (left) and corrected (right) for misalignment between the wire drawing axis and the $\overrightarrow{z}$ direction of the acquired section.

For the undrawn rod and the wire with $\varphi = 0.5$, the circular ring moreover contains a structure that exhibits a six-fold symmetry. The appearance of the 110 pole figures in the wire edge region of the thicker wires is similar, but the six-fold symmetry can still be observed for the wire representing the second drawing stage ($\varphi = 1.4$). The trend of increasing pole density for the centre peak is not as monotonous as in the centre region, since the thinnest wire shown ($\varphi = 9.0$) investigated using EBSD exhibits a lower central pole density than the next-thicker wire ($\varphi = 6.4$).

8.3.3 Quantitative assessment

In order to quantitatively analyse the sharpness (or strength) of the $\langle 110 \rangle$ fibre texture component of tungsten wires, the angle between $\langle 110 \rangle$ and the wire drawing axis[9] $\overrightarrow{D}$ is defined as misalignment angle $\zeta_{\langle 110 \rangle | \overrightarrow{D}}$. In this respect, a misalignment angle of 0° means that $\langle 110 \rangle$ is parallel to $\overrightarrow{D}$. Determining $\zeta_{\langle 110 \rangle | \overrightarrow{D}}$ in different regions of a wire allows for a spatially resolved texture analysis. Taking the radial symmetry of a wire into account, the misalignment angle was averaged over rings with a certain radius, distance from the wire centre and defined radial thickness in order to increase the statistical significance of the analysis. Plotting the mean misalignment angle for a given radial distance r of the ring from the wire centre for all (misalignment-corrected) orientation maps, including the whole wire cross-section (see figure 7.7) yields the plot shown in figure 8.13. Note that only the texture of wires with $\varphi \leq 9.0$ could be quantified using the mentioned procedure, since EBSD orientation maps could not be acquired from the thinnest wire contained in the series ($\varphi = 10.8$). Some ideas for EBSD investigations of the thinnest wires will be presented and discussed in section 10.

The radial evolution of the misalignment angle between $\langle 110 \rangle$ and the wire axis (figure 8.13) can be divided into the two regions already mentioned in section 8.3.2: For $r < 0.4\, r_\mathrm{W}$, i.e. in the wire centre, a trend of lower misalignment angle for wires with higher accumulated drawing strains is apparent. The trend is not immaculate due to some overlap events and the inherent scatter of some wires. A saturation of $\bar{\zeta}_{\langle 110 \rangle | \overrightarrow{D}}$ for $r \leq 0.4\, r_\mathrm{W}$ and wires with $\varphi \geq 6.4$ is observed.

[9] By applying the correction method outlined in section 8.3.1 it is made sure that the wire drawing axis coincides with the $\overrightarrow{z}$ direction of the TCS orientation map

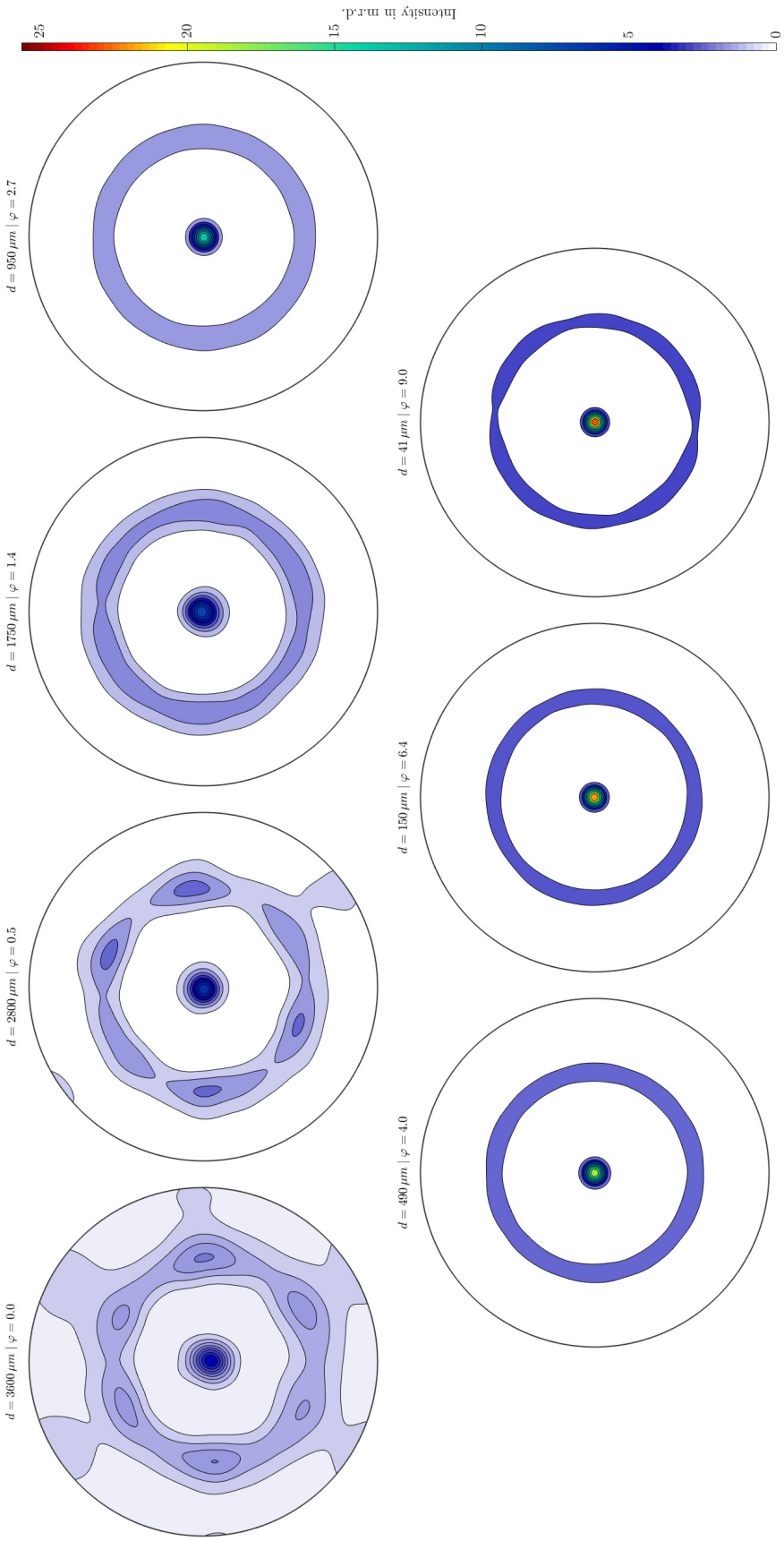

Figure 8.11: 110 pole figures of the **centre** region of representative orientation maps acquired from wires with diameters from 3.6 mm to 41 µm. The intensity of the poles is colour-coded using the colourbar at the right of the figure. The wire diameter and accumulated drawing strain of each wire is indicated above the respective pole figure.

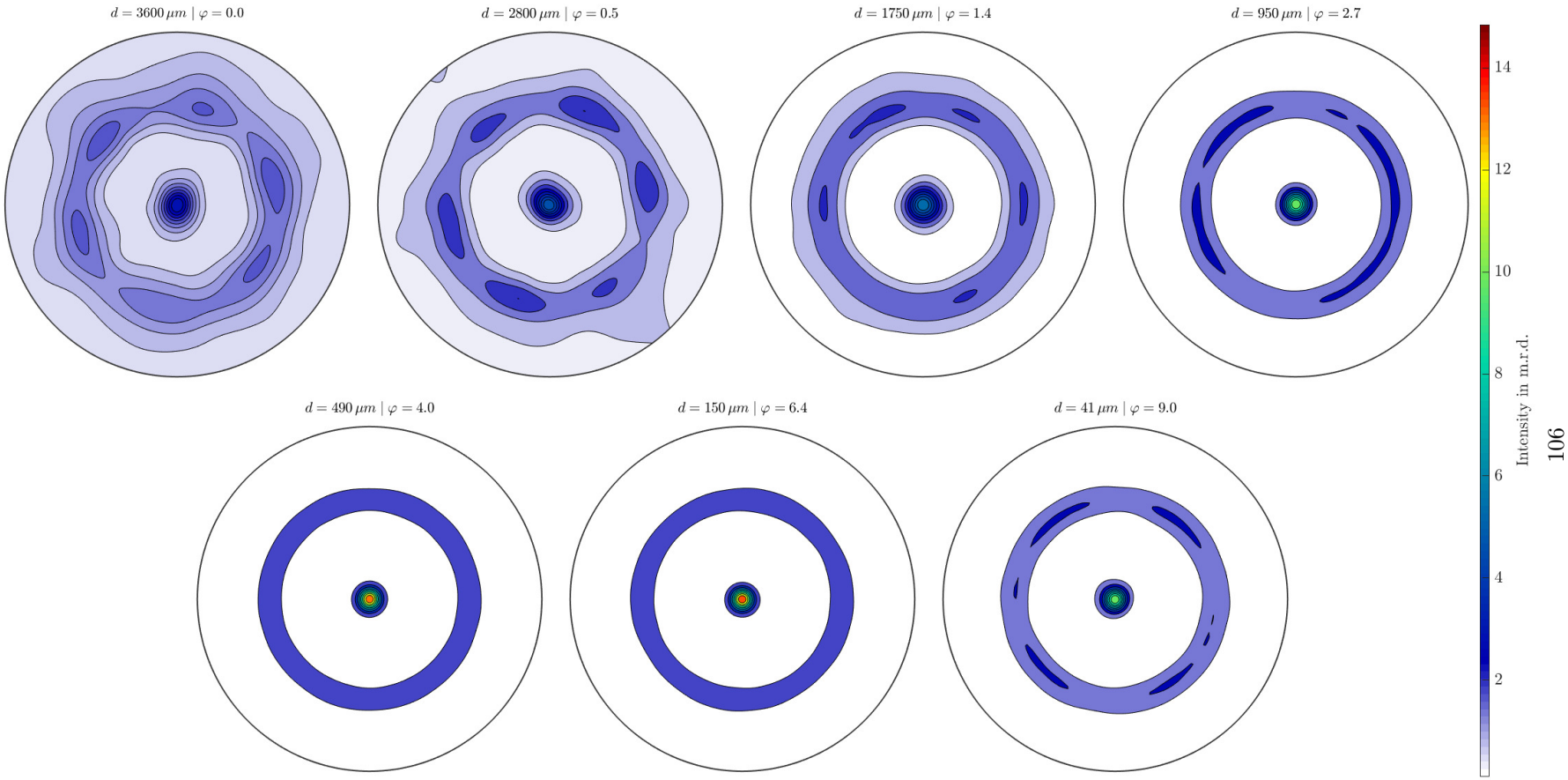

Figure 8.12: 110 pole figures of the **edge** region of representative orientation maps acquired from wires with diameters from 3.6 mm to 41 µm. The intensity of the poles is colour-coded using the colourbar at the right of the figure. The wire diameter and accumulated drawing strain of each wire is indicated above the respective pole figure.

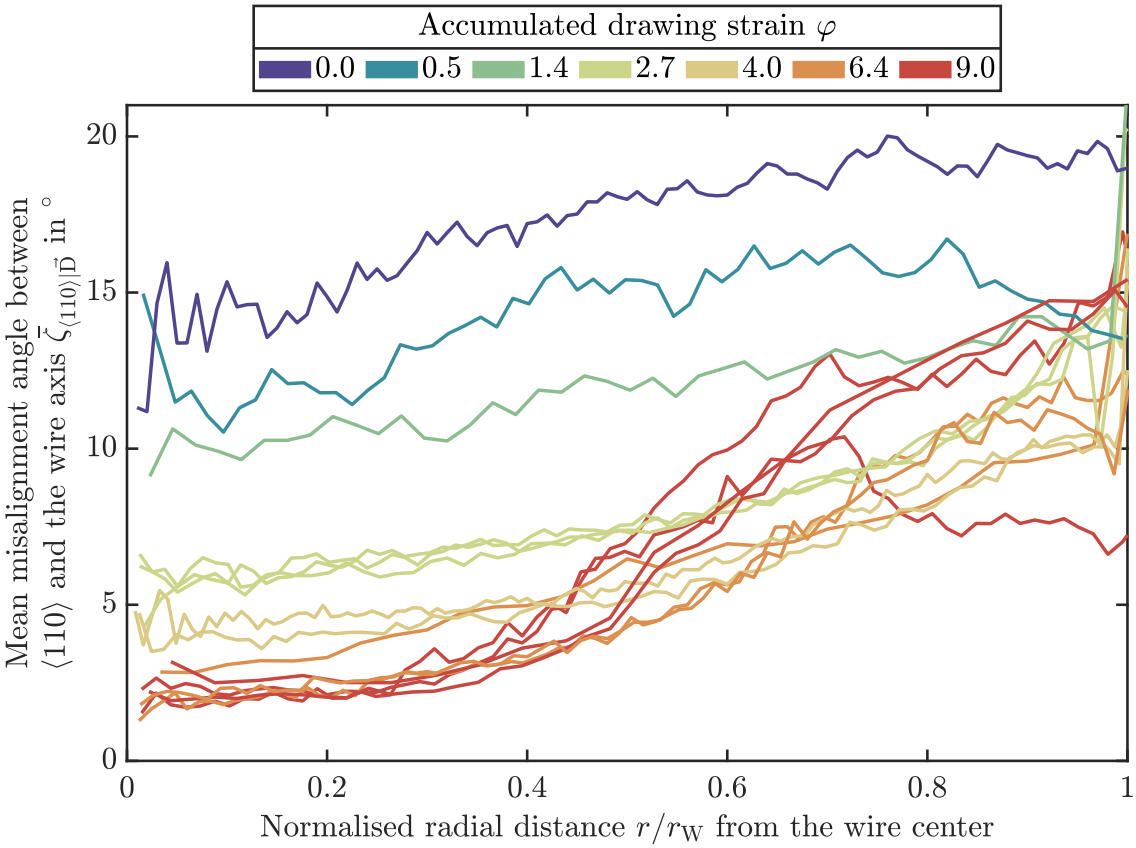

Figure 8.13: Mean inclination angle $\bar{\zeta}_{\langle 110\rangle|\vec{D}}$ between ⟨110⟩ and the wire drawing axis $\vec{D}$ as a function of the distance r of the evaluated pixel from the wire centre, i.e. $r = 0$ and $r = r_W$ representing the wire centre and edge, respectively.

In the wire edge, i.e. $r \geq 0.4\, r_W$, the link of lower misalignment angle for higher φ is much weaker if not completely lost (especially for wires with a high accumulated drawing strain). What can be seen for all wires is that towards the wire edge ($r \to r_W$) the mean misalignment angle between ⟨110⟩ and the drawing axis increases.

8.3.4 Evolution of crystallographic texture during wire drawing

As already mentioned in section 8.3.2, the swaged rod and the wire after the first drawing stage exhibit a six-fold symmetry in their 110 pole figure, as also observed by Ripoll & Očenášek [173]. This is probably due to the deformation during Kocks milling, which is performed after sintering and prior to swaging. The Kocks mill yields a deformation pattern with a six-fold symmetry [32]. It can hence be concluded that the texture of the two thickest wires investigated in this study still contains remnants of the milling texture. Since the deformation during Kocks milling is higher at the surface of the workpiece, remnants of the six-fold symmetry can be seen in the edge region of the wires up to higher accumulated drawing strain when compared to the centre region. The elongation of the workpiece during Kocks milling and swaging leads to the emergence of the central peak that is observed in the 110 pole figure of the rod with a diameter of 3.6 mm. Wires with diameters below 1750 µm show the characteristics of a ⟨110⟩ fibre texture in 110 pole figures. In order to quantitatively discuss the texture evolution, a lower misorientation angle $\bar{\zeta}_{\langle 110\rangle|\vec{D}}$ is interpreted as proof of a sharper ⟨110⟩ fibre texture. In this respect, the trend in the wire centre

is seen as a sharpening of the fibre texture with increasing accumulated drawing strain, which is in line with literature [169, 173, 176]. The reason for the formation and strengthening of the ⟨110⟩ fibre texture upon uniaxial tensile deformation lies in the deformation of the grains, as explained in section 5.1.3. In the edge region, frictional forces acting between the workpiece and the drawing die give rise to a multiaxial stress state [177]. This departure from simple uniaxial stress entails a deformation mechanism of the grains that is different from plane strain elongation, thus yielding a less perfect ⟨110⟩ fibre texture. The link between crystallographic texture and mechanical properties is touched upon in sections 8.7.4 and 10.

8.4 Evolution of the microstructure during wire drawing

8.4.1 Origin and evolution of pores in drawn tungsten wires

Using the open source image processing software ImageJ© [282], the porosity in tungsten wires was evaluated using micrographs with secondary electron contrast. By applying a suitable greyscale threshold, the pores are identified and evaluated. As a first order approach, an ellipse was fitted automatically to each pore in order to estimate its size. From this, the length of the major and minor axis of the fitted ellipse, the ratio between major and minor axis and the overall porosity, i.e. the area coverage of pores was determined. The results are shown in figure 8.14a. Note that all micrographs evaluated were taken from the wire centre of TCS samples.

It is apparent from figure 8.14a that up until $\varphi = 4.0$, the size of pores decreases, stagnates at a low value for $\varphi = 6.4$ and increases again for $\varphi = 9.0$. The order of magnitude of the pore size agrees well with the findings of Hoffmann & Wesemann [283] who also studied the evolution of porosity during the sintering, swaging and first drawing stages of tungsten wires. Wires with higher accumulated drawing strains show an increased size of pores. The pore aspect ratio, i.e. the ratio between major and minor axis, does not change significantly up until $\varphi = 9.0$. Only the thinnest wire investigated in the present study ($\varphi = 10.8$) shows a slight increase in pore aspect ratio. The porosity, which was determined as the ratio between the total area of pores and the total area of the image, seems to decrease or stagnate for $\varphi \leq 6.4$. The two thinnest wires show a strong increase in porosity. The radial distribution of porosity in the wires with $\varphi \geq 9.0$ was also evaluated from the SEM micrographs. The result is shown in figure 8.14b. The figure on the one hand proves that the pores are concentrated in a certain radial distance from the wire centre and illustrates the effect of further cold-working on the location of this "pore zone": The increase of φ from 9.0 to 10.8 moves the pore distribution closer to the wire centre. From a geometrical point of view, it would be expected, that the maximum of the distribution in the thinnest wire ($\varphi = 10.8$) would still lie at $r \approx 0.4\, r_{\mathrm{W}}$. Apparently, the increasing concentration of porosity in the wire centre is thus stronger than what would be expected when taking the geometrical transformation of the wire during the last drawing stage into account.

The porosity observed in drawn tungsten wires can be divided into two subgroups, depending on their origin: The pores in thick wires are most likely residual sintering pores or potassium bubbles, while the porosity in thinner wires develops as a consequence of the deformation mode of grains. After sintering, the wire contains some percent of closed porosity [32]. During swaging and milling, this porosity is reduced but does not vanish entirely [283]. Following the shape change of the workpiece, sintering pores as well as potassium bubbles are elongated during the working process. Due to the Plateau-Rayleigh instability [151], these elongated voids break down into rows of spherical pores/bubbles during static intermediate annealing at high temperatures or as a consequence of dynamical recovery during high-temperature deformation. Repeated deformation reduces the pore volume and size [283]. This theory fits the decrease of void size with increasing accumulated drawing strain, shown in figure 8.14a. A significant increase in porosity is observed

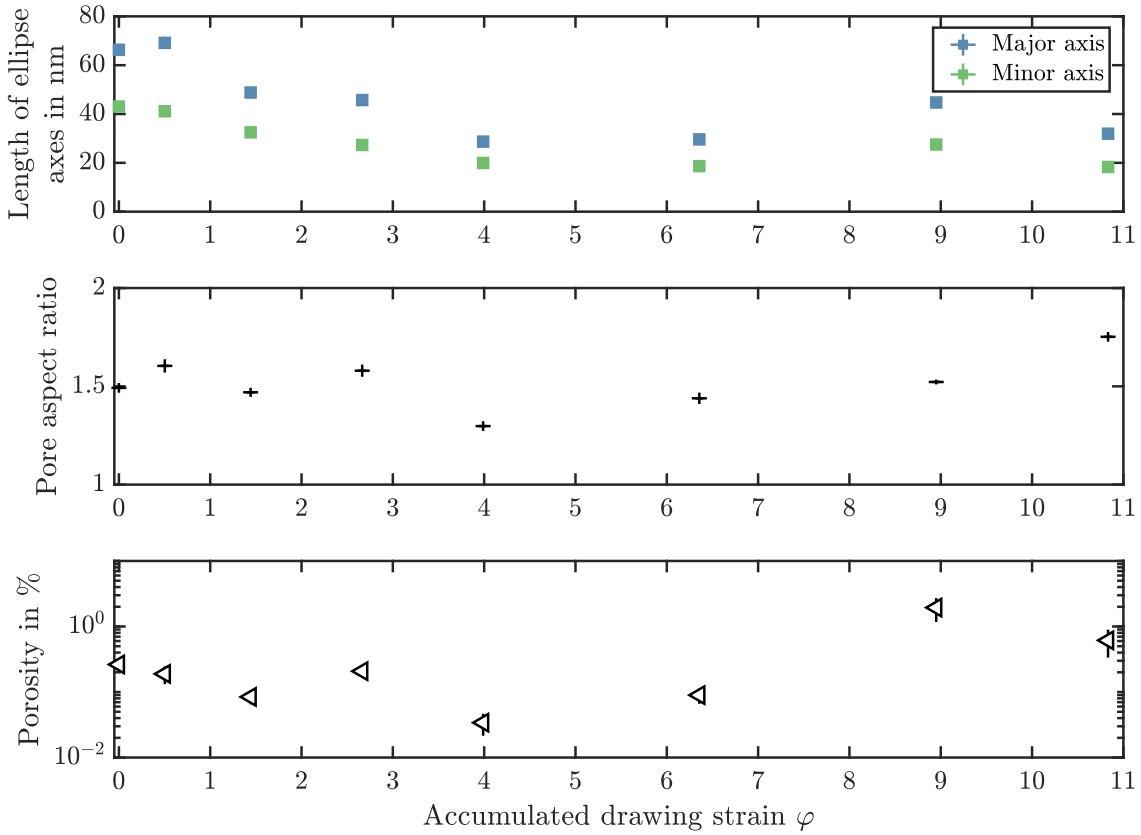

(a) Evolution of mean pore size, mean pore aspect ratio and overall cumulated porosity (area coverage of pores) in the centre region of tungsten wires as a function of their accumulated drawing strain. The error bar in the first subfigure is hidden by the corresponding symbol due to the low uncertainty.

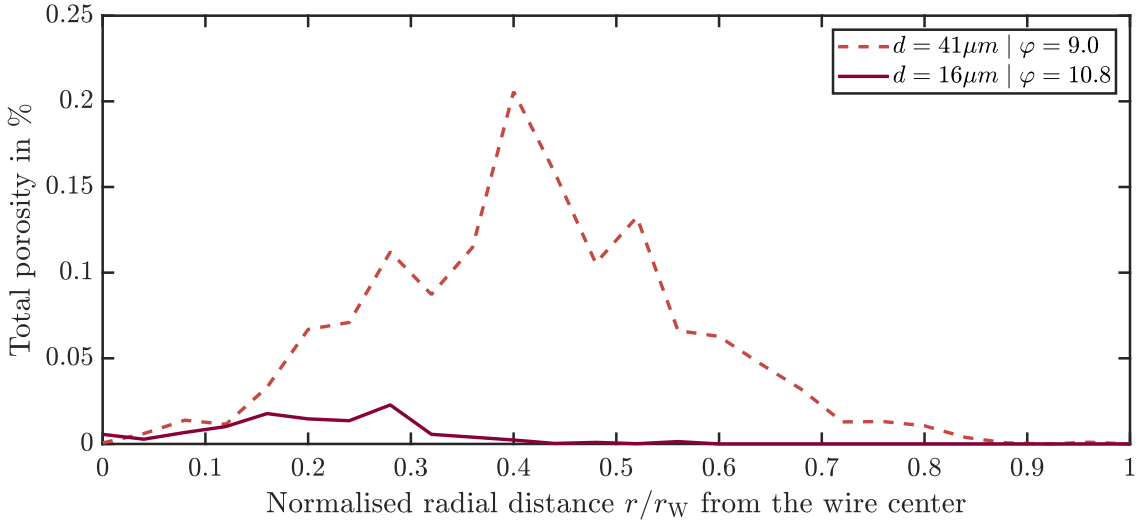

(b) Radial distribution of cumulated porosity (area coverage) in the centre of thin tungsten wires.

Figure 8.14: Evolution of pores in drawn tungsten wires.

if the wires exceed an accumulated drawing strain of 6.4. This porosity has to be different from sintering pores or potassium bubbles, since the sintering pores on the one hand should vanish if the working strain increases. The potassium bubbles on the other hand get smaller and more finely distributed [152, 277] if the wire thickness decreases as a consequence of working. In addition, the working process does not allow for the formation of new pores or potassium bubbles. Thus, the emergence of these pores, which was not yet reported in literature, has to have a different origin. The mode of deformation of grains in b.c.c. metals stressed by uniaxial tension[10] can be used as explanation: As first derived by Hosford in 1964 [170], grains in b.c.c. metals deform by plane strain elongation when loaded with uniaxial tensile stress. This leads to an alignment of a $\langle 110 \rangle$ axis with the stress axis (see section 8.3). In order to keep compatibility with neighbouring grains, the grains have to bend around the $\langle 110 \rangle$ axis. The new evidence gathered from the thin tungsten wires indicates that this bending seems to have a natural limit. If the drawing strain exceeds this limit, which seems to lie in a range of accumulated drawing strains of $6.4 < \varphi < 9.0$, the compatibility between grains cannot be maintained. Thus, pores form between the grains. This hypothesis would also explain why the pores are found close to the wire centre: During wire drawing, the stress state in the wire centre is defined by a pure tensile stress[11] [32], while friction between the die and the wire as well as the geometrical deflection of the wire in the die gives rise to shear forces in wire regions close to the surface. Hence, the deformation of the grains in the near-surface region of the wire deviates from plane strain elongation, an observation which also fits the differences observed in the crystallographic texture when comparing wire centre and edge (cf. 8.3). The potential effects of the porosity on the mechanical properties of tungsten wires will be discussed in sections 8.7.1.1 and 8.7.1.2.

8.4.2 Evolution of grain geometry

8.4.2.1 Method for determining grain shape parameters in TCS and LS orientation maps

In order to determine the grain shape from orientation maps acquired using EBSD, the methods described in section 5.2.3 were combined. The first step hereby was to segment a given orientation map into individual grains using the corresponding algorithm of the MTEX toolbox. Due to the accuracy of the orientation measurement (angular precision of the EBSD system) that can be expected [285], a minimum boundary angle of 2° was chosen, i.e. if the misorientation of two neighbouring pixels differs by more than 2°, it is concluded that these pixels are separated by a grain boundary[12]. Grains with a size less than five pixels were treated as measurement noise and were thus neglected during the evaluation procedure for determining the mean grain shape parameters.

The procedure for determining the shape parameter for a given grain is explained in the following with the help of the example shown in figure 8.15. As a first step, Principal Component Analysis (see section 5.2.3.1) is applied to the pixels with

$$(x_{\mathrm{i,j}} \mid y_{\mathrm{i,j}}) \,,$$

where $x_{\mathrm{i,j}}$: x coordinate $i = 1 \ldots N_{\mathrm{j}}$ of grain number $j = 1 \ldots M$

[10] The curled grain structures in transversal sections are also reported for certain intermetallic compounds after tension and f.c.c. metals after compression loading [170, 171, 284].

[11] The deviatoric stress tensor in the wire centre comprises pure uniaxial stresses. The hydrostatic compressive stress resulting from the interaction of the workpiece with the drawing die can be neglected in this discussion.

[12] The algorithm for determining the grains was applied in a way that pixels belonging to a certain grain do not have to be connected to another pixel belonging to the grain, i.e. pixels are searched across non-indexed holes.

$y_{\mathrm{i,j}}$: y coordinate $i = 1 \ldots N_{\mathrm{j}}$ of grain number $j = 1 \ldots M$
N_{j} : Number of pixels of grain number M
M : Number of grains (e.g. per orientation map) with $j = 1 \ldots M$

belonging to the grain (black squares in figure 8.15) in order to find the major and minor axes. Then, the grain is rotated so that the major axis is parallel to the $\overrightarrow{x}$ axis of a Cartesian coordinate system. Next, in order to determine the grain width, N_{LIM} equidistant lines are drawn cutting the grain vertically, i.e. along the minor axis (grey dashed lines in figure 8.15). The distance between the upper and lower grain boundary, i.e. the positions where the grey lines intersect with the beginning and end of the grain, is then interpreted as the width of the grain at a given x value (see cyan lines in figure 8.15). Then, a circle parameterised by

$$y = f_{\mathrm{c}}(x) = y_0 + \sqrt{r^2 + (x - x_0)^2} \tag{8.15}$$

where $(x_0 \mid y_0)$: Position of circle centre
r : Circle radius

is fitted to the family of points sitting at the centre of the lines connecting the lower and upper grain boundary (see red crosses in figure 8.15) using the method developed by Pratt [286]. The grain length is approximated by the segment of the circle spanning the range from $\min\{x_{\mathrm{i}}\}$ to $\max\{x_{\mathrm{i}}\}$:

$$L_{\mathrm{TCS}} = \int_{\min\{x_{\mathrm{i}}\}}^{\max\{x_{\mathrm{i}}\}} \sqrt{1 + \left(\frac{\partial f_{\mathrm{c}}}{\partial x}\right)^2}\, dx = \int_{\min\{x_{\mathrm{i}}\}}^{\max\{x_{\mathrm{i}}\}} \sqrt{2 - \frac{r^2}{r^2 + (x - x_0)^2}}\, dx \tag{8.16}$$

where L_{TCS} : Grain length (viewed in transversal direction)
f_{c} : Circle equation, see equation (8.15)
$(x_0 \mid y_0)$: Position of circle centre
r : Circle radius

The fitting of a circle also yields the curvature of the grain as

$$k = \frac{1}{r}. \tag{8.17}$$

where k : Grain curvature
r : Circle radius.

In order to eliminate the influence of the finite step size Δx used during acquisition of the orientation map on the mean values characterising the grain shape, an extrapolation method was used. Therefore, the mean width or length is calculated as a function of a hypothetical cut-off width or length. Mathematically, this can be expressed using the set

$$K(x_{\mathrm{co}}) = \{x \mid x \geq x_{\mathrm{co}}\} \tag{8.18}$$

where K : Set containing all grain widths/lengths larger than the cut-off value X_{co}
x_{co} : Cut-off grain width or length
x : Single measurement of grain width or length

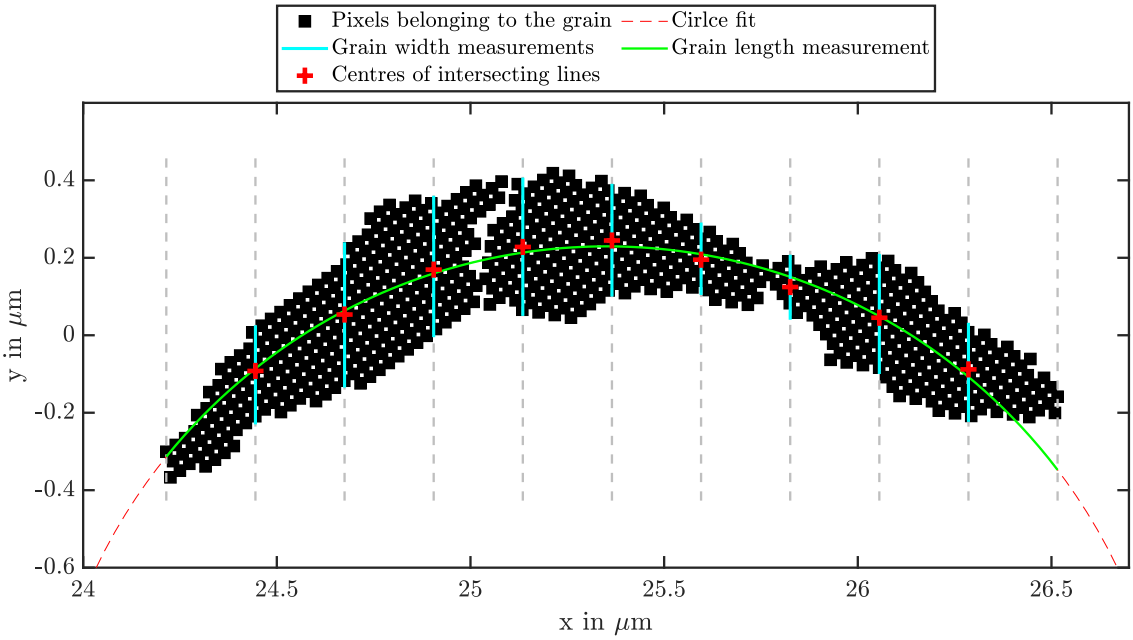

Figure 8.15: Illustration of the method employed to determine the shape parameters of grains. The different steps of the analysis are explained in the text. The derived grain properties are shown in the legend on top of the figure.

For each value of X_{co}, a mean of all elements contained in K, $\bar{K}\left(x_{\mathrm{co}}\right)$ can be determined. By varying x_{co} in a certain range ($\Delta x \leq x_{\mathrm{co}} \leq 4\Delta x$ in the present study) and plotting $\bar{K}\left(x_{\mathrm{co}}\right)$ as a function of x_{co} yields a diagram as shown in figure 8.16. The evolution of $\bar{K}\left(x_{\mathrm{co}}\right)$ vs. x_{co} was approximated using a linear function. The intersection of this function with the ordinate yields an extrapolated mean value that is not influenced by the finite step size used during the acquisition of the orientation map.

8.4.2.2 Grain width

The grain width of tungsten wires is accessible both in transversal cross-sections and longitudinal sections using the evaluation method presented in section 8.4.2.1. The grain width can be discussed from different points of view, namely the influence of sample orientation (longitudinal/transversal) and the position of an orientation map with respect to the wire centre (wire edge/wire centre). The database for this discussion is shown in figure 8.17.

Several trends are apparent from figures 8.17 from which conclusions on the evolution of the grain width during tungsten wire drawing are derived. It is apparent that the scatter of grain widths extracted from individual orientation maps in the thicker wires, i.e. wires with lower accumulated drawing strains φ, is higher than for thinner wires, when neglecting the grain widths determined from SEM/STEM micrographs (see framed data points in figure 8.17) for a moment. This shows that the grain structure in these wires is still quite heterogeneous. The heterogeneity originates from the highly heterogeneous deformation pattern during Kocks milling and swaging. In these deformation processes, the strain is much higher close to the sample surface when compared to the sample centre. The hot working process of Kocks milling and swaging can also be used to explain the strong differences between the grain widths in the wire edge and centre of the two thickest wires: Since the strain in the edges of the swaged and Kocks milled rod is higher than in the centre, the dislocation density and with this the driving force for recovery and recrystallisation is higher in these regions [10]. Prior to wire drawing, the hot worked

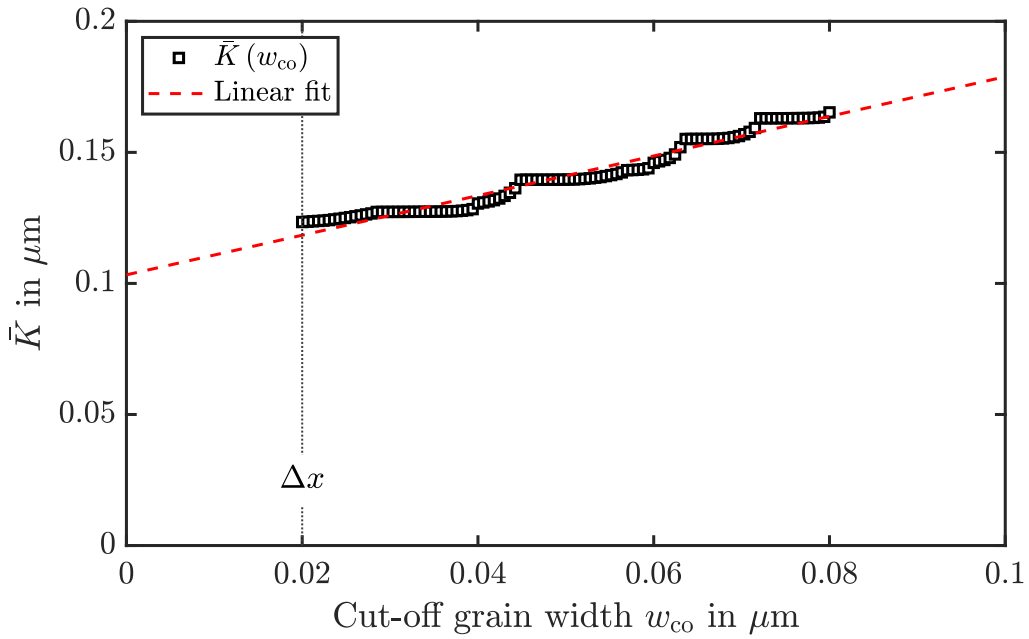

Figure 8.16: Mean grain width as a function of cut-off grain width for a TCS OM acquired from a tungsten wire with a diameter of 150 µm. The step size $\Delta x = 20\,\mathrm{nm}$ used during acquisition of the orientation map is plotted as a vertical dotted line. The linear fit to $\bar{K}\,(w_{\mathrm{co}})$ is drawn as a dashed line. The intercept of this straight line with the ordinate yields the mean grain width for a step size of 0.

rod is annealed at temperatures of 2000 °C to 2300 °C [32]. Since these annealing temperatures clearly exceed the common recrystallisation temperature of mildly deformed tungsten materials of 1000 °C to 1200 °C [287], recrystallisation processes are initiated. Due to the higher driving forces, these processes are more pronounced in the near-surface region of the rods, yielding a larger grain size (see figure 8.18 for the average grain widths for each wire diameter). From the decrease of the scatter of the grain width with increasing accumulated drawing strain, it becomes apparent that the wire drawing process has a homogenising influence on the grain size. Wire drawing also seems to yield a convergence of the grain sizes in the wire centre and edge if one considers the absolute grain widths. The overall decrease of the grain width with increasing drawing strain can be explained by the need of the grains to follow the shape change of the wire. Since the wire gets thinner and longer with increasing accumulated drawing strain, also the grains thin down [113]. Figure 8.17 reveals that there is no systematic influence of the sample orientation (longitudinal/transversal) on the measured grain width. An apparent discrepancy that however has to be discussed is that grain widths determined from EBSD orientation maps are systematically lower than those obtained from evaluating STEM or SEM micrographs (see figure 8.17). The purpose of analysing micrographs was to reinforce the data situation for the grain width of the thinnest wires, which is challenging to measure using EBSD due to the small grain size and the large interaction volume between sample and electron beam, which poses major challenges to sample stability during acquisition of EBSD orientation maps. The discrepancy can however be readily explained: The most common challenge when evaluating micrographs using the line intersection method on (S)TEM or SEM images is to concisely identify grain boundaries. Especially with images with a non-ideal grain boundary contrast, such as those taken on a too thick TEM lamella for instance, it is easy to overlook one or two grain boundaries. Consequently, the mean chord length that is taken as grain width in the present case increases according to equation

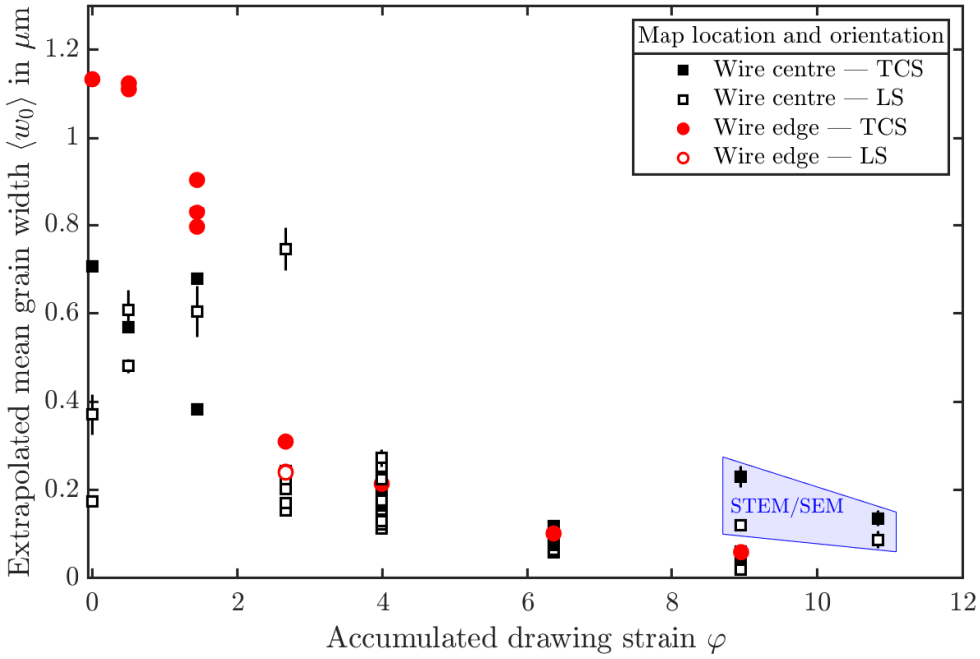

Figure 8.17: Mean extrapolated grain width $\langle w_0 \rangle$ as a function of the accumulated drawing strain of drawn tungsten wires for regions close to the wire surface (red circles) or in the wire centre (black squares). Filled and empty symbols represent data obtained from orientation maps acquired from regions close to the wire centre and edge, respectively. Apart from the data points extracted from STEM and SEM micrographs (blue frame), which were evaluated using the line intersection method, the majority of data was extracted from transversal and longitudinal orientation maps acquired using EBSD. The results of individual orientation maps were shown instead of averaged values in order to show the spread of the grain widths.

(5.26). The data acquired using SEM and STEM show a trend that the grain width acquired from micrographs taken from longitudinal sections is lower than the one from transversal cross-sections.

Figure 8.18 shows a comparison of the mean grain width in the edge and centre region of tungsten wires and literature values already presented in figure 5.6. The comparison clearly reveals that the grain widths determined for the wires of the series investigated in this study are significantly lower (note the logarithmic ordinate in figure 8.18) than literature values. This discrepancy most likely originates from the wires being manufactured by different companies with different manufacturing routes and starting materials on the one hand and the different methods used for determining the grain width on the other hand: Opinsky et al. [34] and Walter & Koch [184] determined the grain width from micrographs, while Nikolić et al. [178] and Michel et al. [189] determined the grain width using EBSD orientation maps. The comparison of grain widths from OM and micrographs was already drawn in the previous paragraph and revealed higher mean grain widths for micrographs. This is in-line with the larger values by Seigle & Dickinson [34] and Walter & Koch [184]. The reason for the discrepancy when comparing grain widths extracted from orientation maps is that Nikolić et al. [178] and Michel et al. [189] did not eliminate the influence of the step size. As shown in figure 8.16, the extrapolation to $\Delta x \to 0$ yields lower mean grain widths. This explains, why Nikolić et al. [178] report larger grain widths for a similar wire with a diameter of 150 µm that was also manufactured by OSRAM GmbH, Schwabmünchen.

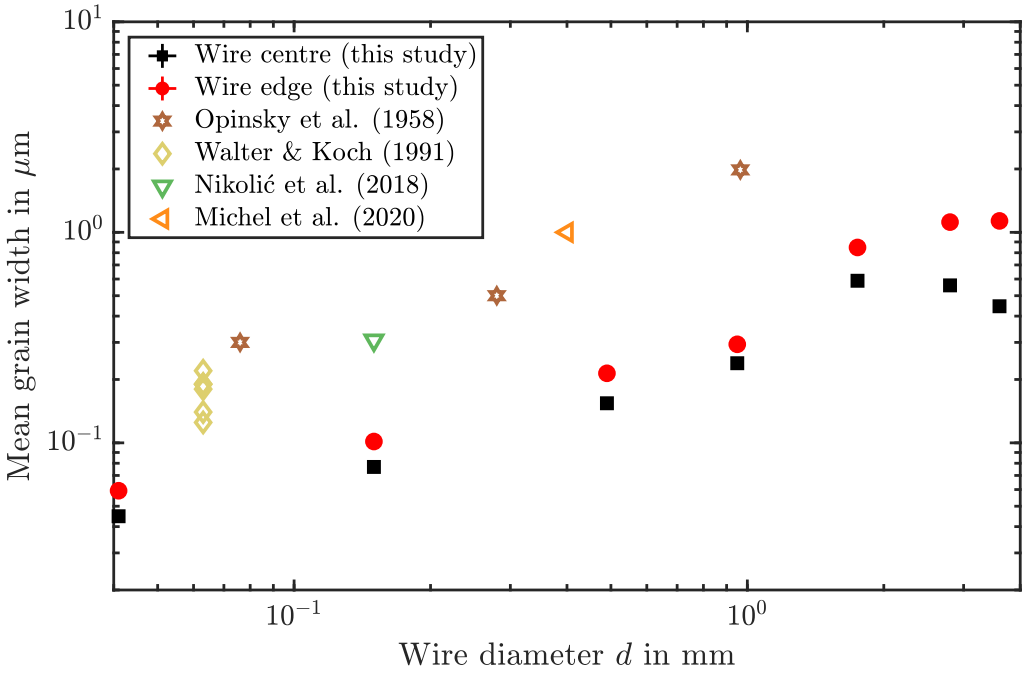

Figure 8.18: Mean grain width in edge (red) and centre regions (black) of drawn tungsten wires in comparison with values from literature (green, orange, yellow and brown symbols) [34, 178, 184, 189] as a function of the wire diameter.

8.4.2.3 Grain curvature

As discussed in section 5.2.3, the curvature radius of a grain in a transversal cross-section is approximated by the radius of a circle fitted to the centre line of the grain. The curvature then follows as the inverse of the radius of the fitted circle. The results for all orientation maps acquired from TCS samples are shown in figure 8.19.

It is apparent from figure 8.19 that the grain curvature increases with increasing accumulated drawing strain for $\varphi \geq 2.7$. Furthermore, treating the lowest curvature for $\varphi = 9.0$ as a singular outlier, a further trend, namely that grains in the wire centre seem to be more strongly curved than grains close to the wire edge, is identifiable. An explanation could again be the different modes of deformation in the centre and near-surface regions of the wire: As discussed in section 5.1.2, the deviatoric stress tensor[13] in the wire centre comprises uniaxial stress during drawing. Grains in the wire centre deform by plane strain elongation [170], which gives rise to the grain curling and is thus causal for the high grain curvature. In the near-surface region, the geometry of the drawing die and friction forces give rise to additional shear components that change the mode of deformation of grains in this region. Hence, the slip pattern of dislocations close to the wire edge is different from the pattern in its centre and as a consequence, the curvature is less pronounced. As the evolution in 8.19 shows, also the difference in grain curvature between edge and centre is increasing with increasing φ. The increase in grain curling upon drawing of tungsten wire was mentioned by many researchers, see for example [66, 170, 171], and successfully modelled by others [173, 284, 288]. The results presented here are however the first successful quantification of grain curling in a drawn refractory metal wire itself and its evolution over the whole drawing process.

[13]Hydrostatic compressive stresses that do not influence dislocation slip processes can be neglected at this point.

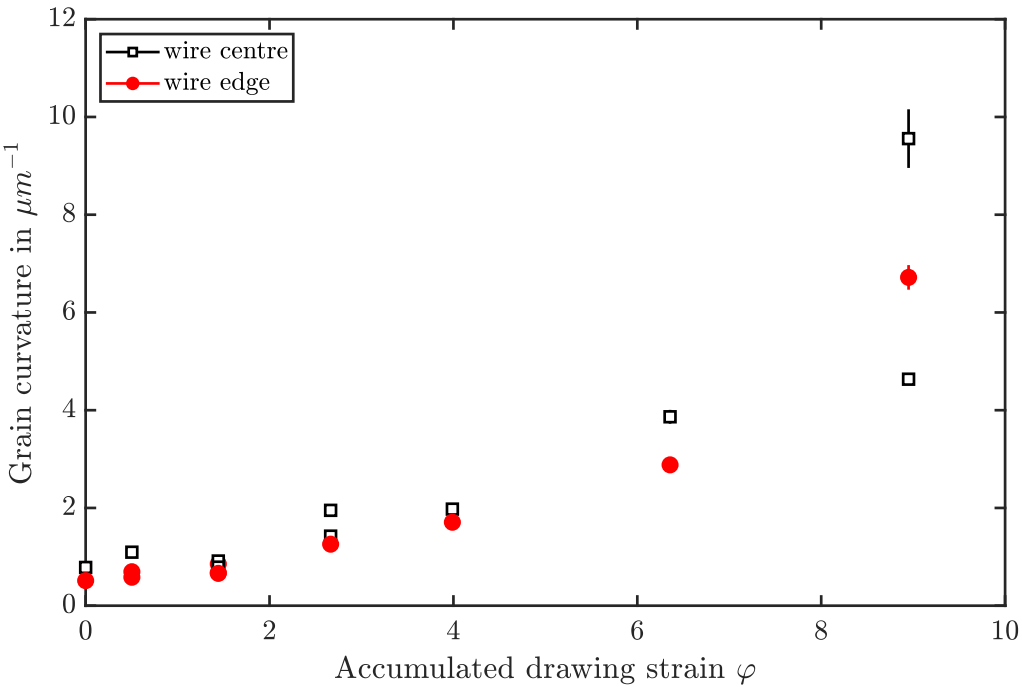

Figure 8.19: Curvature of grains in orientation maps acquired from edge (red circles) and centre regions (black squares) of transversal cross-sections of tungsten wires with different accumulated drawing strains. Each data point represents a singular orientation map.

8.4.2.4 Grain length and grain aspect ratio

The length of the elongated grains in drawn tungsten wires can be estimated from the orientation maps acquired from longitudinal sections (see figure 7.9). The measured length L_m of a grain is determined as

$$L_\mathrm{m} = \max x_i - \min x_i,$$

where x denotes the $\overrightarrow{x}$ coordinate of all pixels ($i = 1 \ldots N$) belonging to a grain in an orientation map acquired from a longitudinal section with the wire direction along the $\overrightarrow{x}$ direction. The measured length cannot be larger than the horizontal width L_HFW of the orientation map. It can however be shown by statistically varying the position of a grain with a true length L_tr within a measuring range of horizontal width $L_\mathrm{HFW,c}$ that the relation between true length and measured length is as follows:

$$L_\mathrm{m} = \frac{L_\mathrm{tr}\, L_\mathrm{HFW,c}}{L_\mathrm{tr} + L_\mathrm{HFW,c}} \tag{8.19}$$

where
L_m : Measured grain length
L_tr : True grain length
$L_\mathrm{HFW,c}$: Width of the orientation map corrected for misalignment between wire axis and horizontal axis of the OM

Equation (8.19) already makes use of the correction of a potential misalignment of the horizontal axis of the OM and wire axis. Instead of using the horizontal width of the OM, L_HFW, the

corrected value

$$L_{\mathrm{HFW,c}} = \frac{L_{\mathrm{HFW}}}{\cos\psi}$$

has to be used for describing the dependence of the measured grain length on the horizontal width of the OM. Applying the Principal Component Analysis (see section 5.2.3.1) to the pixels belonging to a grain yields the angular relationship between the major and minor axes and the Cartesian coordinates of the coordinate system. For an elongated grain, the angle ψ is the angle between the grain's major axis and the $\overrightarrow{x}$ axis of the orientation map's coordinate system. In order to calculate the corrected length of each grains in an orientation map, it is divided by the cosine of the mean angle ψ of all grains contained in the orientation map. A visualisation of the relationship described by equation (8.19) is shown in figure 8.20.

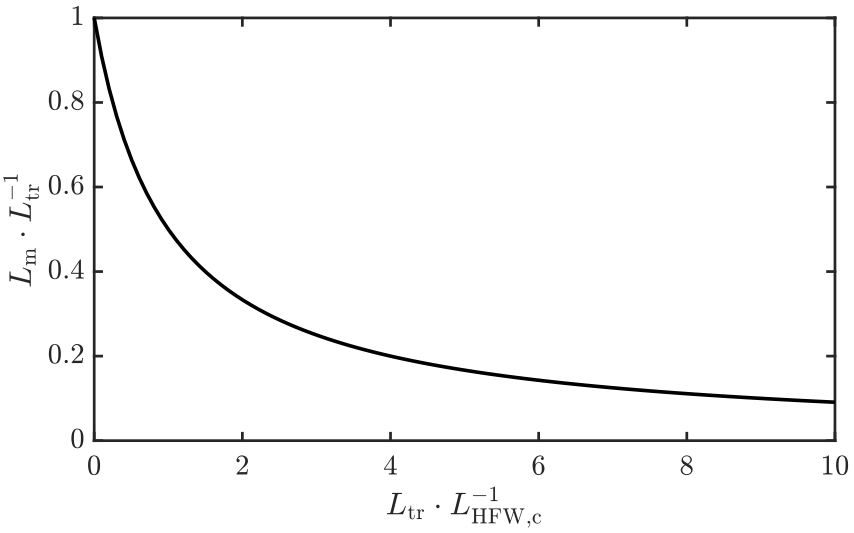

Figure 8.20: Evolution of the ratio of measured to true grain length as a function of the true grain length, normalised by the corrected horizontal width of the orientation maps in which the grains are contained.

Equation (8.19) predicts that the measured grain length asymptotically approaches the true grain length for infinitely high values of $L_{\mathrm{HFW,c}}$:

$$\lim_{L_{\mathrm{HFW,c}} \to \infty} L_{\mathrm{m}} = L_{\mathrm{tr}}.$$

Thus, in order to determine the true grain length, the grain length should be calculated for LS orientation maps with as high horizontal widths as possible. In order to improve statistics, all orientation maps acquired from longitudinal sections of wires with $\varphi \leq 9.0$ were analysed as

$$\text{Segment 1: } 0 \leq x \leq \frac{L_{\mathrm{HFW,c}}}{3}$$
$$\text{Segment 2: } 0 \leq x \leq \frac{2\,L_{\mathrm{HFW,c}}}{3}$$
$$\text{Segment 3: } 0 \leq x \leq L_{\mathrm{HFW,c}}.$$

The length of the grains in each segment was analysed individually. Since orientation maps could not be acquired from longitudinal sections of wires with a diameter of 16 µm, the length of grains in these wires was determined from BSE micrographs. By varying the magnification of the electron

image, different values of $L_{\mathrm{HFW,c}}$ can be realised.

In order to find the average true grain length $\langle L_{\mathrm{tr}} \rangle$ as asymptote of the measured length L_{m} vs. $L_{\mathrm{HFW,c}}$ according to equation (8.19), it is convenient to calculate the average grain length $\langle L_{\mathrm{m}} \rangle$ for each orientation map. As the orientation maps shown in figure 7.9 show, the microstructure of drawn tungsten wires consists of a large number of short and a smaller number of very large grains. In the arithmetic mean of the grain lengths of such an orientation map, the impact of the short grains would be very high and the average thus disproportionately low. This can be averted by using a weighted mean according to the equation shown in the appendix (see equation (A.4)). Using the grain length itself as a weighting factor, the averaged mean is determined as

$$\langle L_{\mathrm{m}} \rangle = \frac{\sum_{j=1}^{M} L_{\mathrm{m,j}}\, L_{\mathrm{m,j}}^{g}}{\sum_{j=1}^{M} L_{\mathrm{m,j}}^{g}}. \tag{8.20}$$

where $\langle L_{\mathrm{m}} \rangle$: Mean weighted grain length
L_{m} : Measured grain length ($j = 1 \ldots M$)
g : Exponent

The exponent g in equation (8.20) can be used to control the weight of long grains on the mean value. Figure 8.21 shows the evolution of $\langle L_{\mathrm{m}} \rangle$ as a function of the corrected horizontal field width of the corresponding orientation map $L_{\mathrm{HFW,c}}$ for $g = 1$.

Neglecting some outliers for wires with $\varphi = 2.7$ and $\varphi = 4.0$, the expected asymptotic evolution of $\langle L_{\mathrm{m}} \rangle$ with the asymptote $\langle L_{\mathrm{r}} \rangle$ can be observed. This confirms the theoretical description expressed in equation (8.19). Average true lengths for each wire diameter were determined by applying equation (8.19) to the data shown in 8.21 with L_{tr} as free fitting variable. Mean weighted measured lengths $\langle L_{\mathrm{m}} \rangle$ obtained from orientation maps with high $L_{\mathrm{HFW,c}}$ were thereby weighted more strongly during fitting. The results of the fitting procedure are shown in figure 8.22. It is evident from figure 8.22 that the determined mean true lengths are very low in comparison to the lengths observed in figure 7.9. This suggests, that the weight of the long grains is still too low. The result of increasing the weight of these long grains by increasing the exponent g is also shown in 8.22.

Increasing g from 1 to 2 or 3 increases the true grain length as expected. Comparing the obtained mean true grain lengths shown in 8.22 with the lengths of grains in figure 7.9, it seems as if low g values underestimate the grain lengths for thick wires (low φ) but more or less capture the apparent grain lengths in thin wires (high φ). For high values of g it is exactly the opposite. The distribution of grain lengths for the different wires can also be studied using the cumulative distribution function (CDF) of the true grain length, shown in figure 8.23. The data for the CDF of each wire diameter are all true grain lengths that were calculated from the measured lengths using equation 8.19 rearranged to L_{tr}. Applied to the case of grain lengths, the cumulative distribution functions describe the probability of observing a certain grain length. Comparing the evolutions of the CDF for the wires with different diameters shows that the probability of observing short grains is higher in thin wires than in thicker ones.

So far, there is no systematic quantitative study of the evolution of grain lengths in tungsten wires in the course of wire drawing available in literature. The obtained grain lengths are higher than the ones reported in recent attempts at determining the grain length of drawn tungsten wires like the one of Nikolić et al. [178] or Terentyev et al. [289], which both investigate drawn tungsten wire with a diameter of 150 µm and obtain grain lengths[14] of 1.2 µm and 7.5 µm, respectively. From the data generated in the course of this study, it can be concluded that some individual

[14]The grain lengths of Nikolić et al. [178] and Terentyev et al. [289] were corrected using equation (8.19).

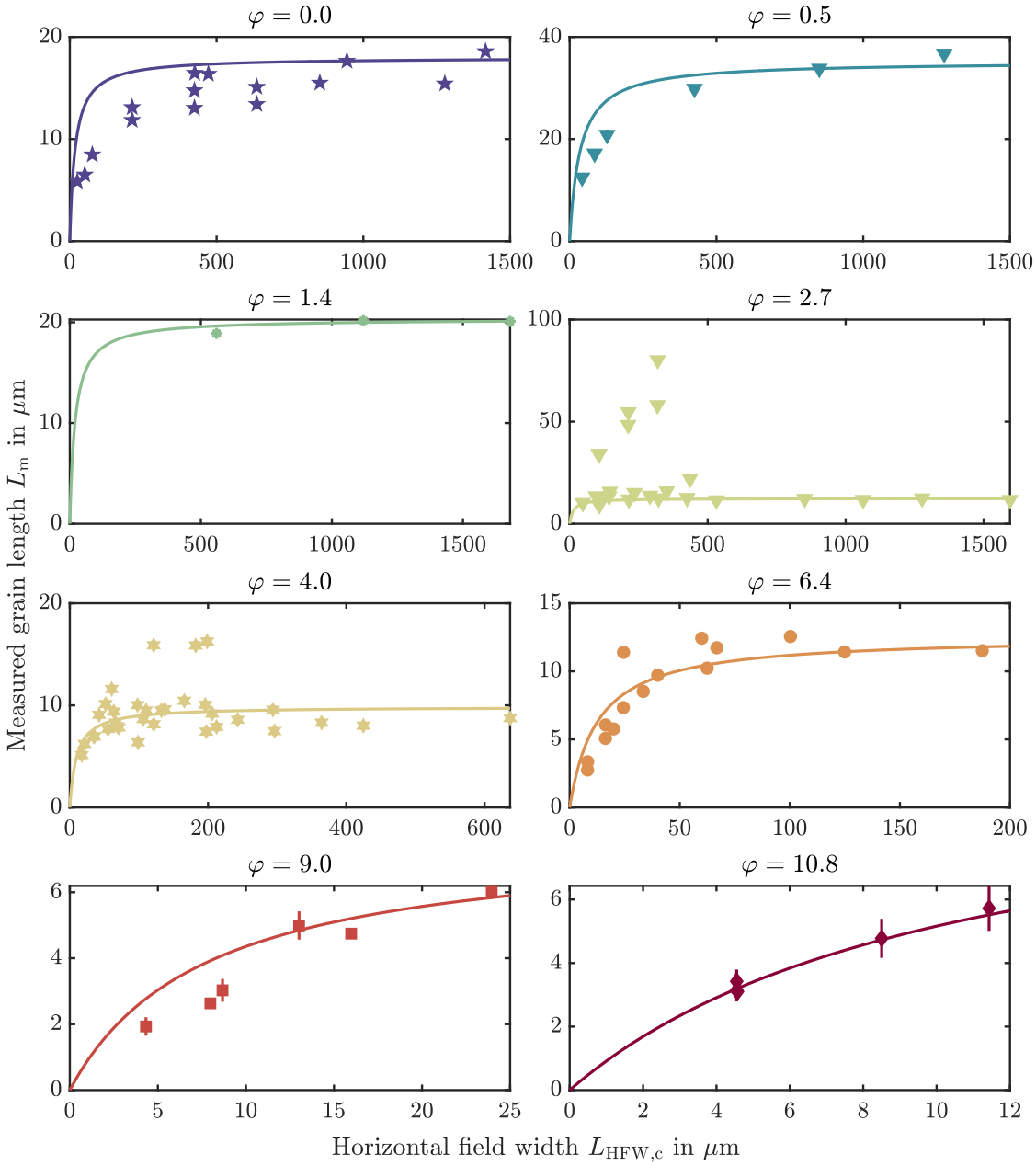

Figure 8.21: Measured grain length of drawn tungsten wires as a function of the (corrected) horizontal field width of the orientation map or BSE image used for determining L_m. Filled and empty symbols represent grain lengths determined from orientation maps and BSE images, respectively. Solid lines are fits according to equation (8.19).

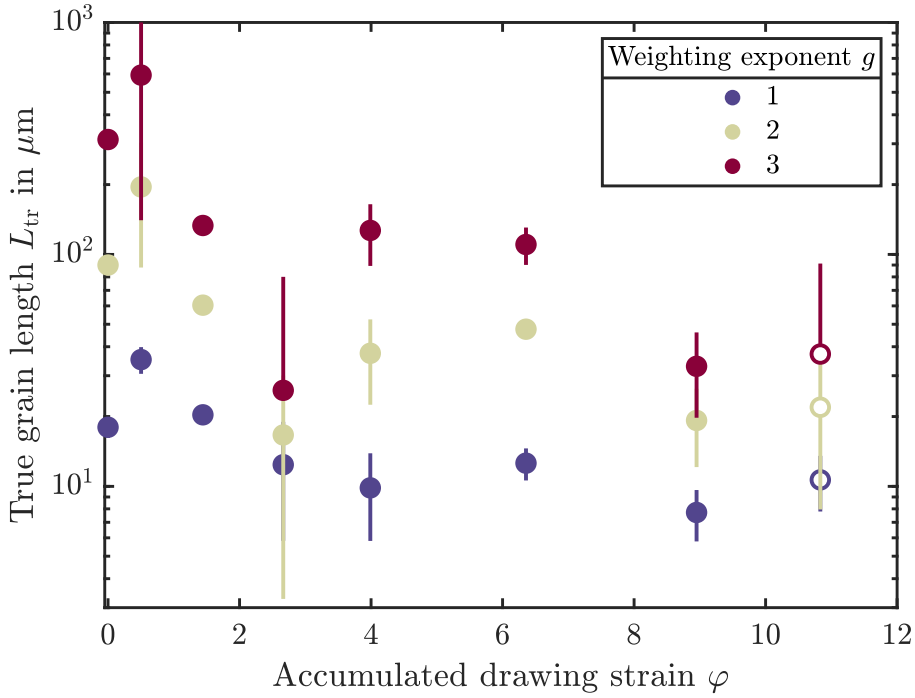

Figure 8.22: True grain length as a function of the accumulated drawing strain of drawn tungsten wires. Filled and empty symbols represent grain lengths determined from orientation maps and BSE images, respectively.

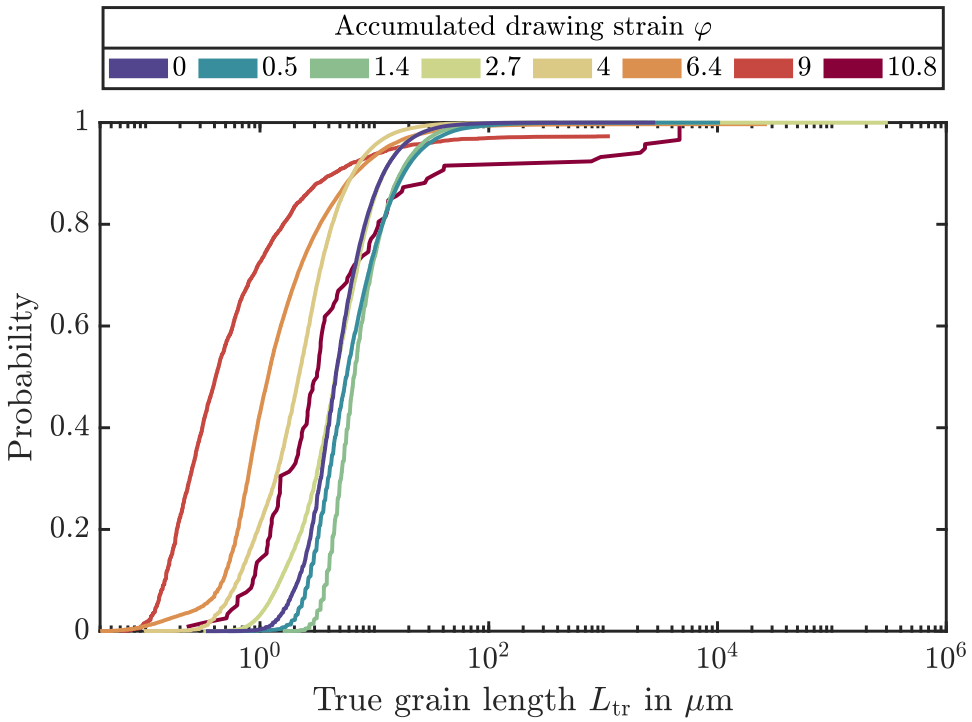

Figure 8.23: Cumulative distribution functions of the true grain length in drawn tungsten wires.

grains elongate strongly as observed qualitatively by several researchers grains [23, 66] but that the length of grains *on average* does not increase. In fact, a decrease of $\langle L_{\mathrm{tr}} \rangle$ with increasing φ is can be observed[15]. This trend appears counterintuitive when taking the shape change of the wire during drawing into account: Just like the decrease of grain width is linked to the decrease of wire diameter, the grain length should theoretically increase in accordance with the increase in wire length [290]. Some explanations can be used to explain the decrease of the grain length with increasing accumulated drawing strain:

- Due to grain curling, the grains are likely to bend in and out of the cut plane that is investigated in orientation maps or SEM/TEM images acquired from LS samples. Thus, the grain length is underestimated. The influence of this effect on the measured grain length is increasing with accumulated drawing strain along with the grain curvature, see section 8.4.2.3.
- Especially for thin wires ($\varphi \geq 9.0$), the low obtained true grain lengths are also due to the low horizontal field width of the micrographs and orientation maps used for measuring the grain length, respectively. This is evident from the course of the respective fit functions shown in figure 8.21, which have not yet reached their saturation value even for the highest values of $L_{\mathrm{HFW,c}}$.

By combining the mean grain width (see figure 8.15) and the true grain length shown in figure 8.22, the aspect ratio of the grains can be determined:

$$A = \frac{\langle L_{\mathrm{tr}} \rangle}{\langle w \rangle} \tag{8.21}$$

where A : Grain aspect ratio
$\langle w \rangle$: Mean grain width
$\langle L_{\mathrm{tr}} \rangle$: Mean true grain length

Since all orientation maps acquired from longitudinal sections were located in the wire centre, the grain width in the centre of the wires is used to determine the grain aspect ratio in the wire centre. The results are shown in figure 8.24.

The grain aspect ratio in the centre of drawn tungsten wires stagnates for $\varphi \leq 4.0$. For these wires, the decrease in mean grain width (see figure 8.17 and the decrease in true grain length balance. The strong decrease in mean grain width for wires with $6.4 \leq \varphi \leq 9.0$ yields a significant increase of the aspect ratio to values around 170. The decrease of A for the thinnest wire investigated is probably due to an underestimation of the true grain length due to the limited horizontal field width of the micrographs that were used to determine the true grain length. Furthermore, the systematically higher grain width extracted from STEM micrographs when compared to EBSD orientation maps contributes to the decrease in grain aspect ratio from $\varphi = 9.0$ to $\varphi = 10.8$. Looking at the grain aspect ratios for wires with accumulated drawing strains $1.5 \leq \varphi \leq 9.0$ in isolation, the trend of increasing grain aspect ratio with increasing φ which was predicted in literature [66] can be confirmed.

8.4.2.5 Grain boundary disorientation

Figure 8.25 shows the evolution of the distribution of disorientation angles between neighbouring pixels in orientation maps acquired from transversal cross-sections of tungsten wires as a function

[15] This trend is not affected by a change in the exponent g used for weighting the individual grain lengths.

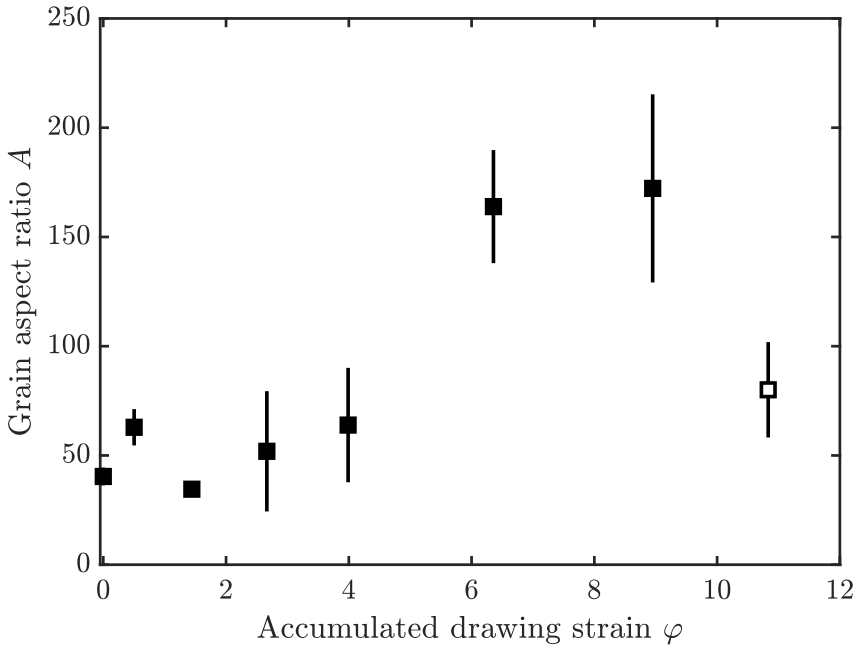

Figure 8.24: Grain aspect ratio in the centre of tungsten wires. Filled and empty symbols represent grain lengths determined from orientation maps and BSE images, respectively.

of the accumulated drawing strain. The distribution of disorientation angles was investigated for disorientation angles between 2° (minimum disorientation angle for a grain boundary used during grain segmentation, see section 8.4.2.1) and 62.8° (maximum disorientation angle for a crystal with cubic symmetry [291]).

Using the commonly used definitions for low-angle (disorientation angle below 15°) and high-angle boundaries (disorientation angle above 15°), clear trends for the evolution of the prevailing grain boundary character can be identified. The relative frequency of low angle boundaries is monotonously decreasing with increasing drawing strain. On the other hand, the relative frequency of high-angle boundaries is increasing with increasing drawing strain. As figure 8.25 reveals, there is no significant difference between regions in the wire centre or close to the wire surface. Literature on the effect of cold working on the grain boundary angle distribution shows a conclusive picture (cf. table 8.4): The studies of Reiser et al. [30] on rolled pure tungsten plates, Li et al. [292] on pure tungsten deformed by high pressure torsion and by Juul Jensen [293] on rolled aluminium show the same evolution of the grain boundary angle distribution as the one obtained for the drawn tungsten wires[16]. The observed evolution for the tungsten wires could be explained by the incorporation of dislocations into boundaries [294]. Since higher dislocation densities were measured in wires with higher accumulated drawing strains (see sections 8.4.2.6 and 8.2.3), thinner wires would incorporate more dislocations in existing grain boundaries through which their disorientation angle would increase. The working temperature of wire drawing for $\varphi \leq 2.7$ lies well above the knee temperature of tungsten ($T_\mathrm{K} = 775\,\mathrm{K}$ [101]), see figure 5.2. Thus, since screw dislocations possess similar mobility as edge dislocations for $T > T_\mathrm{K}$, recovery processes can take place very efficiently [10]. Consequently, recovery-induced low-angle boundary annihilation [295] should contribute to the decreasing frequency of low-angle boundaries in thick drawn tungsten wires with $\varphi \leq 2.7$. This explains why wires with higher accumulated drawing strains exhibit higher fractions of high-angle grain boundaries when compared to less strongly deformed wires.

[16]Thus, the evolution of the relative frequency of low and high angle boundaries is not a function of the crystal structure.

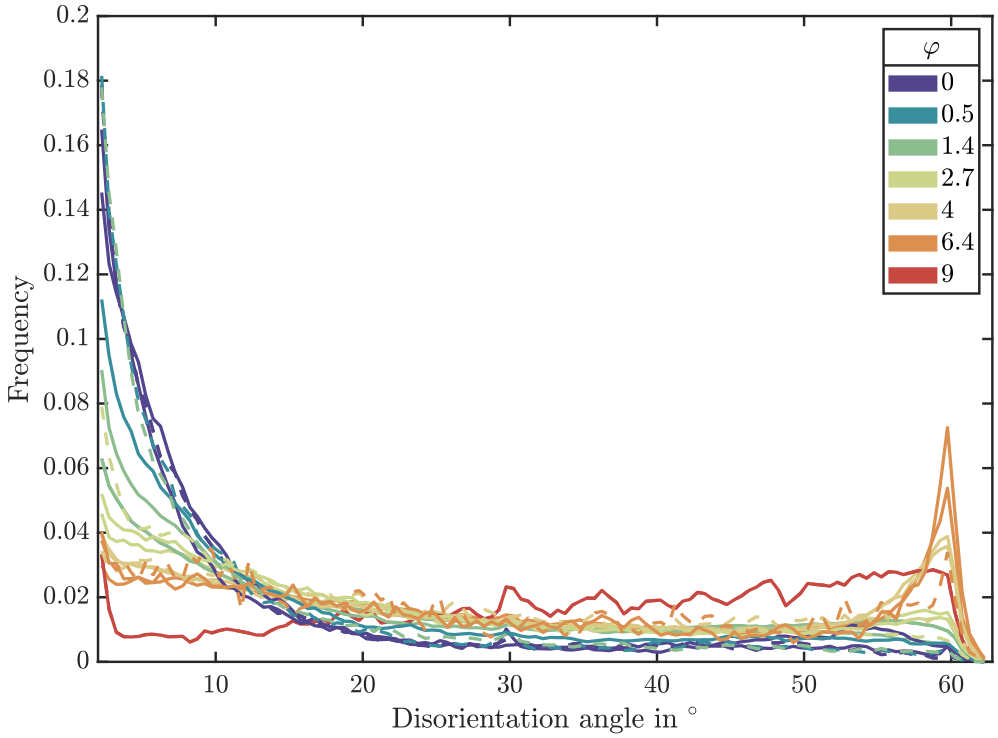

Figure 8.25: Distribution of disorientation angles of neighbouring pixels from transversal orientation maps acquired from tungsten wires with different accumulated drawing strains. Data from orientation maps from the wire centre are drawn as solid lines, while those acquired from maps located close to the wire surface are drawn as dashed lines. The legend in the upper right corner links the line colour and the accumulated drawing strain. For the sake of improved identifiability, a semilogarithmic plot of the same data is included in appendix B.2.6.

Table 8.4: Effect of cold working on the relative frequency of low-angle (LAB) and high-angle boundaries (HAB) in various metallic materials (↑: Increase; ↓: Decrease).

	Cold-working process	LAB	HAB	Source
AKS-doped tungsten wire	wire drawing	↓	↑	this work
Pure tungsten plate	rolling	↓	↑	[30]
Pure tungsten	high pressure torsion	↓	↑	[292]
Aluminium	rolling	↓	↑	[293]

One peculiarity observed in the grain boundary angle distribution of wires with $4.0 \leq \varphi \leq 6.4$ is the peak at a disorientation angle slightly below 60°, which is visible for wires with neither lower nor higher accumulated drawing strain. Since the texture further sharpens in the wire with $\varphi = 9.0$, one would expect to see the peak also in its boundary disorientation distribution function. Since the wire with $\varphi = 9.0$ does not show the characteristic peak, it is questionable if the peak is linked to the crystallographic texture. It could be suspected that the peak is an artefact caused by erroneous indexing of the orientation maps. Using an indexing procedure that does not rely on the Hough transformation (see section 5.2.2.1.3) like the ones discussed in [296, 297] could help to clarify this question.

8.4.2.6 Evolution of redundant dislocation density and coherently scattering domain size

As mentioned in section 7.2.4, the diffractograms acquired from the longitudinal sections of the tungsten wires show some additional peaks. Those can be explained by considering the mounting procedure used to prepare the wire samples for XRD analysis. As mentioned in section 6.3.3, all wires with $\varphi \leq 4.0$ were embedded in a conductive resin containing graphite. The diffractograms obtained from these samples show the distinct peak at 26°. This peak correlates well with the 002 peak found in graphite samples, see for example [263]. Thus, this peak can be explained by the graphite content in the embedding material. For thinner wires, more precisely those with $\varphi \geq 6.4$, several peaks at positions already listed in section 7.2.4, appear in the diffractogram. The respective samples were mounted on aluminium blocks before being embedded and polished (see section 6.3.3). Conveniently, the additional peaks in their diffractograms can be correlated with the peaks for polycrystalline aluminium (equation (5.18) using $a_{\mathrm{Al}} = 4.03\,\text{Å}$ [45]).

In order to perform the modified Williamson-Hall analysis, the peaks of the diffractograms acquired from the LaB_6 standard as well as those of the tungsten wire samples were fitted using the Pearson-VII function [298]. Adapted for the fitting of diffraction peaks, the Pearson VII function reads as follows [299, 300]:

$$I\left(2\theta\right) = I_{\max}\frac{W^{2\mathrm{k}}}{\left[W^2 + \left(2^{\frac{1}{\mathrm{k}}} - 1\right)\left(2\theta - 2\theta_0\right)^2\right]^{\mathrm{k}}} \tag{8.22}$$

where
I : Intensity
$I_{\max}$: Peak maximum
W : Parameter characterising the peak width
k : Parameter characterising the peak shape
2θ : Diffraction angle
$2\theta_0$: Position of the peak centre

The Pearson VII distribution resembles a Cauchy distribution for $m = 1$, a modified Lorentzian distribution for $m = 2$ and a Gaussian distribution for $m \to \infty$ [300]. The variables $I_{\max}$, W, m and $2\theta_0$ were used as free fitting parameters. The integral breadth, i.e. the ratio of peak area to maximum intensity, was used to quantify the broadening of the diffraction peaks. The dependence of the integral breadth of the LaB_6 powder on the diffraction semi-angle is shown in figure 8.26.

The angular dependence of the integral breadth of the NIST standard[17] was modelled using

[17] A similar evolution of β_{inst} with the diffraction angle θ was also observed by van Berkum [301, p. 93].

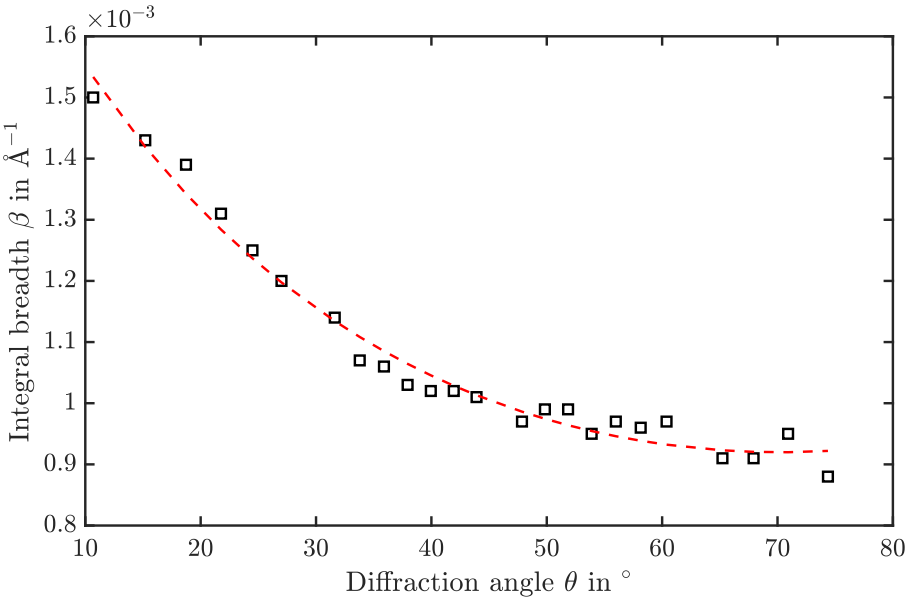

Figure 8.26: Integral breadth as a function of the diffraction semi-angle θ. The empirical fitting function drawn as a dashed red line is explained in the text.

an empirical function of the form

$$\beta_{\text{inst}} = a \cot\left(b\,\theta + c\right)^2 + d \tag{8.23}$$

where β_{inst} : Instrumental contribution to the total peak broadening
θ : Diffraction semi-angle
a, b, c, d : Coefficients

as derived by Schimpf [302, p. 47] following the considerations given in [303]. Since the function satisfactorily describes the experimental data, it was used to estimate the instrumental peak broadening. Since the diffraction peaks acquired from the tungsten wire samples reveal shape factors $m \gg 2$ and they therefore resemble Gaussian peaks, an exponent $n = 2$ could be used to deconvolute the broadening contributions of the diffractometer and the samples' microstructures (see equation (5.17)). The contrast factors required for the modified Williamson-Hall analysis were calculated using the ANIZC programme[18] [304]. Since the dislocation population present in the tungsten wires was not known, averaged contrast factors, averaging between pure $\langle 111 \rangle \{110\}$ edge and $\langle 111 \rangle$ screw dislocations, were determined. The individual and average contrast factors are listed in table 8.5.

Using the average contrast factors listed in table 8.5, a modified Williamson-Hall plot was drawn following equation (5.24). The result is shown in figure 8.27.

As the modified Williamson-Hall plot shows, there are two reflections, namely 200 and 310, that act as outliers and lead to a significant deviation of the experimentally determined peak breadths from a straight line when plotted as a function of $K\sqrt{C}$. Several sources of error can be discussed: On the one hand, the peak height should be causal for the low integral breadths. Using the values from powder diffraction databases [305], the theoretical and measured relative intensities were compared (see appendix B.2.5) in order to find a correlation between I_{rel} and ΔK. Considering the two outliers mentioned before, it is found that the 200 reflection is systematically higher than the value expected from theory, while the 310 reflection is systematically lower and

[18] `http://metal.elte.hu/anizc/`

Table 8.5: Contrast factors calculated for the reflections observed in the diffraction pattern of drawn tungsten wires using the ANIZC program. The contrast factors were determined for the ⟨111⟩ {110} slip system.

	Contrast factors C_{hkl}		
Reflection *hkl*	⟨111⟩ {110} edge dislocations	⟨111⟩ screw dislocations	Average
110	0.184 048	0.111 111	0.147 580
200	0.155 325	0.222 222	0.188 774
211	0.184 048	0.111 111	0.147 580
220	0.184 048	0.111 111	0.147 580
310	0.165 666	0.182 222	0.173 944
222	0.193 623	0.074 074	0.133 849
321	0.184 048	0.111 111	0.147 580

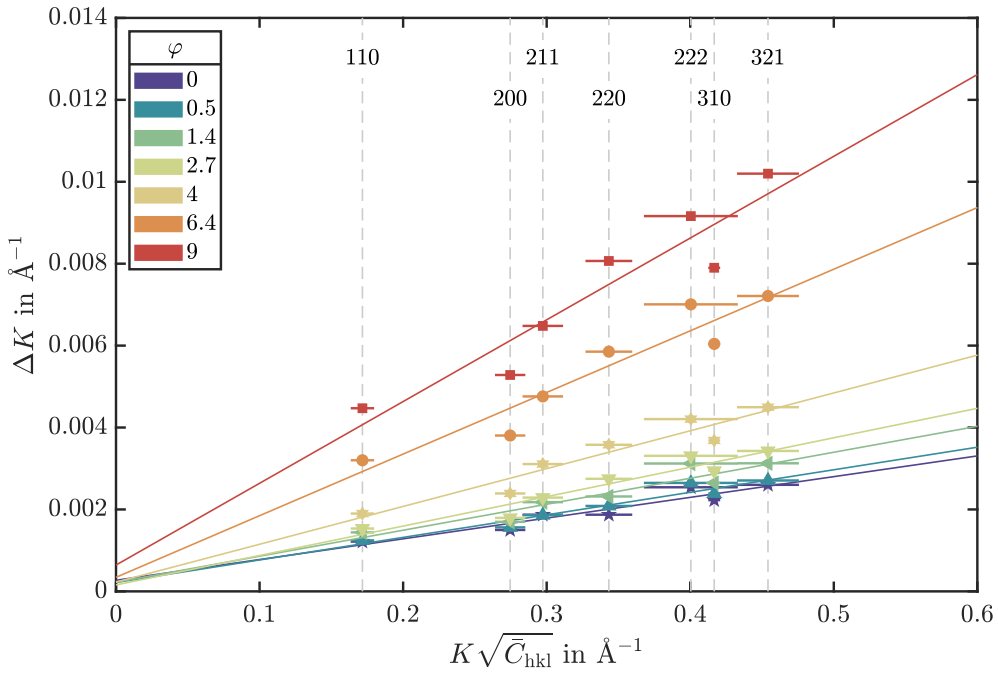

Figure 8.27: Modified Williamson-Hall plot for tungsten wires with different accumulated drawing strains (see legend). The experimental data is plotted as filled symbols (see equation (5.24) for the definition of K and ΔK), while the straight lines represent the fit according to the modified Williamson-Hall model [250]. The errors in the experimental data were taken into account for fitting the model function following the method described in [270, p. 785]. Each $K\sqrt{\bar{C}_{hkl}}$ was assigned the corresponding lattice plane *hkl*.

hardly detectable in diffractograms of wires with a high accumulated drawing strain. Since the deviation of the latter reflection from the expected straight line is more pronounced for thinner wires, it can be concluded that the low peak height is causal for the deviation of the integral breadth of the 310 reflection. The reason for this is that a very shallow peak is difficult to fit properly with equation (8.22) and thus the broadening is not assessed properly. In future studies, this source of error for this reflection could be eliminated by increasing the exposure time at each angular step (see section 6.3.3). Since the 200 reflection is always higher than expected, fitting the peak and extracting the integral breadth should not be the source for the low value of ΔK. Hence, the deviation can be suspected to be an effect of the influence of the sharp fibre texture on the contrast factor. This conclusion would correspond to the observation that the deviation from the straight line is more pronounced for thinner wires, which exhibit a sharper texture (see section 8.3). Thus, a more detailed analysis of the potential influence of the preferred orientations observed in a fibre-textured material on its contrast factors should be performed in the future.

Apart from the discussed outliers, the integral breadths follow a linear course. Thus, two parameters describing the microstructure of the tungsten wires can be extracted from the model functions shown in figure 8.28: On the one hand, the size of coherently scattering domains, which is obtained from the intercept of the straight line with the ordinate. On the other hand, the term $M_{\mathrm{W}}^2\rho_{\mathrm{red}}$, i.e. the product of the square of the Wilkens factor and the redundant dislocation density, is given by the slope of the straight line. Both parameters are shown as a function of the accumulated drawing strain in figure 8.28.

The product $M_{\mathrm{W}}^2\rho_{\mathrm{red}}$ shows a monotonous increase with increasing accumulated drawing strain. Since the Wilkens factor M_{W} cannot be and also should not be attempted to be determined using the (modified) Williamson-Hall method [247], the evolution of the redundant dislocation density cannot be determined exactly. It is however reasonable to assume that the screening of dislocations increases with the accumulated drawing strain, since dislocations tend to form non-randomised structures such as dislocation boundaries or cell walls [306]. Thus, it can be concluded that the Wilkens factor most likely decreases with increasing strain accumulated during the drawing process. A strong argument for a decrease of M_{W} with increasing strain are the results of Scardi & Leoni [307]: Investigating the defect structure of ball-milled Ni powder as a function of milling time[19], they found that the Wilkens factor decreases with increasing milling time. Thus, a continuous plastic deformation leads to an enhanced screening of dislocations and thereby lowers M_{W}. Concluding that M_{W} decreases with increasing accumulated drawing strain and taking into account the monotonous increase of $M_{\mathrm{W}}^2\rho_{\mathrm{red}}$, it can be reasoned that the redundant dislocation density increases with the accumulated drawing strain. Again, this coincides well with the available literature (see figure 5.6) and the basic understanding of the drawing process [32].

The size D of coherently scattering domains shows a plateau for $\varphi \leq 4.0$, which is followed by a decrease of D with increasing accumulated drawing strain. It is worth noting that the coherently scattering domain size is smaller than the mean grain width acquired from EBSD orientation maps for the three thickest wires but coincides well with the values from EBSD for thinner wires. Qualitatively, the existence of the plateau of D for the three thickest wires is in line with the constant average grain width for these wires. Since the grain width decreases for the wire with $\varphi = 4.0$, it is surprising that the size of coherently scattering domains is still on the level of the three thickest wires. It can however be concluded that there are coherently scattering domains which are of more or less constant size in thick wires and are broken up into smaller domains once a certain drawing strain, in the case of tungsten wires, $\varphi \approx 4.0$ is exceeded. Due to the agreement of D and the mean grain width for $\varphi \geq 2.7$, it can be reasoned that the grains in these wires act as coherently scattering domains. Apart from the plateau observed for wires with a low accumulated

[19] The strain imparted on the powder increases with increasing milling time.

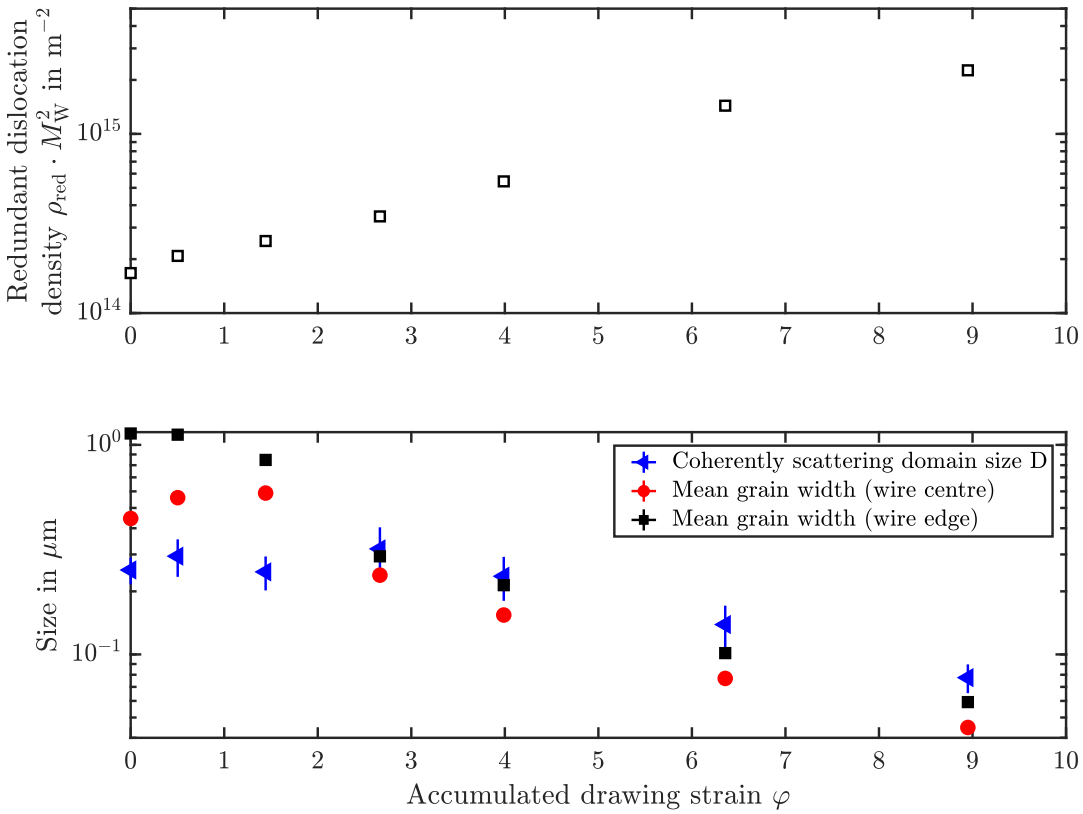

Figure 8.28: The product of the redundant dislocation density ρ_{red} and the square of the Wilkens factor M_W (top, logarithmic ordinate) as well as the coherently scattering domain size D (bottom) as a function of the accumulated drawing strain of tungsten wires. The lower subplot also contains the mean grain width determined from EBSD orientation maps of the centre and edge region of the drawn tungsten wires already shown in figure 8.18.

drawing strain, the XRD analysis furthermore confirms the decrease of grain size with increasing φ in drawn tungsten wires.

8.4.3 Conclusions on the evolution of microstructure and crystallographic texture during drawing of tungsten wire

Throughout the drawing process, significant changes in the microstructure and crystallographic texture of tungsten wires were observed. The starting point of wire drawing, i.e. the rod with a diameter of 3.6 mm, has a quite heterogeneous grain size and exhibits a texture, which is strongly influenced by the mode of deformation during Kocks milling. As an additional consequence of the elongation of the workpiece during milling, the grains in the rod are already elongated and the ⟨110⟩ axis is already aligned with the rod axis. Wire drawing then gradually transforms the microstructure by

- decreasing the grain width,
- increasing the grain curvature,
- increasing the fraction of high-angle grain boundaries at the expense of the fraction of low-angle grain boundaries,
- increasing the grain aspect ratio and
- increasing the dislocation density.

From the available data, it was difficult to verify that the grain length increases with accumulated drawing strain [199]. This is most likely due to the many short grains observed in LS orientation maps that decrease the mean grain length. Hence, a slight decrease of the grain length with increasing φ was observed. Due to the strong decrease in grain width with increasing accumulated drawing strain, the grain aspect ratio, defined as the ratio between mean grain length and mean grain width, however increases alongside φ. Pores are found in the microstructure of each tungsten wire investigated, although their origin is different: Pores in thick wires are most probably residual sintering pores or K bubbles, while pores in very thin wires ($\varphi \geq 9.0$) are believed to be caused by the deformation mode of the wires during drawing. A theoretical explanation or a modelling of the latter effect is so far not available in literature. The crystallographic texture of wires with $\varphi \geq 2.7$ can be described as ideal $\langle 110 \rangle$ fibre texture, that is getting sharper with increasing accumulated drawing strain.

8.5 Strengthening mechanisms in drawn tungsten wires

Taking the microstructural evolution of drawn tungsten wires during the wire drawing process into account, it is reasonable to assume that the strength of the wires increases both due to grain boundary strengthening and Taylor hardening. Since one has to assume that the superposition of both strengthening effects is nonlinear [126, 308, 309], the different contributions are not disentangled[20]. Rather, grain boundary strengthening and Taylor strengthening will be investigated separately in the following. During the analysis of grain boundary strengthening, it is thereby assumed that Taylor strengthening does not contribute to the strength of the investigated tungsten wires and vice versa. Since this approach is a strong oversimplification, the fitting parameters obtained from the analyses are not reported but only the qualitative contribution of a mechanism to the experimentally determined strength of drawn tungsten wires is investigated.

8.5.1 Grain boundary strengthening

In order to verify if grain refinement contributes to the increase in strength of tungsten wires, the method pioneered by Hall [134] and Petch [135] can be used. For this, the yield strength or ultimate tensile strength are plotted against the inverse square root of the grain size (see equation (4.22)). In the present study, the mean grain width $\langle w \rangle$ determined from EBSD orientation maps (see figure 8.17) in the edge and centre of the investigated tungsten wires is used as proxy for the grain size. The result is shown in figure 8.29.

Since $R_{\mathrm{p0.02}}$ and R_{m} follow straight lines, it is concluded that the thinning of elongated grains contributes to the high strength of tungsten wires according to the Hall-Petch model. Grain boundary strengthening in tungsten wires was shown for example by Meieran & Thomas [172] by annealing a wire with a diameter of 762 µm for different durations and subsequently investigating the relationship between tensile strength and the width of the elongated grains. The differences in the slope and initial stress σ_0 calculated using $R_{\mathrm{p0.02}}$ and R_{m}, respectively, can be traced back to the work hardening which occurs in the stress region $R_{\mathrm{p0.02}} < R \leq R_{\mathrm{m}}$.

8.5.2 Taylor/dislocation hardening

The contribution of an increase in dislocation density to the strength of a material is described by the Taylor equation (see equation (4.13) on page 19), which was already introduced in section 4.2.2.1. In the case of the drawn tungsten wires, the relation between strength and dislocation

[20] Note that the model used to investigate strain hardening of tungsten wires (see section 8.2) takes both fixed obstacles, i.e. predominantly grain boundaries in the case of tungsten wires, and forest dislocations into account.

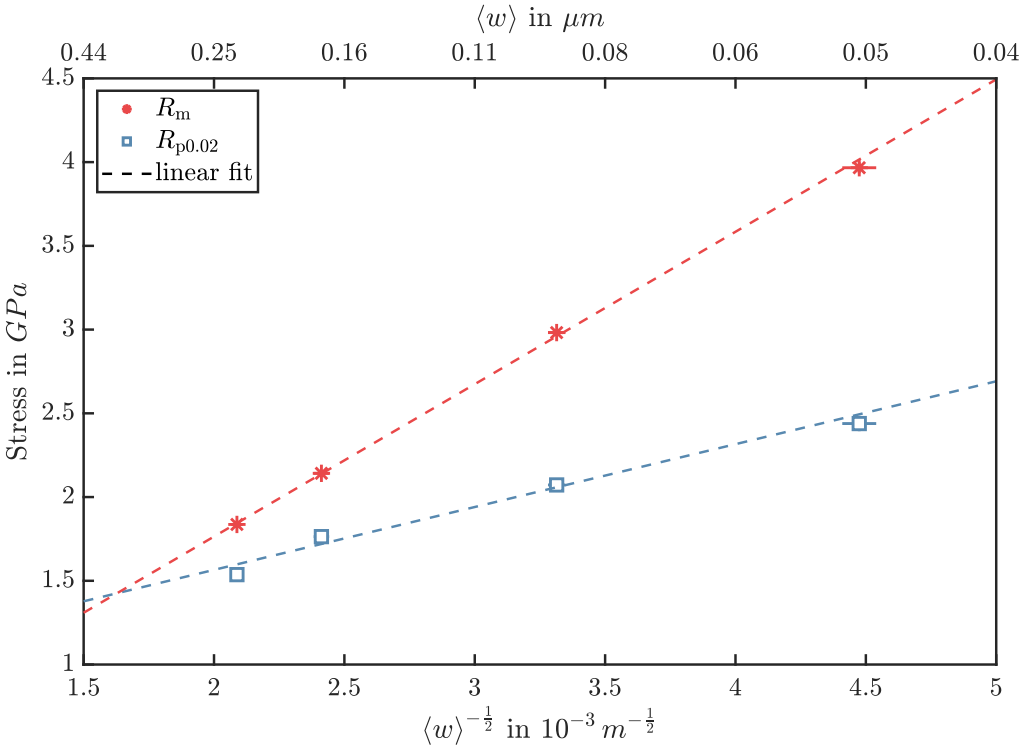

Figure 8.29: Yield strength $R_{p0.02}$ (blue squares) and ultimate tensile strength R_m (red stars) vs. inverse square root of the mean width of elongated grains determined from EBSD orientation maps of drawn tungsten wires with different accumulated drawing strains. The corresponding mean grain width is indicated on the upper x-axis (note that the axis does scale non-linearly with the mean grain width according to equation (4.22)). Linear fits to the different strength values according to the Hall-Petch model are drawn as straight dotted lines.

density can be investigated using the redundant dislocation density from XRD measurements (see section 8.4.2.6). Since the redundant dislocation density ρ_{red} cannot be disentangled from the Wilkens factor M_W, a plot of the true yield stress as a function of $\sqrt{\rho_{red}\, {M_W}^2} = \sqrt{\rho_{red}}\, M_W$ is shown in figure 8.30.

From the positive slope of the linear fit in figure 8.30 it can be deduced, that also the increase of the (redundant) dislocation density contributes to the strengthening of tungsten wires.

If one assumes that grain boundary strengthening does not contribute to the increased strength of tungsten wires with a higher accumulated drawing strain, an approximation of the Wilkens factor is possible. Multiplying equation (4.13) with the Wilkens factor M_W yields the following expression for M_W:

$$M_W = \frac{M_T\, \alpha\, \mu\, b}{m_{fit}} = 1.49 \pm 0.62 \tag{8.24}$$

where
M_W : Wilkens factor
m_{fit} : Slope of the linear function drawn in figure 8.30
$M_T = \sqrt{6}$: Taylor factor
μ : Shear modulus

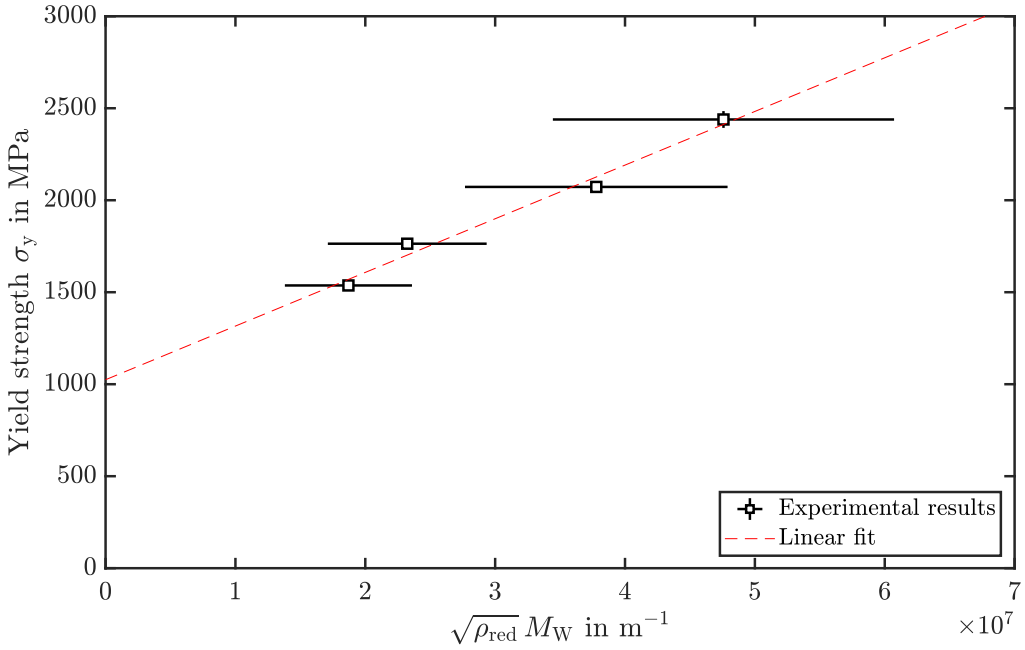

Figure 8.30: True yield stress as a function of the product of the square-root of the redundant dislocation density and the Wilkens factor for drawn tungsten wires. The dashed red line represents a linear fit to the experimental results.

α : Interaction coefficient
b : Norm of the Burgers vector

The approximated Wilkens factor extracted from the Taylor plot lies near the lower end of the reasonable range for M_W (see equation (5.21)) [246] and would thus indicate a very strong screening of dislocations in the tungsten wire samples. Low Wilkens factors are often observed for samples with a high dislocation density ($\rho > 5 \cdot 10^{15}\,\mathrm{m}^{-2}$) [301, 307]. According to Ungár et al. [306], a low Wilkens factor can be a sign for a non-randomised distribution of dislocations, for example high density boundaries and cell walls and low density between cells and/or boundaries. This conclusion would be in line with the observation by Barna et al. [191] and Meieran & Thomas [172], who found largely dislocation-free grains alongside grains and cell boundaries with a very high dislocation density when investigating tungsten wires with a diameter of 762 µm. Note again that the determined Wilkens factor should only be taken as a rough estimate, since the contribution of grain boundary strengthening to the increase of strength is completely neglected. Furthermore, it has to be assumed that the Wilkens factor is different between wires with different accumulated drawing strains, since they will most likely show variations in the distribution of dislocations. In this respect, a decrease of M_W with increasing φ (similar to the results of Scardi & Leoni [307] on ball-milled nickel) is expected (see also the discussion in section 8.4.2.6). For reliably determining the Wilkens factor, the Warren-Averbach method [240, 244, 247] should be applied, see [247].

8.6 Rate-controlling deformation mechanisms in drawn tungsten wires

According to [80], the deformation rate-controlling mechanisms can be determined from the order of magnitude and stress dependence of both the strain-rate sensitivity and the effective activa-

tion volume. Commonly, values of the strain-rate sensitivity and the activation volume without specification of the corresponding stress at which they were determined or values averaged over a large range of stresses are reported in literature. Table 8.6 shows some of those for pure tungsten materials tested at room temperature.

Table 8.6: Strain-rate sensitivities m and activation volumes V of different tungsten materials at room temperature. The values are put into context to the materials' logarithmic strain φ accumulated during cold deformation, their mean grain size L and the type of test by which m and V were obtained. Note that except the of Brunner & Glebovsky [101], who measured the effective activation volume, all other values are apparent activation volumes.

Material	φ	L in µm	Test	V in b^3	m	Source
High-purity SX	0	–	SRE[21], tensile test	14.1	14.6 MPa[22]	[101]
SX	0	–	SRJT, nanoindentation	6	0.024 ± 0.004	[102]
Flattened wire	3.6	1	SRJT, tensile test	10.3	–	[104]
UFG disk	4.3	0.5	SRJT, nanoindentation	5	–	[102]
UFG plate	?	5.4	SRJT, nanoindentation	8	0.021	[103]
Cold-rolled plate	2.5	0.52	SRJT, tensile test	15	0.030	[25]
	2.9	0.48			0.028	
	3.3	0.40			0.026	
	4.0	0.26			0.018	

Judging from the order of magnitude of the obtained effective activation volumes, two rate-controlling deformation mechanisms, namely the overcoming of the Peierls barrier via a kink-pair mechanism, and grain boundary sliding (GBS) have to be considered for the investigated tungsten wires. The characteristic activation volumes and strain-rate sensitivities of the mentioned mechanisms are summarised in table 8.7.

Table 8.7: Activation volumes and strain-rate sensitivities of grain boundary sliding and the kink-pair mechanism.

	Activation volume in b^3	Strain-rate sensitivity m
Grain boundary sliding [310]	1	$0.5 \ldots 1$
Kink-pair mechanism	10...100 [79]	see equation (4.8)

Grain boundary sliding is a deformation mechanism that is observed in coarse-grained (CG) materials at high homologous temperatures ($T > 0.5\,T_\mathrm{m}$), as well as in ultrafine-grained (UFG) or nanocrystalline (NC) materials at low temperatures [311]. GBS was postulated to be contributing to the deformation of tungsten wires during wire drawing and in mechanical tests by Millner et al. [200] in 1972 and before that already by Schultz [201] in 1959. Although stress-driven grain boundary motion has been observed in tungsten materials at room temperature [312], grain boundary sliding can be ruled out as the rate-controlling deformation mechanism during room temperature

[21] Only one relaxation cycle was performed and evaluated for each sample in this study, thus the experiment is called *stress relaxation experiment*.

[22] Brunner & Glebovsky [101] determined the strain-rate sensitivity of the tungsten single crystal via stress relaxation experiments. They used the following definition of the strain-rate sensitivity: $r = {}^{\partial\tau}/_{\partial\dot{\varepsilon}_\mathrm{pl}}\big|_T$, where r is the strain-rate sensitivity, τ the shear stress, T is the absolute temperature and $\dot{\varepsilon}_\mathrm{pl}$ the plastic strain rate. Hence, r has the dimension of a stress.

deformation of tungsten wires as a consequence of the present study's results. This is due to the fact that the three requirements for grain boundary sliding being the rate-controlling deformation mechanism are not met by the experimental results. Firstly, the determined activation volumes for the tungsten wires are too high for the commonly reported value of $1\,b^3$ for grain boundary sliding (cf. table 8.7). Secondly, the experimentally measured strain-rate sensitivity of the tungsten wires is too low ($m \ll 0.5$) for the grain boundary sliding mechanism [310]. Finally, grain boundary sliding is by definition a mechanism that depends on a material's grain boundary density. Thus, the contribution of GBS to the deformation of wires with a smaller grain size and in turn a higher grain boundary density should be higher. Since grain boundary sliding is characterised by a high strain-rate sensitivity (cf. table 8.7) [313], the strain-rate sensitivity of the tungsten wires should be increasing with decreasing grain size and thus increasing accumulated drawing strain [314]. Since the opposite is true (see figures 8.2 and 8.17 for the evolution of strain-rate sensitivity and grain size with φ, respectively), GBS is not likely to control the rate of plastic deformation of drawn tungsten wires at room temperature. This leaves the overcoming of the Peierls barrier by a kink-pair mechanism as the plausible rate-controlling deformation mechanism. This conclusion is in-line with current literature, which refers to the kink-pair mechanism controlling the rate of plastic deformation at temperatures below the knee temperature[23] in various tungsten materials as well as other refractory metals [114, 315], bridging the range from single crystals [100, 102] over coarse-grained materials [103] to ultrafine-grained materials [25, 102, 315]. There does not seem to be a significant influence of the manufacturing process (rolling, severe plastic deformation, powder metallurgical route with subsequent hot working) and the strain accumulated during working on the rate-controlling deformation process. With this conclusion, the up to now sole study on the rate-controlling deformation mechanism of a tungsten wire ($d = 635\,\mu\text{m}$) from $-196\,^\circ\text{C}$ to $327\,^\circ\text{C}$ [104], which was already interpreted as being indicative of a kink-pair mechanism by Pink & Gaál [199], is confirmed.

The decrease of the mean grain width and thus the increase of grain boundary density (see figures 8.18 and 8.22 for the decrease in grain width and length, respectively) in combination with the increase of the dislocation density (see sections 8.2.3 and 8.4.2.6) with increasing accumulated drawing strain should lead to an increase of the athermal stress component σ_μ. According to equation (4.7), this would explain the decrease of the mean strain-rate sensitivity with increasing φ. Methods for determining the athermal stress component are discussed in the outlook.

8.6.1 Conclusions on the rate-controlling deformation mechanisms in drawn tungsten wires

As mentioned before, the rate of plastic deformation of tungsten materials produced by different manufacturing processes and with different microstructures is always controlled by the formation and dissociation of kink pairs on $^{a_0}/_2\,\langle 111\rangle$ screw dislocations. Tungsten wires with different manufacturing histories and thus different microstructures and dislocation densities show starkly different ductile-to-brittle transition temperatures. from $200\,^\circ\text{C}$ to $300\,^\circ\text{C}$ for rolled, polycrystalline material [11, 12] to $-65\,^\circ\text{C}$ in heavily rolled plates [27] and $-148\,^\circ\text{C}$ in very thin wires [34]. Since the rate-controlling deformation mechanisms in all mentioned materials is the kink-pair mechanism, it cannot be responsible for the shift of T_{DBT}. This leaves the microstructure and crystallographic texture as cause for the anomalous ductility of cold-worked tungsten materials. Some thoughts on the influence of certain microstructural features on the ability of tungsten wires to deform plastically at low homologous temperatures will be presented and discussed in section 8.7.

[23] Knee temperature in tungsten: $T_{\text{K}} = 775\,\text{K}$ [101]

8.7 Modelling the influence of the microstructure of tungsten wires and other tungsten materials on their ductility using structure-property relations

As mentioned in section 1, one of the major aims of this study was to identify the reasons for the shift of the ductile-to-brittle transition temperature upon wire drawing in tungsten. Thus, in the following, the results of the microstructural characterisation and the mechanical testing are discussed first with respect to their influence on the ductile-to-brittle transition and the extent of ductility at room temperature. In subsequent sections, the derived model for the shift of T_{DBT} upon cold-working is applied to the deformation of wires at elevated temperatures, to wires in conditions different from the as-drawn state (annealed, ion-irradiated) and to hot-worked and cold-rolled tungsten plates, respectively.

8.7.1 Ductility of as-drawn tungsten wires at room temperature

8.7.1.1 Influence of the microstructure on the shift of T_{DBT}

As already mentioned in chapter 7, the mechanical tests performed on drawn tungsten wires with different accumulated drawing strains revealed that wires with $\varphi \geq 2.7$ ($d \leq 950\,\mu\mathrm{m}$) show ductile behaviour[24] when deformed at room temperature, while thicker wires with a lower accumulated drawing strain behave brittle at the same temperature. This result demonstrates that there is a shift of the wires' ductile-to-brittle transition temperature T_{DBT}. More precisely, $T_{\mathrm{DBT}} > 25\,^{\circ}\mathrm{C}$ for $\varphi < 2.7$ and $T_{\mathrm{DBT}} < 25\,^{\circ}\mathrm{C}$ for $\varphi \geq 2.7$. As already mentioned in section 1, the microstructure, mechanical properties and deformation mechanisms of the wires were analysed in order to be able to understand this shift of T_{DBT}. As summarised in section 8.6.1, there is no difference in the rate-controlling deformation mechanism between hot- and cold-worked tungsten; the kink-pair mechanism controls the rate of plastic deformation independently of grain morphology, crystallographic texture and dislocation density. The explanation for the different deformation mechanisms of heavily and less strongly cold-worked tungsten wires thus has to be rooted in the changes of the microstructure during cold-working. For this, the evolution of microstructural features during the wire drawing process will be analysed for structure-property relationships and their influence on the shift of the ductile-to-brittle transition.

When deforming a material sample with a given strain rate $\dot{\varepsilon}$ either in a controlled test (tensile test etc.) or during application, power has to be dissipated. The dissipated power per volume p can be described as the derivative of work w with respect to time t:

$$p = \frac{dw}{dt} \tag{8.25}$$

where p : Dissipated power per volume
w : Expended work per volume
t : Time

If the deformed sample or component is made from an engineering material, it is very likely to contain flaws, i.e. pores, inclusions or (micro)cracks. When deformed, the work can thus be dissipated by extending a crack starting at a random flaw. The work required for crack extension is intimately linked to the area of the new surfaces that have to be created, as well as the surface

[24] The ability to show ductile behaviour is evidenced by the finite uniform elongation ($\varepsilon_{\mathrm{u}} > 0$).

energy γ [107]. Cracks can thereby grow through the grain interior (transgranular) or along grain boundaries (intergranular). The corresponding work required for incrementally extending an existing crack will be denoted dw_c in the following.

The incremental work dw_{pl} required for plastically deforming the sample by an increment $d\varepsilon$ is given by Hosford [113] as

$$dw_{pl} = \sigma \, d\varepsilon \tag{8.26}$$

where dw : Increment of work per volume required to plastically deform a material with a strength σ by a strain increment $d\varepsilon$
σ : True stress
$d\varepsilon$: Strain increment

The two different modes of deformation mentioned above are illustrated schematically in figure 8.31.

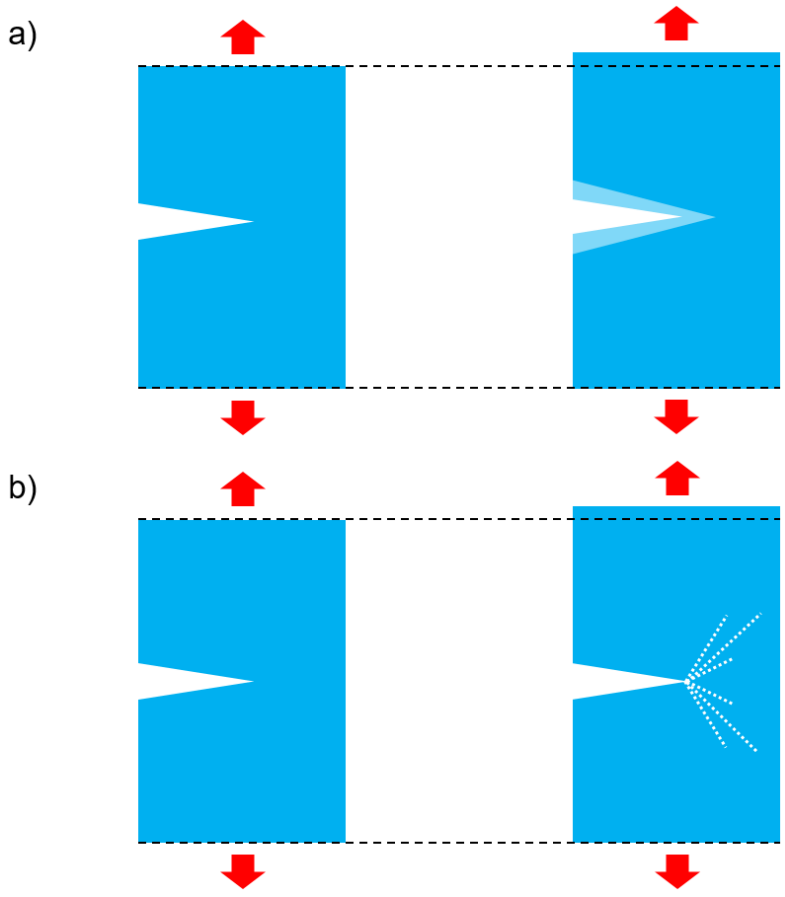

Figure 8.31: Sketch of a sample containing a crack. Under the influence of an external stress, the sample can lengthen either by propagating a crack (a) or by deforming plastically due to dislocation motion (b). The dashed lines in (b) represent slip lines as indicators for dislocation activity.

Whether the material sample deforms via crack growth or plastic deformation, is determined by which of the processes requires less work to incrementally deform the material:

$dw_c < dw_{pl}$: Brittle behaviour
$dw_c > dw_{pl}$: Plastic behaviour

In other words, a positive difference

$$\Delta dw = dw_c - dw_{pl}$$

is beneficial for plastic behaviour. It is convenient to define the critical accumulated drawing strain φ_{crit} as the accumulated drawing strain at which dw_c and dw_{pl} are equal (see figure 8.32). Similarly to the considerations outlined above, brittle behaviour is expected for wires with $\varphi < \varphi_{crit}$ and plastic deformability is predicted for wires with $\varphi \geq \varphi_{crit}$. φ_{crit} is thereby strongly temperature-dependent.

If the processes involved in the deformation of tungsten wires would be strongly rate-dependent, the discussion of the dissipated power instead of the incremental work according to equation (8.25) would be more reasonable. As the analysis in section 8.1 shows, the yield and ultimate tensile strength of the wires are not strongly strain-rate sensitive ($m \leq 0.025$). Thus, the rate-dependence can be neglected in a first-order approximation and the deformation process is not treated globally but focus is laid on the incremental steps of deformation by crack extension or dislocation slip. The subsequent discussion will thus focus on how the transformation of the microstructure with **increasing accumulated drawing strain** ($\varphi \uparrow$) influences the incremental work required for deforming the tungsten wires. These considerations allow for conclusions on how the microstructure controls the ductile-to-brittle transition in drawn tungsten wires, and how it thereby allows the wire to show plastic behaviour at low homologous temperatures. First, the influence of the microstructural changes on the incremental work required for crack extension (dw_c) will be discussed. These considerations are followed by a discussion of the changes in the incremental work linked to plastic deformation (dw_{pl}) due to the transformation of the microstructure.

dw_c

- **Dilution of impurities at grain boundaries due to small grain size:** $dw_c \uparrow$
  Certain foreign atoms like O, N, C, P and S, which have a low solubility in the b.c.c. lattice, tend to segregate to grain boundaries [316, 317]. There, they decrease the cohesion of the boundary and thus its resistance against intergranular crack growth [35, 115]. The decrease of grain size, which was shown from the decrease of the grain width (EBSD) and the decrease of the size of coherently scattering domains (XRD), in turn increases the grain boundary density in tungsten wires with increasing accumulated drawing strain. Hence, the number of foreign atoms per unit grain boundary length decreases. A lower concentration of foreign atoms with increasing φ increases grain boundary cohesion and hence the incremental work required to grow an existing intergranular crack.
- **Effective crack deflection due to increasing grain elongation and strong grain curling:** $dw_c \uparrow$
  Thin drawn tungsten wires show a very anisotropic fracture toughness [197]: Pfeifenberger et al. [318] report that the fracture toughness for transgranular crack growth is more than 4.2-times higher than that measured for intergranular in as-drawn tungsten wire. If intergranular crack growth is favoured, the increasing aspect ratio of the grains (see section 8.4.2.4) means that cracks that want to grow perpendicular to the wire direction (transversal), i.e. from one side of the wire to the other, need to travel along the length of a grain (longitudinal) before being able to grow transversely to the

wire direction again. The increase in grain curvature (curling) further extends[25] the intergranular crack length in longitudinal direction. This crack deflection leads to a significant increase in crack length and an increase in the incremental work required for intergranular crack growth. Pink & Sedlatschek [190] report a direct correlation between the increase in grain aspect ratio and the shift of the ductile-to-brittle transition to lower temperatures for worked and annealed molybdenum.

dw_{pl} - **Increased strength due to grain boundary and work hardening:** $\sigma \uparrow \Rightarrow dw_{\mathrm{pl}} \uparrow$
As discussed at length in sections 8.5.1 and 8.5.2, the decrease of grain width and the increase in dislocation density yield a strengthening of tungsten wire with increasing accumulated drawing strain. This increases the incremental work required for plastic deformation according to equation (8.26).

- **Decreased strength due to the presence of pores:** $\sigma \downarrow, \Rightarrow dw_{\mathrm{pl}}, \downarrow$
It was concluded (see section 8.4.3) that pores are present in all tungsten wires investigated in this study. Since the investigated wire series represents the whole wire drawing process, the existence of pores seems inevitable in drawn tungsten wires. Pores weaken the wires since they reduce the load-bearing cross-section (see equation (5.2)). Due to the low porosity level, the influence of this effect on the strength is however considered minor when compared to the increase of strength by grain boundary strengthening and work hardening.

In conclusion, the transformation of the microstructure with increasing accumulated drawing strain increases both the incremental work required for crack growth and for plastic deformation. Empirically, all wires with $\varphi \geq 2.7$ need to fulfil $dw_{\mathrm{c}} > dw_{\mathrm{pl}}$, since they show ductile behaviour. The evolution of the incremental work of both considered deformation modes is shown schematically in figure 8.32.

8.7.1.2 Influence of the microstructure on the onset of plastic instability at low homologous temperatures

So far, the ability of a wire with a certain microstructure to show ductility, i.e. to reach a finite plastic strain was discussed. This can be coherently explained using the model of incremental work discussed above. The extent of uniform plastic deformation is given by the uniform elongation ε_{u}. Uniaxial tensile tests revealed that the uniform elongation increases by more than 70 % if the accumulated drawing strain increases from 2.7 to 9.0. The thinnest wires tested ($\varphi = 10.8$) show a slight decrease in uniform elongation by 13 % when compared to the next thicker wire. The increase of tensile ductility with increasing accumulated working strain by rolling [26, 320] or severe plastic deformation [19, 21, 321] in pure tungsten have been reported in literature. So far, however, there is no universally valid explanation for the observed phenomenon. The onset of plastic instabilities (necking) and thus the end of uniform plastic deformation can be predicted using the work hardening behaviour (see instability criteria in section 8.2.5). For $\varepsilon \geq \varepsilon_{\mathrm{u}}$, plastic instabilities develop that lead to the formation of a neck and eventually to the sample's failure. Since the necking strain can be predicted using the applied work hardening model, the influence of changes of the different variables (k_2, β, σ_{i} and λ_{f}) can be assessed. This can be done using equation (4.16): A decrease in the coefficient β, the spacing between fixed obstacles λ_{f} and the recovery coefficient k_2 increase the work hardening rate and thus shift the intersection between θ and σ_{tr} to higher plastic strains, thereby increasing the necking elongation. An increase in σ_{i}

[25] Assume that the grains in a tungsten wire can be approximated by a helix (see figure 5.5b). A helical line can be approximated by the function $\vec{x} = (R\cos t, R\sin t, at)$, where R is the radius of the screw line, t is a continuous variable and $2\pi\, a$ is the helix' pitch (distance between turns) [319]. The ratio of the arc length of the helix after one turn to its pitch ($2\pi\, a$) is given as $a^{-1}\sqrt{R^2 + a^2}$. Since this ratio is larger than one $\forall\{a, R\} \in \mathbb{R} > 0$, the length of a curled grain is always larger than the one of an uncurled one for a constant radius R.

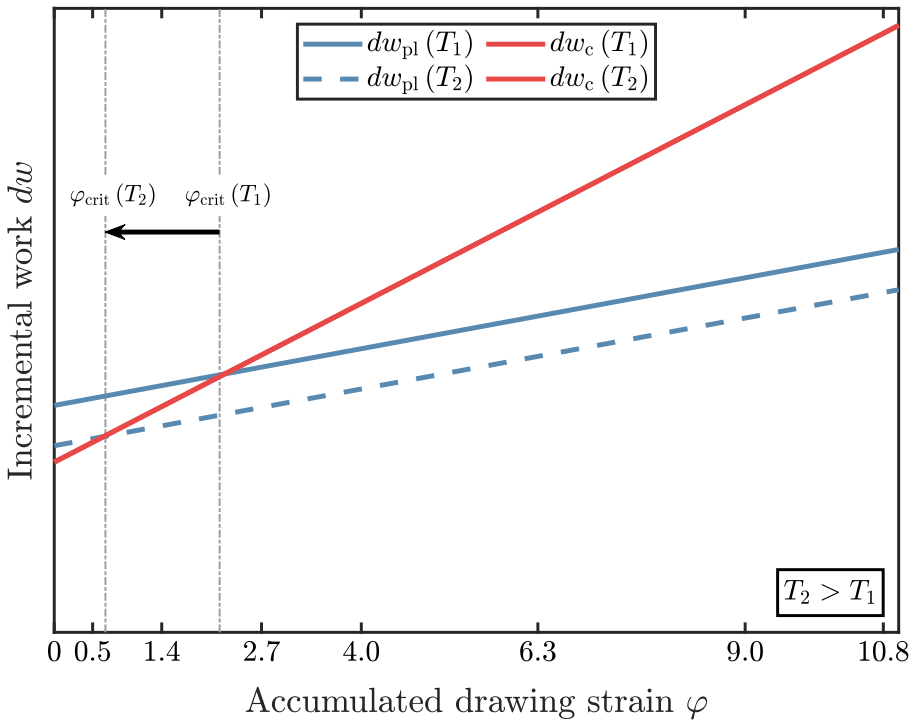

Figure 8.32: Schematic dependence of the incremental work associated with the processes controlling the ductile-brittle transition in drawn tungsten wires at a low temperature (T_1, solid lines) and an elevated temperature ($T_2 > T_1$, dashed lines). For the sake of simplicity and since the exact dependence is not known, a linear dependence of the incremental work on φ was assumed. The slopes and intercepts are chosen arbitrarily. The interceptions of dw_{pl} and dw_{c} are highlighted, since all wires with accumulated drawing strains below the critical accumulated drawing strain are brittle and all wires above φ_{crit} show ductile deformation behaviour. The example shows that wires with a lower accumulated drawing strain can show ductile behaviour at elevated temperatures (shift of the critical φ to lower values) when compared to elevated temperatures, which coincides with the experimental and theoretical findings related to the concept of the ductile-to-brittle transition.

increases the overall stress level. It does not influence the strain-hardening rate since it is added to the true stress and vanishes when the stress is differentiated with respect to plastic strain in order to calculate the strain-hardening rate (see equation 4.20). This is illustrated exemplarily in figure 8.33.

The beneficial influence of a decrease in k_2 was already verified theoretically and experimentally for different materials, among them Cu [281, 322], Fe [133, 274] and Mo [133]. The influence of the mean spacing between fixed obstacles on the necking strain is difficult to examine experimentally since working procedures like severe plastic deformation usually decrease the grain size, which is linked to λ_{f}, but at the same time increase k_2, as shown for example by Yasnikov et al. [280]. In their study, Yasnikov and co-workers conclude that the increase in grain boundary density due to grain refinement might give rise to a strong increase of dislocation annihilation-processes at grain boundaries. Blum & Zeng [323] derived a model that can account for this beneficial influence of the grains on the work-hardening behaviour. The model is deliberately developed for a material in which high-angle boundaries prevail, which is in agreement with the higher relative frequency of high-angle boundaries found in tungsten wires exhibiting higher accumulated drawing strains (see section 8.4.2.5).

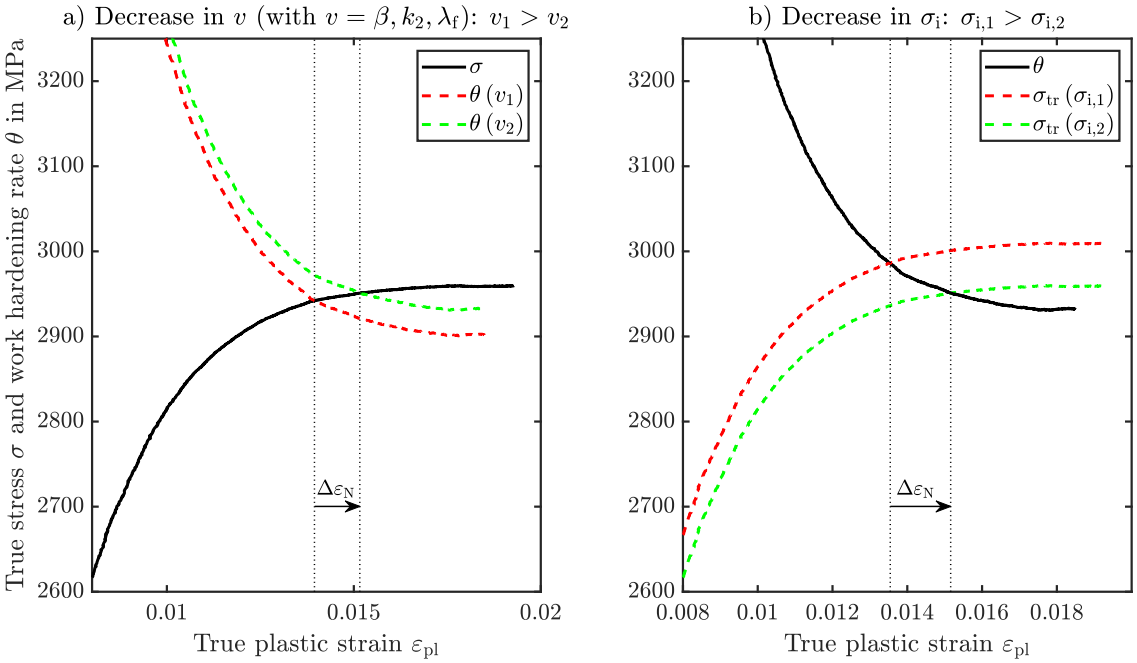

Figure 8.33: Illustration of the influence of a change in the variables of the strain-hardening model on the necking strain: a) A decrease in β, k_2 or λ_f increases the accumulation of dislocations and thus the work hardening rate. The dashed lines represent the work-hardening rate before (red) and after (green) a change in the mentioned variables. The solid black line represents the true stress-true strain curve of a tungsten wire obtained in a tensile test with a constant strain rate of $9.8 \cdot 10^{-5}\,\mathrm{s}^{-1}$ at room temperature. b) A decrease in the internal stress from a value $\sigma_{i,1}$ ($\sigma_{tr}\,(\sigma_{i,1})$, red dashed line) to $\sigma_{i,2}$ ($\sigma_{tr}\,(\sigma_{i,1})$, green dashed line) increases the total stress level, which is evident from the upward shift of the true stress. With this, the necking strain, which is given by the intersection of θ and σ_{true} (Considère criterion), shifts to higher values

In order to approximate the influence of the specific variables on the necking strain, the relative changes between subsequently drawn tungsten wires can be assessed. The related numbers can be found in table 8.8. The list clearly shows, that the monotonous increase in σ_i is always detrimental for higher necking strains. Literature on Ni [280] and Cu [281, 324] predicts that a strong increase of the necking elongation can be observed if k_2 decreases to values of $50 \ldots 80$ and only a very weak k_2 dependence of ε_u for higher values of the recovery coefficient. Since the values of k_2 for drawn tungsten wires are much higher than $50 \ldots 80$, there is no strong influence of k_2 on the necking strain expected. Thus, the increase of ε_u with increasing φ is mainly due to the more effective storage of dislocations due to the decrease in the coefficient β and the mean spacing between fixed obstacles λ_f. The decrease of ε_u for the thinnest wire investigated ($\varphi = 10.8$) is thus also clearly linked to the increase in β. Some ideas concerning suitable experiments for specifically studying the influence of certain microstructural features on the strain-hardening behaviour will be presented in section 10.

It should be noted briefly at this point that the presence of pores in the tungsten wires (see section 8.4.1) does not deteriorate the tensile ductility, and that the increase in porosity from the wire with $\varphi = 9.0$ to the one with $\varphi = 10.8$ cannot explain the observed decrease in uniform elongation. This is due to the fact that for $\varepsilon \leq \varepsilon_u$ the stress in the wire during tensile testing can be described as uniform. Thus, pores are contracted during straining and have no stress-concentrating influence. This influence is only relevant after plastic instability has arisen, and

Table 8.8: Overview over changes in the measured (engineering) uniform elongation and the four fitting variables (coefficient β, internal stress σ_i, mean spacing between fixed obstacles λ_f and recovery coefficient k_2) of the used strain hardening model between two subsequently drawn tungsten wires that were tested in uniaxial tensile tests at room temperature. Following the considerations discussed in section 8.7.1.2, the changes are coloured according to their influence on the necking strain (see also figure 8.33): Green numbers represent a shift of the predicted necking strain to higher values, while red numbers represent a shift to lower strains. In the case of ε_u, a green colouration means an increase and a red colouration a decrease. The original mean values of the fitting variables can be found in table 8.2.

	Relative change in...				
Change in φ	ε_u	β	k_2	σ_i	λ_f
$2.7 \rightarrow 4.0$	$(5 \pm 1)\,\%$	$(-57 \pm 17)\,\%$	$(17 \pm 11)\,\%$	$(15 \pm 2)\,\%$	$(3 \pm 26)\,\%$
$4.0 \rightarrow 6.4$	$(24 \pm 1)\,\%$	$(-91 \pm 2)\,\%$	$(16 \pm 7)\,\%$	$(16 \pm 2)\,\%$	$(-79 \pm 4)\,\%$
$6.4 \rightarrow 9.0$	$(33 \pm 1)\,\%$	$(-36 \pm 11)\,\%$	$(-25 \pm 4)\,\%$	$(4 \pm 2)\,\%$	$(-45 \pm 9)\,\%$
$9.0 \rightarrow 10.8$	$(-13 \pm 1)\,\%$	$(464 \pm 243)\,\%$	$(-27 \pm 5)\,\%$	$(37 \pm 4)\,\%$	$(-17 \pm 15)\,\%$

the neck has formed, since it locally changes the stress distribution to a multi-axial stress state [325]. The developing shear components can be concentrated at defects like pores and lead to a premature failure of the sample [326]. It can however be expected that porosity might be causal for wire drawing failures [177, 327], since the stress state during drawing also comprises shear stress components, especially in the wires' near-surface region [328, 329].

8.7.2 Temperature-dependent ductility of as-drawn tungsten wires

Having discussed the influence of certain microstructural features on the ductility of tungsten wires at room temperature, the temperature dependence of the different contributing processes will be assessed in the following. If the model presented in section 8.7.1.1 is valid, it should agree with the observations of the ductile-to-brittle transition of drawn tungsten wires. In the following, the change of the incremental work associated with the different modes of deformation for *increasing absolute temperature* ($\mathbf{T} \uparrow$) is discussed. It is thereby assumed that the temperature does not increase strongly enough to trigger dynamical recrystallisation processes during deformation.

dw_c: Since dynamical recrystallisation processes are not initiated, the grain morphology does not change. Thus, neither the concentration of foreign atoms at grain boundaries nor the grain length changes significantly. A higher temperature will hence leave dw_c largely unchanged. (see figure 8.32).

σ: Due to dynamical recovery, dislocations annihilate and their density decreases [10]. This decreases the contribution of work hardening to the strengthening of the tungsten wires. Due to the decrease of the Hall-Petch coefficient k_HP with increasing temperature [25], also the efficiency of grain boundary strengthening decreases. Since work hardening and grain boundary strengthening are less effective, the stress σ and thus the incremental work required for plastic deformation decreases (see equation (8.26)).

Apart from the specific incremental work, the elastic moduli of tungsten are also temperature-dependent. Since however both processes, namely dislocation slip and crack propagation, depend similarly on the elastic moduli, there is no qualitative difference at elevated temperature. Thus, in conclusion, the incremental work required for plastic deformation decreases while the work required for crack growth is not affected significantly by the increasing temperature. The temperature-dependent change of dw_pl is illustrated in figure 8.32. It clearly shows that elevating the deformation temperatures allows tungsten wires with a lower accumulated drawing strain to deform plastically since φ_crit, which is marked by the intersection of dw_pl and dw_c, is shifted to

lower φ.

8.7.3 Application of the model to other conditions of tungsten wires and other tungsten materials

The model described and discussed in the previous sections should also be able to explain the ductility of tungsten materials in states other than the as-drawn condition and should in addition also apply to other tungsten materials such as rolled tungsten plates with high and low accumulated rolling strains. The agreement is discussed in the following sections.

8.7.3.1 Annealed tungsten wire

The influence of annealing at different temperatures on the strength, ductility, and microstructure of drawn pure and AKS-doped tungsten wires were investigated by Riesch et al. [73] and Zhao and co-workers [202] using scanning electron microscopy and tensile testing at room temperature. Except for their difference in thermal stability, i.e. the onset temperature for recrystallisation processes, the results for both pure and doped wires are very similar: Annealing at 1000 °C removes the grain curling and reduces the dislocation density observed in the grain interior. Higher annealing temperatures yield grain growth and a further decrease of the dislocation density. The wires however remain ductile and only show a decrease in yield and ultimate strength as well as in uniform elongation. Simultaneously, the work hardening rate decreases. After annealing at a certain elevated temperature (pure tungsten wire: 1627 °C; AKS-doped tungsten wire 2100 °C), the wires show brittle fracture behaviour. This could in both cases be linked to abnormal grain growth and the loss of the elongated grain structure.

Using the model developed in order to explain ductility in as-drawn tungsten wires based on the evolution of their microstructure, the influence of annealing treatments can be assessed. Low-temperature annealing will

- decrease the stress σ entering dw_{pl} by decreasing the dislocation density ρ and increasing the grain width $\langle w \rangle$,
- and slightly increasing the concentration of foreign atoms at grain boundaries by an increase of grain width, which lowers grain boundary cohesion.

In summary, annealing at low temperatures slightly decreases dw_{pl}, while also decreasing dw_{c}. Since the elongated grain structure is however retained, $dw_{\mathrm{pl}} < dw_{\mathrm{c}}$ still holds and the wires still show ductile behaviour. Recrystallisation and abnormal grain growth due to high-temperature annealing however lead to a significant change in the incremental work required for deformation via the two discussed mechanisms: The loss of the elongated grain structure strongly decreases the energy dissipated for inter- and transgranular crack propagation. In addition, grain growth decreases the grain boundary area, prevents the dilution of foreign atoms at grain boundaries and thus further decreases the incremental work that is required for intragranular crack growth. All these effects yield a strong decrease in dw_{c}. Since this decrease is not balanced by the decrease in strength due to grain growth (less effective grain boundary strengthening) and recrystallisation (decrease of dislocation density and thus loss of strain hardening), deformation by crack extension is favoured ($dw_{\mathrm{c}} < dw_{\mathrm{pl}}$) and the wires no longer show ductile behaviour.

8.7.3.2 Irradiated tungsten wire

The influence of the fusion neutrons (peak energy for the D-T reaction: ca. 14 MeV [330]) on the plasma-facing components can currently not be investigated since no suitable neutron source is available. The displacement damage can however be simulated using ion irradiation [52]. Recent

studies [77] on the mechanical properties of thin tungsten wires ($d = 16\,\mu m$) after ion irradiation revealed that the wires show plastic deformation indicated by ductile fracture during room-temperature tensile tests even after an irradiation dose of up to 9 dpa. There was no irradiation hardening observed, but the ultimate tensile strength was rather shown to decrease with increasing irradiation dose. Ion irradiation mainly creates Frenkel pairs [51] and dislocation loops [52]. Thus, the model discussed in section 8.7.1.1 predicts a significant increase in strength σ due to the additional hardening of the irradiation obstacles. The reason the wires still show ductile behaviour should be that the high density of microstructural defects like forest dislocations or grain boundaries act as sinks for irradiation-induced point defects. This mechanism was for example predicted by Ovid'ko & Sheierman [331] for nanocrystalline materials and rationalised for metals by Wurster & Pippan [332]. The effect could recently be verified experimentally for a W-Re alloy by Armstrong & Britton [333] and for rolled tungsten plates by Zinovev et al. [334]. During ion bombardment, the microstructure of tungsten wires is not altered in other ways than the increase in density of irradiation defects. Since grain boundaries and forest dislocations appear to be able to act as sinks for point defects, irradiation hardening is suppressed. In this way, the microstructure of tungsten wires helps to retain their ductility and prevents them from failing brittle after ion irradiation.

8.7.3.3 Rolled tungsten plates

8.7.3.3.1 Hot-rolled tungsten plates

Hot-rolled tungsten plates are rolled at temperatures above their recrystallization temperature, i.e. the temperature at which half of the microstructure is recrystallized after annealing for 1 h [4, 10]. Thus, dynamical recrystallisation prevents grain refinement and yields a very low forest dislocation density [25]. The resulting material has a low strength σ, since neither strengthening by grain boundaries nor by forest dislocations is very effective. The strength is further decreased by the presence of residual sintering pores [335]. The dynamically recrystallised microstructure features grains with a low grain aspect ratio ($A < 5$ [335]). The combination of large grain size (high foreign atom concentration) and low grain aspect ratio (ineffective crack deflection) yields a very low incremental work that is needed for crack extension. Thus, $dw_c \ll dw_{pl}$ and the material deforms brittle at temperatures[26] $T < T_{DBT}$.

8.7.3.3.2 Cold-rolled tungsten plates

The evolution of the microstructure of cold-rolled tungsten plates is in many ways similar to the one of drawn tungsten wires [24, 28]: With increasing accumulated rolling strain, the grains get thinner in the directions perpendicular to the rolling direction. Thus, the grains adopt a "pancake"-like shape. Along with the change in grain morphology, the dislocation density increases and the emergence of a $\{001\}\langle 110\rangle$ (rotated cube [336]) texture is observed. As already mentioned in section 4.2.1.2.1, the ductile-to-brittle transition temperature of tungsten plates and wires decreases with increasing accumulated rolling strain. Due to the similarities in the corresponding microstructural evolution, the same considerations and conclusions discussed for drawn tungsten wires in section 8.7.1.1 apply also for tungsten plates. Differences can be found in the shape of the grains (pancake-like in rolled plates and elongated in wires) and the absence of the additional grain length-extending influence of grain curling in the plate. Since both materials show plasticity at low homologous temperatures, these differences do not seem to be significant.

[26] Note that the temperature dependence of the deformation mechanisms for tungsten plates are very similar to the ones of drawn wires discussed in section 8.7.2.

8.7.4 Conclusions on the developed model for describing the influence of the microstructure on the ductile-to-brittle transition of drawn tungsten wires

The previous sections showed that it is possible to describe the ductile-to-brittle transition and the temperature- and deformation-dependent ability to show plastic deformation of tungsten wires by using structure-property relationships. It was argued that the decrease of grain width, the increase of the grain aspect ratio and grain curvature with increasing accumulated drawing strain φ yield an increase in the incremental work that is required to deform the wire by both crack growth (dw_c) and plastic deformation (dw_pl). Using empirical considerations, it is argued that a wire with a certain accumulated drawing strain φ deforms ductile at a given temperature if $dw_\mathrm{pl} < dw_\mathrm{c}$. Once a certain critical accumulated strain $\varphi_\mathrm{crit}\,(T)$ has been exceeded in the drawing process, the wire shows plastic deformability at the temperature T. A direct relation between the ductile-to-brittle transition temperature and the sharpness of the crystallographic texture was not investigated in the present study. If the relation exists, its influence is believed to be secondary. The developed theory can also successfully describe the influence of the deformation temperature on the ductility of tungsten wires. Based on their specific microstructure, the ductility of tungsten wires in conditions other than the as-drawn state as well as the one of hot- and cold-rolled tungsten plates can be explained.

8.8 Implications for the use of tungsten wires and other tungsten materials in nuclear fusion

As discussed in section 1, the results gathered in the present study has implications for the use of tungsten wires as reinforcing fibres in tungsten fibre-reinforced composites and also for the deformation and ductilisation of tungsten materials intended for the use as plasma-facing materials in future fusion reactors. Apart from the superior high-temperature properties of tungsten wires and their thermal stability, the microstructure of the wires also seems to exhibit a high resistance against neutron-induced embrittlement. The high grain boundary density and the high dislocation density allow for the retention of ductile fracture behaviour after ion irradiation of tungsten wires [77]. Since the properties of the composite are largely determined by the mechanical behaviour of the wire [74], it can be expected, that also the composites retain their pseudo-ductile behaviour after neutron irradiation. Future studies should for example address the role of closed porosity (see section 8.4.1) for the uptake and retention of hydrogen isotopes.
In view of the ongoing efforts [337] to produce a bulk tungsten material that shows ductile behaviour, so far three pure, polycrystalline tungsten materials[27], namely rolled tungsten plates, severely plastically deformed tungsten and drawn tungsten wires, have been identified [114, 115]. All of these materials are first hot- and then cold-worked. Bulk cold-worked materials however can only be produced from plates[28] or SPD-processed tungsten. The specific materials properties of tungsten make it superior to other materials, especially at elevated temperatures [4]. At these temperatures, recovery and recrystallisation processes, above all grain growth, significantly transform the as-deformed microstructure. In this process, the materials' ductile-to-brittle transition temperature increases, which makes them lose their ductility at low homologous temperatures. Thus, in order to preserve the ductility of worked tungsten materials at high temperatures, particles or dopants like K exhibiting a microstructure-stabilising effect have to be added to the material. A successful example is the addition of potassium to tungsten and the working into wires which show exceptional thermal stability. The improvement of the thermal stability of tungsten plates using potassium has recently been investigated by Lied et al. [295, 339]. They could show that while there is some improvement in the microstructure's thermal stability, the distribution of the potassium reservoirs throughout the material is not as good as in tungsten wires due to the lower cold-working strain the plates accumulate during rolling. Substantially higher strain levels can be achieved in SPD processes when compared to rolling. Thus, it might be possible to achieve an elongation of potassium tubes high enough (bubble aspect ratio ≥ 8.89) [277] to make use of the Rayleigh instability and produce a fine distribution of potassium bubbles. This would yield a material, which shows ductile behaviour at low homologous temperatures due to the imparted cold-working strain and a high thermal stability of the microstructure So far, there have been several attempts to produce and characterise SPD-processed tungsten [19, 20, 164, 321, 340] but concurrent AKS-doping was not investigated yet.

[27] in contrast to W−Re alloys and single crystals
[28] A bulk material from thin tungsten plates can either be produced by starting the rolling process with a thicker ingot or by stacking and bonding several thin plates [338].

Chapter 9

Summary and conclusions

The ability of drawn tungsten wires to deform plastically at low homologous temperatures has been known since the patenting of the production of thin, ductile wires in 1912 [149, 341]. Nevertheless, the effect of the shift of the ductile-to-brittle transition temperature to lower temperatures with increasing cold-working strain still awaits a physically sound, mechanistic explanation. In order to gather new and robust data, the evolution of the mechanical properties, the microstructure and crystallographic texture of a series of drawn, potassium-doped[1] tungsten wires was investigated by means of complementary mechanical tests and a microstructural study using electron microscopic and X-ray diffraction techniques. The wire series covers the whole wire drawing process from the hammered rod, which represents the starting point of wire drawing and shows brittle fracture behaviour at room temperature, to very thin drawn wires, which are ductile at room temperature. All observed differences with respect to the deformation behaviour can be traced back to deformation-induced changes of the microstructure and the texture, since all wires investigated are successively drawn from the same sintered rod and hence exhibit the same chemical composition.

Uniaxial tensile tests revealed that wires with a diameter $d \leq 950\,\mu m$ are ductile at room temperature. If the accumulated drawing strain increases, i.e. the wire diameter decreases, the strength of the wires increases while the ductility does not deteriorate significantly. Thus, thin drawn tungsten wires evade the common strength-ductility trade-off. The wires gain their superior strength by grain boundary strengthening, i.e. the increase of strength due to the decrease of the width of elongated grains, as well as the beneficial effect of an increase in dislocation density with decreasing wire diameter. The room temperature strain hardening behaviour of the wires was successfully modelled using the Kocks-Mecking model. From this analysis it could be concluded that the recovery of the dislocations is achieved by cross-slip and annihilation of screw dislocation segments as expected for low-temperature deformation. The wires' accumulated drawing strain influences the storage of dislocations during work hardening: In thick wires, dislocations are predominantly stored at fixed obstacles, which are mainly grain boundaries. In thinner wires, the main storage occurs at forest dislocations. The modelling results line up well with the results acquired using EBSD and XRD analyses in terms of the evolution of defect density and grain morphology. The findings furthermore represent the first systematic study of the influence of cold-working on the strain-hardening behaviour of a polycrystalline, pure refractory metal using the Kocks-Mecking model. The model can also be used to predict the evolution of room-temperature ductility in the tungsten wires based on the microstructural evolution. The findings of this analysis are both in line with current literature and explain the increase of ductility with the accumulated cold-working strain, which was also seen for rolled and severely plastically deformed tungsten

[1] Potassium content: 75 wt. ppm

materials.

Using transient mechanical tests, namely strain rate jump tests and repeated stress relaxation experiments, it was shown that the formation and dissociation of kink pairs on screw dislocations determines the rate of plastic deformation of tungsten wires at room-temperature. The kink-pair mechanism is also rate-controlling during the plastic deformation of tungsten materials with vastly different microstructures from single crystals over polycrystalline materials to severely plastically deformed materials and also at different temperatures (depending on the ductile-to-brittle transition temperature of the respective material) up to the knee temperature of 775 K [101]. Hence, the shift of T_{DBT} upon cold-working must be linked to the deformation-induced microstructural and textural changes.

The wire drawing of tungsten changes many features of its microstructure and crystallographic texture: The texture of the hammered rod shows components that are due to the deformation mode during hammering. Drawing transforms this into a pronounced $\langle 110 \rangle$ fibre texture, which gets sharper as the wire diameter decreases. The rod and the wires after the first drawing stages exhibit a heterogeneous grain size distribution, but already feature an elongated grain shape. Upon further drawing, the grain width decreases. Due to the deformation of the grains by plane strain elongation during drawing, they have to bend around a $\langle 110 \rangle$ axis. The extent of grain bending was quantified for the first time in the present study. It was shown that the curvature of grains increases with increasing accumulated drawing strain. Due to the high number of short grains observed in orientation maps acquired from longitudinal section (LS) samples, the claim [66] of an increase in grain length with increasing accumulated drawing strain could not be verified. It is concluded that the length of individual grains increases alongside φ, but on average the grain length even decreases slightly with increasing φ. Due to the strong decrease in grain width, the grain aspect ratio, i.e. the ratio between grain length and width, increases with increasing accumulated drawing strain, especially for wires with $\varphi > 4.0$. EBSD analysis also reveals that wire drawing transforms the microstructure which is initially dominated by low-angle grain boundaries into a structure in which high-angle grain boundaries prevail.

In order to explain the change in ductility of drawn tungsten wires as a function of their accumulated drawing strain, an empirical model based on the incremental work required for deformation via crack propagation or plastic deformation was used in order to explain the shift of the ductile-to-brittle transition temperature. The model assumes that the deformation mode (brittle/ductile) is determined by whether the work required for crack propagation dw_{c} or the work required for dislocation-mediated plastic deformation dw_{pl} is lower. It was shown that increasing the strain accumulated during wire drawing changes the microstructure in a way that the incremental work required for crack extension dw_{c} increases, due to

- the increase of grain boundary cohesion by dilution of foreign atoms over a larger grain boundary area and
- a more effective crack deflection during intragranular crack growth due to the increase in grain aspect ratio.

On the other hand, the increase in accumulated drawing strain affects the work needed for plastic deformation dw_{pl} by

- increasing the dislocation density and decreasing the grain width, which strengthens the wires and increases dw_{pl}, while
- the increase in porosity, which decreases the load-bearing cross-section and with this also the work required for plastic deformation.

It can be empirically shown that the increase in dw_{c} with increasing φ is much stronger, so

that wires whose accumulated drawing strain exceed a certain threshold value fulfil $dw_c > dw_{pl}$ and deform plastically. The developed model can also explain the influence of temperature on the deformation behaviour and was successfully applied to describe the ductile-brittle transition in wires in other conditions (annealed/irradiated) or other tungsten materials like hot- and cold-rolled plates. Furthermore, no unique characteristics of tungsten could be identified that would hinder the application of this study's results to other group VI metals like Cr or Mo.

Chapter 10

Outlook

Supplementary analyses should be performed in the future in order to fill gaps that the current study left unfilled. In addition, the knowledge gathered in this study facilitates and stimulates new experiments that are worth performing in order to improve the understanding of the deformation of tungsten wires and the microstructural changes during wire drawing.

One of the main difficulties encountered in the present study was to perform both EBSD and XRD measurements on wires with a diameter of 16 µm. Owing to this shortcoming, the grain width and length of this wire had to be determined using other techniques in order to compare them to the thicker wires or even could not be obtained at all, as in the case of the crystallographic texture. The observed systematic differences, for example in the grain width between data extracted from EBSD orientation maps and STEM/SEM micrographs, are believed to be due to the different methods. Thus, it is proposed to prepare a TEM lamella of the wire using FIB techniques and subsequently determine the grain orientations using transmission Kikuchi diffraction (TKD) or transmission EBSD [342]. The benefit of transmission orientation mapping is that the interaction volume is much smaller than in standard EBSD. Hence, it offers a higher resolution, thereby making it the ideal technique for the study of heavily deformed microstructures. In order to determine the dislocation density of the thinnest wire using XRD, a suitable way to mount the wire in order to achieve sufficient count rates needs to be developed. Since the wire with a diameter of 16 µm is very attractive for the study of the synergistic loads present in a fusion environment [77] and has good qualities for the use as reinforcement fibre in tungsten fibre-reinforced composites, the proposed experiments are vital to comprehend the microstructural evolution and to construct valid structure-property relationships for this wire.

The excellent agreement between the experimentally determined stress-strain curves and the predictions of the Kocks-Mecking model substantiate the versatility of the concept. Since the work hardening of the wires in the as-drawn state can be predicted with sufficient accuracy, other wire conditions should be investigated in the future. This includes for example ion-irradiated or annealed wires. Analysing ion-irradiated tungsten wires using the Kocks-Mecking model would help to improve the understanding of the interaction of irradiation defects (vacancies, self-interstitial atoms, dislocation loops) with gliding dislocations and other microstructural constituents. Applying the transient mechanical tests to irradiated wires would allow for studying if irradiation softening [343–345], i.e. the improved mobility of kinks on dislocations in the presence of self-interstitial atoms, also occurs in polycrystalline materials. If this was not the case, it would corroborate the theory that the high number of defects in fine-grained materials acts as a sink for point defects and thus effectively prevents irradiation hardening.

In order to study the influence of the different variables on the strain hardening model, dedicated and expedient changes in the wire have to be triggered. The goal for such modifications would be to change only one variable independently. Some approaches are presented in the following:

- Upon low temperature annealing of doped, drawn tungsten wires, recovery processes lead to a decrease in the density and a change in the arrangement of forest dislocations but keep the grain morphology and the distribution of potassium bubbles largely unchanged [202]. Consequently, the storage of gliding dislocations at forest dislocations would be different from the observed mechanism in as-drawn wires. Thus, such kind of heat-treatments would offer the opportunity to study the parameter β and in addition its observed influence on the necking elongation.
- It was shown that the internal stress is also influenced by the potassium bubble distribution. Hence, studying a pure tungsten wire[1] with a similar grain morphology and a similar dislocation density as a wire contained in the series investigated in this study, would enable a more detailed analysis of the internal stress σ_i. The results might shed new light on the general influence of the potassium bubbles on the deformation behaviour and strength of drawn tungsten wires at low homologous temperatures.

Furthermore, the strain hardening model should also be applied to model the stress-strain characteristic of either cold-rolled tungsten plates or SPD-processed tungsten in order to study the influence of cold working-induced microstructural changes on the strain-hardening behaviour and the onset of plastic instabilities.

A more detailed study of the kink-pair mechanism, for example in terms of potential changes in the shape of the Peierls potential with the accumulated drawing strain, in tungsten wires is hindered by a lack of knowledge of the strain dependence of the athermal stress component. Using rapid stress reduction (strain dip) experiments as proposed by Gibbs [346] this dependence could be determined [347]. From the evolution of σ_μ as a function of strain, the stress dependence of the effective stress would be accessible. Then, the evolution of the effective activation volume as a function of the effective stress could be calculated and investigated further using equations 4.9 and 4.11 in order to decide if kink pairs on screw dislocations in tungsten wires are best described by the elastic interaction or the line tension approximation.

The combination of microstructural investigations and mechanical testing pursued in this study offers all the ingredients for crystal plasticity (CP) simulations [348]: The orientation data comprising information on grain morphology and orientation can be used to generate representative volume elements of the microstructure as input for CP simulations. This could be performed using the DREAM.3D software [349]. Using the results of transient mechanical tests and the strain hardening behaviour, the current material models for tungsten could be updated. MFront [350] would be suited to parameterise the material model for tungsten. Finally, using this optimised material model, the representative volume elements could be stressed in uniaxial tension and benchmarked against the experimentally determined stress-strain curves. Either an FFT-based, e.g. AMITEX [351, 352] or a FEM-based solver, e.g. ABAQUS® or Code_Aster [353], could be used to perform the mechanical analysis of the tungsten wire system. A valid crystal plasticity simulation for tungsten wires could then be used for studying the material's response to the synergistic loads present in a fusion reactor and help qualify tungsten as plasma-facing material

[1] The diameter of the wire should not be too small since it was shown that the potassium bubble distribution influences the spacing of fixed obstacles for very thin wires. Thus, if the chosen pure tungsten wire would be too thin, the comparability to the doped counterpart is not completely given since then the internal stresses could not be studied independently, but the change in λ_f would also have to be considered.

in future fusion reactors. Crystal plasticity would furthermore make the link between grain orientation and the interactions between dislocations with forest dislocations and grain boundaries accessible. Studying this relationship could shed new light on the potential influence of the observed change in crystallographic texture of tungsten wires during drawing on their mechanical behaviour and ductile-to-brittle transition.

Bibliography

[1] E. Lassner and W.-D. Schubert, *Tungsten: Properties, chemistry, technology of the element, alloys, and chemical compounds*, 1st ed. Springer, 1999, ISBN: 9781461372257. DOI: 10.1007/978-1-4615-4907-9.

[2] S. W. Yih and C. T. Wang, *Tungsten: Sources, Metallurgy, Properties and Applications*. New York and London: Plenum Press, 1979, ISBN: 0-306-31144-5.

[3] R. Bürgel, H. J. Maier, and T. Niendorf, *Handbuch Hochtemperatur-Werkstofftechnik: Grundlagen, Werkstoffbeanspruchungen, Hochtemperaturlegierungen und -beschichtungen* (Praxis), 4., überarbeitete Auflage. Wiesbaden: Vieweg+Teubner Verlag / Springer Fachmedien Wiesbaden GmbH Wiesbaden, 2011, ISBN: 9783834813886.

[4] G. W. Meetham and M. H. van de Voorde, "Refractory Metals," in *Materials for High Temperature Engineering Applications*, G. W. Meetham and M. H. van de Voorde, Eds., Berlin, Heidelberg: Springer Berlin Heidelberg, 2000, pp. 86–89, ISBN: 978-3-642-56938-8. DOI: 10.1007/978-3-642-56938-8-9.

[5] G. D. Rieck, *Tungsten and its compounds*, 1st ed. Oxford: Pergamon Press, 1967, ISBN: 9781483226118.

[6] J. W. Christian and B. C. Masters, "Low-temperature deformation of body-centred cubic metals I. Yield and How stress measurements," *Proceedings of the Royal Society of London. Series A. Mathematical and Physical Sciences*, vol. 281, no. 1385, pp. 223–239, 1964, ISSN: 0080-4630. DOI: 10.1098/rspa.1964.0179.

[7] C. St. John, "The brittle-to-ductile transition in pre-cleaved silicon single crystals," *Philosophical Magazine*, vol. 32, no. 6, pp. 1193–1212, 1975, ISSN: 1478-6435. DOI: 10.1080/14786437508228099.

[8] P. B. Hirsch, S. G. Roberts, and J. Samuels, "Dislocation mobility and crack tip plasticity at the ductile-brittle transition," *Revue de Physique Appliquée*, vol. 23, no. 4, pp. 409–418, 1988, ISSN: 0035-1687. DOI: 10.1051/rphysap:01988002304040900.

[9] P. B. Hirsch, S. G. Roberts, and J. Samuels, "The brittle-ductile transition in silicon. II. Interpretation," *Proceedings of the Royal Society of London. Series A. Mathematical and Physical Sciences*, vol. 421, pp. 25–53, 1989, ISSN: 0080-4630.

[10] J. Humphreys, G. S. Rohrer, and A. Rollett, *Recrystallization and Related Annealing Phenomena*, 3rd ed. Elsevier, 2017, ISBN: 9780080982359.

[11] E. Gaganidze, A. Chauhan, and J. Aktaa, "Fracture-mechanical behaviour of ITER grade tungsten subjected to three different rolling processes," *Fusion Engineering and Design*, vol. 184, 2022, ISSN: 09203796. DOI: 10.1016/j.fusengdes.2022.113300.

[12] A. Giannattasio and S. G. Roberts, "Strain-rate dependence of the brittle-to-ductile transition temperature in tungsten," *Philosophical Magazine*, vol. 87, no. 17, pp. 2589–2598, 2007, ISSN: 1478-6435. DOI: 10.1080/14786430701253197.

[13] P. L. Raffo, "Yielding and fracture in tungsten and tungsten-rhenium alloys," *Journal of the Less Common Metals*, vol. 17, no. 2, pp. 133–149, 1969, ISSN: 00225088. DOI: 10.1016/0022-5088(69)90047-2.

[14] W. D. Klopp, W. R. Witzke, and P. L. Raffo, *Mechanical Properties of Dilute Tungsten-Rhenium Alloys*, Springfield, Virginia, 1966.

[15] Y. Mutoh, K. Ichikawa, N. Nagata, and M. Takeuchi, "Effect of rhenium addition on fracture toughness of tungsten at elevated temperatures," *Journal of Materials Science*, vol. 38, pp. 770–775, 1995.

[16] J. Riesch, "Entwicklung und Charakterisierung eines wolframfaserverstärkten Wolfram-Verbundwerkstoffs," Doktorarbeit, Technische Universität München, München, 2012. [Online]. Available: https://pure.mpg.de/rest/items/item_2145498_1/component/file_2145497/content.

[17] J. Riesch *et al.*, "In situ synchrotron tomography estimation of toughening effect by semi-ductile fibre reinforcement in a tungsten-fibre-reinforced tungsten composite system," *Acta Materialia*, vol. 61, no. 19, pp. 7060–7071, 2013, ISSN: 13596454. DOI: 10.1016/j.actamat.2013.07.035.

[18] J. G. Hill and F. L. Banta, *Characterization of Wire-Wound Tungsten Composite*, 1971.

[19] H. Yuan, Y. Zhang, A. V. Ganeev, J. T. Wang, and I. V. Alexandrov, "Strengthening and Toughening Effect on Tungsten Subjected to Multiple ECAP," *Materials Science Forum*, vol. 667-669, pp. 701–706, 2010. DOI: 10.4028/www.scientific.net/MSF.667-669.701.

[20] I. V. Alexandrov, G. I. Raab, V. U. Kazyhanov, L. O. Sheastakova, R. Z. Valiev, and R. J. Dowding, "Ultrafine-Grained Tungsten Produced by SPD Techniques," in *Ultrafine Grained Materials II*, Wiley, 2002, pp. 199–207, ISBN: 9781118804537.

[21] Z. S. Levin and K. T. Hartwig, "Strong ductile bulk tungsten," *Materials Science and Engineering: A*, vol. 707, pp. 602–611, 2017, ISSN: 09215093. DOI: 10.1016/j.msea.2017.09.100.

[22] K. Xue, Y. Guo, J. Shi, X. Wei, and P. Li, "The brittle-to-ductile transition of pure tungsten processed by closed dual equal channel angular pressing process," *Materials Science and Engineering: A*, vol. 832, p. 142 513, 2022, ISSN: 09215093. DOI: 10.1016/j.msea.2021.142513. [Online]. Available: https://www.sciencedirect.com/science/article/pii/S0921509321017743.

[23] P. Schade, "100 years of doped tungsten wire," *International Journal of Refractory Metals and Hard Materials*, vol. 28, no. 6, pp. 648–660, 2010, ISSN: 02634368. DOI: 10.1016/j.ijrmhm.2010.05.003.

[24] S. Bonk, J. Reiser, J. Hoffmann, and A. Hoffmann, "Cold rolled tungsten (W) plates and foils: Evolution of the microstructure," *International Journal of Refractory Metals and Hard Materials*, vol. 60, pp. 92–98, 2016, ISSN: 02634368. DOI: 10.1016/j.ijrmhm.2016.06.020.

[25] S. W. Bonk, "Plastische Verformungsmechanismen in hochgradig kaltgewalzten, ultrafeinkörnigen Wolframblechen," Ph.D. Thesis, Karlsruher Institut für Technologie, Karlsruhe, 2018.

[26] S. Bonk, J. Hoffmann, A. Hoffmann, and J. Reiser, "Cold rolled tungsten (W) plates and foils: Evolution of the tensile properties and their indication towards deformation mechanisms," *International Journal of Refractory Metals and Hard Materials*, vol. 70, pp. 124–133, 2018, ISSN: 02634368. DOI: 10.1016/j.ijrmhm.2017.09.007.

[27] C. Bonnekoh, A. Hoffmann, and J. Reiser, "The brittle-to-ductile transition in cold rolled tungsten: On the decrease of the brittle-to-ductile transition by 600 K to 65 °C," *International Journal of Refractory Metals and Hard Materials*, vol. 71, pp. 181–189, 2018, ISSN: 02634368. DOI: 10.1016/j.ijrmhm.2017.11.017.

[28] C. Bonnekoh *et al.*, "The brittle-to-ductile transition in cold rolled tungsten plates: Impact of crystallographic texture, grain size and dislocation density on the transition temperature," *International Journal of Refractory Metals and Hard Materials*, vol. 78, pp. 146–163, 2019, ISSN: 02634368. DOI: 10.1016/j.ijrmhm.2018.09.010.

[29] C. Bonnekoh, J. Reiser, A. Hartmaier, S. Bonk, A. Hoffmann, and M. Rieth, "The brittle-to-ductile transition in cold-rolled tungsten sheets: the rate-limiting mechanism of plasticity controlling the BDT in ultrafine-grained tungsten," *Journal of Materials Science*, vol. 55, no. 26, pp. 12 314–12 337, 2020, ISSN: 0022-2461. DOI: 10.1007/s10853-020-04801-5.

[30] J. Reiser *et al.*, "Ductilisation of tungsten (W): On the shift of the brittle-to-ductile transition (BDT) to lower temperatures through cold rolling," *International Journal of Refractory Metals and Hard Materials*, vol. 54, pp. 351–369, 2016, ISSN: 02634368. DOI: 10.1016/j.ijrmhm.2015.09.001.

[31] J. Reiser, "Duktilisierung von Wolfram: Synthese, Analyse und Charakterisierung von Wolframlaminaten aus Wolframfolie," Dissertation, Karlsruher Institut für Technologie, Karlsruhe, 2012.

[32] J. A. Mullendore, "The Technology of Doped-Tungsten Wire Manufacturing," in *The Metallurgy of Doped/Non-Sag Tungsten*, E. Pink and L. Bartha, Eds., Essex: Elsevier Applied Science, 1989, pp. 61–82, ISBN: 1-85166-390-8.

[33] S. Leber, J. Tavernelli, D. D. White, and R. F. Hehemann, "Fracture Modes in Tungsten Wire," *Journal of the Less-Common Metals*, vol. 48, pp. 119–133, 1976.

[34] L. L. Seigle and C. D. Dickinson, *Refractory Metals and Alloys: Effect of Mechanical and Structural Variables on the Ductile-Brittle Transition in Refractory Metals*. New York: Interscience, 1963.

[35] A. M. Russell and K. L. Lee, *Structure-Property Relations in Nonferrous Metals*. Hoboken, New Jersey: Wiley-Interscience, 2005, ISBN: 978-0-471-64952-6.

[36] U. Stroth, *Plasmaphysik: Phänomene, Grundlagen, Anwendungen*, 1st ed. Vieweg + Teubner, 2011.

[37] A. Einstein, "Ist die Trägheit eines Körpers von seinem Energieinhalt abhängig?" *Annalen der Physik*, vol. 323, no. 13, pp. 639–641, 1905, ISSN: 00033804. DOI: 10.1002/andp.19053231314.

[38] G. McCracken and P. Stott, *Fusion: The Energy of the Universe*, 2nd ed. Elsevier and Academic Press, 2013, ISBN: 978-0-78-384656-3.

[39] S. Pfalzner, *An Introduction to Intertial Confinement Fusion*. Bacon Rota, Florida, USA: CRC Press, 2006, vol. Series in Plasma Physics, ISBN: 9781420011845.

[40] C. Breton, C. de Michelis, M. Finkenthal, and M. Mattioli, *Ionization Equilibrium of Selected Elements from Neon to Tungsten of Interest in Tokamak Plasma Research*, 1978.

[41] D. Naujoks, *Plasma-material interaction in controlled fusion* (Springer series on atomic, optical, and plasma physics). Berlin and New York: Springer, 2006, vol. 39, ISBN: 3540321489.

[42] T. S. Pedersen *et al.*, "Confirmation of the topology of the Wendelstein 7-X magnetic field to better than 1:100,000," *Nature communications*, vol. 7, p. 13 493, 2016. DOI: 10.1038/ncomms13493.

[43] B. Magaud, G. Marbach, and I. Cook, "Nuclear Fusion Reactors," in *Encyclopedia of Energy*, B. J. Cleveland, Ed., Elsevier Science, 2004, ISBN: 978-0-12-176480-7. DOI: 10.1016/B0-12-176480-X/00305-3.

[44] T. Okazaki, *Fusion Reactor Design: Plasma Physics, Fuel Cycle System, Operation and Maintenance*. Berlin: Wiley-VCH Verlag GmbH & Co. KGaA, 2021, ISBN: 978-3-527-41403-1.

[45] J. R. Rumble, Ed., *CRC Handbook of Chemistry and Physics*, Boca Rota, Florida.

[46] J. H. You *et al.*, "Divertor of the European DEMO: Engineering and technologies for power exhaust," *Fusion Engineering and Design*, vol. 175, p. 113 010, 2022, ISSN: 09203796. DOI: 10.1016/j.fusengdes.2022.113010.

[47] L. V. Boccaccini *et al.*, "Objectives and status of EUROfusion DEMO blanket studies," *Fusion Engineering and Design*, vol. 109-111, pp. 1199–1206, 2016, ISSN: 09203796. DOI: 10.1016/j.fusengdes.2015.12.054.

[48] P. Rindt, J. L. van den Eijnden, T. W. Morgan, and N. J. Lopes Cardozo, "Conceptual design of a liquid-metal divertor for the European DEMO," *Fusion Engineering and Design*, vol. 173, p. 112 812, 2021, ISSN: 09203796. DOI: 10.1016/j.fusengdes.2021.112812.

[49] T. W. Morgan, P. Rindt, G. G. van Eden, V. Kvon, M. A. Jaworksi, and N. J. L. Cardozo, "Liquid metals as a divertor plasma-facing material explored using the Pilot-PSI and Magnum-PSI linear devices," *Plasma Physics and Controlled Fusion*, vol. 60, no. 1, p. 014 025, 2018, ISSN: 0741-3335. DOI: 10.1088/1361-6587/aa86cd.

[50] R. Neu, "Tungsten as a plasma facing material in fusion devices," Habilitationsschrift, Eberhard-Karls-Universität zu Tübingen, Tübingen, 2003. [Online]. Available: https://pure.mpg.de/rest/items/item_2137808/component/file_2137807/content.

[51] J. Frenkel, "Über die Wärmebewegung in festen und flüssigen Körpern," *Zeitschrift für Physik*, vol. 36, pp. 652–669, 1926. DOI: 10.1007/BF01379812.

[52] G. S. Was, *Fundamentals of Radiation Materials Science*. New York, NY: Springer New York, 2017, ISBN: 978-1-4939-3436-2. DOI: 10.1007/978-1-4939-3438-6.

[53] K. Whittle, *Nuclear Materials Science*, 2nd ed. Bristol: IOP Publishing, 2020, ISBN: 978-0-7503-2376-5.

[54] J. Roth and K. Schmid, "Hydrogen in tungsten as plasma-facing material," *Physica Scripta*, vol. T145, p. 014 031, 2011, ISSN: 0031-8949. DOI: 10.1088/0031-8949/2011/T145/014031.

[55] J. P. Coad *et al.*, "Erosion/deposition issues at JET," *Journal of Nuclear Materials*, vol. 290-293, pp. 224–230, 2001, ISSN: 00223115.

[56] T. H. Courtney, *Mechanical Behaviour of Materials*, Second Edition. Long Grove, Illinois: Waveland Press, 2000, ISBN: 978-1-57766-425-3.

[57] R. Behrisch and W. Eckstein, *Sputtering by Particle Bombardement: Experiments and Computer Calculations from Threshold to MeV Energies* (Topics in Applied Physics), 1st ed. Berlin and Heidelberg: Springer, 2007, ISBN: 978-3-642-07944-3. DOI: 10.1007/978-3-540-44502-9.

[58] C. B. Alcock, V. P. Itkin, and M. K. Horrigan, "Vapour Pressure Equations for the Metallic Elements: 298–2500K," *Canadian Metallurgical Quarterly*, vol. 23, no. 3, pp. 309–313, 1984.

[59] F. Koch and H. Bolt, "Self passivating W-based alloys as plasma facing material for nuclear fusion," *Physica Scripta*, vol. T128, pp. 100–105, 2007, ISSN: 0031-8949. DOI: 10.1088/0031-8949/2007/T128/020.

[60] T. Wegener *et al.*, "Development and analyses of self-passivating tungsten alloys for DEMO accidental conditions," *Fusion Engineering and Design*, vol. 124, pp. 183–186, 2017, ISSN: 09203796. DOI: 10.1016/j.fusengdes.2017.03.072.

[61] A. Calvo *et al.*, "Self-passivating W-Cr-Y alloys: Characterization and testing," *Fusion Engineering and Design*, vol. 124, pp. 1118–1121, 2017, ISSN: 09203796. DOI: 10.1016/j.fusengdes.2017.03.001.

[62] A. Calvo *et al.*, "Self-passivating tungsten alloys of the system W-Cr-Y for high temperature applications," *International Journal of Refractory Metals and Hard Materials*, vol. 73, pp. 29–37, 2018, ISSN: 02634368. DOI: 10.1016/j.ijrmhm.2018.01.018.

[63] X. Hu, "Recent progress in experimental investigation of neutron irradiation response of tungsten," *Journal of Nuclear Materials*, vol. 568, 2022, ISSN: 00223115. DOI: 10.1016/j.jnucmat.2022.153856.

[64] W. Pantleon, "Thermal stability of the microstructure in rolled tungsten for fusion reactors," *Physica Scripta*, vol. 96, no. 12, p. 124 036, 2021, ISSN: 0031-8949. DOI: 10.1088/1402-4896/ac2854.

[65] M. Li and J.-H. You, "Interpretation of the deep cracking phenomenon of tungsten monoblock targets observed in high-heat-flux fatigue tests at 20 MW/m 2," *Fusion Engineering and Design*, vol. 101, pp. 1–8, 2015, ISSN: 09203796. DOI: 10.1016/j.fusengdes.2015.09.008.

[66] E. Pink and L. Bartha, Eds., *The Metallurgy of Doped/Non-Sag Tungsten*, 1st ed. Essex: Elsevier Applied Science, 1989, ISBN: 1-85166-390-8.

[67] M. Rieth *et al.*, "Recent progress in research on tungsten materials for nuclear fusion applications in Europe," *Journal of Nuclear Materials*, vol. 432, no. 1-3, pp. 482–500, 2013, ISSN: 00223115. DOI: 10.1016/j.jnucmat.2012.08.018.

[68] M. Rieth and A. Hoffmann, "Influence of microstructure and notch fabrication on impact bending properties of tungsten materials," *International Journal of Refractory Metals and Hard Materials*, vol. 28, no. 6, pp. 679–686, 2010, ISSN: 02634368.

[69] P. Krautwasser, H. Derz, and E. Kny, "Influence of fast neutron fluence on the ductile-brittle transition temperature of tungsten, W-10Re and W-3.4Ni-1.6Fe," *High Temperatures - High Pressures*, vol. 22, no. 1, pp. 25–32, 1990.

[70] S. Wurster, B. Gludovatz, and R. Pippan, "High temperature fracture experiments on tungsten-rhenium alloys," *International Journal of Refractory Metals and Hard Materials*, vol. 28, no. 6, pp. 692–697, 2010, ISSN: 02634368. DOI: 10.1016/j.ijrmhm.2010.03.002.

[71] M. Rieth *et al.*, "A brief summary of the progress on the EFDA tungsten materials program," *Journal of Nuclear Materials*, vol. 442, no. 1-3, S173–S180, 2013, ISSN: 00223115. DOI: 10.1016/j.jnucmat.2013.03.062.

[72] A. G. Evans, F. W. Zok, and J. Davis, "The Role of Interfaces in Fiber-Reinforces Brittle Matrix Composites," *Composites Science and Technology*, vol. 42, pp. 3–24, 1991. DOI: 10.1016/0266-3538(91)90010-M.

[73] J. Riesch *et al.*, "Development of tungsten fibre-reinforced tungsten composites towards their use in DEMO—potassium doped tungsten wire," *Physica Scripta*, vol. T167, p. 014 006, 2016, ISSN: 0031-8949. DOI: 10.1088/0031-8949/T167/1/014006.

[74] H. Gietl, J. Riesch, J. W. Coenen, T. Höschen, C. Linsmeier, and R. Neu, "Tensile deformation behavior of tungsten fibre-reinforced tungsten composite specimens in as-fabricated state," *Fusion Engineering and Design*, vol. 124, pp. 396–400, 2017, ISSN: 09203796. DOI: 10.1016/j.fusengdes.2017.02.054.

[75] R. Neu *et al.*, "Advanced tungsten materials for plasma-facing components of DEMO and fusion power plants," *Fusion Engineering and Design*, vol. 109-111, pp. 1046–1052, 2016, ISSN: 09203796. DOI: 10.1016/j.fusengdes.2016.01.027.

[76] D. Terentyev *et al.*, "Recent progress in the assessment of irradiation effects for in-vessel fusion materials: tungsten and copper alloys," *Nuclear Fusion*, vol. 62, no. 2, p. 026 045, 2022, ISSN: 0029-5515. DOI: 10.1088/1741-4326/ac4062.

[77] J. Riesch *et al.*, "Irradiation effects in tungsten—From surface effects to bulk mechanical properties," *Nuclear Materials and Energy*, vol. 30, p. 101 093, 2022, ISSN: 23521791. DOI: 10.1016/j.nme.2021.101093.

[78] J. Riesch *et al.*, "Chemically deposited tungsten fibre-reinforced tungsten – The way to a mock-up for divertor applications," *Nuclear Materials and Energy*, vol. 9, pp. 75–83, 2016, ISSN: 23521791. DOI: 10.1016/j.nme.2016.03.005.

[79] H. Conrad, "Thermally Activated Deformation of Metals," *Journal of Metals*, vol. 16, no. 7, pp. 582–588, 1964.

[80] D. Caillard and J. L. Martin, *Thermally Activated Mechanisms in Crystal Plasticity* (Pergamon Material Series), 1st ed. Amsterdam: Pergamon, 2003, vol. 8.

[81] E. Orowan, "Problems of plastic gliding," *Proceedings of the Physical Society of London*, vol. 52, pp. 8–22, 1940.

[82] A. Seeger, "The temperature dependence of the critical shear stress and of work-hardening of metal crystals," *The London, Edinburgh, and Dublin Philosophical Magazine and Journal of Science*, vol. 45, no. 366, pp. 771–773, 1954, ISSN: 1941-5982. DOI: 10.1080/14786440708520489.

[83] A. Seeger and U. Holzwarth, "Slip planes and kink properties of screw dislocations in high-purity niobium," *Philosophical Magazine*, vol. 86, no. 25-26, pp. 3861–3892, 2006, ISSN: 1478-6435. DOI: 10.1080/14786430500531769.

[84] V. I. Dotsenko, "Stress Relaxation in Crystals," *Physica Status Solidi (b)*, vol. 11, no. 93, pp. 11–43, 1979. DOI: 10.1046/j.0013-0427.2003.00027.x.

[85] J. Riedle, "Bruchwiderstand in Wolfram-Einkristallen: Einfluss der kristallographischen Orientierung, der Temperatur und der Lastrate," Dissertation, Universität Stuttgart, Stuttgart, 1995.

[86] V. Vitek and M. S. Duesburg, *Mechanical Properties of bcc Metals*. Warrendale: TMS-AIME, 1982.

[87] C. R. Weinberger, B. L. Boyce, and C. C. Battaile, "Slip planes in bcc transition metals," *International Materials Reviews*, vol. 58, no. 5, pp. 296–314, 2013, ISSN: 0950-6608. DOI: 10.1179/1743280412Y.0000000015.

[88] X. Liu, S. Golubov, C. Woo, and H. Huang, "Glide of edge dislocations in tungsten and molybdenum," *Materials Science and Engineering: A*, vol. 365, no. 1-2, pp. 96–100, 2004, ISSN: 09215093. DOI: 10.1016/j.msea.2003.09.012.

[89] A. Seeger, "Peierls barriers, kinks, and flow stress: Recent progress," *Zeitschrift für Metallkunde*, vol. 93, no. 8, pp. 760–777, 2002, ISSN: 0044-3093. DOI: 10.3139/146.020760.

[90] H.-D. Dietze, "Die Temperaturabhängigkeit der Versetzungsstruktur," *Zeitschrift für Physik*, vol. 132, pp. 107–110, 1952.

[91] P. M. Anderson, J. P. Hirth, and J. Lothe, *Theory of Dislocations*, 3rd edition. Cambridge University Press, 2017, ISBN: 9780521864367.

[92] F. Ackermann, H. Mughrabi, and A. Seeger, "Temperature- and Strain-Rate Dependence of the Flow Stress of Ultrapure Niobium Single Crystals in Cyclic Deformation," *Acta Metallurgica*, vol. 31, no. 9, 1983.

[93] L. Hollang, M. Hommel, and A. Seeger, "The Flow Stress of Ultra-High-Purity Molybdenum Single Crystals," *Physica Status Solidi (a)*, vol. 160, no. 2, pp. 329–354, 1997, ISSN: 00318965. DOI: 10.1002/1521-396X(199704)160:2<329::AID-PSSA329>3.0.CO;2-O.

[94] L. Hollang, D. Brunner, and A. Seeger, "Work hardening and flow stress of ultrapure molybdenum single crystals," *Materials Science and Engineering: A*, vol. 319-321, pp. 233–236, 2001, ISSN: 09215093. DOI: 10.1016/S0921-5093(01)01002-4.

[95] D. Brunner and J. Diehl, "Temperature and Strain-Rate Dependence of the Tensile Flow Stress of High-Purity α-Iron below 250 K. I. Stress/Temperature Regime III," *Physica Status Solidi (a)*, vol. 124, no. 455, pp. 455–464, 1991, ISSN: 00318965.

[96] D. Brunner and J. Diehl, "Temperature and Strain-Rate Dependence of the Tensile Flow Stress of High-Purity α-Iron below 250 K: II. Stress/Temperature Regime II and Its Transitions to Regimes I and III," *Physica Status Solidi (a)*, vol. 125, pp. 203–216, 1991, ISSN: 00318965.

[97] D. Brunner and J. Diehl, "Strain-Rate and Temperature Dependence of the Tensile Flow Stress of High-Purity α-Iron above 250 K (Regime I) Studied by Means of Stress-Relaxation Tests," *Physica Status Solidi (a)*, vol. 124, pp. 155–170, 1991, ISSN: 00318965.

[98] M. Werner, "Temperature and strain-rate dependence of the flow stress of ultrapure tantalum single crystals," *Physica Status Solidi (a)*, vol. 104, no. 1, pp. 63–78, 1987, ISSN: 00318965. DOI: 10.1002/pssa.2211040105.

[99] S. Takeuchi and K. Maeda, "Slip in high purity tantalum between 0.7 and 40 K," *Acta Metallurgica*, vol. 25, no. 12, pp. 1485–1490, 1977. DOI: 10.1016/0001-6160(77)90078-5.

[100] D. Brunner, "Comparison of Flow-Stress Measurements on High-Purity Tungsten Single Crystals with the Kink-Pair Theory," *Materials Transactions*, vol. 41, no. 1, pp. 152–160, 2000.

[101] D. Brunner and V. Glebovsky, "Analysis of flow-stress measurements of high-purity tungsten single crystals," *Materials Letters*, vol. 44, no. 3-4, pp. 144–152, 2000. DOI: 10.1016/S0167-577X(00)00017-3.

[102] D. Kiener, R. Fritz, M. Alfreider, A. Leitner, R. Pippan, and V. Maier-Kiener, "Rate limiting deformation mechanisms of bcc metals in confined volumes," *Acta Materialia*, vol. 166, pp. 687–701, 2019, ISSN: 13596454. DOI: 10.1016/j.actamat.2019.01.020.

[103] J. Kappacher, A. Leitner, D. Kiener, H. Clemens, and V. Maier-Kiener, "Thermally activated deformation mechanisms and solid solution softening in W-Re alloys investigated via high temperature nanoindentation," *Materials & Design*, vol. 189, p. 108 499, 2020, ISSN: 02641275. DOI: 10.1016/j.matdes.2020.108499.

[104] O. Boser, "The Temperature Dependence of the Flow-Stress of Heavily-Deformed Tungsten," *Journal of the Less-Common Metals*, vol. 23, pp. 427–435, 1971.

[105] D. Raabe, *Morde, Macht, Moneten: Metalle zwischen Mythos und High-Tech*. Weinheim: Wiley-VCH Verlag GmbH & Co. KGaA, 2001, ISBN: 9783527304196.

[106] J. Sumpter and J. S. Kent, "Prediction of ship brittle fracture casualty rates by a probabilistic method," *Marine Structures*, vol. 17, no. 8, pp. 575–589, 2004, ISSN: 09518339. DOI: 10.1016/j.marstruc.2005.03.003.

[107] W. D. Callister and D. G. Rethwisch, *Materials Science and Engineering: An Introduction*, 8th ed. Wiley, 2009, ISBN: 978-0-470-41997-7.

[108] C. W. Marschall and F. C. Holden, "Fracture Toughness of Refractory Metals and Alloys," in *High Temperature Refractory Metals*, R. W. Fountain, J. Malt, and L. S. Richardson, Eds., New York: Gordon and Breach Science Publishers, Inc., 1964, pp. 129–159.

[109] American Petroleum Institute, *API 579-1/ASME FFS-1*, 2021.

[110] E. Tarleton and S. G. Roberts, "Dislocation dynamic modelling of the brittle–ductile transition in tungsten," *Philosophical Magazine*, vol. 89, no. 31, pp. 2759–2769, 2009, ISSN: 1478-6435. DOI: 10.1080/14786430902992619.

[111] R. Eck, "Production and Properties of Powder Metallurgy Molybdenum and Tungsten Doped Wires," *METALL*, vol. 33, no. 8, pp. 819–827, 1979.

[112] J. Reiser and A. Hartmaier, "Elucidating the dual role of grain boundaries as dislocation sources and obstacles and its impact on toughness and brittle-to-ductile transition," *Scientific reports*, vol. 10, no. 1, p. 2739, 2020. DOI: 10.1038/s41598-020-59405-5.

[113] W. F. Hosford, *The Mechanics of Crystals and Textured Polycrystals*. New York and Oxford: Oxford University Press, 1993, ISBN: 978-0195077445.

[114] B. G. Butler *et al.*, "Mechanisms of deformation and ductility in tungsten – A review," *International Journal of Refractory Metals and Hard Materials*, vol. 75, pp. 248–261, 2018, ISSN: 02634368. DOI: 10.1016/j.ijrmhm.2018.04.021.

[115] C. Ren, Z. Fang, M. Koopman, B. Butler, J. Paramore, and S. Middlemas, "Methods for improving ductility of tungsten - A review," *International Journal of Refractory Metals and Hard Materials*, vol. 75, pp. 170–183, 2018, ISSN: 02634368. DOI: 10.1016/j.ijrmhm.2018.04.012.

[116] G. I. Taylor, "The mechanism of plastic deformation of crystals. Part I.—Theoretical," *Proceedings of the Royal Society of London. Series A. Mathematical and Physical Sciences*, vol. 145, no. 855, pp. 362–387, 1934, ISSN: 0080-4630.

[117] H. Wiedersich, "Hardening Mechanisms and the Theory of Deformation," *Journal of Metals*, vol. 16, pp. 425–430, 1964.

[118] A. D. Rollett and U. F. Kocks, "A Review of the Stages of Work Hardening," in *Dislocations 93: Microstructures and Physical Properties*, J. Rabier, A. George, Y. Brechet, and L. Kubin, Eds., vol. 1, Trans Tech Pubn, 1993, ISBN: 978-3908450023.

[119] U. F. Kocks and H. Mecking, "Physics and phenomenology of strain hardening: The fcc case," *Progress in Materials Science*, vol. 48, pp. 171–273, 2003.

[120] E. Voce, "The relation between stress and strain for homogenous deformation," *Journal of the Institute of Metals*, vol. 74, pp. 537–562, 1948.

[121] U. F. Kocks, "Laws for Work-Hardening and Low-Temperature Creep," *Journal of Engineering Materials and Technology*, vol. 98, no. 1, pp. 76–85, 1976, ISSN: 0094-4289. DOI: 10.1115/1.3443340.

[122] E. Aernoudt, J. Gil Sevillano, and P. van Houtte, in *Constitutive Relations and Their Physical Basis*, S. I. Andersen *et al.*, Eds., Roskilde: Risø National Laboratory, 1987, ISBN: 87-550-1331-7.

[123] M. J. Zehetbauer, "Cold Work Hardening in Stages IV and V of F.C.C. Metals: II. Model fits and Physical Results," *Acta Metallurgica et Materialia*, vol. 41, no. 2, pp. 589–599, 1993.

[124] M. J. Zehetbauer and V. Seumer, "Cold Work Hardening in Stages IV and V of F.C.C. Metals: I. Experiments and Interpretation," *Acta Metallurgica et Materialia*, vol. 41, no. 2, pp. 577–588, 1993.

[125] Y. Estrin and H. Mecking, "A Unified Phenomenological Description of Work Hardening and Creep based on One-Parameter Models," *Acta Metallurgica*, no. 1, pp. 57–70, 1983.

[126] H. Mecking and U. F. Kocks, "Kinetics of Flow and Strain-Hardening," *Acta Metallurgica*, vol. 29, pp. 1865–1875, 1981.

[127] U. F. Kocks and A. S. Argon, "Thermodynamics and Kinetics of Slip," *Progress in Materials Science*, vol. 19, 1974.

[128] Y. Estrin, "Dislocation-Density-Related Constitutive Modeling," in *Unified Constitutive Laws of Plastic Deformation*, A. S. Krausz and K. Krausz, Eds., San Diego: Academic Press, 1996, pp. 69–107, ISBN: 0-12-425970-7.

[129] U. Essmann and H. Mughrabi, "Annihilation of dislocations during tensile and cyclic deformation and limits of dislocation densities," *Philosophical Magazine A*, vol. 40, no. 6, pp. 731–756, 1979, ISSN: 0141-8610. DOI: 10.1080/01418617908234871.

[130] D. Breuer, W. Pantleon, U. Martin, U. Mühle, H. Oettel, and O. Vöhringer, "Modelling of the creep behaviour of a cobalt-based alloy by applying the Kocks-Mecking model," *Physica Status Solidi (a)*, vol. 150, no. 1, pp. 281–295, 1995, ISSN: 00318965. DOI: 10.1002/pssa.2211500125.

[131] J. W. Dunlop, Y. Bréchet, L. Legras, and Y. Estrin, "Dislocation density-based modelling of plastic deformation of Zircaloy-4," *Materials Science and Engineering: A*, vol. 443, no. 1-2, pp. 77–86, 2007, ISSN: 09215093. DOI: 10.1016/j.msea.2006.08.085.

[132] G. Langford and M. Cohen, "Strain Hardening of Iron by Severe Plastic Deformation," *Transaction of the ASM*, vol. 62, pp. 623–638, 1969.

[133] G. A. Malygin, "Structure factors that influence the stability of plastic strain of bcc metals under tensile load," *Physics of the Solid State*, vol. 47, no. 5, pp. 896–902, 2005.

[134] E. O. Hall, "The Deformation and Ageing of Mild Steel: III Discussion of Results," *Proceedings of the Physical Society. Section B*, vol. 64, no. 9, pp. 747–753, 1951, ISSN: 0370-1301. DOI: 10.1088/0370-1301/64/9/303.

[135] N. J. Petch, "The Cleavage Strength of Polycrystals," *Journal of the Iron and Steel Institute*, vol. 174, no. 25-28, 1953.

[136] Y. Li, A. J. Bushby, and D. J. Dunstan, "The Hall-Petch effect as a manifestation of the general size effect," *Proceedings. Mathematical, physical, and engineering sciences*, vol. 472, no. 2190, p. 20 150 890, 2016, ISSN: 1364-5021. DOI: 10.1098/rspa.2015.0890.

[137] A. Turnbull and E. R. de los Rios, "The Effect of Grain Size on the Fatigue of Commercially Pure Aluminium," *Fatigue & Fracture of Engineering Materials and Structures*, vol. 18, no. 12, pp. 1455–1467, 1995, ISSN: 8756-758X. DOI: 10.1111/j.1460-2695.1995.tb00868.x.

[138] Z. C. Cordero, B. E. Knight, and C. A. Schuh, "Six decades of the Hall–Petch effect – a survey of grain-size strengthening studies on pure metals," *International Materials Reviews*, vol. 61, no. 8, pp. 495–512, 2016, ISSN: 0950-6608. DOI: 10.1080/09506608.2016.1191808.

[139] J. D. Eshelby, F. C. Frank, and F. Nabarro, "XLI. The equilibrium of linear arrays of dislocations," *The London, Edinburgh, and Dublin Philosophical Magazine and Journal of Science*, vol. 42, no. 327, pp. 351–364, 1951, ISSN: 1941-5982. DOI: 10.1080/14786445108561060.

[140] A. H. Cottrell and B. A. Bilby, "Dislocation Theory of Yielding and Strain Ageing of Iron," *Proc. Phys. Soc. A (Proceedings of the Physical Society. Section A)*, no. 62, pp. 49–62, 1949.

[141] J. C. M. Li, "Petch Relation and Grain Boundary Sources," *Transaction of the Metallurgical Society of AIME*, vol. 227, pp. 239–247, 1963.

[142] L. E. Murr, "Some observations of grain boundary ledges and ledges as dislocation sources in metals and alloys," *Metallurgical Transactions A*, vol. 6, no. 3, pp. 505–513, 1975, ISSN: 0360-2133. DOI: 10.1007/BF02658408.

[143] L. E. Murr, "Dislocation Ledge Sources: Dispelling the Myth of Frank–Read Source Importance," *Metallurgical and Materials Transactions A*, vol. 47, no. 12, pp. 5811–5826, 2016, ISSN: 1073-5623. DOI: 10.1007/s11661-015-3286-5.

[144] M. F. Ashby, "The deformation of plastically non-homogeneous materials," *The Philosophical Magazine: A Journal of Theoretical Experimental and Applied Physics*, vol. 21, no. 170, pp. 399–424, 1970, ISSN: 0031-8086. DOI: 10.1080/14786437008238426.

[145] H. Conrad, S. Feuerstein, and L. Rice, "Effects of Grain Size on the Dislocation Density and Flow Stress of Niobium," *Materials Science and Engineering*, no. 2, pp. 157–168, 1967, ISSN: 00255416.

[146] K.-H. Chia, K. Jung, and H. Conrad, "Dislocation density model for the effect of grain size on the flow stress of a Ti–15.2 at.% Mo β-alloy at 4.2–650K," *Materials Science and Engineering: A*, vol. 409, no. 1-2, pp. 32–38, 2005, ISSN: 09215093. DOI: 10.1016/j.msea.2005.03.117.

[147] H. Conrad, "Effect of grain size on the lower yield and flow stress of iron and steel," *Acta Metallurgica*, vol. 11, pp. 75–77, 1963.

[148] G. Langford and M. Cohen, "Calculation of cell-size strengthening of wire-drawn iron," *Metallurgical Transactions A*, vol. 1, no. 5, pp. 1478–1480, 1970.

[149] C. L. Briant and B. P. Bewlay, "The Coolidge Process for Making Tungsten Ductile: The Foundation of Incandescent Lightning," *MRS Bulletin*, pp. 67–73, 1995.

[150] A. Pacz, "Metal and its Manufacture," 1,410,499, 1922.

[151] J. W. S. Rayleigh, "On the instability of Jets," *Proceeding of the London Mathematical Society*, vol. 10, no. 4, 1878.

[152] P. Schade, "Potassium bubble growth in doped tungsten," *International Journal of Refractory Metals and Hard Materials*, vol. 16, pp. 77–87, 1997, ISSN: 02634368. DOI: 10.1016/S0026-0657(99)80183-0.

[153] *Member States approve the phasing-out of incandescent bulbs by 2012*, Brussels, 2008. [Online]. Available: https://ec.europa.eu/commission/presscorner/detail/en/IP_08_1909.

[154] H.-J. Lunk, "Incandescent lighting and powder metallurgical manufacturing of tungsten wire," *ChemTexts*, vol. 1, no. 1, 2015. DOI: 10.1007/s40828-014-0003-8.

[155] A. Kelly and W. R. Tyson, "Tensile Properties of Fibre Reinforced Metals: II. Creep of Silver-Tungsten," *J. Mech. Phys. Solids*, vol. 14, pp. 177–186, 1966.

[156] A. Kelly and H. Lilholt, "Stress-strain curve of a fibre-reinforced composite," *Philosophical Magazine*, vol. 20, no. 164, pp. 311–328, 1969, ISSN: 1478-6435. DOI: 10.1080/14786436908228703.

[157] A. Wolfenden and J. M. Wolla, "Mechanical damping and dynamic modulus measurements in alumina and tungsten fibre-reinforced aluminium composites," *Journal of Materials Science*, vol. 24, no. 9, pp. 3205–3212, 1989, ISSN: 0022-2461. DOI: 10.1007/BF01139042.

[158] R. C. Wetherhold and L. J. Westfall, "Thermal cycling of tungsten-fibre-reinforced superalloy composites," *Journal of Materials Science*, vol. 23, pp. 713–717, 1988. DOI: 10.1016/0010-4361(88)90174-7.

[159] A. W. H. Morris and A. Burwood-Smith, "Some properties of a fibre-reinforced nickel-base alloy," *Fibre Science and Technology*, vol. 3, pp. 53–78, 1970. DOI: 10.1016/0010-4361(70)90308-3.

[160] D. H. Bowen, "Fibre-reinforced Ceramics," *Fibre Science and Technology*, vol. 1, pp. 85–112, 1968.

[161] R. Neu *et al.*, "Tungsten fibre-reinforced composites for advanced plasma facing components," *Nuclear Materials and Energy*, vol. 12, pp. 1308–1313, 2017, ISSN: 23521791. DOI: 10.1016/j.nme.2016.10.018.

[162] A. von Müller *et al.*, "Melt infiltrated tungsten–copper composites as advanced heat sink materials for plasma facing components of future nuclear fusion devices," *Fusion Engineering and Design*, vol. 124, pp. 455–459, 2017, ISSN: 09203796. DOI: 10.1016/j.fusengdes.2017.01.042.

[163] M. N. Samodurova, O. I. Karandaeva, V. R. Khramshin, and I. V. Liubimov, "Calculating Power Parameters of Rolling Mill Based on Model of Deformation Zone with Four-Roll Passes," *Machines*, vol. 8, no. 4, p. 73, 2020. DOI: 10.3390/machines8040073.

[164] S. Alexandrov, Y.-M. Hwang, and H. S. R. Tsui, "Determining the Drawing Force in a Wire Drawing Process Considering an Arbitrary Hardening Law," *Processes*, vol. 10, no. 7, p. 1336, 2022. DOI: 10.3390/pr10071336.

[165] C. J. Smithells, *Tungsten: A Treatise on its Metallurgy, Properties and Applications*, 1st ed. Chapman & Hall Ltd., 1927.

[166] C. Agte and J. Vacek, *Wolfram und Molybdän*. Berlin: Akademie Verlag, 1959.

[167] S. Zhou, J. Yang, Y. Zhang, P. Zhang, and Z. Nie, "Effect of grain size on rotary swaging of sintered tungsten rod," *Journal of Materials Research and Technology*, vol. 15, pp. 6434–6441, 2021, ISSN: 22387854. DOI: 10.1016/j.jmrt.2021.11.079.

[168] X. Zhang, Q. Yan, S. Lang, M. Xia, and C. Ge, "Texture evolution and basic thermal–mechanical properties of pure tungsten under various rolling reductions," *Journal of Nuclear Materials*, vol. 468, pp. 339–347, 2016, ISSN: 00223115. DOI: 10.1016/j.jnucmat.2015.04.001.

[169] S. Leber, "Preferred Orientations in Swaged and Drawn Tungsten Wire," *Transaction of the Metallurgical Society of AIME*, vol. 233, pp. 953–959, 1965.

[170] W. J. Hosford Jr., "Microstructural Changes During Deformation of [011] Fiber-Textured Metals," *Transaction of the Metallurgical Society of AIME*, no. 230, pp. 12–15, 1964.

[171] J. F. Peck and D. A. Thomas, "A Study of Fibrous Tungsten and Iron," *Transaction of the Metallurgical Society of AIME*, vol. 221, pp. 1240–1246, 1961.

[172] E. S. Meieran and D. A. Thomas, "Structure of Drawn and Annealed Tungsten Wire," *Transaction of the Metallurgical Society of AIME*, vol. 223, pp. 937–943, 1965.

[173] M. R. Ripoll and J. Očenášek, "Microstructure and texture evolution during the drawing of tungsten wires," *Engineering Fracture Mechanics*, vol. 76, no. 10, pp. 1485–1499, 2009, ISSN: 00137944. DOI: 10.1016/j.engfracmech.2009.02.012.

[174] P. Van Houtte, "Some Recent Developments in the Theories for Deformation Texture Prediction," in *Proceedings of 7. Inter. Conf. on Texture of Materials*, C. M. Brakman, Ed., Zwijndrecht: Netherlands Society for Materials, 1984, pp. 7–23.

[175] L. Haus, "Tungsten Composites and their Recrystallization Behaviour," Master Thesis, TU Bergakademie Freiberg, Freiberg, 2018.

[176] S. K. Yerra, B. Verlinden, and P. van Houtte, "On Crystallographic Texture of As-Drawn Doped-W Wires," *Materials Science Forum*, vol. 495-497, pp. 913–918, 2005. DOI: 10.4028/www.scientific.net/MSF.495-497.913.

[177] P. F. Browning, C. L. Briant, K. Rajan, and B. A. Knudsen, "An Analysis of Splitting Failures during the Drawing of Tungsten Wires," *Engineering Failure Analysis*, vol. 2, no. 2, pp. 105–115, 1995. DOI: 10.1016/1350-6307(95)00010-N.

[178] V. Nikolić, J. Riesch, and R. Pippan, "The effect of heat treatments on pure and potassium doped drawn tungsten wires: Part I - Microstructural characterization," *Materials Science and Engineering: A*, vol. 737, pp. 422–433, 2018, ISSN: 09215093. DOI: 10.1016/j.msea.2018.09.027.

[179] D. B. Snow, "The recrystallization of commercially pure and doped tungsten wire drawn to high strain," *Metallurgical Transactions A*, vol. 10, no. 7, pp. 815–821, 1979, ISSN: 0360-2133. DOI: 10.1007/BF02658299.

[180] L. Uray, A. Sulyok, and P. Tekula-Buxbaum, "Factors Influencing the Recrystallization of Non-Sag Tungsten Wires Indicated by the Out-Diffusion of Cobalt," *High Temperatures Materials and Processes*, vol. 24, no. 5, 2005.

[181] G. Rieck, "Growth and preferred orientations of crystals in tungsten wires," *Acta Metallurgica*, vol. 6, no. 5, pp. 360–366, 1958. DOI: 10.1016/0001-6160(58)90073-7.

[182] G. D. Rieck, "The Effect of Temperature and Deformation on the Recrystallization of Doped Tungsten Wires," *Acta Metallurgica*, vol. 9, pp. 825–834, 1961.

[183] D. B. Snow, "The Recrystallization of Heavily-Drawn Doped Tungsten Wire," *Metallurgical Transactions A*, vol. 7, pp. 783–794, 1976.

[184] J. L. Walter and E. F. Koch, "The relationship of microstructure to mechanical properties of Al-, Si-, K-doped tungsten wire," *Journal of Materials Science*, vol. 26, pp. 505–509, 1991.

[185] A. Butz, M. Rodriguez Ripoll, and O. Benevolenski, "Modeling the evolution of microstructure in single and dual phase polycrystalline metals under large plastic deformation," in *Modelling of Heterogeneous Materials with Applications in Construction and Biomedical Engineering*, Z. Bittnar and B. Mang, Eds., 2007.

[186] L. Bartha, E. Lassner, W.-D. Schubert, and B. Lux, *The Chemistry of Non-Sag Tungsten*, 1st ed. Oxford: Pergamon, 1995, ISBN: 9780080426761. [Online]. Available: http://gbv.eblib.com/patron/FullRecord.aspx?p=1838339.

[187] A. Szökefalvi-Nagy, G. Radnoczi, and I. Gaal, "Stage IV recovery in deformed tungsten," *Materials Science and Engineering*, vol. 93, pp. 39–43, 1987, ISSN: 00255416. DOI: 10.1016/0025-5416(87)90410-1.

[188] A. J. Opinsky, J. L. Orehotsky, and C. W. W. Hoffman, "X-Ray Diffraction Analysis of Crystallite Size and Lattice Strain in Tungsten Wire," *Journal of Applied Physics*, vol. 33, no. 2, pp. 708–712, 1962, ISSN: 0965-9773. DOI: 10.1063/1.1702492.

[189] R. Michel, Y. Bienvenu, A. Chesnaud, and A. Thorel, "Study of the tensile behaviour of tungsten wires from ambient temperature to 320 °C in relation to their microstructure," *International Journal of Refractory Metals and Hard Materials*, vol. 92, p. 105 325, 2020, ISSN: 02634368. DOI: 10.1016/j.ijrmhm.2020.105325.

[190] E. Pink and K. Sedlatschek, "The Brittle-Ductile Transition of Body-Centered Cubic Metals with Special Consideration of Tungsten and Molybdenum: Part I: Experimental Methods," *METALL*, vol. 23, no. 12, pp. 1249–1257, 1969.

[191] A. Barna, I. Gaal, O. Geszti-Herkner, G. Radnóczi, and L. Uray, "Comments on the Fibre Structure of K-Si-Al Doped Tungsten Wires," *High Temperatures - High Pressures*, vol. 10, no. 2, 1978.

[192] G. L. Davis, "Recrystallisation of Tungsten Wires," *Metallurgia*, vol. 58, pp. 177–183, 1958.

[193] D. M. Moon and R. Stickler, "Creep of fine wires of powder metallurgical tungsten," *Philosophical Magazine*, vol. 24, no. 191, pp. 1087–1094, 1971, ISSN: 1478-6435. DOI: 10.1080/14786437108217071.

[194] P. K. Wright, "The high temperature creep behavior of doped tungsten wire," *Metallurgical Transactions A*, vol. 9, no. 7, pp. 955–963, 1978, ISSN: 0360-2133. DOI: 10.1007/BF02649840.

[195] J. Riesch *et al.*, "Tensile behaviour of drawn tungsten wire used in tungsten fibre-reinforced tungsten composites," *Physica Scripta*, vol. T170:014032 // T170, p. 014 032, 2017. DOI: 10.1088/1402-4896/aa891d.

[196] J. Riesch *et al.*, "Properties of drawn W wire used as high performance fibre in tungsten fibre-reinforced tungsten composite," *IOP Conference Series: Materials Science and Engineering*, vol. 139, p. 012 043, 2016, ISSN: 1757-8981. DOI: 10.1088/1757-899X/139/1/012043.

[197] V. Nikolić, J. Riesch, M. J. Pfeifenberger, and R. Pippan, "The effect of heat treatments on pure and potassium doped drawn tungsten wires: Part II – Fracture properties," *Materials Science and Engineering: A*, vol. 737, pp. 434–447, 2018, ISSN: 09215093. DOI: 10.1016/j.msea.2018.09.029.

[198] K. Ren, L. Chen, Y. Cheng, J. Wang, and H. Duan, "A grain level model for deformation and failure of ultrafine-grained tungsten," *Science China Technological Sciences*, vol. 62, no. 5, pp. 755–761, 2019, ISSN: 1674-7321. DOI: 10.1007/s11431-018-9439-4.

[199] E. Pink and I. Gaál, "Mechanical Properties and Deformation Mechanisms of Non-Sag Tungsten Wires," in *The Metallurgy of Doped/Non-Sag Tungsten*, E. Pink and L. Bartha, Eds., Essex: Elsevier Applied Science, 1989, pp. 209–234, ISBN: 1-85166-390-8.

[200] T. Millner, L. Varga, and B. Verö, "The Role of Fibre Boundaries During Drawing of Powder Metallurgical Tungsten Wires," *Zeitschrift für Metallkunde*, vol. 63, no. 11, pp. 754–756, 1972.

[201] H. Schultz, "Untersuchungen über Gitterfehlstellen in kaltverformtem Wolfram mit Hilfe von Restwiderstandsmessungen," *Zeitschrift für Naturkunde*, vol. 14, pp. 361–373, 1959.

[202] P. Zhao *et al.*, "Microstructure, mechanical behaviour and fracture of pure tungsten wire after different heat treatments," *International Journal of Refractory Metals and Hard Materials*, vol. 68, pp. 29–40, 2017, ISSN: 02634368. DOI: 10.1016/j.ijrmhm.2017.06.001.

[203] D. Terentyev, J. Riesch, S. Lebediev, A. Bakaeva, and J. W. Coenen, "Mechanical properties of as-fabricated and 2300 °C annealed tungsten wire tested up to 600 °C," *International Journal of Refractory Metals and Hard Materials*, vol. 66, pp. 127–134, 2017, ISSN: 02634368. DOI: 10.1016/j.ijrmhm.2017.03.011.

[204] J. R. Davis, *Tensile Testing*, 1st ed. Ohio: ASM International, 2004, ISBN: 0-87170-806-X.

[205] DIN EN ISO, *Metallic materials – Tensile testing: Part 1: Method of test at room temperature*, Berlin, 2017.

[206] M. P. Groover, *Fundamentals of Modern Manufacturing: Materials, Processes, and Systems*, 4th ed. Hoboken, New Jersey: John Wiley & Sons, Inc., 2010, ISBN: 9780470467002.

[207] D. W. A. Rees, *Basic engineering plasticity: An introduction with engineering and manufacturing applications*, 1st ed. Boston MA: Elsevier, 2006, ISBN: 0750680253.

[208] D. G. Morris, "Strengthening mechanisms in nanocrystalline metals," in *Nanostructured Metals and Alloys*, S. H. Wang, Ed., Amsterdam: Elsevier, 2011, pp. 299–328, ISBN: 9781845696702. DOI: 10.1533/9780857091123.3.299.

[209] J. L. Martin, B. Lo Piccolo, T. Kruml, and J. Bonneville, "Characterization of thermally activated dislocation mechanisms using transient tests," *Materials Science and Engineering: A*, vol. 322, no. 1-2, pp. 118–125, 2002, ISSN: 09215093. DOI: 10.1016/S0921-5093(01)01124-8.

[210] P. Spätig, J. Bonneville, and J.-L. Martin, "A new method for activation volume measurements: application to Ni3(Al,Hf)," *Materials Science and Engineering: A*, no. 167, pp. 73–79, 1993, ISSN: 09215093.

[211] B.J. Inkson, "Scanning electron microscopy (SEM) and transmission electron microscopy (TEM) for materials characterization," in *Materials Characterization Using Nondestructive Evaluation (NDE) Methods*, Gerhard Hübschen, Iris Altpeter, Ralf Tschuncky, and Hans-Georg Herrmann, Eds., Woodhead Publishing, 2016, pp. 17–43, ISBN: 978-0-08-100040-3. DOI: 10.1016/B978-0-08-100040-3.00002-X. [Online]. Available: https://www.sciencedirect.com/science/article/pii/B978008100040300002X.

[212] E. L. Murphy and R. H. Good and Jr., "Thermionic Emission, Field Emission, and the Transition Region," *Physical Review*, vol. 102, no. 6, pp. 1464–1473, 1956. DOI: 10.1103/PhysRev.102.1464.

[213] D. Shindo and T. Oikawa, *Analytical Electron Microscopy for Materials Science*. Tokyo: Springer Japan KK, 2002, ISBN: 978-4-431-70336-5. DOI: 10.1007/978-4-431-66988-3.

[214] E. Fuchs, H. Oppholzer, and H. Rehme, *Particle Beam Microanalysis: Fundamentals, Methods and Applications*. New York: Weinheim/VCH Publishers, 1990, ISBN: 3-527-26884-7.

[215] J. I. Goldstein *et al.*, *Scanning Electron Microscopy and X-Ray Microanalysis*, 3rd ed. New York et al.: Kluwer Academic/Plenum Publishers, 2003, ISBN: 0-306-47292-9.

[216] T. E. Everhart and R. F. M. Thornley, "Wide-band detector for micro-microampere low-energy electron currents," *Journal of Scientific Instruments*, vol. 37, pp. 246–248, 1960. DOI: 10.1088/0950-7671/37/7/307.

[217] A. J. Schwartz, M. Kumar, B. L. Adams, and D. P. Field, *Electron Backscatter Diffraction in Materials Science*. Boston, MA: Springer US, 2009, ISBN: 978-0-387-88135-5. DOI: 10.1007/978-0-387-88136-2.

[218] W. H. Bragg and W. L. Bragg, "The reflection of X-rays by crystals," *Proceedings of the Royal Society of London. Series A, Containing Papers of a Mathematical and Physical Character*, vol. 88, no. 605, 1913. DOI: 10.1098/rspa.1913.0040.

[219] O. Engler and V. Randle, *Introduction to texture analysis: Macrotexture, microtexture, and orientation mapping*, 2nd ed. Boca Raton: CRC Press, 2010, ISBN: 9781420063653.

[220] S. Nishikawa and S. Kikuchi, "Diffraction of Cathode Rays by Mica," *Nature*, vol. 30, pp. 1019–1020, 1928. DOI: 10.1038/1211019a0.

[221] N. C. Krieger Lassen, "Automated Determination of Crystal Orientations from Electron Backscattering Patterns," Ph.D. thesis, Technical University of Denmark, Lyngby, 1994.

[222] Y. H. Chen *et al.*, "A Dictionary Approach to Electron Backscatter Diffraction Indexing," *Microscopy and microanalysis : the official journal of Microscopy Society of America, Microbeam Analysis Society, Microscopical Society of Canada*, vol. 21, no. 3, pp. 739–752, 2015. DOI: 10.1017/S1431927615000756.

[223] N. C. Krieger Lassen, D. Juul Jensen, and K. Conradsen, "Image Processing Procedures for Analysis of Electron Back Scattering Patterns," *Scanning Microscopy*, vol. 6, no. 1, pp. 115–121, 1992.

[224] P. C. Hough, "Method and means for recognizing complex patterns," 3,069,654, 25.3.1960.

[225] J. Radon, "Über die Bestimmung von Funktionen längs gewisser Mannigfaltigkeiten," *Berichte über die Verhandlungen der Königlich-Sächsischen Akademie der Wissenschaften zu Leipzig. Mathematisch-Physische Klasse*, vol. 69, pp. 262–277, 1917.

[226] F. Humphreys, "Characterisation of fine-scale microstructures by electron backscatter diffraction (EBSD)," *Scripta Materialia*, vol. 51, no. 8, pp. 771–776, 2004, ISSN: 13596462. DOI: 10.1016/j.scriptamat.2004.05.016.

[227] F. J. Humphreys, Y. Huang, I. Brough, and C. Harris, "Electron backscatter diffraction of grain and subgrain structures - resolution considerations," *Journal of microscopy*, vol. 195, no. 3, pp. 212–216, 1999. DOI: 10.1046/j.1365-2818.1999.00579.x.

[228] F. Bachmann, R. Hielscher, and H. Schaeben, "Texture Analysis with MTEX – Free and Open Source Software Toolbox," *Solid State Phenomena*, vol. 160, pp. 63–68, 2010. DOI: 10.4028/www.scientific.net/SSP.160.63.

[229] P. R. Munroe, "The application of focused ion beam microscopy in the material sciences," *Materials Characterization*, vol. 60, no. 1, pp. 2–13, 2009, ISSN: 10445803. DOI: 10.1016/j.matchar.2008.11.014.

[230] J. Orloff, *Handbook of charged particle optics*, 2nd ed. Boca Raton: CRC Press/Taylor & Francis, 2009, ISBN: 9781420045543.

[231] R. M. Langford, "Focused ion beams techniques for nanomaterials characterization," *Microscopy research and technique*, vol. 69, no. 7, pp. 538–549, 2006, ISSN: 1059-910X. DOI: 10.1002/jemt.20324.

[232] D. B. Williams and C. B. Carter, *Transmission electron microscopy: A textbook for materials science*, 2nd ed. New York: Springer, 2008, ISBN: 9780387765006.

[233] C. Colliex, "From early to present and future achievements of EELS in the TEM," *The European Physical Journal Applied Physics*, vol. 97, p. 38, 2022, ISSN: 1286-0042. DOI: 10.1051/epjap/2022220012.

[234] L. Reimer and H. Kohl, *Transmission electron microscopy: Physics of image formation* (Springer series in optical sciences), 5th ed. New York NY: Springer, 2008, vol. 36, ISBN: 9780387400938.

[235] B. Fultz and J. Howe, *Transmission Electron Microscopy and Diffractometry of Materials*. Berlin, Heidelberg: Springer Berlin Heidelberg, 2013, ISBN: 978-3-642-29760-1. DOI: 10.1007/978-3-642-29761-8.

[236] L. Spieß, G. Teichert, R. Schwarzer, H. Behnken, and C. Genzel, *Moderne Röntgenbeugung: Röntgendiffraktometrie für Materialwissenschaftler, Physiker und Chemiker* (Studium), 2., überarb. und erw. Aufl. Wiesbaden: Vieweg + Teubner, 2009, ISBN: 9783835101661.

[237] D. Rafaja, "Röntgendiffraktometrie," in *Moderne Methoden der Werkstoffprüfung*, H. Biermann and L. Krüger, Eds., Wiley-VCH Verlag GmbH & Co. KGaA, 2015, pp. 255–298.

[238] G. F. Harrington and J. Santiso, "Back-to-Basics tutorial: X-ray diffraction of thin films," *Journal of Electroceramics*, vol. 47, no. 4, pp. 141–163, 2021, ISSN: 1385-3449. DOI: 10.1007/s10832-021-00263-6.

[239] G. Williamson and W. Hall, "X-ray line broadening from filed aluminium and wolfram," *Acta Metallurgica*, vol. 1, no. 1, pp. 22–31, 1953. DOI: 10.1016/0001-6160(53)90006-6.

[240] B. E. Warren and B. L. Averbach, "The Effect of Cold-Work Distortion on X-Ray Patterns," *Journal of Applied Physics*, vol. 21, no. 6, pp. 595–599, 1950, ISSN: 0965-9773. DOI: 10.1063/1.1699713.

[241] E. J. Mittemeijer and P. Scardi, Eds., *Diffraction Analysis of the Microstructure of Materials* (Springer Series in Materials Science), 1st ed. Springer Berlin Heidelberg, 2004, vol. 68, ISBN: 978-3-642-07352-6. DOI: 10.1007/978-3-662-06723-9.

[242] U. F. Kocks, C. N. Tomé, and H.-R. Wenk, *Texture and Anisotropy: Preferred Orientations in Polycrystals and their Effect on Materials Properties*. Cambridge: Cambridge University Press, 1998, ISBN: 0521465168.

[243] T. Ungár, G. Ribárik, J. Gubicza, and P. Hanák, "Dislocation Structure and Crystallite Size Distribution in Plastically Deformed Metals Determined by Diffraction Peak Profile Analysis," *Journal of Engineering Materials and Technology*, vol. 124, no. 1, pp. 2–6, 2002, ISSN: 0094-4289. DOI: 10.1115/1.1418364.

[244] T. Ungár, "Dislocation densities, arrangements and character from X-ray diffraction experiments," *Materials Science and Engineering: A*, vol. 309-310, pp. 14–22, 2001, ISSN: 09215093. DOI: 10.1016/S0921-5093(00)01685-3.

[245] M. Wilkens, "Theoretical Aspects of Kinematical X-Ray Diffraction Profiles from Crystals containing Dislocation Distributions," in *Fundamental Aspects of Dislocation Theory*, J. A. Simmons, R. de Wit, and R. Bullough, Eds., 1969, pp. 1195–1221.

[246] M. Wilkens, "The determination of density and distribution of dislocations in deformed single crystals from broadened X-ray diffraction profiles," *Physica Status Solidi (a)*, vol. 2, pp. 359–370, 1970, ISSN: 00318965.

[247] A. Borbély, "The modified Williamson-Hall plot and dislocation density evaluation from diffraction peaks," *Scripta Materialia*, vol. 217, p. 114 768, 2022, ISSN: 13596462. DOI: 10.1016/j.scriptamat.2022.114768.

[248] T. Ungár and G. Tichy, "The Effect of Dislocation Contrast on X-Ray Line Profiles in Untextured Polycrystals," *Physica Status Solidi (a)*, vol. 171, no. 2, pp. 425–434, 1999, ISSN: 00318965. DOI: 10.1002/(SICI)1521-396X(199902)171:2<425::AID-PSSA425>3.0.CO;2-W.

[249] T. Ungár, I. Dragomir, Á. Révész, and A. Borbély, "The contrast factors of dislocations in cubic crystals: the dislocation model of strain anisotropy in practice," *Journal of Applied Crystallography*, vol. 32, no. 5, pp. 992–1002, 1999. DOI: 10.1107/S0021889899009334.

[250] T. Ungár and A. Borbély, "The effect of dislocation contrast on x-ray line broadening: A new approach to line profile analysis," *Applied Physics Letters*, vol. 69, no. 21, pp. 3173–3175, 1996, ISSN: 0003-6951. DOI: 10.1063/1.117951.

[251] P. Scardi, M. Leoni, and R. Delhez, "Line broadening analysis using integral breadth methods: a critical review," *Journal of Applied Crystallography*, vol. 37, no. 3, pp. 381–390, 2004. DOI: 10.1107/S0021889804004583.

[252] I. Groma, T. Ungár, and M. Wilkens, "Asymmetric X-ray line broadening of plastically deformed crystals. I. Theory," *Journal of Applied Crystallography*, vol. 21, no. 1, pp. 47–54, 1988. DOI: 10.1107/S0021889887009178.

[253] I. T. Jolliffe and J. Cadima, "Principal component analysis: a review and recent developments," *Philosophical transactions. Series A, Mathematical, physical, and engineering sciences*, vol. 374, no. 2065, p. 20 150 202, 2016. DOI: 10.1098/rsta.2015.0202.

[254] C. Suh, A. Rajagopalan, X. Lo, and K. Rajan, "The application of Principal Component Analysis to materials science data," *Data Science Journal*, vol. 1, no. 1, pp. 19–26, 2006. DOI: 10.2481/dsj.1.19.

[255] H. Abdi and L. J. Williams, "Principal component analysis," *Wiley Interdisciplinary Reviews: Computational Statistics*, vol. 2, no. 4, pp. 433–459, 2010, ISSN: 19395108. DOI: 10.1002/wics.101.

[256] E. Macherauch and H.-W. Zoch, *Praktikum in Werkstoffkunde: 91 ausführliche Versuche aus wichtigen Gebieten der Werkstofftechnik*, 11th ed. Vieweg+Teubner Verlag / Springer Fachmedien Wiesbaden GmbH Wiesbaden, 2011, ISBN: 978-3-8348-0343-6.

[257] J. C. Russ and R. T. Dehoff, *Practical Stereology*, 2nd ed. New York: Springer Science+Business Media, LLC, 2000, ISBN: 978-1-4613-5453-6.

[258] B. Ilschner and R. F. Singer, *Werkstoffwissenschaften und Fertigungstechnik*. Berlin, Heidelberg: Springer Berlin Heidelberg, 2016, ISBN: 978-3-642-53890-2. DOI: 10.1007/978-3-642-53891-9.

[259] Deutsches Institut für Normung and International Organization for Standardization, *DIN EN ISO 643:2020-06: Stahl - Mikrophotographische Bestimmung der erkennbaren Korngröße*. DOI: 10.31030/3141695.

[260] G. Baldwin-Olguin, "Telecentric lens for precision machine vision," in *Proceedings of the Second Iberoamerican Meeting on Optics*, D. Malacara, Ed., SPIE, 1996, pp. 440–443.

[261] W. J. Smith, *Modern Optical Engineering*, 4th ed. McGraw-Hill Education Ltd and SPIE Press, 2007, ISBN: 978-0071476874.

[262] R. Lowrie and A. M. Gonas, "Single-Crystal Elastic Properties of Tungsten from 24° to 1800°C," *Journal of Applied Physics*, vol. 38, no. 11, pp. 4505–4509, 1967, ISSN: 0965-9773. DOI: 10.1063/1.1709158.

[263] B. Ilkiv *et al.*, "Electronic Structure of Hollow Graphitic Carbon Nanoparticles Fabricated from Acetylene Carbon Black," *Fullerenes, Nanotubes and Carbon Nanostructures*, vol. 23, no. 5, pp. 449–454, 2015, ISSN: 1536-383X. DOI: 10.1080/1536383X.2014.885957.

[264] Z. L. Zhang, Hauge, M., Ødegård, J., and C. Thaulow, "Determining material true stress-strain curve from tensile specimens with rectangular cross!section," *International Journal of Solids and Structures*, vol. 36, pp. 3497–3516, 1999.

[265] F. F. Schmidt and H. R. Ogden, "The Engineering Properties of Tungsten and Tungsten Alloys," in *Defense Metals Infomation Centre Reports*, vol. 191, Columbus, Ohio, 1963. [Online]. Available: https://apps.dtic.mil/sti/pdfs/AD0425547.pdf.

[266] J. H. Hollomon, "Tensile Deformation," *Transactions of the Metallurgical Society of AIME*, vol. 162, pp. 268–290, 1945.

[267] P. Ludwik, *Elemente der Technologischen Mechanik*, 1st ed. Berlin and Heidelberg: Springer, 1909, ISBN: 978-3-662-40293-1. DOI: 10.1007/978-3-662-40293-1.

[268] H. Alexander and P. Haasen, "Dislocations and Plastic Flow in the Diamond Structure," in ser. Solid State Physics, Seitz, Turnbull, and Ehrenreich, Eds., vol. 22, Elsevier, 1969, pp. 27–158. DOI: 10.1016/S0081-1947(08)60031-4.

[269] U. Essmann and M. Rapp, "Slip in Copper Crystals following Weak Neutron Bombardement," *Acta Metallurgica*, vol. 21, pp. 1305–1317, 1973.

[270] W. H. Press, S. A. Teukolsky, W. T. Vetterling, and B. P. Flannery, *Numerical Recipes: The Art of Scientific Computing*, 3rd ed. Cambridge: Cambridge University Press, 2007, ISBN: 978-0-511-33555-6.

[271] P. E. Gill, W. Murray, and M. H. Wright, *Practical Optimization*, 1st edition. London: Academic Press, 1982.

[272] M.S. Duesbery, N.P. Louat, and K. Sadananda, "The mechanics and energetics of cross-slip," *Acta Metallurgica et Materialia*, vol. 40, no. 1, pp. 149–158, 1992. DOI: 10.1016/0956-7151(92)90208-V. [Online]. Available: https://www.sciencedirect.com/science/article/pii/095671519290208V.

[273] W. Püschl, "Models for dislocation cross-slip in close-packed crystal structures: a critical review," *Progress in Materials Science*, vol. 47, no. 4, pp. 415–461, 2002. DOI: 10.1016/S0079-6425(01)00003-2. [Online]. Available: https://www.sciencedirect.com/science/article/pii/S0079642501000032.

[274] I. S. Yasnikov, A. Vinogradov, and Y. Estrin, "Revisiting the Considère criterion from the viewpoint of dislocation theory fundamentals," *Scripta Materialia*, vol. 76, pp. 37–40, 2014, ISSN: 13596462. DOI: 10.1016/j.scriptamat.2013.12.009.

[275] H. Becker and W. Pantleon, "Work-hardening stages and deformation mechanism maps during tensile deformation of commercially pure titanium," *Computational Materials Science*, vol. 76, pp. 52–59, 2013, ISSN: 09270256. DOI: 10.1016/j.commatsci.2013.03.028.

[276] P. S. Follansbee, *Fundamentals of Strength: Principles, Experiment, and Applications of an Internal State Variable Constitutive Formulation*. Hoboken, New Jersey: John Wiley & Sons, 2014, ISBN: 978-1-118-41341-8.

[277] P. Schade, "Bubble evolution and effects during tungsten processing," *International Journal of Refractory Metals and Hard Materials*, vol. 20, pp. 301–309, 2002, ISSN: 02634368.

[278] A. Considère, *Annales des ponts et chaussées I*, no. 574, 1885.

[279] E. W. Hart, "Theory of the Tensile Test," *Acta Metallurgica*, vol. 15, pp. 351–355, 1967.

[280] I. S. Yasnikov, Y. Kaneko, M. Uchida, and A. Vinogradov, "The grain size effect on strain hardening and necking instability revisited from the dislocation density evolution approach," *Materials Science and Engineering: A*, vol. 831, p. 142 330, 2022, ISSN: 09215093. DOI: 10.1016/j.msea.2021.142330.

[281] A. Vinogradov, "Mechanical Properties of Ultrafine-Grained Metals: New Challenges and Perspectives," *Advanced Engineering Materials*, vol. 17, no. 12, pp. 1710–1722, 2015, ISSN: 14381656. DOI: 10.1002/adem.201500177.

[282] C. A. Schneider, W. S. Rasband, and K. W. Eliceiri, "NIH Image to ImageJ: 25 years of image analysis," *Nature methods*, vol. 9, no. 7, pp. 671–675, 2012. DOI: 10.1038/nmeth.2089.

[283] A. Hoffmann and I. Wesemann, "Potassium Doped Tungsten beyond Incandescent Lamp Wires," *International Journal of Powder Metallurgy*, vol. 47, no. 1, 2011.

[284] J. Gil Sevillano, C. García-Rosales, and J. Flaquer Fuster, "Texture and large-strain deformation microstructure," *Philosophical transactions. Series A, Mathematical, physical, and engineering sciences*, vol. 357, pp. 1603–1619, 1999. DOI: 10.1098/rsta.1999.0392.

[285] F. J. Humphreys, "Grain and subgrain characterisation by electron backscatter diffraction: A review," *Journal of Materials Science*, vol. 36, pp. 3833–3854, 2001.

[286] V. Pratt, "Direct least-squares fitting of algebraic surfaces," *ComputerGraphics*, vol. 21, no. 4, 1987. DOI: 10.1145/37402.37420.

[287] E. Pink and R. Eck, "Refractory Metals and Their Alloys," in *Materials Science and Technology*, R. W. Cahn and E. J. Kramer, Eds., Weinheim: Wiley-VCH Verlag GmbH & Co. KGaA, 1996.

[288] J. Očenášek, M. R. Ripoll, S. M. Weygand, and H. Riedel, "Multi-grain finite element model for studying the wire drawing process," *Computational Materials Science*, vol. 39, no. 1, pp. 23–28, 2007, ISSN: 09270256. DOI: 10.1016/j.commatsci.2006.01.024.

[289] D. Terentyev *et al.*, "Micromechanical and microstructural properties of tungsten fibers in the as-produced and annealed state: Assessment of the potassium doping effect," *International Journal of Refractory Metals and Hard Materials*, vol. 81, pp. 253–271, 2019, ISSN: 02634368. DOI: 10.1016/j.ijrmhm.2019.03.012.

[290] D. B. Snow, "The Recrystallization of Non-Sag Tungsten Wire," in *The Metallurgy of Doped/Non-Sag Tungsten*, E. Pink and L. Bartha, Eds., Essex: Elsevier Applied Science, 1989, pp. 189–202, ISBN: 1-85166-390-8.

[291] J. K. Mackenzie, "Second Paper on Statistics associated with the Random Distribution of Cubes," *Biometrika*, vol. 45, no. 1, pp. 229–240, 1958.

[292] P. Li, Y.-L. Hua, S.-L. Yan, Y.-F. Zhou, X.-F. Wei, and K.-M. Xue, "Strengthening mechanisms of pure tungsten subjected to high pressure torsion: Deviation from classic Hall-Petch relation," *Materialwissenschaft und Werkstofftechnik*, vol. 51, no. 3, pp. 338–348, 2020, ISSN: 0933-5137. DOI: 10.1002/mawe.201900052.

[293] D. Juul Jensen, "Effects of orientation correlations on misorientation distributions in cold-deformed aluminium," *Materials Science and Engineering: A*, vol. 234, pp. 762–765, 1997, ISSN: 09215093.

[294] D. A. Hughes and N. Hansen, "High Angle Boundaries Formed by Grain Subdivision Mechanisms," *Acta Materialia*, vol. 45, no. 9, pp. 3871–3886, 1997, ISSN: 13596454.

[295] P. Lied, C. Bonnekoh, W. Pantleon, M. Stricker, A. Hoffmann, and J. Reiser, "Comparison of K-doped and pure cold-rolled tungsten sheets: As-rolled condition and recrystallization behaviour after isochronal annealing at different temperatures," *International Journal of Refractory Metals and Hard Materials*, vol. 85, p. 105 047, 2019, ISSN: 02634368. DOI: 10.1016/j.ijrmhm.2019.105047.

[296] S. Singh, Y. Guo, B. Winiarski, T. L. Burnett, P. J. Withers, and M. de Graef, "High resolution low kV EBSD of heavily deformed and nanocrystalline Aluminium by dictionary-based indexing," *Scientific reports*, vol. 8, no. 1, p. 10 991, 2018. DOI: 10.1038/s41598-018-29315-8.

[297] Z. Ding, E. Pascal, and M. de Graef, "Indexing of electron back-scatter diffraction patterns using a convolutional neural network," *Acta Materialia*, vol. 199, pp. 370–382, 2020, ISSN: 13596454. DOI: 10.1016/j.actamat.2020.08.046.

[298] K. Pearson, "IX. Mathematical contributions to the theory of evolution.—XIX. Second supplement to a memoir on skew variation," *Philosophical Transactions of the Royal Society of London. Series A, Containing Papers of a Mathematical or Physical Character*, vol. 216, pp. 429–457, 1916. DOI: 10.1098/rsta.1916.0009.

[299] P. Barnes, S. Jacques, and M. Vickers, *Peak Shape Functions: III. Pearson VII*, London, 2006. [Online]. Available: http://pd.chem.ucl.ac.uk/pdnn/peaks/pvii.htm.

[300] M. M. Hall Jr., V. G. Veeraraghavan, H. Rubin, and P. G. Winchell, "The approximation of symmetric X-ray peaks by Pearson type Vll distributions," *Journal of Applied Crystallography*, vol. 10, pp. 66–68, 1977.

[301] J. G. van Berkum, "Strain fields in crystalline materials: Methods of analysis based on X-ray diffraction-line broadening," Dissertation, TU Delft, Delft, 1994. [Online]. Available: https://repository.tudelft.nl/islandora/object/uuid:f59cd03e-fd2d-43cf-98e3-001ca630f9b6/datastream/OBJ/download.

[302] C. Schimpf, "On the microstructure defects in hexagonal BN and their impact on the high pressure/high temperature phase transition to the dense BN polymorphs," Dissertation, Technische Universität Bergakademie Freiberg, Freiberg, 2013.

[303] A. Wilson, *Röntgenstrahlpulverdiffraktometrie: Mathematische Theorie*. Eindhoven: Philips Technische Bibliothek, 1965.

[304] A. Borbély, J. Dragomir-Cernatescu, G. Ribárik, and T. Ungár, "Computer program ANIZC for the calculation of diffraction contrast factors of dislocations in elastically anisotropic cubic, hexagonal and trigonal crystals," *Journal of Applied Crystallography*, vol. 36, no. 1, pp. 160–162, 2003. DOI: 10.1107/S0021889802021581.

[305] International Centre for Diffraction Data, Ed., *Powder Diffraction File 4-806*, 2014.

[306] T. Ungár, H. Mughrabi, D. Rönnpagel, and M. Wilkens, "X-Ray Line-Broadening Study of the Dislocation Cell Structure in Deformed [001]-Oriented Copper Single Crystals," *Acta Metallurgica et Materialia*, vol. 32, no. 3, pp. 333–342, 1984.

[307] P. Scardi and M. Leoni, "Whole Powder Pattern Modelling: Theory and Applications," in *Diffraction Analysis of the Microstructure of Materials*, ser. Springer Series in Materials Science, E. J. Mittemeijer and P. Scardi, Eds., Springer Berlin Heidelberg, 2004, pp. 51–92, ISBN: 978-3-642-07352-6.

[308] H. Mecking, "Deformation of Polycrystals," in *Strength of Metals and Alloys*, P. Haasen, V. Gerold, and G. Kostorz, Eds., vol. 3, Oxford: Pergamon, 1979, pp. 1573–1594.

[309] U. F. Kocks, "Superposition of Alloy Hardening, Strain Hardening, and Dynamic Recovery," in *Strength of Metals and Alloys*, P. Haasen, V. Gerold, and G. Kostorz, Eds., vol. 3, Oxford: Pergamon, 1979, pp. 1661–1680.

[310] Y. M. Wang, Hamza A. V., and E. Ma, "Temperature-dependent strain rate sensitivity and activation volume of nanocrystalline Ni," *Acta Materialia*, vol. 54, no. 10, pp. 2715–2726, 2006, ISSN: 13596454. DOI: 10.1016/j.actamat.2006.02.013.

[311] J. Gubicza, *Defect Structure and Properties of Nanomaterials*, 1st edition. Elsevier, 2017, ISBN: 978-0-08-101917-7.

[312] F. Javaid and K. Durst, "Stress-driven grain boundary movement during nanoindentation in tungsten at room temperature," *Materialia*, vol. 1, pp. 99–103, 2018, ISSN: 25891529. DOI: 10.1016/j.mtla.2018.04.002.

[313] R. Z. Valiev, I. V. Alexandrov, Y. T. Zhu, and T. C. Lowe, "Paradox of strength and ductility in metals processed by severe plastic deformation," *Journal of Materials Research*, vol. 17, no. 1, pp. 5–8, 2002.

[314] R. N. Stevens, "Grain-Boundary Sliding in Metals," *Metallurgical Reviews*, vol. 11, no. 1, pp. 129–142, 1966, ISSN: 0076-6690. DOI: 10.1179/mtlr.1966.11.1.129.

[315] Q. Wei, S. Cheng, K. Ramesh, and E. Ma, "Effect of nanocrystalline and ultrafine grain sizes on the strain rate sensitivity and activation volume: fcc versus bcc metals," *Materials Science and Engineering: A*, vol. 381, no. 1-2, pp. 71–79, 2004, ISSN: 09215093. DOI: 10.1016/j.msea.2004.03.064.

[316] K. Leitner, "The role of grain boundaries and segregation effects in molybdenum and its alloys," Dissertation, Montanuniversität Leoben, Leoben, 2017.

[317] B. Gludovatz, S. Wurster, T. Weingärtner, A. Hoffmann, and R. Pippan, "Influence of impurities on the fracture behaviour of tungsten," *Philosophical Magazine*, vol. 91, no. 22, pp. 3006–3020, 2011, ISSN: 1478-6435. DOI: 10.1080/14786435.2011.558861.

[318] M. J. Pfeifenberger, V. Nikolić, S. Žák, A. Hohenwarter, and R. Pippan, "Evaluation of the intergranular crack growth resistance of ultrafine grained tungsten materials," *Acta Materialia*, vol. 176, pp. 330–340, 2019, ISSN: 13596454. DOI: 10.1016/j.actamat.2019.06.051.

[319] G. Merziger, G. Mühlbach, D. Wille, and T. Wirth, *Formeln + Hilfen Höhere Mathematik*, 7th ed. Barsinghausen: Binomi Verlag, 2014.

[320] Q. Wei, L. J. Kecskes, and K. T. Ramesh, "Effect of low-temperature rolling on the propensity to adiabatic shear banding of commercial purity tungsten," *Materials Science and Engineering: A*, vol. 578, pp. 394–401, 2013, ISSN: 09215093. DOI: 10.1016/j.msea.2013.04.109.

[321] T. Hao *et al.*, "Strength and ductility improvement of ultrafine-grained tungsten produced by equal-channel angular pressing," *Journal of Nuclear Materials*, vol. 455, no. 1-3, pp. 595–599, 2014, ISSN: 00223115. DOI: 10.1016/j.jnucmat.2014.08.044.

[322] I. S. Yasnikov, Y. Estrin, and A. Vinogradov, "What governs ductility of ultrafine-grained metals? A microstructure based approach to necking instability," *Acta Materialia*, vol. 141, pp. 18–28, 2017, ISSN: 13596454. DOI: 10.1016/j.actamat.2017.08.069.

[323] W. Blum and X. H. Zeng, "A simple dislocation model of deformation resistance of ultrafine-grained materials explaining Hall–Petch strengthening and enhanced strain rate sensitivity," *Acta Materialia*, vol. 57, no. 6, pp. 1966–1974, 2009, ISSN: 13596454. DOI: 10.1016/j.actamat.2008.12.041.

[324] A. Vinogradov and Y. Estrin, "Analytical and numerical approaches to modelling severe plastic deformation," *Progress in Materials Science*, vol. 95, pp. 172–242, 2018. DOI: 10.1016/j.pmatsci.2018.02.001.

[325] J. Rösler, H. Harders, and M. Bäker, *Mechanisches Verhalten der Werkstoffe*. Wiesbaden: Springer Fachmedien Wiesbaden, 2012, ISBN: 978-3-8348-1818-8. DOI: 10.1007/978-3-8348-2241-3.

[326] R. Reiff-Musgrove *et al.*, "Effect of Relatively Low Levels of Porosity on the Plasticity of Metals and Implications for Profilometry-Based Indentation Plastometry," *Advanced Engineering Materials*, vol. 24, no. 12, p. 2 200 642, 2022, ISSN: 1438-1656. DOI: 10.1002/adem.202200642.

[327] P. Schade, "Wire drawing failures and tungsten fracture phenomena," *International Journal of Refractory Metals and Hard Materials*, vol. 24, no. 4, pp. 332–337, 2006, ISSN: 02634368. DOI: 10.1016/j.ijrmhm.2005.09.003.

[328] N. H. Loh, "The Mechanics of Drawing Wire at Elevated Temperatures," Ph.D. thesis, University of Aston, Birmingham, 1983.

[329] E. Felder, C. Levrau, M. Mantel, and N. G. Truong Dinh, "Identification of the work of plastic deformation and the friction shear stress in wire drawing," *Wear*, vol. 286-287, pp. 27–34, 2012, ISSN: 00431648. DOI: 10.1016/j.wear.2011.05.029.

[330] G. Ericsson, "Advanced Neutron Spectroscopy in Fusion Research," *Journal of Fusion Energy*, vol. 38, no. 3-4, pp. 330–355, 2019, ISSN: 0164-0313. DOI: 10.1007/s10894-019-00213-9.

[331] I. A. Ovid'ko and A. G. Sheinerman, "Irradiation-induced amorphization processes in nanocrystalline solids," *Applied Physics A*, vol. 81, no. 5, pp. 1083–1088, 2005, ISSN: 0947-8396. DOI: 10.1007/s00339-004-2960-z.

[332] S. Wurster and R. Pippan, "Nanostructured metals under irradiation," *Scripta Materialia*, vol. 60, no. 12, pp. 1083–1087, 2009, ISSN: 13596462. DOI: 10.1016/j.scriptamat.2009.01.011.

[333] D. E. Armstrong and T. B. Britton, "Effect of dislocation density on improved radiation hardening resistance of nano-structured tungsten–rhenium," *Materials Science and Engineering: A*, vol. 611, pp. 388–393, 2014, ISSN: 09215093. DOI: 10.1016/j.msea.2014.06.013.

[334] A. Zinovev *et al.*, "Effect of neutron irradiation on ductility of tungsten foils developed for tungsten-copper laminates," *Nuclear Materials and Energy*, vol. 30, p. 101 133, 2022, ISSN: 23521791. DOI: 10.1016/j.nme.2022.101133.

[335] C. Wang *et al.*, "Microstructures, Thermal and Mechanical Properties of Pure Tungsten—A Comparison Between Selective Laser Melting and Hot Rolling," *Chinese Journal of Mechanical Engineering*, vol. 35, no. 1, 2022, ISSN: 1000-9345. DOI: 10.1186/s10033-022-00712-5.

[336] I. L. Dillamore and W. T. Roberts, "Preferred Orientation in Wrought and Annealed Metals," *Metallurgical Reviews*, vol. 10, no. 1, pp. 271–380, 1965, ISSN: 0076-6690. DOI: 10.1179/mtlr.1965.10.1.271.

[337] G. Pintsuk *et al.*, "Materials for in-vessel components," *Fusion Engineering and Design*, vol. 174, p. 112 994, 2022, ISSN: 09203796. DOI: 10.1016/j.fusengdes.2021.112994.

[338] J. Reiser *et al.*, "Ductilisation of tungsten (W): Tungsten laminated composites," *International Journal of Refractory Metals and Hard Materials*, vol. 69, pp. 66–109, 2017, ISSN: 02634368. DOI: 10.1016/j.ijrmhm.2017.07.013.

[339] P. Lied *et al.*, "Comparison of K-doped and pure cold-rolled tungsten sheets: Microstructure restoration in different temperature regimes," *International Journal of Refractory Metals and Hard Materials*, vol. 113, 2023, ISSN: 02634368.

[340] T. Hao, Z. Q. Fan, S. X. Zhao, G. N. Luo, C. S. Liu, and Q. F. Fang, "Microstructures and properties of ultrafine-grained tungsten produced by equal-channel angular pressing at low temperatures," *Journal of Nuclear Materials*, vol. 433, no. 1-3, pp. 351–356, 2013, ISSN: 00223115. DOI: 10.1016/j.jnucmat.2012.10.007.

[341] W. D. Coolidge, "Tungsten and method of making the same for use as filaments of incandescent electric lamps and for other purposes," 1913.

[342] P. W. Trimby, "Orientation mapping of nanostructured materials using transmission Kikuchi diffraction in the scanning electron microscope," *Ultramicroscopy*, vol. 120, pp. 16–24, 2012. DOI: 10.1016/j.ultramic.2012.06.004.

[343] K. Makii, T. Tsutsumi, Y. Aono, and E. Kuramoto, "Understanding of Irradiation Softening in α-Iron from the Viewpoint of the Direct Interaction between a Screw Dislocation and Self Interstitial Atoms under Stress," *Materials Transactions*, vol. 30, no. 7, pp. 505–515, 1989.

[344] D. Brunner and J. Diehl, "The Effect of Atomic Lattice Defects on the Softening Phenomena of High-Purity α-Iron," *Physica Status Solidi (a)*, vol. 160, no. 2, pp. 355–372, 1997, ISSN: 00318965. DOI: 10.1002/1521-396X(199704)160:2<355::AID-PSSA355>3.0.CO;2-S.

[345] Y. Aono, E. Kuramoto, D. Brunner, and J. Diehl, "Irradiation Softening and the Interaction of Moving Dislocations with Frenkel-Pairs in α-Iron," *Materials Science Forum*, vol. 15-18, pp. 801–808, 1987. DOI: 10.4028/www.scientific.net/MSF.15-18.801.

[346] G. B. Gibbs, "The activation parameters for dislocation glide," *Philosophical Magazine*, vol. 16, no. 139, pp. 97–102, 1967, ISSN: 1478-6435. DOI: 10.1080/14786436708229259.

[347] T. Kruml, O. Coddet, and J. L. Martin, "About the determination of the thermal and athermal stress components from stress-relaxation experiments," *Acta Materialia*, vol. 56, no. 3, pp. 333–340, 2008, ISSN: 13596454. DOI: 10.1016/j.actamat.2007.09.027.

[348] F. Roters, "A new concept for the calculation of the mobile dislocation density in constitutive models of strain hardening," *physica status solidi (b)*, vol. 240, no. 1, pp. 68–74, 2003, ISSN: 0370-1972. DOI: 10.1002/pssb.200301873.

[349] M. A. Groeber and M. A. Jackson, "DREAM.3D: A Digital Representation Environment for the Analysis of Microstructure in 3D," *Integrating Materials and Manufacturing Innovation*, vol. 3, no. 5, 2014.

[350] T. Helfer, B. Michel, J.-M. Proix, M. Salvo, J. Sercombe, and M. Casella, "Introducing the open-source mfront code generator: Application to mechanical behaviours and material knowledge management within the PLEIADES fuel element modelling platform," *Computers & Mathematics with Applications*, vol. 70, no. 5, pp. 994–1023, 2015, ISSN: 08981221. DOI: 10.1016/j.camwa.2015.06.027.

[351] H. Moulinec and P. Suquet, "A numerical method for computing the overall response of nonlinear composites with complex microstructure," *Computer Methods in Applied Mechanics and Engineering*, vol. 157, pp. 69–94, 1998.

[352] F. Willot, "Fourier-based schemes for computing the mechanical response of composites with accurate local fields," *Comptes Rendus Mécanique*, vol. 343, no. 3, pp. 232–245, 2015, ISSN: 16310721. DOI: 10.1016/j.crme.2014.12.005.

[353] J.-P. Aubry, *Beginning with Code_Aster*, 2nd ed. Lyon: Framasoft, 2019, ISBN: 979-10-92674-03-3.

[354] Deutsches Institut für Normung, *Grundlagen der Messtechnik - Teil 4: Auswertung von Messungen; Meßunsicherheit*, 1999. DOI: 10.31030/8036548.

[355] W. Leo, *Techniques for Nuclear and Particle Physics Experiments*, 1st ed. Springer, 1987, ISBN: 978-3-540-57280-0. DOI: 10.100/978-3-642-57920-2.

[356] W. Walcher, *Praktikum der Physik*, 8th ed. Wiesbaden: Vieweg+Teubner Verlag, 2004, ISBN: 978-3-519-43016-2. DOI: 10.1007/978-3-322-96815-9.

Appendices

Appendix A

Uncertainty estimation

A.1 Fundamental equations

Error calculations and estimations were performed in order to enable an assessment of the quality and reliability of the measured datasets and their evaluation. The equation used for calculating the error of a function $f(x_i)$ $(i = 1 \dots N)$, Δf, with respect to independent variables x_i possessing themselves errors Δx_i is taken from the German standard DIN 1319-4 [354] and is known as the *Gaussian error propagation equation*:

$$\begin{aligned}\Delta f &= \sqrt{\left(\frac{\partial f}{\partial x_1}\cdot\Delta x_1\right)^2+\left(\frac{\partial f}{\partial x_2}\cdot\Delta x_2\right)^2+\dots+\left(\frac{\partial f}{\partial x_N}\cdot\Delta x_N\right)^2}\\ &= \sqrt{\sum_{i=1}^{N}\left(\frac{\partial f}{\partial x_i}\cdot\Delta x_i\right)^2}\end{aligned} \tag{A.1}$$

where f : Function
Δf : Uncertainty of the function f
x_i : Variables characterising the function f with $i = 1 \dots N$
Δx_i : Individual uncertainties of the variables entering the function f with $i = 1 \dots N$

If several values x_i $(i = 1 \dots N)$ shall be combined to calculate a mean value $\langle x \rangle$ and its associated error $\Delta\langle x \rangle$, the errors of the variables can be considered following [355, p. 90]

$$\langle x \rangle = \frac{\sum_{i=1}^{N}\frac{x_i}{(\Delta x_i)^2}}{\sum_{i=1}^{N}\frac{1}{(\Delta x_i)^2}} \tag{A.2}$$

$$\Delta\langle x \rangle = \sqrt{\frac{1}{\sum_{i=1}^{N}\frac{1}{(\Delta x_i)^2}}}. \tag{A.3}$$

where $\langle x \rangle$: Mean of the individual values
$\Delta\langle x \rangle$: Uncertainty of the mean value
x_i : Individual values with $i = 1 \dots N$
Δx_i : Uncertainties associated with the individual values with $i = 1 \dots N$

A weighted mean can be calculated according to the following equation [356]:

$$\langle x_\omega \rangle = \frac{\sum_{i=1}^{N} x_i \, \omega_\mathrm{i}}{\sum_{i=1}^{N} \omega_\mathrm{i}} = \sum_{i=1}^{N} x_i \, \tilde{\omega}_\mathrm{i} \tag{A.4}$$

where $\langle x_\omega \rangle$: Weighted mean of the individual values
ω_i : Individual weight for variable i with $i = 1 \ldots N$
$\tilde{\omega}_\mathrm{i}$: Normalised individual weight for variable i with $i = 1 \ldots N$
x_i : Individual values $(i = 1 \ldots N)$

The uncertainty of the weighted mean [270] can be estimated using

$$\Delta\langle x_\omega \rangle = \sqrt{\frac{1}{N-1} \sum_{i=1}^{N} \tilde{\omega}_\mathrm{i} \, (x_\mathrm{i} - \langle x_\omega \rangle)^2}. \tag{A.5}$$

where $\langle x_\omega \rangle$: Weighted mean of the individual values
ω_i : Individual weight for variable i with $i = 1 \ldots N$
$\tilde{\omega}_\mathrm{i}$: Normalised individual weight for variable i with $i = 1 \ldots N$
x_i : Individual values $(i = 1 \ldots N)$

A.2 Implementation of uncertainty estimations for the study of drawn tungsten wires

Although it can only serve as an estimate, the benefit of using the Gaussian error propagation for approximating the uncertainty is that it requires a small number of assumptions. The basic errors used in the course of this study are summarised in table A.1.

Table A.1: Basic error estimates used for the Gaussian error propagation method. The symbols d and F represent the wire diameter and the mechanical load, respectively.

Type of uncertainty		Magnitude	Source
Error of conversion factor px $\rightarrow$ m in µm px^{-1}		0.025	measured
Tracking error of digital image correlation software in px		0.25	approximated
Relative error of wire diameter d		$0.015\,d$	manufacturer
Error of temperature measurement in K		1	approximated
Relative error of load measurement as a function of the load cell capacity	20 N	$0.025\,F$	manufacturer
	200 N	$0.025\,F$	
	5 kN	$0.02\,F$	

Appendix B

Additional information on mechanical properties and microstructure of drawn tungsten wires

B.1 Mechanical properties and deformation mechanisms

B.1.1 Statistics of (successful) mechanical tests

Table B.1 shows the number of valid uniaxial tensile tests, strain-rate jump tests and repeated stress relaxation experiments performed in the course of this study. The details of the tests like the chosen strain-rates and the relaxation time, load and number can be found in section 5.2.1.2.2 and in figures 7.1, 7.2, 7.3 and 7.4.

Table B.1: Number of mechanical tests performed in the course of this study.

		Number of valid...		
Wire diameter d in µm	φ	...uniaxial tensile tests	...strain-rate jump tests	...repeated stress relaxation experiments
950	2.7	20	6	5
490	4.0	37	6	11
150	6.4	19	3	13
41	9.0	13	5	3
16	10.8	13	3	7

B.1.2 Scatter of elastic moduli determined in mechanical tests

As mentioned in section 6, the elastic moduli determined in mechanical tests deviated slightly from the ideal value at room temperature [262]. As a consequence, the strain was adjusted so that the slope in the elastic region matched E_{ideal}. The scatter of the measured elastic moduli is shown in figure B.1.

The scatter of the experimentally determined Young's modulus clearly shows that the moduli of thick wires ($d \geq 490\,\mu\mathrm{m}$) are systematically lower than the ones for thinner wires. This is

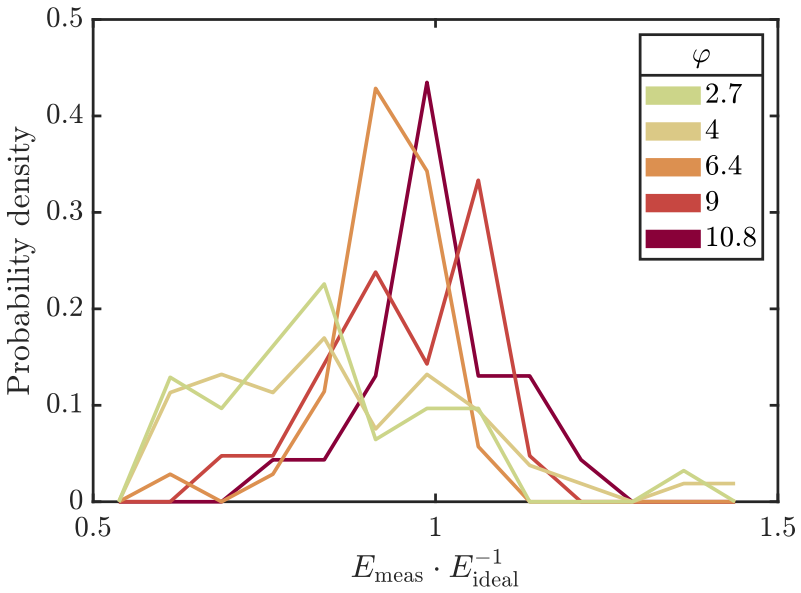

Figure B.1: Probability density of the ratio of measured to ideal Young's modulus [262] of tungsten wires at room temperature for different wire diameters. The values for E_{meas} were extracted from uniaxial tensile tests, repeated stress relaxation experiments and strain-rate jump tests.

most likely due to the different testing setup. The elastic moduli determined from thin wires ($d \leq 150\,\mu\mathrm{m}$) however, line up well with the ideal value.

B.1.3 Direct comparison of stress-strain behaviour of drawn tungsten wires with different accumulated drawing strains

For better comparability and to see the evolution of strength and stress with accumulated drawing strain, the engineering and true stress-strain curves are again shown in figure B.2.

B.1.4 Strain-rate sensitivity of the free fitting variables of the strain hardening model

Figure B.3 shows the extrapolated saturation stress as a function of the plastic strain rate.

The strain-rate sensitivities of all free fitting parameters of the strain hardening model are listed in table B.2.

Table B.2: Strain-rate sensitivities of σ_{i}, β, λ_{f} and k_2 determined following equation 8.1. Note that the strain-rate sensitivity n_{k_2} is the negative value of n'_{k_2} (see table 8.3) due to the definition of the strain-rate sensitivity (equation 4.17).

φ	$n_{\sigma_{\mathrm{i}}}$	n_{β}	n_{k_2}	$n_{\lambda_{\mathrm{f}}}$
2.7	(0.007 ± 0.006)	(0.108 ± 0.974)	(0.078 ± 0.268)	(-0.201 ± 0.505)
4.0	(0.012 ± 0.014)	(-0.201 ± 0.204)	(0.006 ± 0.065)	(-0.022 ± 0.157)
6.4	(0.009 ± 0.015)	(-0.0248 ± 0.1210)	(0.006 ± 0.029)	(0.002 ± 0.055)
9.0	(0.0110 ± 0.0138)	(-0.013 ± 0.134)	(-0.007 ± 0.057)	(0.007 ± 0.164)
10.8	(0.018 ± 0.030)	(0.088 ± 0.391)	(0.034 ± 0.073)	(0.067 ± 0.126)

Using the Considère criterion [278] (see equation 8.11 and (for the sake of simplicity) the Voce equation (cf. equation 4.14), a concise expression for the true stress at which plastic instabilities

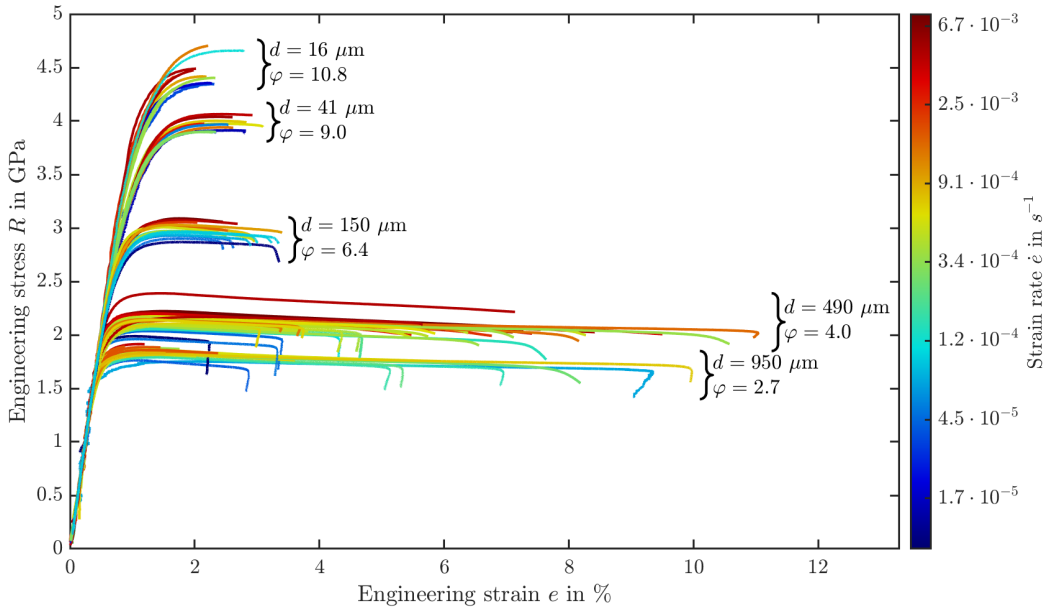

(a)

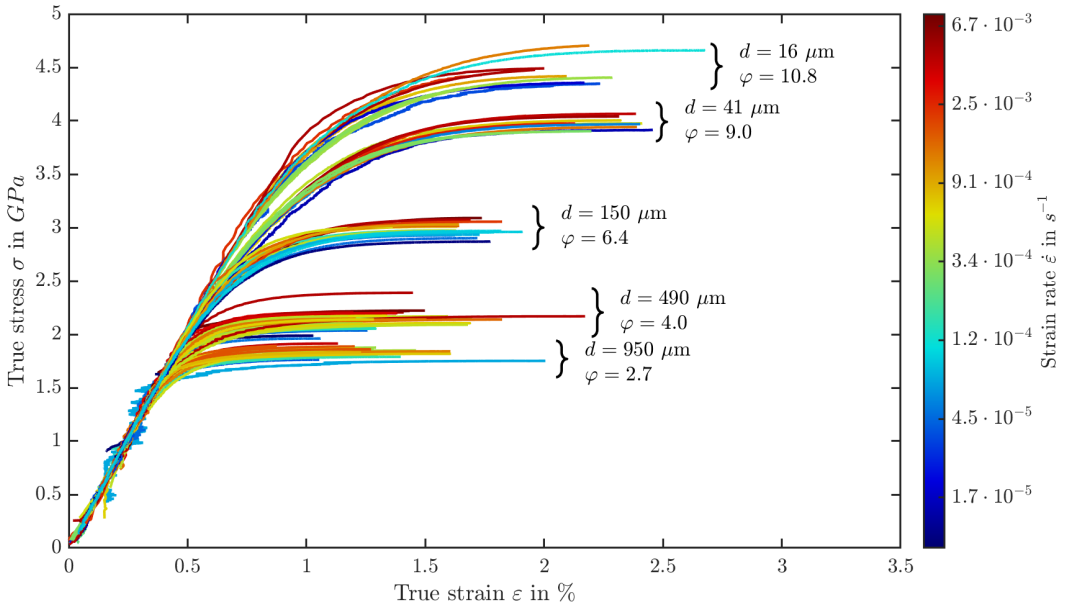

(b)

Figure B.2: Engineering (a) and true stress-strain curves (b) of tungsten wires with diameters between 950 µm and 16 µm. The strain rate is colour-coded using the colourbars to the right side of the diagrams.

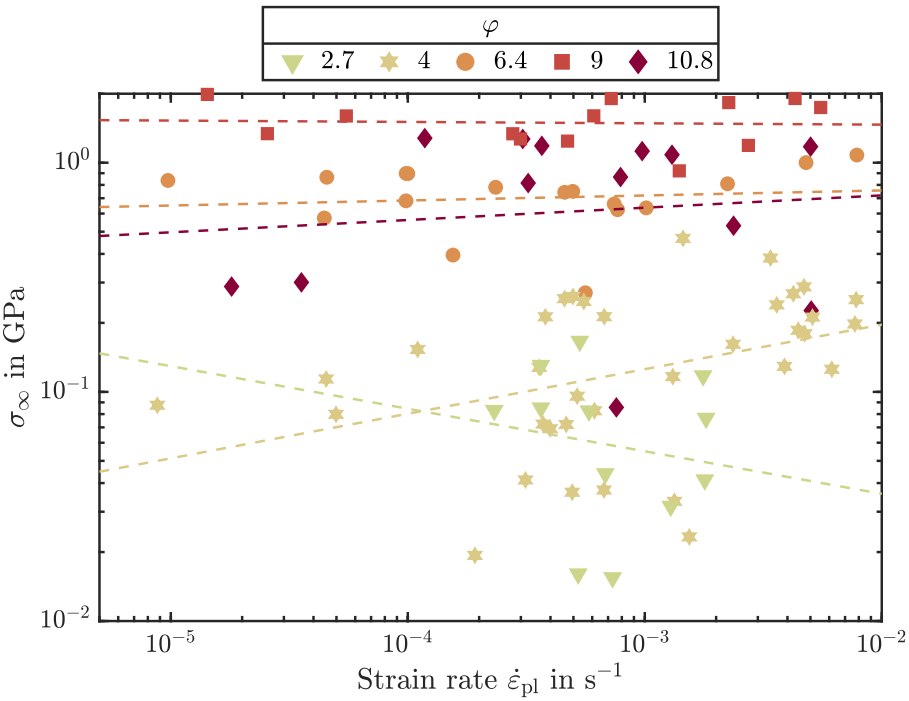

Figure B.3: Saturation stress σ_∞ vs. plastic strain rate $\dot{\varepsilon}_{\mathrm{pl}}$ for tungsten wires with different drawing strain φ. The straight lines fitted to the data (double logarithmic plot) belonging to one wire diameter represent a power-law relation. The slope of the straight lines thus equal the strain-rate sensitivity n of the saturation stress.

are expected (Considère stress), can be derived:

$$\sigma_{\mathrm{C}} = \frac{\sigma_\infty\,\theta_0}{\sigma_\infty + \theta_0} = \left(\frac{1}{\sigma_\infty} + \frac{1}{\theta_0}\right)^{-1} \tag{B.1}$$

where
σ_{C} : Considère stress
σ_∞ : Saturation stress
θ_0 : Initial strain hardening rate

Equation B.1 shows that the Considère equation is only different from the saturation stress by a factor proportional to θ_0^{-1}. Since the mean initial work hardening rate is very large ($13\,\mathrm{GPa} \leq \theta_0 \leq 510\,\mathrm{GPa}$, mean values for β from table 8.2), the inverse of the initial work hardening rate is very small. Converting the true Considère stress to an engineering Considère stress by using 5.5 and the uniform elongation furthermore represents a very small alteration. Thus, it can be concluded that it is permissible to use the ultimate tensile strength as a proxy for σ_∞ in order to estimate the strain-rate dependence of the recovery coefficient k_2.

B.1.5 Comparison of apparent and effective activation volumes

Figure B.4 shows both the apparent activation volume V_{app} (from strain-rate jump tests) and effective activation volume V_{eff} (from repeated stress relaxation experiments) in one diagram.

Since the two activation volumes were not measured at exactly the same applied stress, calcu-

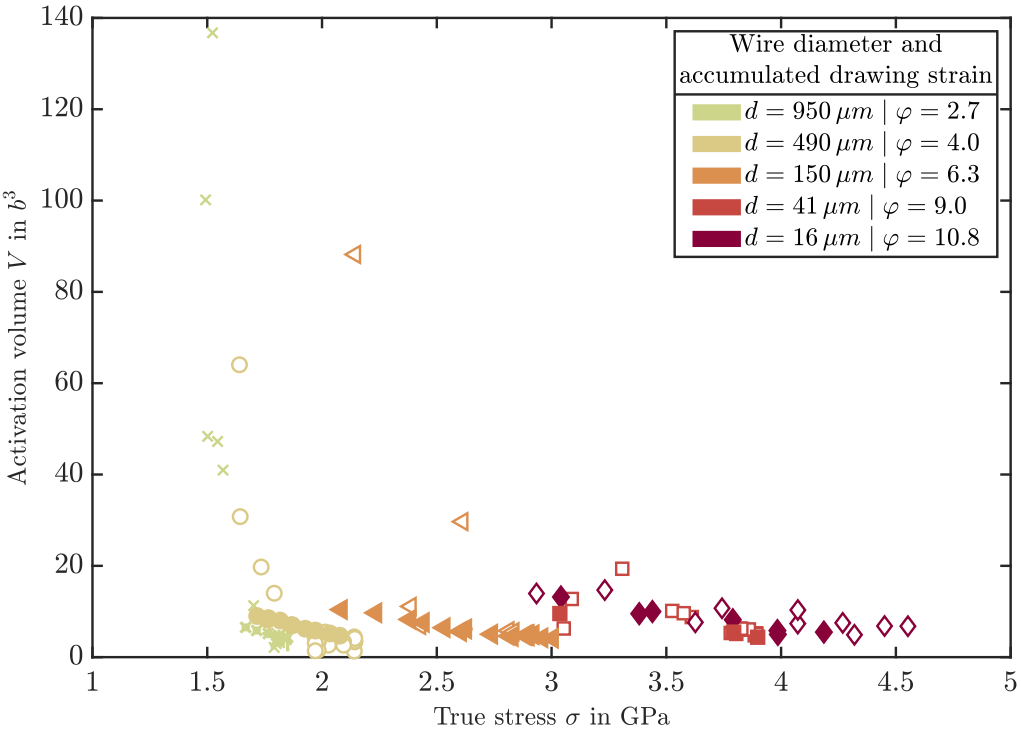

Figure B.4: Apparent (empty symbols, from SRJT) and effective activation volume (filled, from RSRE) as a function of true applied stress.

lating the commonly used ratio [80]

$$\Omega = \frac{V_{\text{app}}}{V_{\text{eff}}} \tag{B.2}$$

is not possible. Figure B.4 reveals that for high stresses, applied and effective activation volumes line up well. With decreasing accumulated drawing strain, the number of outliers at low stresses increases. One might hence argue that for high stresses, the apparent activation volume should have been treated as an equivalent to the effective activation volume. What is however not shown in figure B.4 for better visibility is the error of the apparent activation volume because it assumes values of

$$\Delta V_{\text{app}} \gg V_{\text{app}}.$$

It is concluded that the Gaussian error propagation (see equation A.1) is not able to treat the uncertainty of the apparent activation volume correctly. Thus, only the effective activation was used for the interpretation and discussion performed in section 8.

B.2 Microstructural evolution

B.2.1 Statistics of EBSD orientation maps

The number of orientation maps acquired for a given wire diameter, sample orientation (longitudinal section/transversal cross-section) and wire region (edge/centre) are listed in table B.3. Note that the orientation maps acquired for the thinnest wire were only used for analysing the radial

evolution of the misalignment angle between ⟨110⟩ and the wire (drawing) axis. For each wire with $\varphi \leq 9.0$, one of the LS samples was used for XRD analysis.

Table B.3: Number of orientation maps acquired from the wire edge or centre of longitudinal sections (LS) or transversal cross-sections of tungsten wire samples (accumulated drawing strain φ) using EBSD.

$\varphi = 0$	Edge	Centre
LS	0	5
TCS	1	1

$\varphi = 0.5$	Edge	Centre
LS	0	2
TCS	2	1

$\varphi = 1.4$	Edge	Centre
LS	0	1
TCS	3	2

$\varphi = 2.7$	Edge	Centre
LS	2	6
TCS	1	2

$\varphi = 4.0$	Edge	Centre
LS	0	11
TCS	1	2

$\varphi = 6.4$	Edge	Centre
LS	0	5
TCS	1	3

$\varphi = 9.0$	Edge	Centre
LS	0	2
TCS	1	2

$\varphi = 10.8$	Edge	Centre
LS	0	0
TCS	13	4

B.2.2 Aspect ratio of grains observed in transversal cross-sections

The ratio of the length and width A_{TCS} of grains in orientation maps acquired from TCS samples using EBSD are shown in B.5 as a function of the accumulated drawing strain. The transversal grain aspect ratio is defined as follows:

$$A_{\mathrm{TCS}} = \frac{L_{\mathrm{TCS}}}{w} \tag{B.3}$$

where
A_{TCS} : Transversal grain aspect ratio
w : Grain width
L_{TCS} : Grain length viewed in transversal direction

As the plot shows, the grain morphology deviates from an equiaxed shape ($A_{\mathrm{TCC}} = 1$). Instead, the grain length is about 2.5 to 3 times longer than the width. A_{TCS} seems to increase up to $\varphi = 6.4$ followed by a decrease for $\varphi = 9.0$. Based on equation B.3, an increase of the grain aspect ratio can be explained by an increase of grain length and/or a decrease of grain width with increasing φ. The latter has been verified experimentally, see section 8.4.2.2. The decrease of the grain aspect ratio can thus only be due to a decrease in grain length, since the width was shown to decrease further when increasing the accumulated drawing strain further from 6.4 to 9.0.

B.2.3 Geometrical considerations concerning slip in drawn tungsten wires

Due to the sharp fibre texture observed in drawn tungsten wires, the mean free path of dislocations emitted at a grain boundary can be estimated. The angle κ between two direction $[u_1 v_1 w_1]$ and $[u_2 v_2 w_2]$ in a cubic system is given by Hosford [113] as:

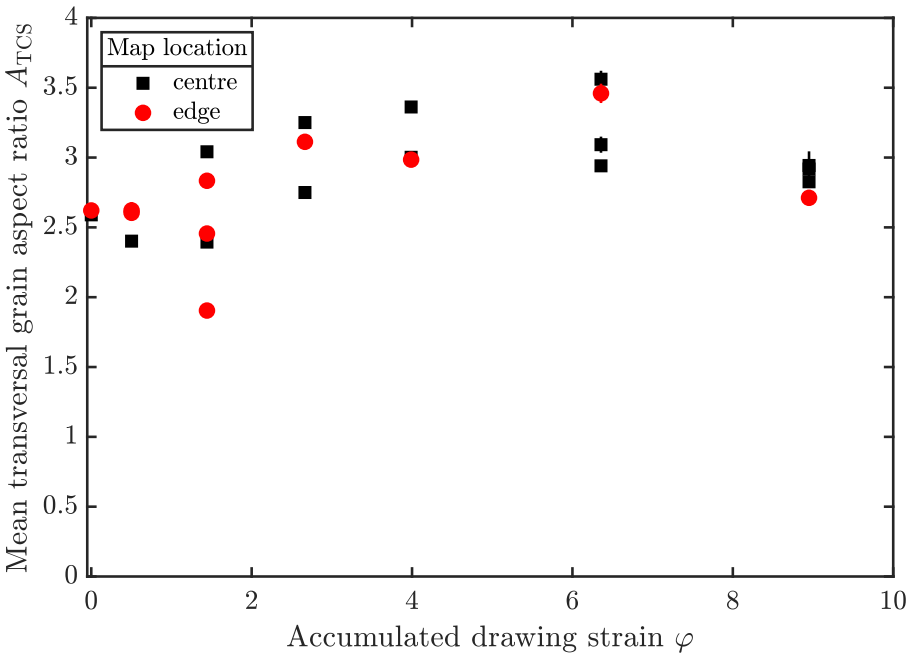

Figure B.5: Mean aspect ratio A_{TCS} of grains observed in transversal cross-sections of tungsten wires as a function of the wires' accumulated drawing strain. Aspect ratios of grains in the wire centre and edge are shown as black squares and red circles, respectively.

$$\cos\kappa = \frac{u_1\,u_2 + v_1\,v_2 + w_1\,w_2}{\sqrt{(u_1^2 + v_1^2 + w_1^2)\,(u_2^2 + v_2^2 + w_2^2)}} \tag{B.4}$$

where κ : Angle
$[u_1 v_1 w_1]$: Crystal direction 1
$[u_2 v_2 w_2]$: Crystal direction 2

In a tungsten wire exhibiting a perfect ⟨110⟩ fibre texture, the major axis of the elongated grains is parallel to the drawing direction. Assuming slip along ⟨111⟩ during a uniaxial tensile test, the angle between slip direction and load axis would be given by κ. Since the texture of tungsten wires deviates slightly from a perfect ⟨110⟩ fibre texture (see section 8.3.3), the misalignment angle between ⟨110⟩ and the wire axis $\vec{D}$, $\zeta_{\langle 110\rangle|\vec{\mathrm{D}}}$, can be used as an uncertainty of κ in order to estimate the real angle between load axis and slip direction. A sketch of the geometry is shown in figure B.6.

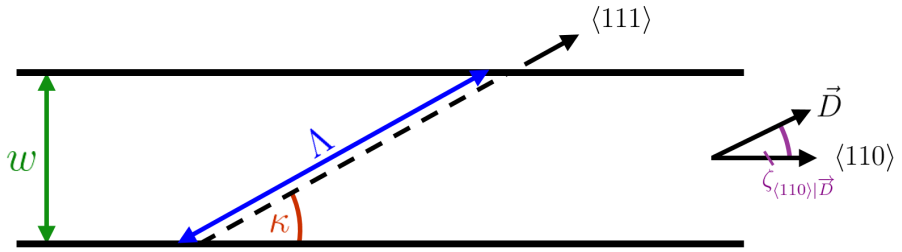

Figure B.6: Simplified sketch describing the geometry of an elongated grain with width w, which has an angle $\zeta_{\langle 110\rangle|\vec{\mathrm{D}}}$ between its ⟨110⟩ direction and the wire (drawing) axis $\vec{D}$. The dashed line represents the ⟨111⟩ slip direction.

Assuming the mean free path Λ of a dislocation emitted at a grain boundary source and traveling through the grain along a $\langle 111 \rangle$ slip direction by combining the determined misorientation angles $\zeta_{\langle 110 \rangle | \tilde{\mathrm{D}}}$ (see figure 8.13) and the mean grain widths (see figure 8.18), the mean free path Λ shown in figure B.7 can be determined.

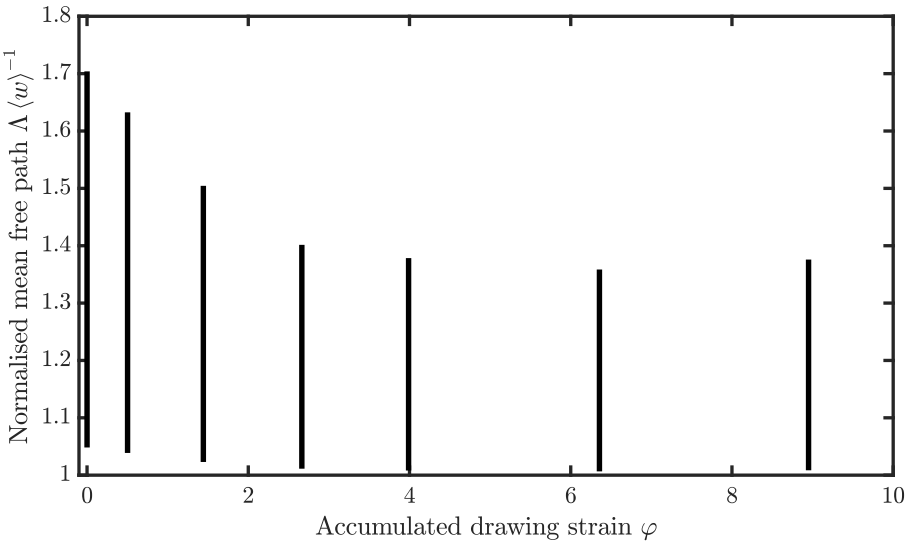

Figure B.7: Theoretical mean free path of dislocations emitted at a grain boundary in a drawn tungsten wire and slipping along $\langle 111 \rangle$. The range of the mean free path Λ (black lines) is normalised with the mean grain width determined for wires with the respective diameter.

As figure B.7 illustrates, the mean free path of a dislocation gliding according to the simple geometry shown in figure B.6 can be up to 170 % of the mean grain width $\langle w \rangle$.

B.2.4 Observation of porosity in STEM images

As clearly observable in the bottom part of figure B.8, the porosity of 16 µm tungsten wires is also visible in HAADF-STEM images. Thus, it can be concluded that the detection of pores in FIB-cut cross-sections of tungsten wires with diameters of 16 µm and 41 µm are not an artefact of the preparation but a microstructural feature.

B.2.5 Relative intensities of XRD peaks

The relative intensity

$$I_{\mathrm{rel,theor}} = \frac{I_{(\mathrm{hkl})}}{\max_{\{(hkl)\}} I_{(\mathrm{hkl})}} \tag{B.5}$$

where $I_{\mathrm{rel,theor}}$: Theoretical relative intensity
$I_{(\mathrm{hkl})}$: Intensity of the (hkl) reflection

of diffraction peaks should be independent of the instrument [236]. Calculating the relative intensities from the diffractograms helps to identify outliers. The results are shown in table B.4.

Considering the mean difference between measured and theoretical relative intensity, three outliers, namely the reflections 200, 211 and 321 are identified. Redrawing the modified Williamson-Hall plot, without considering these outliers, yields the result shown in figure B.9.

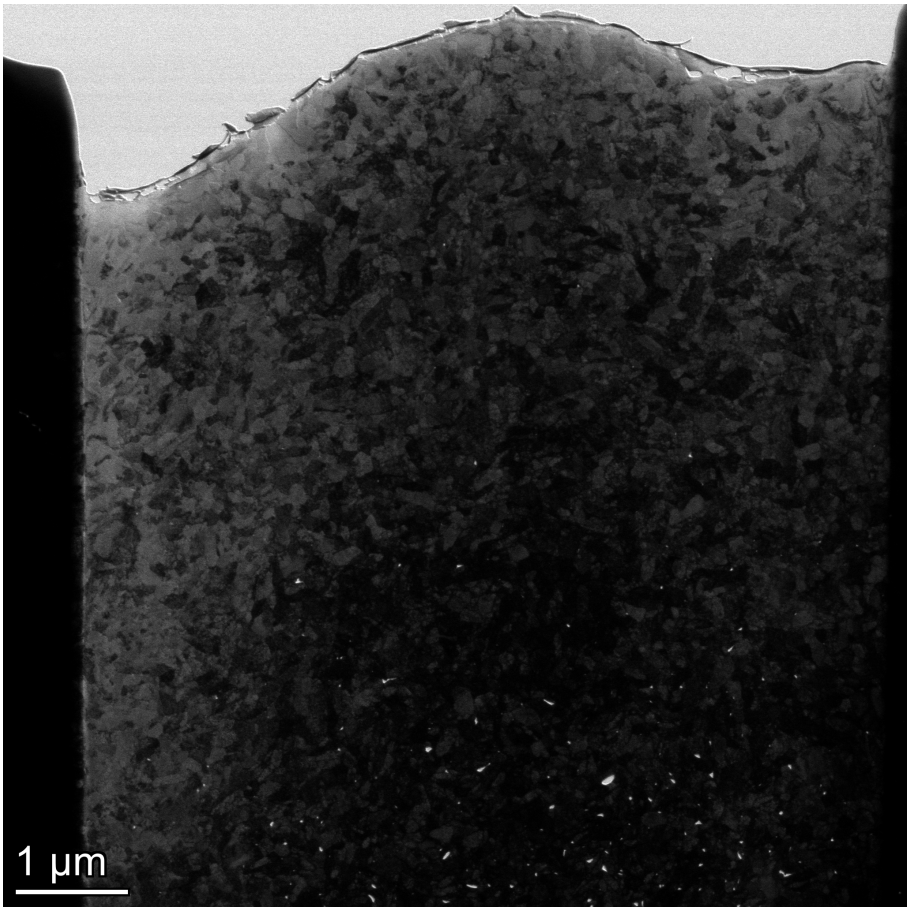

Figure B.8: HAADF-STEM image of the whole lamella cut from a drawn tungsten wire with a diameter of 16 µm. The bright regions in the lower part of the lamella can be clearly interpreted as pores.

Comparing the coefficients of determination of the fit of equation 5.24 to the data shown in figure B.9 (R^2_{purged}) to the one obtained from the fit of the same equation to the data with all reflections (R^2_{all}) shows that neglecting the outliers leads to an even worse description than considering all reflections:

$$R^2_{\text{all}} \geq R^2_{\text{purged}}.$$

Possible reasons for the low values of the integral breadth B of 310 and 200 reflection are discussed in section 8.4.2.6.

B.2.6 Grain boundary disorientation angle distribution

Figure B.10 shows the same plot as figure 8.25 but in a semilogarithmic way, making it easier to follow the evolution of the grain boundary disorientation angle with increasing accumulated drawing strain.

Table B.4: Relative intensities of diffraction peaks in the diffractograms of tungsten wires: For each reflection hkl, the theoretical [305] and the measured relative intensity is listed. The absolute deviation of the measured relative intensity from the theoretical value, $|I_{\mathrm{rel,theor}} - I_{\mathrm{rel,m}}|$, is also tabulated. Note that all values except for the accumulated drawing strain are given in %.

Reflection (hkl)		110	200	211	220	310	222	321
	Theoretical relative intensity $I_{\mathrm{rel,theor}}$	100	15	23	8	11	4	18
$\varphi\downarrow$	Mean deviation	0	53	42	2	8	6	12
0	$I_{\mathrm{rel,m}}$	100	46	57	10	21	11	26
	$\lvert I_{\mathrm{rel,theor}} - I_{\mathrm{rel,m}}\rvert$	0	31	34	2	10	7	8
0.5	$I_{\mathrm{rel,m}}$	100	100	92	6	17	5	28
	$\lvert I_{\mathrm{rel,theor}} - I_{\mathrm{rel,m}}\rvert$	0	85	69	2	9	1	10
1.4	$I_{\mathrm{rel,m}}$	100	99	98	7	10	9	21
	$\lvert I_{\mathrm{rel,theor}} - I_{\mathrm{rel,m}}\rvert$	0	84	75	1	1	5	3
2.7	$I_{\mathrm{rel,m}}$	100	89	70	7	3	11	6
	$\lvert I_{\mathrm{rel,theor}} - I_{\mathrm{rel,m}}\rvert$	0	74	47	1	8	7	12
4.0	$I_{\mathrm{rel,m}}$	100	79	71	9	1	13	2
	$\lvert I_{\mathrm{rel,theor}} - I_{\mathrm{rel,m}}\rvert$	0	64	48	1	10	9	16
6.4	$I_{\mathrm{rel,m}}$	100	26	28	6	1	6	1
	$\lvert I_{\mathrm{rel,theor}} - I_{\mathrm{rel,m}}\rvert$	0	11	5	2	10	9	16
9.0	$I_{\mathrm{rel,m}}$	100	36	36	6	2	15	3
	$\lvert I_{\mathrm{rel,theor}} - I_{\mathrm{rel,m}}\rvert$	0	21	13	2	9	11	15

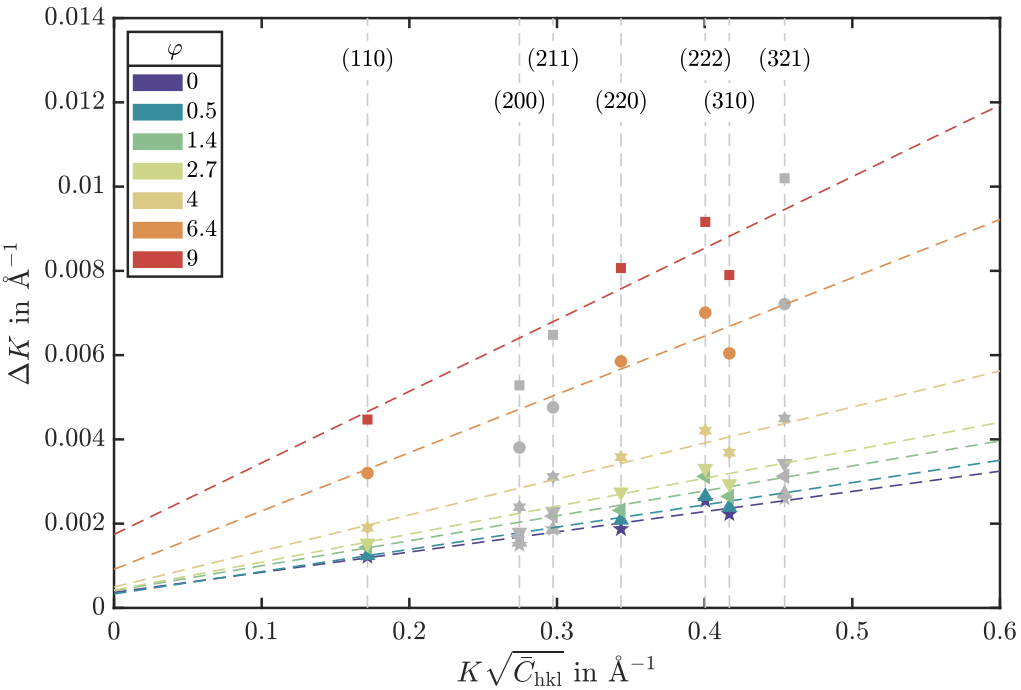

Figure B.9: Modified Williamson-Hall plot similar to figure 8.27 but without considering the 200, 211 and 321 reflection. Gray symbols mark the outliers. For details on the plot, see section 8.4.2.6.

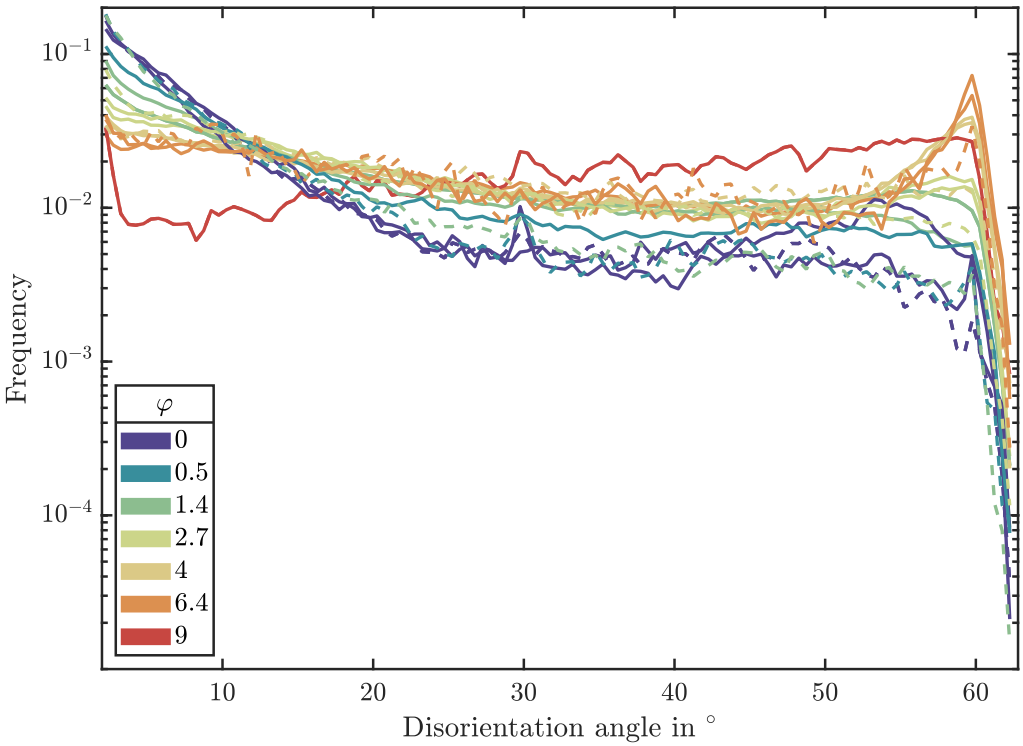

Figure B.10: Disorientation angle distribution between pixels in orientation maps for tungsten wires with different accumulated drawing strains. The ordinate is displayed logarithmically.

Acknowledgements

Zusammenfassend denke ich, äh, danke ich
Ihnen für dieses . . . für dies und das.
—Loriot

Since this work was not a one-man-show, I would like to use the opportunity to thank all colleagues and contributors for their collaboration and support.

First of all, I would like to thank Prof. Dr. Ulrich Stroth, head of the department "Plasma Edge and Wall" (E2M) at the Max Planck Insitute for Plasma Physics (IPP), for allowing me to conduct the research related to this dissertation at his department.

A very big "Thank you" goes to my doctoral supervisor Prof. Dr. Rudolf Neu (Max Planck Institute for Plasma Physics & Technical University of Munich) for his interest in my somewhat exotic topic and his support throughout the dissertation project. Thank you for critically assessing the progress and for many valuable suggestions.

I would like to thank Dr. Johann Riesch from the Max Planck Institute for Plasma Physics for mentoring me during my time as a Ph.D. student (and before that). Thanks for keeping me motivated, for asking the right (critical) question at the right time, for connecting me to the relevant persons, for showing empathy and simply for being a good guy!

Next, I would like to say "tusind tak" to Prof. Dr. Wolfgang Pantleon from the Technical University of Denmark, who served as Technical Advisor as well as second examiner of the dissertation. Thank you for all the stimulating discussions and for sharing your knowledge on all different topics related to this project with me.

Furthermore, I would like to thank Prof. Dr. Peter Mayr from the Technical University of Munich for chairing the examination committee.

A big “Thank You” goes to Till Höschen from the Max Planck Institute for Plasma Physics for his help with all things involving mechanical testing and design. Thanks for making time to support me, for your great ideas and your enjoyably bad sense of humour.

I would like to thank my collaborators from the ams OSRAM GmbH, Dr. Jürgen Almanstötter and Rainer Himml (1965-2022), for their unbureaucratic help and their valuable suggestions.

Moreover, I am grateful to Dr. Martin Balden, Katja Hunger and Stefan Elgeti from the Max Planck Institute for Plasma Physics for their support during sample preparation, electron

microscopic analyses and EBSD.

I would like to thank my "external" collaborators
- Dr. Barbara Wieluńska-Kús (Technical University of Warsaw) for STEM and TEM measurements,
- Dr. Marcin Rasiński (Forschungszentrum Jülich GmbH) for EBSD analyses,
- Prof. Dr. David Rafaja & Dr. Christian Schimpf (TU Bergakademie Freiberg) for their help with XRD analyses,
- Dr. Max Boleininger (UK Atomic Energy Authority) for fruitful discussions as well as
- Dr. Nico Hempel (Technical University of Munich) and Michael Pegritz (Erich-Schmid-Insitut für Materialwissenschaften) for their help and patience in the (so far) not yet rewarded efforts to perform high-temperature tensile tests on tungsten wires.

I am very grateful to all the students I had the pleasure to work with during my time as Ph.D. student — you guys taught me a lot. Thus, thanks to Nuttawan Ketkao, Omar Mohamed Abdelmoneim Abdelrahman, Batuhan Sancak, Sebastian Estermann, Ulrich Pototschnig and Johannes Mais.

The hard-working and diligent men of the workshop of the division E2M, in particular Robert Gieb, Robert Lang and Karl-Heinz Stemmer, cannot be thanked enough. Thanks for your speed, precision and the multitude of good ideas.

Moreover, I would like to thank my fellow Ph.D. students Alexander Feichtmayer, Robert Lürbke, Annemarie Kärcher, Philipp Sand and Dr. Kristof Kremer as well as all other colleagues at the IPP who have not been mentioned by name, for the nice working atmosphere.

Last but not least, I would like to thank my family for their continuous support, encouragement, interest, and love. You were always there for me to celebrate good times and helped me to overcome rougher times. I would not have made it without you.

Finally, I don't want to forget thanking my lovely partner and GöGa Lorena for her love, support, her sympathetic ear and for putting up with me in some of the more stressful periods in the course of this study. I'm very much looking forward to everything that is still to come for the two of us.